



UNA PUBLICACIÓN DE LA  
**SOMIB**  
Sociedad Mexicana de  
Ingeniería Biomédica

# Revista Mexicana de Ingeniería Biomédica

## New publishing model

*Continuous publication:*  
as soon as an article is prepared,  
it will be released online



**SOMIB**  
Sociedad Mexicana de  
Ingeniería Biomédica

# Sociedad Mexicana de Ingeniería Biomédica

La Mesa Directiva de la Sociedad Mexicana de Ingeniería Biomédica hace una extensa invitación a las personas interesadas en participar, colaborar y pertenecer como Socio Activo de la SOMIB. La SOMIB reúne a profesionistas que se desarrollan en áreas de Ingeniería Biomédica, principalmente ingenieros biomédicos, así como otros profesionistas afines con el desarrollo de tecnología para la salud.

## Membresía Estudiante

**\$850.00 PESOS MXN**

15% de descuento para grupos de 5 o más personas.

## Membresía Profesional

**\$1,450.00 PESOS MXN**

15% de descuento para grupos de 5 o más personas.

## Membresía Institucional

**\$11,600.00 PESOS MXN**

No aplica descuento.

## Membresía Empresarial

**\$20,000.00 PESOS MXN**

La suscripción empresarial requiere invitación.

EL PAGO CUBRE UN AÑO DE CUOTA. EN CASO DE REQUERIR FACTURA FAVOR DE SOLICITARLA, ADJUNTANDO COMPROBANTE DE PAGO Y ESPECIFICANDO CONCEPTO, AL CORREO ELECTRÓNICO: [facturación@somib.org.mx](mailto:facturación@somib.org.mx)

## **ib** Revista Mexicana de Ingeniería Biomédica

### AUTORES

Los trabajos a publicar en la RMIB, deben ser originales, inéditos y de excelencia. Los costos de publicación para autores son los siguientes:

**NO SOCIOS: \$4,060.00 PESOS MXN (INCLUYE I.V.A.)**

**SOCIOS: \$1,276.00 PESOS MXN (INCLUYE I.V.A.)**

### PUBLICIDAD

A las empresas e instituciones interesadas en publicitar su marca o productos en la RMIB, los costos por número son los siguientes:

**MEDIA PLANA: \$4,999.00 PESOS MXN (INCLUYE I.V.A.)**

**UNA PLANA: \$6,799.00 PESOS MXN (INCLUYE I.V.A.)**

**CONTRAPORTADA: \$7,799.00 PESOS MXN (INCLUYE I.V.A.)**

**FORROS INTERIORES: \$7,799.00 PESOS MXN (INCLUYE I.V.A.)**

DESCUENTO DEL 20% AL CONTRATAR PUBLICIDAD EN DOS O MÁS NÚMEROS.

## Para ser socio

- Realiza el pago de derechos, de acuerdo a la categoría que te corresponde.
- Ingresa a [www.somib.org.mx/membresia](http://www.somib.org.mx/membresia) y elige el tipo de membresía por el cual realizaste el pago de derechos.
- Completa el formulario correspondiente y envíalo.
- Se emitirá carta de aceptación y número de socio por parte de la mesa directiva (aprobada la solicitud).
- Para mayor información sobre beneficios, ingresar a: [www.somib.org.mx](http://www.somib.org.mx) o comunícate al correo [socios@somib.org.mx](mailto:socios@somib.org.mx).

## Datos bancarios

- Beneficiario:** Sociedad Mexicana de Ingeniería Biomédica A. C.
- Banco:** Scotiabank
- Referencia:** 1000000333
- Cuenta:** 11006665861
- CLABE Interbancaria:** 044770110066658614

La inserción de la publicidad será publicada en el libro electrónico y en el área de patrocinios en el sitio Web de la revista (RMIB), disponible en:

<http://rmib.mx>

**Fundador**  
**Dr. Carlos García Moreira**

## COMITÉ EDITORIAL

**Editor en Jefe**  
**Dr. César A. González Díaz**  
INSTITUTO POLITÉCNICO NACIONAL-MÉXICO

### Editores Asociados Nacionales

**Dra. Dora-Luz Flores**  
UNIVERSIDAD AUTÓNOMA DE BAJA CALIFORNIA

**Dr. Aldo Rodrigo Mejía Rodríguez**  
FACULTAD DE CIENCIAS  
UNIVERSIDAD AUTÓNOMA DE SAN LUIS POTOSÍ

**Dra. Citlalli Jessica Trujillo Romero**  
DIVISIÓN DE INVESTIGACIÓN EN INGENIERÍA MÉDICA  
INSTITUTO NACIONAL DE REHABILITACIÓN-LUIS GUILLERMO IBARRA IBARRA

**Dr. Christian Chapa González**  
INSTITUTO DE INGENIERÍA Y TECNOLOGÍA  
UNIVERSIDAD AUTÓNOMA DE CIUDAD JUÁREZ

**Dr. Rafael Eliecer González Landaeta**  
UNIVERSIDAD AUTÓNOMA DE CIUDAD JUÁREZ

### Editores Asociados Internacionales

**Dr. Leonel Sebastián Malacrida Rodríguez**  
UNIVERSIDAD DE LA REPÚBLICA, URUGUAY

**Dra. Elisa Scalco**  
INSTITUTE OF BIOMEDICAL TECHNOLOGY  
ITALIAN NATIONAL RESEARCH COUNCIL, MILAN, ITALY

**Dra. Natali Olaya Mira**  
INSTITUTO TECNOLÓGICO METROPOLITANO  
ITM, MEDELLÍN, COLOMBIA

### Índices

La Revista Mexicana de Ingeniería Biomédica aparece en los siguientes índices científicos:  
**Sistema de Clasificación de Revistas Científicas y Tecnologías del CONACYT - Q4, SCOPUS, SciELO, EBSCO, Medigraphic Literatura Biomédica, Sociedad Iberoamericana de Información Científica - SIIC.**

[www.rmib.mx](http://www.rmib.mx)  
ISSN 2395-9126

**Asistente Editorial**  
**Carla Ivonne Guerrero Robles**

**Editor Técnico y en Internet**  
**Enrique Ban Sánchez**

Se autoriza la reproducción parcial o total de cualquier artículo a condición de hacer referencia bibliográfica a la Revista Mexicana de Ingeniería Biomédica y enviar una copia a la redacción de la misma.





**SOMIB**  
Sociedad Mexicana de  
Ingeniería Biomédica

### **MESA DIRECTIVA**

**Ing. Herberth Bravo Hernández**

PRESIDENTE

**Ing. Eduardo Méndez Palos**

VICEPRESIDENTE

**Ing. Janette Mariana Tarín León**

SECRETARIA

**Mtro. Jaime Arturo Quirarte Tejeda**

TESORERO

**Dr. César A. González Díaz**

EDITOR DE RMIB

### **Afiliada a:**

International Federation of Medical and Biological Engineering (IFMB-IUPSM-ICSU)  
Federación de Sociedades Científicas de México, A.C. (FESOCIME)  
Consejo Regional de Ingeniería Biomédica para América Latina (CORAL)

### **SOMIB**

Periferico Sur #5374, Col. Olímpica, Alc. Coyoacán, C. P. 04710, Ciudad de México, CDMX, México (555) 574-4505

[www.somib.org.mx](http://www.somib.org.mx)

**REVISTA MEXICANA DE INGENIERÍA BIOMÉDICA**, Vol. 42, No. 2, Mayo-Agosto 2021, es una publicación cuatrimestral editada por la Sociedad Mexicana de Ingeniería Biomédica A.C., Periferico Sur #5374, Col. Olímpica, Alc. Coyoacán, C. P. 04710, (555) 574-4505, [www.somib.org.mx](http://www.somib.org.mx), [rmib.somib@gmail.com](mailto:rmib.somib@gmail.com). Editor responsable: César Antonio Díaz González. Reserva de Derechos al Uso Exclusivo No. 04-2015-041310063800-203, ISSN (impreso) 0188-9532; ISSN (electrónico) 2395-9126, ambos otorgados por el Instituto Nacional del Derecho de Autor. Responsable de la última actualización de este número: Lic. Enrique Federico Ban Sánchez, Periferico Sur #5374, Col. Olímpica, Alc. Coyoacán, C. P. 04710, (555) 574-4505, fecha de última modificación, 1 de agosto de 2020.

El contenido de los artículos, así como las fotografías son responsabilidad exclusiva de los autores. Las opiniones expresadas por los autores no necesariamente reflejan la postura del editor de la publicación.

Queda estrictamente prohibida la reproducción total o parcial de los contenidos e imágenes de la publicación sin previa autorización de la Sociedad Mexicana de Ingeniería Biomédica.

**Disponible en línea:**

[www.rmib.mx](http://www.rmib.mx)

**CONTENTS**

**CONTENIDO**

<b>Contents</b>	p 5	<b>Review Article</b>	p 90
<b>Research Article</b>	p 6	Efficacy of Virtual Reality in Neurorehabilitation of Spinal Cord Injury Patients: A Systematic Review	
Determination of early bone metastasis on Bone Scans Using the Gray Levels Histogram		<i>Eficacia de la Realidad Virtual en la Neurorehabilitación de Pacientes con Lesión de Médula Espinal: una Revisión Sistemática</i>	
<i>Búsqueda de metástasis ósea temprana en gammagramas óseos usando el histograma de tonos de gris</i>			
<b>Research Article</b>	p 15	<b>Review Article</b>	p 104
Theoretical Study of the Function of the IP3 Receptor/BK Channel Complex in a Single Neuron		Numerical Simulation of a Physiological Mathematical Model of Energy Consumption in a Sarcomere	
<i>Estudio Teórico de la Función del Complejo Receptor-IP3/canales BK en Neurona Única</i>		<i>Simulación Numérica de un Modelo Matemático Fisiológico de Consumo de Energía en un Sarcómero</i>	
<b>Review Article</b>	p 32	<b>Research Article</b>	p 119
Three-dimensional printing in healthcare		Development of Films, Based on Oxidized Ipomea Batatas Starch, with Protein Encapsulation	
<i>Impresión 3D en cuidado de la salud</i>		<i>Desarrollo de Películas, Basadas en Almidón Oxidado de Ipomea Batatas, con Encapsulación de Proteínas</i>	
<b>Research Article</b>	p 49	<b>Review Article</b>	p 132
Antibacterial Activity Analysis of Hydroxyapatite Based Materials with Fluorine and Silver		Pressure Pain Threshold Values Obtained Through Algometers	
<i>Análisis de la Actividad Antibacteriana de Materiales a Base de Hidroxiapatita con Flúor y Plata</i>		<i>Valores de umbral de dolor por presión obtenidos mediante Algómetros</i>	
<b>Research Article</b>	p 58	<b>Research Article</b>	p 149
Biomechanical Evaluation of Hemiarthroplasty in the First Proximal Phalanx. A Finite Element Study		Evaluation of Parameters in PLA and PCL Scaffolds to be Used in Cartilaginous Tissues	
<b>Research Article</b>	p 67	<i>Evaluación de Parámetros en Andamios de PLA y PCL a ser Utilizados en Tejidos Cartilagosos</i>	
Detection of Exudates and Microaneurysms in the Retina by Segmentation in Fundus Images		<b>Research Article</b>	p 160
<i>Detección de Exudados y Microaneurismas en la Retina por Segmentación en Imágenes de Fondo</i>		Autonomic Face Mask Detection with Deep Learning: an IoT Application	
<b>Research Article</b>	p 78	<i>Detección Autónoma de Cubrebocas con Aprendizaje Profundo: una Aplicación del IoT</i>	
Feature Extraction from Distributions of Phase Synchronization Values of EEG Recordings			

[dx.doi.org/10.17488/RMIB.42.2.1](https://dx.doi.org/10.17488/RMIB.42.2.1)

E-LOCATION ID: 1119

## Determination of early bone metastasis on Bone Scans Using the Gray Levels Histogram

### Búsqueda de metástasis ósea temprana en gammagramas óseos usando el histograma de tonos de gris

M. Pérez-Meza<sup>1</sup>; A. Jaramillo-Núñez<sup>2</sup>; B. Cuevas-Otahola<sup>2</sup>; J. A. Arriaga-Hernández<sup>3</sup>; B. E. Sánchez-Rinza<sup>4</sup>

<sup>1</sup>Licenciatura en Informática, Universidad de la Sierra Sur

<sup>2</sup>Coordinación de Óptica, Instituto Nacional de Astrofísica, Óptica y Electrónica

<sup>3</sup>Facultad de Ciencias Fisicomatemáticas, Benemérita Universidad Autónoma de Puebla

<sup>4</sup>Facultad de Ciencias de la Computación, Benemérita Universidad Autónoma de Puebla

#### ABSTRACT

The aim of this paper is to show a technique to speed up the interpretation of bone scans in order to determine the presence of early bone metastasis. This is done using the gray levels histogram of the region of interest. The technique is intended to assist in the bone scans interpretation in order to provide a successful diagnosis. During the analysis, three types of histograms were observed on the regions of interest. If the histogram is narrow and shifted toward the origin, the bone scan is free of metastasis. If it is shifted to the right and slightly broadened, indicates the presence of a bone anomaly different from a metastasis. On the other hand, if the histogram is more broadened and shifted to the right, it suggests the presence of metastasis. This histogram is characterized by displaying small curls on the right side providing information about the metastatic disease stage, which could be low-amplitude peaks and have a short length, if the metastasis is in early stage, or high-amplitude peaks and a long length, if it is advanced. Finally, the analyzed region is displayed in false color considering the minimum gray levels observed in the histogram.

**KEYWORDS:** Bone scan; skeletal metastasis; image histogram; digital image processing

#### Corresponding author

TO: Mónica Pérez Meza

INSTITUTION: Universidad de la Sierra Sur

ADDRESS: Guillermo Rojas Mijangos S/N, esquina con

Avenida Universidad, A. P. 70800, Miahuatlán de

Porfirio Díaz, Oaxaca, México

E-MAIL: arielmonp@hotmail.com

#### Received:

24 September 2020

#### Accepted:

16 December 2020

## INTRODUCTION

Among malignant neoplasms, prostate cancer has a considerably high incidence rate in 65-year-old men and older. For instance, 230000 new cases were diagnosed in the US in 2005 <sup>[1]</sup>. In 2018, between 21000 and 25000 new cases were diagnosed in Mexico, representing 11.7% of the total cancer-detected cases. From this total approximately 7000 patients died during the course of the year <sup>[2]</sup>. The main prostate cancer risk factors are age, race, as well as genetics (if a first-grade relative suffers the disease, the probability increases by a factor of 2). Hence, an objective of the health system is the early detection using screening strategies, through the use of specific prostatic antigen, focused in 50-year-old men and above.

The bone is third most common location likely to develop metastatic disease, below the lungs and liver <sup>[3]</sup>. It is well known that once the patient has been diagnosed with metastatic disease, the prognosis of life expectancy is short, due to the dissemination of the disease to the bones, being unlikely to be cured. However, in each case, available treatments can be used to retard the disease advance, and increase the life expectancy.

The patients' knowledge of such a treatment is essential for the treatments choice. Thus, the purpose of imaging techniques is to identify the early phases of an ongoing bone disease, in order to determine its extension, and subsequently address the possible complications, such as pain, pathological fractures, hypercalcemia or medullary compression. Also, it is remarkably useful in evaluating the response to a treatment, serving as a guide during a biopsy procedure to obtain a diagnostic confirmation of the disease.

Diagnosis of bone metastases through imaging techniques basically consists of direct visualization of tumor infiltration or detection of bone reaction to the tumor process.

Bone scintigraphy is the most common imaging modality used to evaluate cancer-to-bone dispersion. In most cancer centers their interpretation is performed visually, however, to give successful diagnoses a vast experience is required due to the difficulties associated with the recognition of hot spots (areas with high marker content). Hence, a quantitative rather than a qualitative interpretation would be more useful in the bone scans interpretation to improve and standardize diagnoses <sup>[4]</sup>.

## Background

Several computer-assisted methods have been developed to find metastasis. Some techniques use the bone scan index <sup>[5]</sup>, neural networks <sup>[6]</sup> and false color <sup>[7]</sup>. All of them require a large number of bone scans datasets to calibrate the system, resulting in time-consuming procedures.

In this work we introduce a method based on the patients' bone scans analysis, intended to determine the presence of metastatic disease. To this aim a segmentation procedure is required, which is the first step. Subsequently, the gray levels histogram of the region of interest (ROI) is displayed and observed. The image segmentation is required for performing the analysis by region due to the diverse bone densities and their probability to develop a metastatic disease. The diagnosis of bone metastasis using image processing techniques is based on the direct visualization of tumor infiltration or bone reaction to metastatic disease.

Bone scans images are often stored in an archive, where a pixel can contain up to 1024 values (210 umbers, bit depth). In the case of a healthy skull, free of bone diseases, we observed that its gray tones did not reach values above 60. The same behavior holds for healthy bones <sup>[8]</sup>. There are only two regions where the gray levels could reach the value 1024: the zone where the radiotracer is injected and the bladder, which is where the unsorted marker is stored.

However, these regions do not matter for diagnosis, given their high values, being inconclusive to detect metastasis. Throughout the whole analysis and visualization data is always used in DICOM format (“raw” DICOM images).

In the case of a bone free of metastasis, the image gray levels interval is small, of the order of 60 tones. This interval is larger in the presence of a bone anomaly.

The main objective of the method presented in this work is to detect early bone metastasis. The specialist should draw special attention to the gray levels of the regions of interest (ROI) with values less than 80. Gray tones above such value correspond to advanced bone metastasis, easily observable in the bone scan, so these images don't matter to the method.

Histograms actually obtained from the ROI's are of bimodal type, in such a way that the determination of a malignant bone abnormality will be based mainly on the observation of the right end of the histogram of the ROI.

## **MATERIALS AND METHODS**

An observational, retrospective, and analytic study was conducted in the Nuclear Medicine Department of the National Medical Center “La Raza” at IMSS [7]. The sample consists 138 patients diagnosed with prostate cancer with ages ranging from 47 to 85 years. The detection was performed in bone gammagrams following the Gleason classification. The gammagrams were captured after giving an intravenous dose of 25 mCi de <sup>99m</sup>Tc-MDP and 2 liters of water to the patients. The whole-body scans were performed two hours after giving the patients the radiopharmaceutical, using a dual-head MEDISO INTERVIEW XP VERSION 1.05014 with a LEHR collimator with a velocity of 12 cm/min in anterior and posterior projections. The bone gammagrams were subsequently visually inspected by three specialists in the Nuclear Medicine Department, inde-

pendently. We used the obtained diagnoses as a reference during this research. Out of the 138 bone gammagrams, 43 were of the whole-body type, constituting the sample used for our purposes.

In the context of image processing, image segmentation is among the most intricate techniques. It is used to split a given image into several sub-images having common features. The main goal of such a technique is to simplify the image representation in terms of meaningful data. There are two types of image segmentation: local (concerning to separate image regions) and global (concerning to the segmentation procedure of a complete image formed by a large pixel number).

The local image segmentation is the main scope of this research. Such procedure is considered as part of the developed software along with the previously mentioned techniques. Image segmentation using the histogram-based thresholding procedure is probably the most common approach, since it is easy to implement and requires less computational resources to be executed. These methods generally employ the maximization or minimization of a criterion function based on the image histogram. The optimal threshold is the gray level intensity at which the criterion function reaches its maximum or minimum values. In our case we use the minimum value.

Several methods for image segmentation are available in the literature. We used the variance between classes method (VBC), in this work, to find the minimum value between two Gaussian distributions. Such a method uses a discriminant function to determine the optimal threshold of an image histogram, in order to perform the image segmentation in near uniform regions [9].

In some cases, it is required to perform the segmentation procedure in tri-modal histograms, hence two thresholds are required. An iterative algorithm based

on the maximization of the VBC was proposed in Reddi, Rudin and Keshavan [10]. We will refer to these images as tri-modal images.

The algorithms used in this work were developed in Matlab. These algorithms determine one or two thresholds, depending on each case, similar to the procedures in the algorithms developed by Demirkaya *et al* [11]. For the two-thresholds case, an iterative implementation for the VBC method was used.

We display the segmented ROI in color, and we regard the region edges as level contours or curves since pixels with equal gray tones form a contour.

### Development

Our proposed software splits the bone scan in six ROIs: skull, shoulders, thorax, vertebral spine, scapula and pelvis. Such a segmentation is performed considering the higher probabilities of the bones in these regions to develop a metastatic disease.

Subsequently, the split image histogram is displayed, showing its bi-modality. The first global histogram minimum indicates the gray tone separating the ROI image background, which will refer to as min. When the ROI is constituted by a metastasis-free bone, the right end of the histogram drops to zero quickly. We will refer to this minimum as “max”. However, if the ROI contains a metastasis-free bone, with another pathology or disease, the histogram will broaden in the presence of a degenerative disease, such as osteoporosis, osteopenia, etc.

On the other hand, if the ROI shows signs of metastatic disease, the right end of the histogram will approach zero slowly and monotonically, showing small lobes (local maxima with low amplitude). The lobes extension will depend on the metastatic disease stage. Early metastatic disease is characterized by small-amplitude and short-extension lobes.

In order to illustrate this method, we show the analysis of the skull and pelvis ROIs (the segmentation procedure was performed in the whole-body scan using the previously mentioned techniques). We show only two regions since the rest of the regions show a similar behavior.

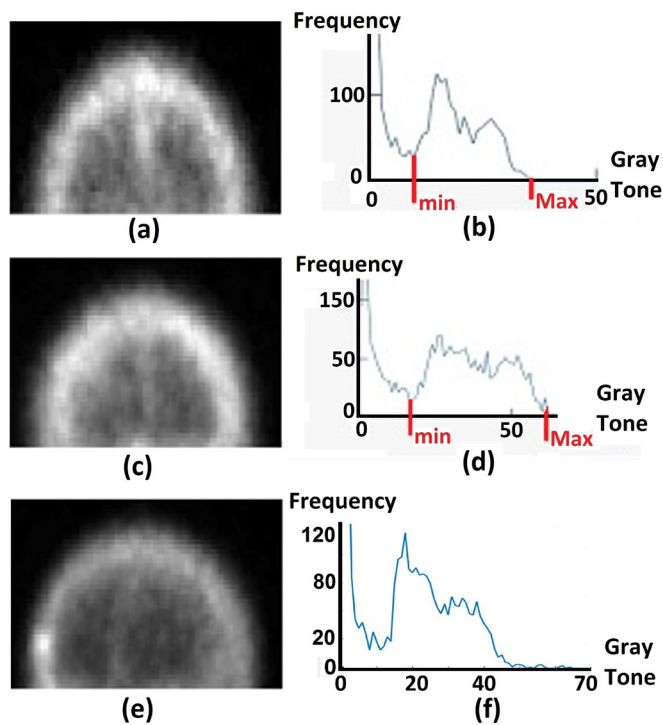


**FIGURE 1.** ROI images of the skull. In (a) healthy case, in (c) degenerative disease, in (e) metastatic disease. The corresponding histograms of (a), (c) and (e), are shown in (b), (d) and (f), respectively.

If the region is embedded in a dark background, as in the skull case, the histogram will be similar to the one shown in Figure 1.a. The minimum gray tone is shown by a red line in the left of the plot, separating the dark background from the ROI. In the case of healthy skull, the maximum gray tone value will be below 50. Moreover, the histogram will quickly approach to zero. In the presence of a degenerative disease the max value will be above 50 and the plot width will increase, as in Figure 1d. The histogram end will approach to zero in descending form, shifted to the right regarding the healthy body histogram.

The most relevant case corresponds to that showing an early-stage metastasis, which is analyzed in the histogram in Figure 1f. In the figure the gray tones corresponding to such a case are beyond the ending region of the healthy-body histogram (beyond the gray tone with value 50), shown as small variations, extending along the gray tone axis.

The pelvis bone probability to develop degenerative diseases as well as metastasis, is high. Hence, the corresponding histograms are similar the previous case. The skull ROI, displays as well a high probability of developing several types of pathology, implying that the different pathology cases (including pathology types different than cancer) have similar histograms, as seen in Figure 2.

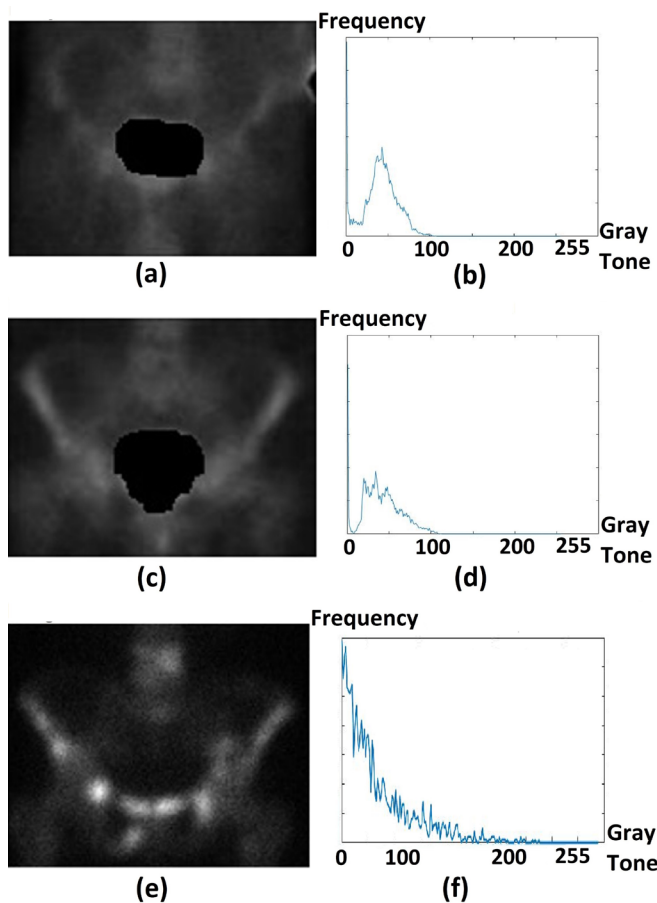


**FIGURE 2.** ROI images of the pelvis. In (a) healthy case, in (c) degenerative disease, in (e) metastatic disease. The corresponding histograms of (a), (c) and (e), are shown in (b), (d) and (f), respectively.

Such a knowledge can be obtained by the specialist from training devoted to study the bone scans histograms. On the other hand, the software includes a visualization tool to display the analyzed ROI's using false color. Such a tool adds color from a list of seven colors assigned to gray levels intervals, setting as a reference the min and max observed values obtained from the histogram analysis. The color assignment scheme is summarized in Table 1.

**TABLE 1.** Assigned color intervals in terms of the min and max values.

Interval Number	Minimum Value	Maximum Value	Assigned Color
1	0	min	Blue
2	min + 1	max	Royal Blue
3	max + 1	max+11	Green-Blue
4	max + 12	max+22	Green
5	max+23	max+33	Yellow-Green
6	max+34	254	Yellow
7	255	1024	White

The proposed software eases the analysis of bone scan allowing the specialist to determine the presence or absence of metastatic disease, from the observation of the histograms along with a previous knowledge of thresholding or filtering techniques, without the necessity of directly observing the bone scan.

The intervals 3-5 are useful to illustrate the metastatic disease advance. The intervals 3 and 4 indicate the presence of early-stage metastasis, and intervals 5 and 6 an ongoing metastasis. The intervals used to indicate early-stage metastatic disease have an incremental step of 10 gray tones each. The rest of the intervals indicate the presence of advanced metastasis, with the gray tone value scaling with the metastasis stage. The latter three colors in Table 1 can be arbitrarily chosen based on the specialist requirements. Tones closer to yellow in the resulting image

will indicate a more advanced stage of the metastatic disease in the ROI. Regions with metastatic disease as well as those with gray tones above 255, corresponding to the bladder case or to cases where radiotracer was injected, will be displayed in white in the visualization tool.

### RESULTS AND DISCUSSION

The previously shown Table 1 was obtained from the histogram analysis, considering its minimum and maximum values.

We apply the scheme in the table to three healthy skulls free of metastasis and we show the results in false color in Figure 3. In this case, the three images colors should be royal blue for the background and blue for the ROI. It should be noticed that as in the case of Figure 2d and 2f, the max values for both ROIs were not suitable since the three ROIs are free of metastasis. However, in this case, it did not alter the diagnosis. The tones problem could be corrected using the min and max values for each age, considering that the ranges in the table for each ROI as well as the corresponding analysis are dynamical, leaving room for a manual correction.

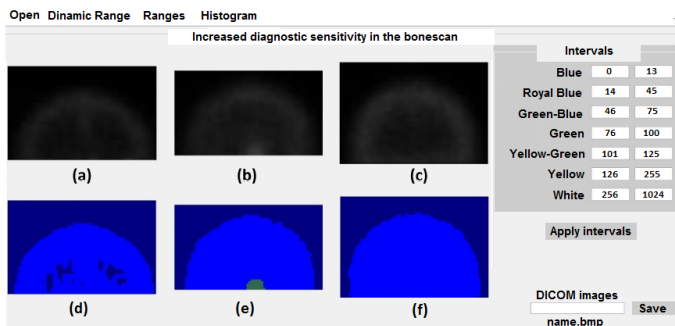


**FIGURE 3. Application of the scheme shown in the table in the right panel of the figure for three healthy skulls.**

In Figure 4 we show the results for three skulls with degenerative diseases. Figure 4e and 4f show and increase in the radiotracer absorption, with the extension and geometry of non-malignant diseases.

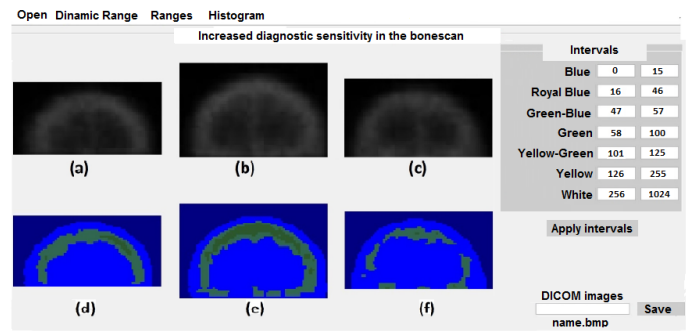


**FIGURE 4. Application of the scheme shown in the table in the right panel of the figure for three skulls with bone degenerative diseases.**

In Figure 5 we show the results for the pelvis case. We observe a region with high gray tone values, and two regions in black. The bladder tones were set to zero to ease the visualization of the ROI.

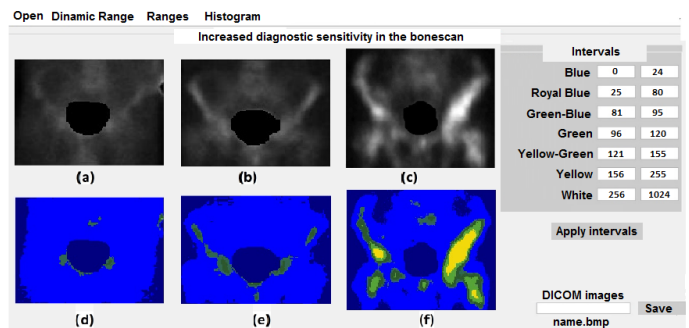


**FIGURE 5. Application of the scheme shown in the table in the right panel of the figure for three pelvises.**

In the case of a ROI free of metastasis but with a broadened histogram (Figures 1.c and 1.d), it is proposed to split the interval 2 of Table 1 in two extra sub-intervals in order to find the cause of the broadening and the advance of the disease. This division eases the observation of the degenerative diseases in the displayed ROI. This procedure is highly recommended in pelvis and skull cases, where the bones have the highest probability of generate degenerative diseases.

The image in the bottom left-most panel corresponds to a healthy pelvis. The image in the bottom middle panel illustrates the application of the comparison technique,

thoroughly explained in a work developed by Jaramillo *et al* [8], intended to assist the diagnosis procedure. It should be noticed that two regions of the pelvis have the same colors, corresponding to early stages of a bone degenerative disease, such as osteopenia or osteoporosis. These regions are shown in the right-most panels. If the differences are present only in one side, such a difference suggests the presence of a severe disease. Despite the similarities between the middle and right panels, the mild differences in the extension and geometry suggest different bone degenerative diseases in each case.

Finally, Figure 6 shows the histogram corresponding to a shoulder region. It could be noticed that the histogram values are irregular, hindering the visual acquisition of the min and max values. Hence, such values could be obtained only by applying the software.

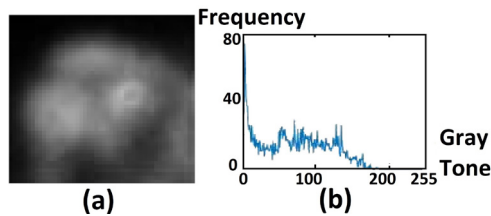


FIGURE 6. Histogram corresponding to a right shoulder.

## Discussion

We recall that the gray tone values of a histogram corresponding to a patient free of bone metastatic disease are below 60. For a patient with an ongoing metastasis, the gray tones increase, being below 100, except in the case of advanced metastatic disease. Our choice of the 7-colors palette is then suitable for visualizing the bone scan in colors. The boundaries between colors observed in the ROIs can be related to the results obtained by applying edge detection techniques. Such techniques are widely-used in the segmentation of images. In this case, the edges correspond to the pixels with gray tones equal to the upper limits of the intervals described in the tables. Such limits could be regarded as level curves of a function  $f(x, y) = cte$  corresponding to a ROI [12].

As we have previously stressed, there are only two regions reaching the highest gray tone value (1024), the bladder and the region where the radiotracer was injected. The bladder stores the non-absorbed radiotracer, which is subsequently expelled through the urine. These two regions are not considered as regions of interest for diagnosis purposes. Hence, we set the gray tones of those regions to zero to ease the ROI visualization procedure, which can be observed in black in Figures 4 and 5.

The gray tones of the bone scan images are low in general, yet considering the high bit depths, which are not fully exploited. Hence, early-stage metastatic disease cannot be diagnosed by directly observing an image, it is necessary to use the image gray tones histogram.

Our proposed method involves a simple technique with potential to be used in oncology centers requiring accuracy and experience. For example, a shift to the left of the min and max values of the histograms, would suggest the presence of bone anomaly in the ROI. The same results would be obtained from a broadened histogram. Additional gray tones observed along the x-axis indicate the presence of metastatic diseases in the ROI. The advance of the metastasis is given in terms of the gray tones extension along the x-axis, i.e., the highest gray tone and the fraction of pixels reaching such a value.

This technique is particularly useful in oncology centers with large patients flow, or with limited resource due to its efficiency and execution times, allowing the specialists to diagnose more patients faster.

On the other hand, considering that a LUT table is built from a mathematical principle, with each element having an input value and assigned resulting output value, we classify table 1 as a LUT table. In nuclear medicine, LUT tables are built for each detec-

tor as a function of the quantitative physical parameters, having several applications. In our particular case, such a table has only one application: converting input gray tones into an output colors. However, in general cases, for some intervals, for instance, 6 and 7, the input values are assigned without following any specific criterion, which is not the case of the LUT tables in Nuclear Medicine <sup>[13]</sup>.

## CONCLUSIONS

In this work we introduced a method to analyze bone scans based on the visualization of a ROI gray levels histogram. We subsequently assigned false color to segmented regions in order to determine the advance of metastatic disease. The colors are assigned in terms of the max and min values of the observed histogram, with the last assignation intervals used for the metastasis detection and stage classification purposes only. Hence, such intervals are used only for visualization of the infiltrated regions, increasing their contrast, with the aim of comparing them with the healthy zones. This method allows a practical evaluation using the histogram of the image gray levels or the visualization of the ROI in color. The software interface is friendly. It is constituted by a straightforward Matlab GUI, with the potential to be used in oncology centers.

## AUTHOR CONTRIBUTIONS

B.S. introduced the most specific Matlab algorithms, and performed the interpretation of mathematical-physical models applied to the analysis of Scintigraphy. She also contributed to building the Matlab GUIs (Graphical User Interfaces) following the specifications of the other authors, that contains and execute all the developed algorithms, to optimize the operation for users unfamiliar with our proposal but with prior knowledge in bone cancer diagnosis from gamma

scans. B.C. contributed to translating the paper to English language, she also contributed to the implementation of algorithms and their performance comparison in other programming languages such as Python and Fortran to improve our research. She also contributed to the GUIs development by optimizing the visualization tasks, as well as the comparison of the model of our proposal with other methods using image processing and analysis of medical images for diagnosis. M.P. the corresponding author, submitted the manuscript to the SOMIB platform and sent the requested information to the journal. She received the notifications and reviewer's reports. She kept the authors up to date regarding the manuscript's status and related journal protocols. Her support was important during the results visualization as well as in the last details of the GUI. A.J. the main researcher (P.I.), has been working on this idea for several years and published papers with related results in the area. He is the liaison with the IMSS staff (Instituto Mexicano del Seguro Social-Mexican Social Security Institute), who were responsible for providing the gamma scans used in our work, following all the legal, safety and security protocols. He wrote the research protocol required for using the gamma scans and specialists' evaluations in the present research. J.A. contributed to editing and correcting the manuscript before submission to the journal and during the reviewing process. He actively contributed with A.J. in the construction of the mathematical physical model relating the histogram analysis, image processing, and filtering to build the used algorithms as well as the tables and figures preparation.

## ETHICAL STATEMENT

Ethical Research Committee of IMSS approved and supervised the study complied with all applicable research and ethical standards and laws.

## REFERENCES

- [1] McAninch J, Lue T. Smith and Tanagho's General Urology. 19th ed. EUA: The McGraw-Hill Companies, Inc; 2008. 351- 376p.
- [2] Secretaria de Salud. Cáncer de próstata, padecimiento mortal y silencioso. Secretaría de Salud México [Internet]. 2017; Available from: <https://www.gob.mx/salud/prensa/514-cancer-de-prostata-padecimiento-mortal-y-silencioso>
- [3] Coleman RE. Metastatic bone disease: clinical features, pathophysiology and treatment strategies. Cancer Treat Rev [Internet]. 2001;27(3):165-76. Available from: <https://doi.org/10.1053/ctrv.2000.0210>
- [4] Zafeirakis A. Scoring systems of quantitative bone scanning in prostate cancer: historical overview, current status and future perspectives. Hell J Nucl Med [Internet]. 2014;17(2):136-144. Available from: <https://doi.org/10.1967/s002449910134>
- [5] Koizumi M, Wagatsuma K, Miyaji N, et al. Evaluation of a computer-assisted diagnosis system, BONENAVI version 2, for bone scintigraphy in cancer patients in a routine clinical setting. Ann Nucl Med [Internet]. 2015;29(2):138-148. Available from: <https://doi.org/10.1007/s12149-014-0921-y>
- [6] Sadik M, Suurkula M, Höglund P, Järund A, Edenbrandt L. Improved classifications of planar whole-body bone scans using a computer-assisted diagnosis system: a multicenter, multiple-reader, multiple-case study. J Nucl Med [Internet]. 2009;50(3):368-375. Available from: <https://doi.org/10.2967/jnumed.108.058883>
- [7] Pérez-Meza M, Jaramillo-Núñez A, Sánchez-Rinza BE. Visualizando Gammagramas Óseos en Colores. RMIB [Internet]. 2018;39(3):225-237. Available from: <https://doi.org/10.17488/rmib.39.3.2>
- [8] Jaramillo-Núñez A, Gómez-Conde JC. Método para incrementar la sensibilidad diagnóstica del gammagrama óseo. An Radiol Mex. 2015;14(1):11-19.
- [9] Otsu NA. Threshold selection method from gray-level histograms. IEEE Trans Syst Man Cyb [Internet]. 1979;9(1):62-66. Available from: <https://doi.org/10.1109/TSMC.1979.4310076>
- [10] Reddi SS, Rudin SF, Keshavan HK. An optimal multiple threshold scheme for image segmentation. IEEE Trans Syst Man Cyb [Internet]. 1984;SMC-14(4):661-665. Available from: <https://doi.org/10.1109/TSMC.1984.6313341>
- [11] Demirkaya O, Asyali MH, Sahoo PK. Image Processing with MATLAB: Applications in Medicine and Biology. EUA: CRC Press; 2009. 458p.
- [12] Leithold L. El cálculo con geometría analítica. 6th ed. Distrito Federal: Harla; 1992. 1175-78p.
- [13] Peinado MA. Monitores e impresoras. In Sociedad Española de Física Médica. Introducción al control de calidad en radiología. España: ADI: Librería/editorial científico-técnica; 2013. 147-148p.

[dx.doi.org/10.17488/RMIB.42.2.2](https://doi.org/10.17488/RMIB.42.2.2)

E-LOCATION ID: 1125

## Theoretical Study of the Function of the IP<sub>3</sub> Receptor/BK Channel Complex in a Single Neuron

### Estudio Teórico de la Función del Complejo Receptor-IP<sub>3</sub>/Canales BK en Neurona Única

*M. E. Pérez-Bonilla; M. Reyes-Monreal; J. Quintero-Pérez; M. F. Pérez-Escalera; A. Reyes-Lazalde*

Benemérita Universidad Autónoma de Puebla

#### ABSTRACT

Large conductance calcium-activated potassium (BK) channels carry out many functions in the central nervous system. These channels open in response to increased cytosolic calcium ( $[Ca^{2+}]_{cyt}$ ) concentration. The influx of calcium ions to the cytosol can occur through voltage-gated calcium channels (VGCCs) on the plasma membrane and/or through IP<sub>3</sub> receptors (IP<sub>3</sub>-Rs) and ryanodine receptors (RyRs) on the endoplasmic reticulum membrane. The BK channel/IP<sub>3</sub>-R/RyR interaction has been widely reported in smooth muscle but scarcely investigated in relation to neurons. The aim of this study was to theoretically explore the function of the BK/IP<sub>3</sub>-R complex by means of a computational model of a neuron that replicates the interaction between the release of Ca<sup>2+</sup> from the endoplasmic reticulum (through IP<sub>3</sub>-Rs) and the opening of the BK channels. The mathematical models are based on the Hodgkin-Huxley formalism and the Goldbeter model. These models were implemented on Visual Basic® and differential equations were solved numerically. Distinct conditions were contemplated for BK conductance and the efflux of endoplasmic Ca<sup>2+</sup> to the cytosol. An abrupt rise in  $[Ca^{2+}]_{cyt}$  ( $\geq 5 \mu M$ ) and short duration (spark) was found to activate BK channels and either pause or stop the action potential train.

**KEYWORDS:** BK channels; IP<sub>3</sub> receptor; Ca<sup>2+</sup> microdomains; Single-neuron simulations; SERCA pump

## RESUMEN

Los canales de potasio activados por calcio de gran conductancia (canales BK) cumplen múltiples funciones en el sistema nervioso central. Estos canales se abren en respuesta al incremento de la concentración de calcio citosólico ( $[Ca^{2+}]_{cyt}$ ). La entrada de  $Ca^{2+}$  puede ocurrir a través de canales de calcio dependientes de voltaje (VGCCs) localizados en la membrana plasmática y por eflujo de  $Ca^{2+}$  del retículo endoplásmico (ER) causado por 1,4,5-Trifosfato ( $IP_3$ ) o rianodina (RyR). La interacción BK/ $IP_3$ /RyR ha sido ampliamente estudiada en músculo liso, pero escasamente en neuronas. El objetivo de este estudio fue explorar teóricamente la función del complejo BK/ $IP_3$ -R mediante un modelo computacional de una neurona que replica la interacción entre la liberación de  $Ca^{2+}$  del retículo endoplásmico (a través de  $IP_3$ -Rs) y la apertura de los canales BK. Los modelos matemáticos se basan en el formalismo de Hodgkin-Huxley y el modelo de Goldbeter. Estos modelos fueron implementados en Visual Basic® y las ecuaciones diferenciales fueron resueltas por métodos numéricos. Se contemplaron distintas condiciones para la conductancia del canal BK y la salida de  $Ca^{2+}$  endoplásmico al citosol. Los resultados muestran que un incremento abrupto de  $[Ca^{2+}]_{cyt}$  ( $\geq 5 \mu M$ ) y de corta duración (spark) activa los canales BK y producen una pausa o detiene el tren de potenciales de acción.

**PALABRAS CLAVE:** BK channels;  $IP_3$  receptor;  $Ca^{2+}$  microdomains; Single-neuron simulations; SERCA pump

### Corresponding author

TO: Arturo Reyes Lazalde

INSTITUTION: Benemérita Universidad  
Autónoma de Puebla

ADDRESS: 15 Poniente #1102-A, Col. Álvaro Obregón,  
C. P. 74260, Atlixco, Puebla, México

E-MAIL: arturoreyeslazalde@gmail.com

### Received:

17 October 2020

### Accepted:

6 January 2021

## INTRODUCTION

In neurons, maintaining the homeostasis of calcium ions ( $\text{Ca}^{2+}$ ) is essential for proper signaling and function. The endoplasmic reticulum (ER) serves as the main  $\text{Ca}^{2+}$  storage organelle in neurons and has mechanisms of influx and efflux of this ion. Such mechanisms, located on the ER membrane, help to regulate the cytosolic concentration of  $\text{Ca}^{2+}$ . The influx mechanism is based on  $\text{Ca}^{2+}$  pumps, while the most important efflux mechanisms are triggered by inositol 1,4,5-trisphosphate ( $\text{IP}_3$ ) receptors ( $\text{IP}_3$ -Rs) and ryanodine receptors (RyRs). The rise in the level of  $\text{Ca}^{2+}$  in the cytosol activates the large-conductance calcium-activated potassium channels, or big potassium (BK) channels.

Various mathematical models have been developed to replicate the release of  $\text{Ca}^{2+}$  from the ER and the pattern of the cytosolic  $\text{Ca}^{2+}$  concentration, hereafter denominated  $[\text{Ca}^{2+}]_{\text{cyt}}$ . However, they have not been associated with BK channels in order to research their joint function at the somatic level, explore the mechanisms involved, and determine the importance they have in neuronal activity. A theoretical study was carried out on the functional coupling of  $\text{IP}_3$ -Rs to BK channels in a single neuron and the effects produced. An interaction is proposed in the soma of the neuron in a microdomain formed by the proximity of the BK channels of the plasma membrane to the calcium efflux channels triggered by the  $\text{IP}_3$ -Rs located on the ER membrane.

## BK channels

Large conductance (BK) channels are part of the family of calcium-activated potassium channels. They are distinguished from other calcium-activated potassium channels (small and intermediate conductance) by their capacity to couple  $[\text{Ca}^{2+}]_{\text{cyt}}$  and sense the membrane potential variations. BK channels are widespread in the brain, being found in the cerebral cortices, cerebellar cortex, hippocampus, olfactory bulb, vestibular nuclei, basal ganglia, hypothalamus, and thalamus [1].

Calcium-activated potassium channels exist in diverse cell types [2]. On neurons, BK channels are present in dendrites, soma, axons, and synaptic terminals [1]. Upon analyzing aplysia nerve cells, Meech [3] identified for the first time a potassium current activated by a rise in the level of  $[\text{Ca}^{2+}]_{\text{cyt}}$ . After microinjection of calcium, the cell membrane was hyperpolarized and an increase in  $\text{Ca}^{2+}$ -activated  $\text{K}^+$  conductance ( $g_{\text{K}_{\text{Ca}}}$ ) occurred concomitantly [3]. Since then, these channels have been investigated to characterize their molecular structure, electrophysiology, and pharmacology [4]. According to their single-channel conductance,  $\text{K}_{\text{Ca}}$  channels are divided into three main subfamilies: (1) small conductance (SK) (4-14 pS), (2) intermediate conductance (IK) (32-39 pS), and (3) large conductance (BK) (200-300 pS) channels [4] [5].

The BK channels have several distinctive characteristics. (1) They are homotetramers with two regulatory domains containing two high-affinity  $\text{Ca}^{2+}$  binding sites. (2) They are voltage and calcium-dependent, requiring both membrane depolarization and calcium for their activation.  $\text{Ca}^{2+}$  binding and voltage sensor activation act almost independently to enhance channel opening [6]. BK channels can open in the absence of calcium but are more sensitive to calcium at depolarizing voltage steps [2]. Hence, their sensitivity to calcium is strongly dependent on the membrane potential. The dissociation constant (Kd) for calcium is in the micromolar range at -60 mV and in the nanomolar range at +20 to +40 mV [7]. (3) BK channels are fast activating (on the order of 1 ms or less) compared to IK and SK channels, which have a slow activation time (lasting hundreds of milliseconds or over a second, respectively) [8].

BK channels have various functions in the central nervous system. At the soma of many neuronal cells, they control the speed of action potential repolarization and mediate the rapidity of afterhyperpolarization. Therefore, they can influence spike frequency adaptation [9] [10]. They are often physically associated

with voltage-gated calcium channels (VGCCs), thus forming microdomains with them [11] [12]. Due to their presence in nerve terminals and their co-assembly with VGCCs at active zones, BK channels are particularly suitable for regulating the release of neurotransmitters, increase the duration of PA, prevent back-propagation in dendrites, and produce a decrease in firing frequency [9] [13] [14].

The concentration of free and bound  $[Ca^{2+}]_{cyt}$  is reported to be approximately 100 nM and 10  $\mu$ M, respectively [15]. While a localized increase in  $[Ca^{2+}]_{cyt}$  has been evidenced in some studies, others show spatio-temporal calcium signaling restricted to nano and microdomains in neurons [16] and smooth muscle [17] [18]. In a BK channel-VGCC microdomain, according to Fakler and Adelman [18], the kinetics of  $[Ca^{2+}]_{cyt}$  exhibit a localized boost of up to 20  $\mu$ M in neurons. The  $[Ca^{2+}]_{cyt}$  concentration decreases with distance due to the diffusion process and interaction with the chelators (1,2-bis(o-aminophenoxy)ethane-N,N,N',N'-tetraacetic acid (BAPTA) and ethylene glycol-bis(b-aminoethyl ether)-N,N,N',N'-tetraacetic acid (EGTA) [18].

### Endoplasmic reticulum (ER)

Because of containing a high concentration of  $Ca^{2+}$  binding proteins, the ER is the main  $Ca^{2+}$  storage organelle in cells. Indeed, the total amount of  $Ca^{2+}$  may be >1 mM, while the concentration of free  $[Ca^{2+}]_{ER}$  ( $Ca^{2+}$  in the ER) has been quantified at 100-700  $\mu$ M [19].

To maintain equilibrium, mechanisms of influx and efflux of  $Ca^{2+}$  are activated on the ER membrane. There are two types of processes related to the efflux of  $Ca^{2+}$  from the ER, being the  $Ca^{2+}$ -induced  $Ca^{2+}$  release (CICR) and  $IP_3$ -induced  $Ca^{2+}$  release (IICR) processes. The  $[Ca^{2+}]_{cyt}$  interacts with ryanodine receptors and  $IP_3$  receptors (RyRs,  $IP_3$ -Rs) in the former and  $IP_3$  with its receptors ( $IP_3$ -Rs) in the latter, in both cases to release  $Ca^{2+}$  from the ER [20]. On the other hand,  $Ca^{2+}$  is recaptured into the ER by the activity of smooth endoplas-

mic reticulum  $Ca^{2+}$ -ATP<sub>ase</sub> (SERCA) pumps [21]. Thus, a low concentration of  $[Ca^{2+}]_{cyt}$  (50 - 100 nM) is maintained by the coordinated action of the inflow of  $Ca^{2+}$  to the ER through pumps on the ER membrane, and the efflux of  $Ca^{2+}$  from the cytosol to the extracellular space through pumps (PMCA) on the plasma membrane [22].

### BK channel - $IP_3$ receptor interaction

The BK channel/ $IP_3$ -R microdomain has received less attention, and its role is controversial.  $IP_3$ -Rs are localized in the ER membrane and the BK channels in the plasma membrane. The BK channels and  $IP_3$  receptors are very close to one another [23]. The ER membrane is believed to be initially generated as part of the nuclear envelope, which then expands and morphs into a complex reticulum that can extend to distant cellular compartments such as the axons, dendrites, and dendritic spines of neurons, but with a similar morphology and there is closeness between the ER membrane and the cytoplasmic membrane [24] [25] [26]. The cisternae of the ER are classified in accordance with their proximity to the plasma membrane. Type I is the farthest from the plasma membrane, while type II and III are nearer, frequently following its profile [26].

Pan et al., reported the interaction between BK channels and  $IP_3$ -Rs in human embryonic kidney cells (HEK293) [27]. Neuropeptide galanin activates galanin receptors (GalR2s), and  $IP_3$ -Rs are activated through the protein kinase G pathway. The increase in  $[Ca^{2+}]_{cyt}$  is due to  $Ca^{2+}$  efflux from the ER through  $IP_3$ -Rs. The authors demonstrated that the rise in the level of  $[Ca^{2+}]_{cyt}$  comes from the ER but did not quantify this change.

In arterial smooth muscle cells, relaxation and contraction are regulated by calcium released from the sarcoplasmic reticulum. The flow of calcium from the ER to the cytosol (induced by  $IP_3$  and ryanodine) activates the BK channels, thus facilitating a negative feedback mechanism in opposition to vasoconstriction.

tion<sup>[17]</sup>. There is evidence of the proximity of BK channels and calcium release sites. This is further supported by co-immunoprecipitation experiments<sup>[28]</sup>. As a consequence, such channels would be exposed to a high calcium concentration (>10  $\mu\text{M}$ , in the order of 1-100  $\mu\text{M}$ ).

In neurons, Irie and Trussell<sup>[23]</sup> described a nanodomain between RyRs on the ER membrane and plasma membrane VGCCs (voltage-gated  $\text{Ca}^{2+}$  channels), and another one between RyRs and BK channels in the soma of cartwheel inhibitory interneurons of the dorsal cochlear nucleus. Through the VGCC-RyR interaction, the latter receptors trigger the release of  $\text{Ca}^{2+}$ . The internal increase in calcium acts on plasma membrane BK channels to control action potential activity and shape the burst. The interaction of the nanodomains and the  $\text{Ca}^{2+}$  transients must be very rapid (in a millisecond timescale), and thus arise only tens of nanometers from the plasma membrane<sup>[23]</sup>.

IP<sub>3</sub> is highly mobile in the cytosol. It is synthesized in the plasma membrane and diffuses into the cell where it encounters its specific receptors (IP<sub>3</sub>-Rs) on the ER<sup>[29]</sup>. In neocortical pyramidal neurons, IP<sub>3</sub> produces calcium waves via activation of metabotropic glutamate receptors. When measured with non-buffering low-affinity  $\text{Ca}^{2+}$  indicators, such waves have a peak amplitude of over 5  $\mu\text{M}$ <sup>[30]</sup> and propagate with a velocity of  $\sim 100 \mu\text{m/s}$ <sup>[31]</sup>. According to Ross<sup>[31]</sup>, the release of  $\text{Ca}^{2+}$  from ER has been less studied because it is not associated with specific changes in the membrane potential. As can be seen in this work, the impact of the release of  $\text{Ca}^{2+}$  from ER on the membrane potential was researched indirectly through the BK channels.

The importance of the interaction between BK channels and voltage-gated calcium channels has been demonstrated in the release of neurotransmitters, where they play a regulatory role that prevents excito-

toxicity<sup>[32]</sup>; in the smooth muscle of blood vessels, where it regulates blood pressure and plays an important role in preventing hypertension<sup>[33]</sup>. In these cases, the prevention mechanism is a negative feedback system. The experimental study is facilitated because both channels are found on the same membrane, and voltage clamping and transfections can be performed to combine different types of VGCC channels with the BK channel, etc. On the other hand, the experimental study of the BK/IP<sub>3</sub>-R complex is more difficult, the channels are in different membranes and consequently, voltage clamping cannot be performed. This justifies a theoretical study of the BK/IP<sub>3</sub>-R. It is unknown whether, at a somatic level in neurons, the BK/IP<sub>3</sub>-R interaction is present as a protective mechanism. Based on the reported studies, the coexistence of BK and IP<sub>3</sub>-R channels at the somatic level is known<sup>[23]</sup> and of the proximity of the cell membrane and the endoplasmic reticulum and contact sites between these structures<sup>[24]</sup>, necessary conditions for the presence of BK/IP<sub>3</sub>-R. The proposed hypothesis is that: in neurons, at the somatic level, there is a BK/IP<sub>3</sub>-R interaction. If this is so, what would its role be in neuronal activity? What would be the mechanisms involved? It is not known whether an abrupt and short-term outflow of  $\text{Ca}^{2+}$  could activate BK channels in the neuron's soma; it is also not known whether there is a commitment between the number of BK channels present in the membrane and the response of the neuron to  $[\text{Ca}^{2+}]_{\text{cyt}}$ .

### Modeling of $\text{Ca}^{2+}$ release from IP<sub>3</sub>R

Based on detailed knowledge of the timescales of  $\text{Ca}^{2+}$  release from the ER and the pattern of  $[\text{Ca}^{2+}]_{\text{cyt}}$  concentration, mathematical models have been developed to replicate variations in  $[\text{Ca}^{2+}]_{\text{cyt}}$ . The resulting models are of three types. Firstly, there are models for the release of  $\text{Ca}^{2+}$  (with simplified dynamics) from the ER or the sarcoplasmic reticulum through the IP<sub>3</sub>-R. Such early models are purely phenomenological<sup>[34]</sup><sup>[35]</sup>. Secondly, some models incorporate molecular details of the interaction of IP<sub>3</sub> and  $\text{Ca}^{2+}$  with the IP<sub>3</sub>-R, consid-

ering microscopic kinetics and a detailed gating scheme for the receptor [36] [37] [38] [39] [40] [41]. Thirdly, some models (e.g., the one created by Blackwell and Kotaleski, in [39]) also incorporate second messengers within the biochemical reactions that are triggered by metabotropic glutamate receptor (mGluR) activation and lead to IP<sub>3</sub> production. Each group of models has different timescales.

The mathematical models are related to the molecular interaction of IP<sub>3</sub> with the IP<sub>3</sub>-R and the Ca<sup>2+</sup>-activated channel, which are activated sequentially for the release of Ca<sup>2+</sup> from the ER. These models have employed different mathematical techniques [40]. The current contribution focuses on the interaction of [Ca<sup>2+</sup>]<sub>ER</sub> with BK channels. Detailed molecular kinetics of the mechanisms of release of Ca<sup>2+</sup> from the ER is not essential for the purpose of this work. The phenomenological model of Goldbeter of such Ca<sup>2+</sup> release was herein found to be sufficiently accurate and appropriate in its timescale and was combined with the phenomenological model of Hodgkin and Huxley. The latter formulation describes the electrical activity of neurons [41]. Based on the aforementioned models, the present study theoretically explored the function of a BK/IP<sub>3</sub>-R microdomain.

## MATERIALS AND METHODS

In the development of a new model, consideration was given to the spatial structure of the soma and some key concepts related to the kinetics of Ca<sup>2+</sup>. The increase in Ca<sup>2+</sup> is located in the microdomain [16] formed mainly by the following factors [28]: the BK channels on the soma membrane [1] [44] and the Ca<sup>2+</sup>- and IP<sub>3</sub>-R-sensitive channels on the ER membrane [42]. The two membranes are very close to one another [26]. There is evidence from electron microscopy, with 3D reconstructions, of the proximity of the plasmatic membrane with the ER membrane and of numerous contact sites between these structures, mainly in the neuron soma [24].

## The Hodgkin and Huxley formalism and the BK model

The electrical activity of the neuron was reproduced with the Hodgkin and Huxley formalism (H-H model), consisting of an equation that represents the membrane potential (Equation 1) and others that define channel gating variables (Equations 2-5) [45] [46].

$$C_m \frac{dV}{dt} = -\bar{g}_{Na} m^3 h (V - E_{Na}) - \bar{g} n^4 (V - E_K) - \bar{g}_L (V - E_L) - \bar{g}_{BK} q (V - E_K) \quad (1)$$

$$\frac{dm}{dt} = \alpha_m(V)(1 - m) - \beta_m(V)m \quad (2)$$

$$\frac{dh}{dt} = \alpha_h(V)(1 - h) - \beta_h(V)h \quad (3)$$

$$\frac{dn}{dt} = \alpha_n(V)(1 - n) - \beta_n(V)n \quad (4)$$

$$\frac{dq}{dt} = \alpha_q(V)(1 - q) - \beta_q(V)q \quad (5)$$

Where  $\alpha_m(V)$ ,  $\beta_m(V)$ ,  $\alpha_h(V)$ ,  $\beta_h(V)$ ,  $\alpha_n(V)$ ,  $\beta_n(V)$ ,  $\alpha_q(V)$ , and  $\beta_q(V)$  are activation and inactivation gating variables and are defined according to the following empirical equations (Equations 6-13) [45] [46] [47]:

$$\alpha_m(V) = \frac{-0.1(V+40)}{1 - \exp\left(\frac{-(V+40)}{10}\right)} \quad (6)$$

$$\beta_m(V) = 4 \exp\left(\frac{-(V+65)}{18}\right) \quad (7)$$

$$\alpha_h(V) = 0.07 \exp\left(\frac{-(V+65)}{20}\right) \quad (8)$$

$$\beta_h(V) = \frac{1}{1 + \exp\left(\frac{-(V+35)}{10}\right)} \quad (9)$$

$$\alpha_n(V) = \frac{0.01(V+55)}{1 - \exp\left(\frac{-(V+55)}{10}\right)} \quad (10)$$

$$\beta_n(V) = 0.125 \exp\left(\frac{-(V+65)}{80}\right) \quad (11)$$

$$\alpha_q(V) = e^{\left(\frac{V}{27}\right)} 0.005 \frac{200 - [Ca^{2+}]_{cyt}}{\exp\left(\frac{200 - [Ca^{2+}]_{cyt}}{20}\right) - 1} \quad (12)$$

$$\beta_q(V) = 0.0004 \text{ to } 0.002 \quad (13)$$

**TABLE 1. The parameters of the H-H model (from [45]).**

Symbol	Values	Units	Definitions
V	-90*	mV	Membrane potential
C <sub>m</sub>	1	μF·cm <sup>-2</sup>	Membrane capacitance
E <sub>Na</sub>	50	mV	Equilibrium potential for Na <sup>+</sup> , K <sup>+</sup> , and leak
E <sub>K</sub>	-77		
E <sub>L</sub>	-22		
ḡ <sub>Na</sub>	120	mS·cm <sup>-2</sup>	Maximum conductance for Na <sup>+</sup> , K <sup>+</sup> , leak and BK
ḡ <sub>K</sub>	20		
ḡ <sub>L</sub>	0.3		
ḡ <sub>BK</sub>	**		
[Ca <sup>2+</sup> ] <sub>cyt</sub>	***	μM	Calcium ions in the cytosol

\*Initial condition

\*\*Input into the simulator

\*\*\*Is taken from the Goldbeter model

## Goldbeter Model

The mathematical model of Goldbeter (1990) was found to be adequate [32] because the time involved in the BK channel is on a millisecond scale [48] [49] [50] and our interest is in the [Ca<sup>2+</sup>]<sub>cyt</sub> concentration and not in the details of the interaction of IP<sub>3</sub> with IP<sub>3</sub>-R. Hence, two different mechanisms were contemplated for the release of Ca<sup>2+</sup> from the ER, one sensitive to IP<sub>3</sub> (the IICR) [38], and the other to Ca<sup>2+</sup> (the CICR) [48].

Dupont and Goldbeter developed another model with a single compartment. In a single group, considering the existence of the same two types of channels (one

sensitive to Ca<sup>2+</sup> and the other to IP<sub>3</sub>), no oscillations occur unless the contribution of the IICR is insignificant compared to that of the CICR [49]. Oscillations in [Ca<sup>2+</sup>]<sub>cyt</sub> are similar in the one- and two-compartment models [49]. The latter was employed in the present study since it does not require such an extreme decrease in the contribution of the IICR as needed in the one-compartment model.

The model has two variables, free [Ca<sup>2+</sup>]<sub>cyt</sub> (Z) and free [Ca<sup>2+</sup>]<sub>ER</sub> concentrations, modulated through the Ca<sup>2+</sup>-sensitive mechanism (Y). The system is governed by the two kinetic equations [32]:

$$\frac{dZ}{dt} = V_0 + V_1 * \beta - V_2 + V_3 + K_f Y - k Z \quad (14)$$

$$\frac{dY}{dt} = V_2 - V_3 - k_f Y \quad (15)$$

Where V<sub>0</sub> is related to the flow of Ca<sup>2+</sup> into the cell, k to its flow out of the cell, V<sub>1</sub> to its flow into the cytosol from the IP<sub>3</sub>-sensitive mechanism, β to the saturation function of IP<sub>3</sub>-Rs (cooperative nature), and K<sub>f</sub> to the leaky transport of Y into Z. Finally, V<sub>2</sub> expresses the rate of the SERCA pump and V<sub>3</sub> the rate of transport of Ca<sup>2+</sup> released from the IP<sub>3</sub>-sensitive mechanism into the cytosol.

$$V_2 = V_{M2} \frac{Z^{n_{Hill}}}{K_2^{n_{Hill}} + Z^{n_{Hill}}} \quad (16)$$

$$V_3 = V_{M3} \frac{Y^{m_{Hill}}}{K_R^{m_{Hill}} + Y^{m_{Hill}}} \frac{Z^{p_{Hill}}}{K_A^{p_{Hill}} + Z^{p_{Hill}}} \quad (17)$$

V<sub>M2</sub> denotes the maximum rate at which Ca<sup>2+</sup> is pumped into the ER store and V<sub>M3</sub> the IP<sub>3</sub>-sensitive release of ions from this location. The complementary processes are represented by Hill functions. Thus, n<sub>Hill</sub> and m<sub>Hill</sub> depict the cooperativity coefficients, p<sub>Hill</sub> reflects the degree of cooperativity of activation, and the constants K<sub>2</sub>, K<sub>R</sub>, and K<sub>A</sub> designate the point at

which pumping, release, and activation are triggered [49]. Since the ATPase pump (SERCA) binds to two calcium ions per molecule of ATP, its activity is expressed by using Michaelis-Menten kinetics and a value of 2 for the Hill coefficient (Equation 16) [50].

TABLE 2. Parameters of the Goldbeter model [32].

Symbol	Values	Units	Definitions
Rate of transport from Ca <sup>2+</sup> -sensitive pool into the cytosol			
V <sub>3</sub>			flow rate of Ca <sup>2+</sup> from the ER to the cytosol
V <sub>M3</sub>	500	μM/s	maximum V <sub>3</sub>
K <sub>R</sub>	2	μM	constants
K <sub>A</sub>	.09	μM	
k <sub>f</sub>	1	1/s	rate constant (Ca <sup>2+</sup> leak)
ATP-driven pumping of Ca <sup>2+</sup> from the cytosol into the Ca <sup>2+</sup> -sensitive pool			
V <sub>2</sub>			pumping rate of Ca <sup>2+</sup> into the ER (by SERCA)
V <sub>M2</sub>	65	μM/s	maximum V <sub>2</sub>
K <sub>2</sub>	1	μM	constants
Efflux of Ca <sup>2+</sup> out of the cell (PMCA bomb)			
K	10	1/s	rate constant
Hill coefficients			
n <sub>Hill</sub>	2		Hill coefficient (SERCA bomb)
m <sub>Hill</sub>	2		Hill coefficients Ca <sup>2+</sup> release from Ca <sup>2+</sup> -sensitive pool
p <sub>Hill</sub>	4		

The system of equations was solved simultaneously by the numerical method with a fourth-order Runge-Kutta algorithm (dt = 0.01) written on Visual Basic [53] [54]. The initial conditions were V = -90 mV, and [Ca<sup>2+</sup>]<sub>cyt</sub> = 0.1 μM (value entered in the simulator). The simulator was developed and compiled to use in the Windows® environment.

## RESULTS AND DISCUSSION

The module for inputting data into the simulator (Figure 1) provides an interactive resource for experimental recordings, allowing for access to all the parameters of the Goldbeter model [49]. There are three types of variables: those that increase or decrease [Ca<sup>2+</sup>]<sub>cyt</sub>, as well as the ones related to the degree of cooperativity of the activation process (n<sub>Hill</sub>, m<sub>Hill</sub>, and p<sub>Hill</sub>).

Firstly, the influx of Ca<sup>2+</sup> to the cytosol depends on the rate of transport through the IP<sub>3</sub>-sensitive mechanism ( $r = V_1 \cdot \beta$ ) and the Ca<sup>2+</sup>-sensitive mechanism (V<sub>3</sub>), the maximum rate of Ca<sup>2+</sup> pumping release from the ER store (V<sub>M3</sub>), the threshold constants for release and activation (K<sub>R</sub> and K<sub>A</sub>, respectively) (Figures 1 and 5), and the passive leak (k<sub>f</sub>). Secondly, the efflux of Ca<sup>2+</sup> out of the cytosol depends on the outflow of Ca<sup>2+</sup> from the cell (k) (due to the PMCA pump), the inflow rate of Ca<sup>2+</sup> into the ER from the cytosol, involving the rate and maximum rate of the SERCA pump (V<sub>2</sub> and V<sub>M2</sub>), and the threshold constant for the latter pumping action (K<sub>2</sub>) (Figures 1 and 7). Thirdly, variables must consider the cooperativity degree of the activation process. The range of values for free [Ca<sup>2+</sup>]<sub>cyt</sub> is 0.05 to 0.1, and that for free [Ca<sup>2+</sup>]<sub>ER</sub> is 100 to 700 μM [53].

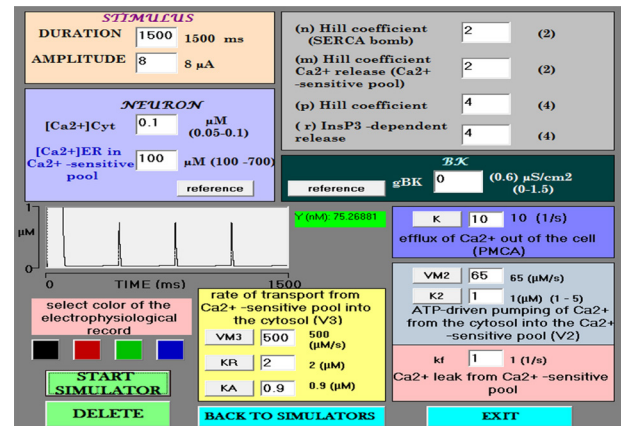
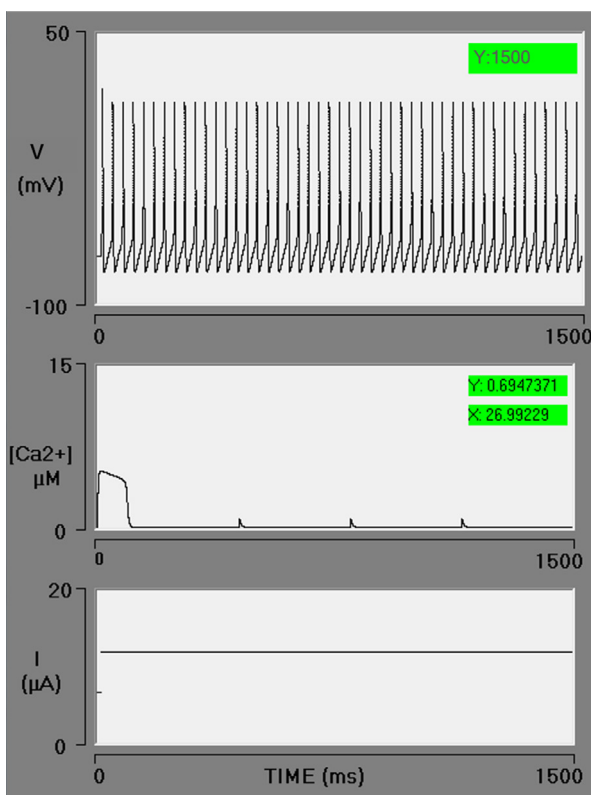


FIGURE 1. Data entry module. The simulator begins at default values for each variable. An enlargement of the small Ca<sup>2+</sup> spikes is shown in the center (amplitude = 763 nM). Under such conditions, the control neuron does not have BK channels (g<sub>BK</sub> = 0).

When opening the simulator, the default values for each variable appear. The BK channel conductance value starts at zero. The value of free [Ca<sup>2+</sup>]<sub>cyt</sub> and free [Ca<sup>2+</sup>]<sub>ER</sub> are 0.1 and 100 to 700 μM, respectively. Each simulation was carried out with the current clamp protocol. To match the timescales of the ion channels in the model with those of the Goldbeter model, a long depolarizing current pulse (1.5 s) is used. Upon start-

ing a simulation under these conditions, the recorded action potentials correspond to the Hodgkin and Huxley model with only voltage-dependent Na<sup>+</sup> and K<sup>+</sup> channels. The parameters of the Goldbeter model leading to oscillations in Ca<sup>2+</sup> begin at the reference values, and immediately after there is an increase in [Ca<sup>2+</sup>]<sub>cyt</sub> of 5 μM with a duration of 96 ms, (a local [Ca<sup>2+</sup>]<sub>cyt</sub> transient) followed by calcium spikes of 741 nM (Figure 2).



**FIGURE 2. Electrophysiology interface simulator with three oscilloscope screens. In the control simulation, the spike train generated by the Hodgkin and Huxley model is displayed on the upper screen. The local cytosolic Ca<sup>2+</sup> transient followed by three Ca<sup>2+</sup> spikes is exhibited on the middle screen. The stimulus current pulse (with a duration of 1500 ms) is illustrated on the bottom screen. In this simulation, the BK conductance is zero.**

Khodakhah and Ogden<sup>[54]</sup> reported that IP<sub>3</sub> triggers a release of Ca<sup>2+</sup> from the ER with an initial well-defined delay, which decreases as the concentration of IP<sub>3</sub> rises

(mean, 85 ms at 10 μM IP<sub>3</sub>). In the present study, the simulation is initiated at the moment Ca<sup>2+</sup> is released from the ER. Hence, a series of factors are not considered in the model: the interaction of the first messenger with the receptor on the plasma membrane, the cascade of second messengers, the explicit interaction of IP<sub>3</sub> and Ca<sup>2+</sup> with IP<sub>3</sub>-Rs, and the corresponding delay in the release of Ca<sup>2+</sup>. The dynamics of Ca<sup>2+</sup> is local. The diffusion and chelation of Ca<sup>2+</sup> are not simulated.

Diverse physiological processes (including pathological phenomena) are modulated by the generation and propagation of [Ca<sup>2+</sup>]<sub>cyt</sub> signals. The release of Ca<sup>2+</sup> from the ER takes place through sparklets, sparks, blink, scintilla, puffs, and other forms<sup>[16]</sup>. Since such elementary events are produced in microdomains, the multiple forms of Ca<sup>2+</sup> release confer intracellular Ca<sup>2+</sup> signaling with a broad architecture in space, time, and intensity, which in turn underlies signaling efficiency, stability, specificity, and diversity<sup>[55]</sup>. The calcium buffers are instrumental in achieving temporal, spatial, and functional compartmentalization under these conditions, creating steep gradients in a close proximity of channels, until reaching an internal calcium concentration on the order of tens of micromoles<sup>[56]</sup>. The local [Ca<sup>2+</sup>]<sub>cyt</sub> transient in this simulation corresponds to a Ca<sup>2+</sup> spark, characterized by Cheng and Lederer as having an approximate amplitude of 5 μM and a duration of 35 milliseconds in a space of 30 nm<sup>[55]</sup>. Under the current conditions, the duration of the spark is three times longer and a space of 90-100 nm would be expected. The activation of BK channels by spark coming from the ER has been described in smooth muscle<sup>[17]</sup> but not in neuronal cell bodies. The microdomains of Ca<sup>2+</sup> consist of very small spaces (nm) between structures (e.g., voltage-gated Ca<sup>2+</sup> channels and BK channels or IP<sub>3</sub>-Rs), thus involving very local increases in Ca<sup>2+</sup><sup>[57]</sup>. Microdomains between BK channels and IP<sub>3</sub>-Rs have been found in different cells, including neurons, with distances of 100 nm or less<sup>[23][59]</sup>.

Figure 3 presents four simulations with the following values of  $\text{Ca}^{2+}$  in the endoplasmic reticulum pool: 100, 300, 600, and 700  $\mu\text{M}$ . As a consequence, there is an increase in amplitude (5, 7, 10, and 11  $\mu\text{M}$ ) and duration (96, 235, 389, and 431 ms), respectively, of  $[\text{Ca}^{2+}]_{\text{cyt}}$ .

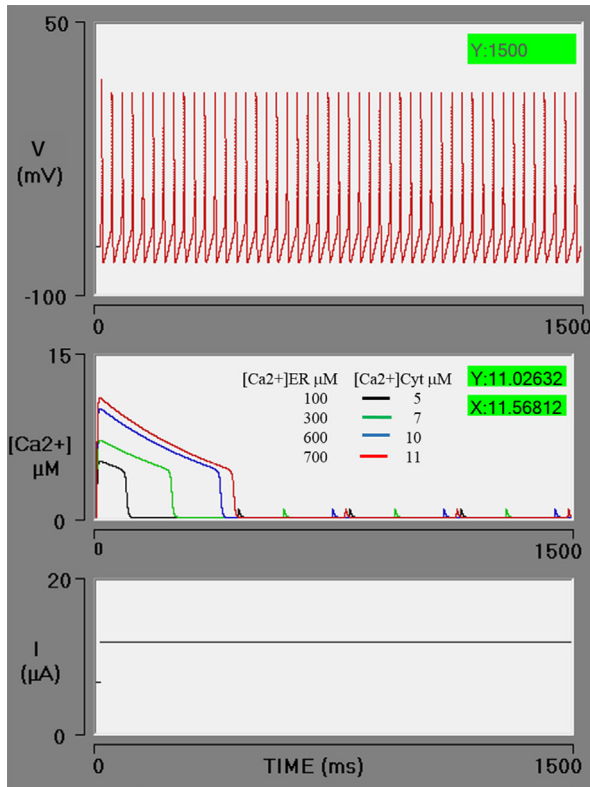


**FIGURE 3. Simulations of the effect of an increasing concentration of free  $[\text{Ca}^{2+}]_{\text{ER}}$  ( $\text{Ca}^{2+}$  in the endoplasmic reticulum) on the level of free  $[\text{Ca}^{2+}]_{\text{cyt}}$  ( $\text{Ca}^{2+}$  in the cytosol). When the simulations have an  $[\text{Ca}^{2+}]_{\text{ER}}$  value of 100, 300, 600, or 700  $\mu\text{M}$  (red box), curves the calcium (sparks) are generated on the middle oscilloscope screen in black, green, blue, and red, with an amplitude or 5, 7, 10 and 11  $\mu\text{M}$ , respectively. The PA train is unaffected because the neuron does not have BK channels ( $g_{\text{BK}} = 0$ ).**

The level of  $[\text{Ca}^{2+}]_{\text{cyt}}$  rises in function of the difference in concentration between free  $[\text{Ca}^{2+}]_{\text{cyt}}$  and the free  $[\text{Ca}^{2+}]_{\text{ER}}$ , quantified with the Hodgkin and Huxley formalism (Equation 18).

$$V_3 = V_{M3} R[\text{Ca}^{2+}] ([\text{Ca}^{2+}]_{\text{ER}} - [\text{Ca}^{2+}]_{\text{cyt}}) \quad (18)$$

Where  $V_3$  is the  $\text{IP}_3$ -sensitive  $\text{Ca}^{2+}$  efflux out of the ER through its membrane and into the cytosol,  $V_{M3}$  denotes the maximum rate of such  $\text{Ca}^{2+}$  release, and  $R[\text{Ca}^{2+}]$  depicts the fraction of the calcium channels in the open state, which depends on the  $[\text{Ca}^{2+}]_{\text{cyt}}$  concentration. The function  $R$  has been described by the same sort of mathematical formulations as for the opening of voltage-gated channels, in most cases either by Markov kinetic schemes or by Hodgkin-Huxley-style gating particles. The Goldbeter model uses a simpler approach with a suitable Hill coefficient,  $n_{\text{Hill}}$  (Equation 17) [32].

### Interaction of $\text{IP}_3$ - $R/[\text{Ca}^{2+}]_{\text{cyt}}$ /BK channels

The opening of BK channels is governed by membrane depolarization and a rise in the concentration of  $[\text{Ca}^{2+}]_{\text{cyt}}$ . Figure 4, shows the effect of a 5  $\mu\text{M}$  increment in  $[\text{Ca}^{2+}]_{\text{cyt}}$  on the action potential train in the presence of the BK channel. Each simulation has 100  $\mu\text{M}$  of  $[\text{Ca}^{2+}]_{\text{ER}}$ , with all variables set at the previously described initial values. A range was established for the BK channel conductance values, generally considered as 0.1  $\mu\text{S}/\text{cm}^2$  in hippocampal neurons and 1.2  $\mu\text{S}/\text{cm}^2$  in sympathetic ganglion cells, in agreement with the values proposed by Traub and Miles and by Koch and Segev, respectively [46] [60]. Four simulations were carried out with a BK conductance of 0.1, 0.6, 1.2, and 1.5  $\mu\text{S}/\text{cm}^2$ , affording the following results (respectively): no effect on the PA train (1500 ms), braking of the PA train at 1050 ms, fast braking at 83 ms, and braking immediately after the first action potential (values in green boxes in Figure 4 A, B, C, and D). Hence, there was a conductance-dependent effect of the  $[\text{Ca}^{2+}]_{\text{cyt}}$ : the higher the conductance, the greater the effect of the  $[\text{Ca}^{2+}]_{\text{cyt}}$  concentration.

The dependence of the BK channel on the voltage is of an allosteric type. It has been proposed that the increase in  $[\text{Ca}^{2+}]_{\text{cyt}}$  could occur almost simultaneously with a rise in voltage, as long as the calcium source is close, as in the case of the BK/VGCC complex [60]. In the present study, a BK/ $\text{IP}_3$ -R complex is assumed. Each stimulus

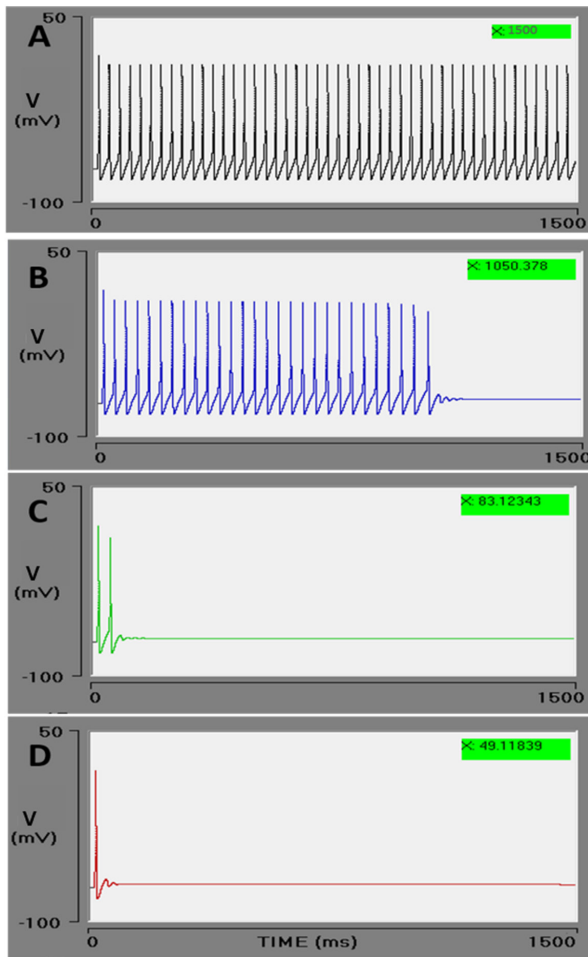


**FIGURE 4. Effect of BK conductance on the action potential train. The Goldbeter model produces a 5  $\mu\text{M}$  increment in cytosolic calcium. In these conditions, increasingly rapid braking of the action potential train is observed during the interaction of the BK channel with cytosolic calcium. As the conductance of BK channel ( $g_{\text{BK}}$ ) is intensified ( $\mu\text{S}/\text{cm}^2$ ): 0.1 (A), 0.6 (B), 1.2 (C), and 1.5 (D), the PA train durations decreases: 1500, 1050, 83, and 49 (ms), respectively (green boxes). The effect is to stop the action potential train.**

(voltage and  $\text{Ca}^{2+}$ ) interacts with different parts of the channel [7]. The overall conductance of BK channels on the plasma membrane is determined by the conductance of each channel as well as the number and open state probability of these channels (Equation 19) [61].

$$g_{\text{BK}}(V, [\text{Ca}^{2+}]_{\text{cyt}}) = n_c \hat{g} P_o(V, [\text{Ca}^{2+}]_{\text{cyt}}) \quad (19)$$

Where  $n_c$  denotes the number of ion channels,  $\hat{g}$  represents single-channel conductance (200 to 300 pS), and  $P_o$  is the open state probability value (0 to 1).

The activation of BK channels by a rise in  $[\text{Ca}^{2+}]_{\text{cyt}}$  results in a greater open state probability and an enhanced  $\text{K}^+$  efflux. This is the molecular kinetics of channel opening induced by  $\text{Ca}^{2+}$  and voltage. The  $[\text{Ca}^{2+}]_{\text{cyt}}$  concentration continues to be optimal for a greater channel opening until the saturation point is reached. Consequently, the conductance for each cell depends on the number of channels, and the unit conductance of each one. The results of the simulation indicate that the ease of response of the neuron to the concentration of  $\text{Ca}^{2+}$  depends on the number of BK channels present in its membrane. The higher the conductance, the higher the response to  $\text{Ca}^{2+}$  and vice versa.

Subsequently, an evaluation was made of enhancing the rate of the IP<sub>3</sub>-sensitive release of  $[\text{Ca}^{2+}]_{\text{ER}}$  to the cytosol. The parameters of the neuron were fixed to the default values and the BK conductance set at 0.6  $\mu\text{S}/\text{cm}^2$  (an intermediate value). By increasing the value of  $V_{\text{M3}}$  from 500 to 600, a higher level of  $[\text{Ca}^{2+}]_{\text{cyt}}$  is obtained. An abrupt release of  $\text{Ca}^{2+}$  from the ER boosts the  $[\text{Ca}^{2+}]_{\text{cyt}}$  from 5 to 6  $\mu\text{M}$  (red lines). In the previous simulation (blue lines), corresponding to the effect of  $[\text{Ca}^{2+}]_{\text{cyt}}$  at 5  $\mu\text{M}$ , the action potential train was found to brake at 721 ms. When the concentration of  $[\text{Ca}^{2+}]_{\text{cyt}}$  is increased, calcium acts on the BK channel, stopping the action potential train after the second action potential (Figure 5). It is observed that at greater CICR pumping rates, the level of  $[\text{Ca}^{2+}]_{\text{cyt}}$  rises by a calcium-induced calcium release process and/or by the direct action of IP<sub>3</sub> on the calcium-IP<sub>3</sub>-R channel (by Schetter and Smolen in [59]).

An increment in  $V_{\text{M3}}$  to 700  $\mu\text{M}/\text{s}$  generates a rise in  $[\text{Ca}^{2+}]_{\text{cyt}}$  to 7  $\mu\text{M}$ . Under these conditions, the neuron stops firing immediately after the first action potential (Figure 6). Although the model of Goldbeter contemplates the action of IP<sub>3</sub> on IP<sub>3</sub>-R and offers a good

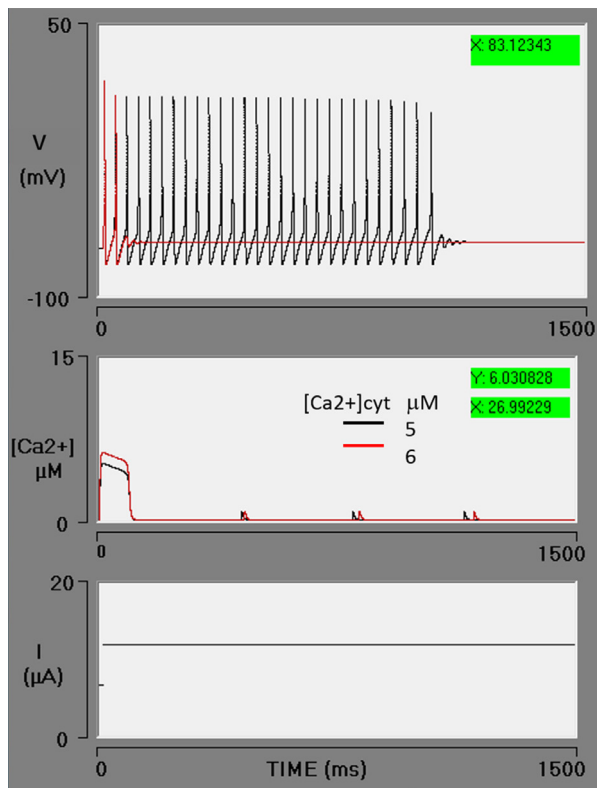


**FIGURE 5.** Effect of an enhanced  $\text{Ca}^{2+}$  efflux from the endoplasmic reticulum to the cytosol. An increment in  $V_{M3}$  from 500 to 600  $\mu\text{M/s}$  causes a greater outflow of  $\text{Ca}^{2+}$  from the ER to the cytosol, leading to a rise in the cytosolic  $\text{Ca}^{2+}$  concentration from 5 to 6  $\mu\text{M}$ . With an intensified activation of BK channels, the action potential train stops after the second firing. The lines in black depict the previous simulation, while the lines in red illustrate this simulation with an increased  $V_{M3}$  (red box).

approximation of the experimental data, it does not provide a dose-response relationship. It has been documented in the literature that the higher the level of  $\text{IP}_3$ , the greater the release of  $\text{Ca}^{2+}$  from the ER [62]. Taking the limitations of the Goldbeter model into account, this simulation reasonably resembles the  $\text{IP}_3$ -sensitive  $\text{Ca}^{2+}$  release from the  $[\text{Ca}^{2+}]_{\text{ER}}$  pool.

According to the results,  $\text{Ca}^{2+}$  released from the ER to the cytosol can effectively gate BK channels, and the main effect is to stop the spike train (Figure 6). These findings are consistent with reported experimental data. The  $\text{Ca}^{2+}$

released from ER stores, specifically through  $\text{IP}_3$ Rs but not RyRs, produces pauses in the firing of spiny projection neurons due to the activation of BK and SK channels [63]. The author proposes two  $\text{Ca}^{2+}$  signaling pathways:

- (1) action potential  $\rightarrow$  VGCC  $\rightarrow$  RyR  $\rightarrow$  BK & SK  $\rightarrow$  sAHP (slow afterhyperpolarization); and
- (2) mGluR/mAChR (metabotropic glutamate receptors / muscarinic acetylcholine receptors)  $\rightarrow$   $\text{IP}_3$   $\rightarrow$   $\text{IP}_3\text{R}$   $\rightarrow$  BK & SK  $\rightarrow$  firing pause.

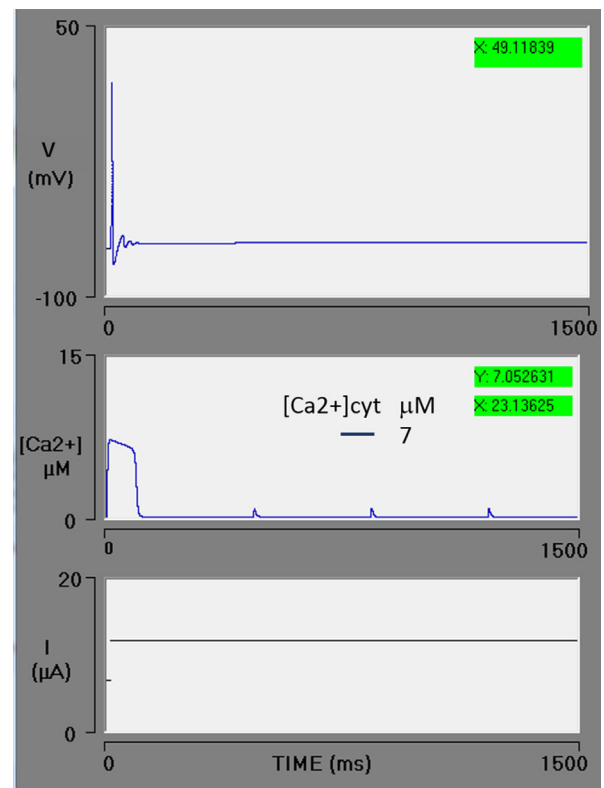


**FIGURE 6.** Spike train simulation with high efflux of  $\text{Ca}^{2+}$  from the endoplasmic reticulum (ER) pool. The maximum rate of  $\text{Ca}^{2+}$  efflux ( $V_{M3}$ ) = 700  $\mu\text{M/s}$ , resulting in a cytosolic  $\text{Ca}^{2+}$  transient increase with an amplitude of 7  $\mu\text{M}$ . The greater level of cytosolic  $\text{Ca}^{2+}$  activated the BK channels, immediately stopping the spike train.

In the current contribution, a theoretical evaluation was made of the level of  $[\text{Ca}^{2+}]_{\text{cyt}}$ , mainly considering the interaction of  $\text{IP}_3$ -Rs with BK channels. The find-

ings support the possible existence of a microdomain. In places where the ER membrane and the cytoplasmic membrane are far apart, the diffusion and chelation will decrease the amplitude of the Ca<sup>2+</sup> signal and this mechanism may not be activated. This depends, according to the results presented here, on the number of BK channels present in the membrane. The diffusion and chelation processes of Ca<sup>2+</sup> are not contemplated in this model.

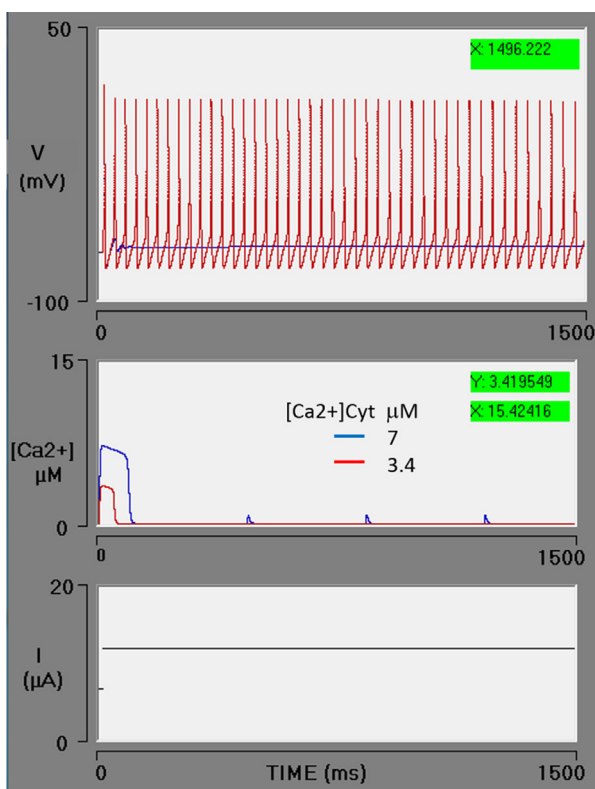


**FIGURE 7. Ca<sup>2+</sup> uptake from the cytosol by the SERCA pump. The action of the SERCA pump is increased by an increment in the  $K_2$  parameter (from 1 to 2  $\mu\text{M}$ , being the threshold constant for pumping; red box).**

The concentration of cytosolic calcium decreases from 7 to 3.4  $\mu\text{M}$ . Consequently, cytosolic calcium is below the threshold required for the activation of the BK channels and the neuron has a sustained action potential train. The blue line portrays the previous simulation (Figure 6), using the same value of  $V_{M3}$  (blue box) in this simulation. The red line depicts the present simulation (with the SERCA pump set at a higher rate).

The effect of accelerating the action of the ATPase pump (SERCA) was explored under conditions of high Ca<sup>2+</sup> efflux (the previous simulation). An increase in the  $K_2$  parameter (the threshold constant for pumping) from 1 to 2  $\mu\text{M}$  decreases the concentration of  $[\text{Ca}^{2+}]_{\text{cyt}}$  from 7 to 3.4  $\mu\text{M}$ . As can be appreciated, the action potential train is reversed and the neuron fires continuously during the simulated time (Figure 7).

Under physiological conditions, the PMCA pump and the SERCA pump are responsible for avoiding an excess concentration of  $[\text{Ca}^{2+}]_{\text{cyt}}$ , which could be toxic to the cell [22] [49]. Such an excess concentration of Ca<sup>2+</sup> would inhibit IP<sub>3</sub>-R [22]. Calcium oscillations have been demonstrated to move like waves with an amplitude in the order of nM [21] [36] and a range dependent on their diffusion and binding with chelating molecules [18]. These oscillations have been proposed as signals for various cellular processes, including synaptic plasticity, regulation of neurotransmission, cell differentiation, apoptosis, embryonic development, and secretion [21]. The abrupt influx of Ca<sup>2+</sup> into the cell by voltage-gated calcium channels in the plasma membrane activates BK channels and triggers a change in action potential frequency [18]. The results of the present simulation show how an abrupt, focused increase in  $[\text{Ca}^{2+}]_{\text{cyt}}$  from the endoplasmic reticulum store, very similar to those described as “spark”, favors the activation of BK channels and produces a pause in the action potential train. This would imply that, under certain conditions, a mechanism capable of stopping neuronal signaling is activated.

## CONCLUSIONS

A theoretical study of the IP<sub>3</sub>-R/BK channel interaction was carried out by means of a simulator. Consequently, it was possible to modify the parameters to regulate the concentration of Ca<sup>2+</sup> in the cytosol in order to monitor the effects. The variables considered are related to the flow of Ca<sup>2+</sup> from cytosol: out of the cytosol to the ER (the SERCA pump) and to extra-

cellular space (the PMCA pump), as well as into the cytosol from the ER (through the  $IP_3$ -Rs) and from extracellular space (the VGCCs). Additionally, the conductance of the BK channel and the parameters of the Goldbeter model are included.

Some insights were provided into the general character of the  $IP_3$ -R/BK channel interaction. (1) The  $[Ca^{2+}]_{cyt}$  concentration required to activate BK channels varies in accordance with the conductance of the channel. With a greater conductance, the concentration of  $Ca^{2+}$  necessary for activation is lower. (2) The BK channel is activated by an abrupt release of  $Ca^{2+}$  from the ER. This increase in  $Ca^{2+}$  is local and resembles spark. (3) The amplitude and duration of the abrupt efflux of  $Ca^{2+}$  from the ER depends on the difference in the concentration between the free  $[Ca^{2+}]_{cyt}$  and the free  $[Ca^{2+}]_{ER}$ . The higher the concentration of the latter, the greater the amplitude and duration of the efflux. (4) A rise in the concentration of  $[Ca^{2+}]_{cyt}$  increases the concentration of  $[Ca^{2+}]_{cyt}$  and favors the activation of BK channels. (5) An acceleration of the SERCA and/or PMCA pumps decreases the concentration of  $[Ca^{2+}]_{cyt}$ , thus reducing or avoiding the activation of BK channels. (6) A rise in  $[Ca^{2+}]_{cyt}$  activates the BK channels, leading to an immediate pause or stop of the spike train. This function will allow the neuron to generate a firing pattern in bursts and under certain conditions be a possible mechanism for resetting or preventing sustained abnormal PA activities (7). The colocalization of the BK and  $IP_3$ -R channels in a microdomain is a necessary

condition for the manifestation of the following pathway in a neuron:  $IP_3 \rightarrow IP_3\text{-R} \rightarrow Ca^{2+} \rightarrow BK\text{ channels} \rightarrow$  pause (stop). This sequence is the regulatory mechanism (8) For neurons with a low  $g_{BK}$ , a high  $[Ca^{2+}]_{cyt}$  concentration, and a greater difference between this parameter and free  $[Ca^{2+}]_{ER}$  is necessary to activate BK channels. (9) In case of having an elevated level of  $g_{BK}$  conductance, neurons activate the BK channels more easily. The aforementioned theoretical results help to explain the experimental data of Clements et al. [63] and are in accordance with the proposal made by these authors about the existence of  $Ca^{2+}$  signaling pathways that mediate BK channel activation according to the level of  $[Ca^{2+}]_{ER}$ .

#### AUTHOR CONTRIBUTIONS

M.E.P.B. consultant in physiology and in charge of the simulated experiments. M.R.M. was responsible for programming the design of interfaces and figures. J.Q.P. supervised the union of the models and the bibliographic review. M.F.P.E. oversaw the programming and compilation of the simulators. A.R.L. consulting in neuroscience and programming, in charge of mathematical models and their numerical solution. All authors participated in the structural analysis, review, and correction of the work.

#### ACKNOWLEDGMENTS

The authors thank Bruce Allan Larsen and Laura Flores for proofreading the manuscript, and Dr. Jorge Flores-Hernández for useful comments.

## REFERENCES

- [1] Sausbier U, Sausbier M, Sailer CA, Arntz C, Knaus HG, Neuhuber W, et al. Ca<sup>2+</sup>-activated K<sup>+</sup> channels of the BK-type in the mouse brain. *Histochem Cell Biol* [Internet]. 2005;125(6):725-41. Available from: <https://doi.org/10.1007/s00418-005-0124-7>
- [2] Faber ESL, Sah P. Calcium-Activated Potassium Channels: Multiple Contributions to Neuronal Function. *Neurosci* [Internet]. 2003;9(3):181-94. Available from: <https://doi.org/10.1177/1073858403009003011>
- [3] Meech RW. Intracellular calcium injection causes increased potassium conductance in Aplysia nerve cells. *Comp Biochem Physiol Part A Physiol* [Internet]. 1972;42(2):493-9. Available from: [https://doi.org/10.1016/0300-9629\(72\)90128-4](https://doi.org/10.1016/0300-9629(72)90128-4)
- [4] Latorre R, Castillo K, Carrasquel-Ursulaez W, Sepulveda RV, Gonzalez-Nilo F, Gonzalez C, et al. Molecular determinants of BK channel functional diversity and functioning. *Physiol Rev* [Internet]. 2017;97(1):39-87. Available from: <https://doi.org/10.1152/physrev.00001.2016>
- [5] Kshatri AS, Gonzalez-Hernandez A, Giraldez T. Physiological Roles and Therapeutic Potential of Ca<sup>2+</sup> Activated Potassium Channels in the Nervous System. *Front Mol Neurosci* [Internet]. 2018;11:1-18. Available from: <https://doi.org/10.3389/fnmol.2018.00258>
- [6] Lee US, Cui J. BK channel activation: structural and functional insights. *Trends Neurosci* [Internet]. 2010;33(9):415-23. Available from: <https://doi.org/10.1016/j.tins.2010.06.004>
- [7] Horrigan FT, Aldrich RW. Coupling between voltage sensor activation, Ca<sup>2+</sup> binding and channel opening in large conductance (BK) potassium channels. *J Gen Physiol* [Internet]. 2002;120:267-305. Available from: <https://doi.org/10.1085/jgp.20028605>
- [8] Ha GE, Cheong E. Spike frequency adaptation in neurons of the central nervous system. *Exp Neurobiol* [Internet]. 2017;26(4):179-85. Available from: <https://doi.org/10.5607/en.2017.26.4.179>
- [9] Bock T, Stuart GJ. The Impact of BK Channels on Cellular Excitability Depends on their Subcellular Location. *Front Cell Neurosci* [Internet]. 2016;10:1-8. Available from: <https://doi.org/10.3389/fncel.2016.00206>
- [10] Gu N, Vervaeke K, Storm JF. BK potassium channels facilitate high-frequency firing and cause early spike frequency adaptation in rat CA1 hippocampal pyramidal cells. *J Physiol* [Internet]. 2007;3:859-82. Available from: <https://doi.org/10.1113/jphysiol.2006.126367>
- [11] Berkefeld H, Fakler B, Schulte U. Ca<sup>2+</sup>-Activated K<sup>+</sup> Channels: From Protein Complexes to Function. *Physiol Rev* [Internet]. 2010;90(4):1437-59. Available from: <https://doi.org/10.1152/physrev.00049.2009>
- [12] Misonou H, Menegola M, Buchwalder L, Park E, Meredith A, Rhodes K, et al. Immunolocalization of the Ca<sup>2+</sup>-activated K<sup>+</sup> channel Slo1 in axons and nerve terminals of mammalian brain and cultured neurons. *J Comp Neurol* [Internet]. 2006;496(3):289-302. Available from: <https://doi.org/10.1002/cne.20931>
- [13] Wang Z-W. Regulation of Synaptic Transmission by Presynaptic CaMKII and BK Channels. *Mol Neurobiol* [Internet]. 2008;38(2):153-66. Available from: <https://doi.org/10.1007/s12035-008-8039-7>
- [14] Griguoli M, Sgritta M, Cherubini E. Presynaptic BK channels control transmitter release: physiological relevance and potential therapeutic implications. *J Physiol* [Internet]. 2016;13:3489-500. Available from: <https://doi.org/10.1113/JP271841>
- [15] Bygrave FL, Benedetti A. What is the concentration of calcium ions in the endoplasmic reticulum? *Cell Calcium* [Internet]. 1996;19(6):547-51. Available from: [https://doi.org/10.1016/s0143-4160\(96\)90064-0](https://doi.org/10.1016/s0143-4160(96)90064-0)
- [16] Berridge MJ. Calcium microdomains: Organization and function. *Cell Calcium* [Internet]. 2006;40(5-6):405-12. Available from: <https://doi.org/10.1016/j.ceca.2006.09.002>
- [17] Dopico AM, Bukiya AN, Jaggar JH. Calcium- and voltage-gated BK channels in vascular smooth muscle. *Pflügers Archiv* [Internet]. 2018;470(9):1271-89. Available from: <https://doi.org/10.1007/s00424-018-2151-y>
- [18] Fakler B, Adelman JP. Control of KCa Channels by Calcium Nano/Microdomains. *Neuron* [Internet]. 2008;59(6):873-81. Available from: <https://doi.org/10.1016/j.neuron.2008.09.001>
- [19] Samtleben S, Jaepel J, Fecher C, Andreska T, Rehberg M, Blum R. Direct imaging of ER calcium with targeted-esterase induced dye loading (TED). *J Vis Exp* [Internet]. 2013;(75):1-17. Available from: <https://doi.org/10.3791/50317>
- [20] Verkhratsky A. Physiology and Pathophysiology of the Calcium Store in the Endoplasmic Reticulum of Neurons. *Physiol Rev* [Internet]. 2005;85(1):201-79. Available from: <https://doi.org/10.1152/physrev.00004.2004>
- [21] Karagas NE, Venkatachalam K. Roles for the Endoplasmic Reticulum in Regulation of Neuronal Calcium Homeostasis. *Cells* [Internet]. 2019;8(10):1232. Available from: <https://doi.org/10.3390/cells8101232>
- [22] Foskett JK, White C, Cheung K-H, Mak D-OD. Inositol Trisphosphate Receptor Ca<sup>2+</sup> Release Channels. *Physiol Rev* [Internet]. 2007;87(2):593-658. Available from: <https://doi.org/10.1152/physrev.00035.2006>
- [23] Irie T, Trussell LO. Double-Nanodomain Coupling of Calcium Channels, Ryanodine Receptors, and BK Channels Controls the Generation of Burst Firing. *Neuron* [Internet]. 2017;96(4):856-870.e4. Available from: <https://doi.org/10.1016/j.neuron.2017.10.014>
- [24] Wu Y, Whiteus C, Xu CS, Hayworth KJ, Weinberg RJ, Hess HF, et al. Contacts between the endoplasmic reticulum and other membranes in neurons. *Proc Natl Acad Sci U S A* [Internet]. 2017;114(24):E4859-67. Available from: <https://doi.org/10.1073/pnas.1701078114>
- [25] Terasaki M, Shemesh T, Kasthuri N, Klemm RW, Hayworth KJ, Hand AR, et al. Stacked endoplasmic reticulum sheets are connected by helical membrane motifs. *Cell* [Internet]. 2013;154(2):285-96. Available from: <https://doi.org/10.1016/j.cell.2013.06.031>
- [26] Takahashi K, Wood RL. Subsurface cisterns in the Purkinje cells of cerebellum of Syrian hamster. *Zeitschrift für Zellforsch und Mikroskopische Anat* [Internet]. 1970;110(3):311-20. Available from: <https://doi.org/10.1007/BF00321144>

- [27] Pan NC, Bai YF, Yang Y, Hökfelt T, Xu ZQD. Activation of galanin receptor 2 stimulates large conductance  $Ca^{2+}$ -dependent  $K^+$  (BK) channels through the  $IP_3$  pathway in human embryonic kidney (HEK293) cells. *Biochem Biophys Res Commun* [Internet]. 2014;446(1):316-21. Available from: <https://doi.org/10.1016/j.bbrc.2014.02.110>
- [28] Mujica PE, González FG. Interaction between  $IP_3$  receptors and BK channels in arterial smooth muscle: Non-canonical  $IP_3$  signaling at work. *J Gen Physiol* [Internet]. 2011;137(5):473-7. Available from: <https://doi.org/10.1085/jgp.201110607>
- [29] Bootman MD, Collins TJ, Peppiatt CM, Prothero LS, MacKenzie L, De Smet P, et al. Calcium signalling - An overview. *Semin Cell Dev Biol* [Internet]. 2001;12(1):3-10. Available from: <https://doi.org/10.1006/scdb.2000.0211>
- [30] Larkum ME, Watanabe S, Nakamura T, Lasser-Ross N, Ross WN. Synaptically Activated  $Ca^{2+}$  Waves in Layer 2/3 and Layer 5 Rat Neocortically Pyramidal Neurons. *J Physiol* [Internet]. 2003;549(2):471-88. Available from: <https://doi.org/10.1113/jphysiol.2002.037614>
- [31] Ross WN. Understanding calcium waves and sparks in central neurons. *Nat Rev Neuroscience* [Internet]. 2015;13(3):157-68. Available from: <https://doi.org/10.1038/nrn3168>
- [32] Goldbeter A, Dupont G, Berridge MJ. Minimal model for signal-induced  $Ca^{2+}$  oscillations and for their frequency encoding through protein phosphorylation. *Proc Natl Acad Sci U S A* [Internet]. 1990;87(4):1461-5. Available from: <https://doi.org/10.1073/pnas.87.4.1461>
- [33] De Young GW, Keizer J. A single-pool inositol 1,4,5-trisphosphate-receptor-based model for agonist-stimulated oscillations in  $Ca^{2+}$  concentration. *Proc Natl Acad Sci U S A* [Internet]. 1992;89(20):9895-9. Available from: <https://doi.org/10.1073/pnas.89.20.9895>
- [34] Li Y-X, Rinzel J. Equations for  $InsP_3$  Receptor-mediated  $[Ca^{2+}]_i$  Oscillations Derived from a Detailed Kinetic Model: A Hodgkin-Huxley Like Formalism. *J Theor Biol* [Internet]. 1994;166(4):461-73. Available from: <https://doi.org/10.1006/jtbi.1994.1041>
- [35] Bezprozvanny I, Ehrlich BE. Inositol (1,4,5)-trisphosphate ( $InsP_3$ )-gated Ca channels from cerebellum: Conduction properties for divalent cations and regulation by intraluminal calcium. *J Gen Physiol* [Internet]. 1994;104(5):821-56. Available from: <https://doi.org/10.1085/jgp.104.5.821>
- [36] Keizer J, Li YX, Stojilkovic S, Rinzel J. Essay  $InsP_3$ -induced  $Ca^{2+}$  excitability of the endoplasmic reticulum. *Mol Biol Cell* [Internet]. 1995;6:945-51. Available from: <https://doi.org/10.1091/mbc.6.8.945>
- [37] Tang Y, Stephenson JL, Othmer HG. Simplification and Analysis of Models of Calcium Dynamics Based on  $IP_3$ -Sensitive Calcium Channel Kinetics. *Biophys J* [Internet]. 1996;70(1):246-63. Available from: [https://doi.org/10.1016/S0006-3495\(96\)79567-X](https://doi.org/10.1016/S0006-3495(96)79567-X)
- [38] Sneyd J, Falcke M. Models of the inositol trisphosphate receptor. *Prog Biophys Mol* [Internet]. 2005;89(3):207-45. Available from: <https://doi.org/10.1016/j.pbiomolbio.2004.11.001>
- [39] Kötter R. *Neuroscience Databases: A Practical Guide*. New York: Springer; 2003. 310 p.
- [40] Hituri K, Linne M-L. Comparison of Models for  $IP_3$  Receptor Kinetics Using Stochastic Simulations. *PLoS One* [Internet]. 2013;8(4): e59618. Available from: <https://doi.org/10.1371/journal.pone.0059618>
- [41] Edgerton JR, Reinhart PH. Distinct contributions of small and large conductance  $Ca^{2+}$ -activated  $K^+$  channels to rat Purkinje neuron function. *J Physiol* [Internet]. 2003;548(1):53-69. Available from: <https://doi.org/10.1113/jphysiol.2002.027854>
- [42] Blaustein MP, Golovina VA. Structural complexity and functional diversity of endoplasmic reticulum  $Ca^{2+}$  stores. *Trends Neurosci* [Internet]. 2001;24(10):602-8. Available from: [https://doi.org/10.1016/S0166-2236\(00\)01891-9](https://doi.org/10.1016/S0166-2236(00)01891-9)
- [43] Sterratt D, Graham B, Gillies A, Willshaw D. *Principles of Computational Modelling in Neuroscience*. Cambridge: Cambridge University Press; 2011. 300p.
- [44] Traub RD, Miles R. *Neuronal Networks Hippocampus*. Cambridge: Cambridge University Press; 1991. 281p.
- [45] Hodgkin AL, Huxley AF. A quantitative description of membrane current and its application to conduction and excitation in Nerve. *J Physiol* [Internet]. 1952;117(4):500-44. Available from: <https://doi.org/10.1113/jphysiol.1952.sp004764>
- [46] McCarron JG, Chalmers S, Bradley KN, MacMillan D, Muir TC.  $Ca^{2+}$  microdomains in smooth muscle. *Cell Calcium* [Internet]. 2006;40(5-6):461-93. Available from: <https://doi.org/10.1016/j.ceca.2006.08.010>
- [47] Blackwell KT. Approaches and tools for modeling signaling pathways and calcium dynamics in neurons. *J Neurosci Methods* [Internet]. 2013;220(2):131-140. Available from: <https://doi.org/10.1016/j.jneumeth.2013.05.008>
- [48] Chen-Engerer HJ, Hartmann J, Karl RM, Yang J, Feske S, Konnerth A. Two types of functionally distinct  $Ca^{2+}$  stores in hippocampal neurons. *Nat Commun* [Internet]. 2019;10(1):1-8. Available from: <https://doi.org/10.1038/s41467-019-11207-8>
- [49] Dupont G, Goldbeter A. One-pool model for  $Ca^{2+}$  oscillations involving  $Ca^{2+}$  and inositol 1,4,5-triphosphate as co-agonists for  $Ca^{2+}$  release. *Cell Calcium* [Internet]. 1993;14(4):311-22. Available from: [https://doi.org/10.1016/0143-4160\(93\)90052-8](https://doi.org/10.1016/0143-4160(93)90052-8)
- [50] Blackwell KT. Modeling calcium concentration and biochemical reactions. *Brains, Minds, and Media* [Internet]. 2005;1:1-27. Available from: <https://www.brains-minds-media.org/archive/224>
- [51] Zill DG. *Ecuaciones diferenciales con aplicaciones*. México: Grupo Editorial Iberoamérica; 1988. 516p. Spanish.
- [52] Constantinides A. *Applied Numerical Methods with Personal Computers*. New York, USA: McGraw-Hill International Editions; 1987. 626p.
- [53] Foskett JK, White C, Cheung K-H, Mak D-OD. Inositol Trisphosphate Receptor  $Ca^{2+}$  release channels. *Physiol Rev* [Internet]. 2007;87(2):593-658. Available from: <https://doi.org/10.1152/physrev.00035.2006>
- [54] Khodakhah K, Ogden D. Fast activation and inactivation of inositol trisphosphate evoked  $Ca^{2+}$  release in rat cerebellar Purkinje neurones. *J Physiol* [Internet]. 1995;487(2):343-58. Available from: <https://doi.org/10.1113/jphysiol.1995.sp020884>
- [55] Cheng H, Lederer WJ. Calcium Sparks. *Physiol Rev* [Internet]. 2008;88(4):1491-545. Available from: <https://doi.org/10.1152/physrev.00030.2007>
- [56] Naraghi M, Neher E. Linearized Buffered  $Ca^{2+}$  Diffusion in Microdomains and Its Implications for Calculation of  $[Ca^{2+}]_i$  at the Mouth of a Calcium Channel. *J Neurosci* [Internet]. Available from: 1997;17(18):6961-73. Available from: <https://doi.org/10.1523/JNEUROSCI.17-18-06961.1997>

- [57] Rizzuto R, Pozzan T. Microdomains of Intracellular  $Ca^{2+}$ : Molecular Determinants and Functional Consequences. *Physiol Rev* [Internet]. 2006;86(1):369-408. Available from: <https://doi.org/10.1152/physrev.00004.2005>
- [58] Weaver AK, Olsen ML, McFerrin MB, Sontheimer H. BK Channels Are Linked to Inositol 1,4,5-Triphosphate Receptors via Lipid Rafts: A novel mechanism for coupling  $[Ca^{2+}]_i$  to ion channel activation. *J Biol Chem* [Internet]. 2007;282(43):31558-68. Available from: <https://doi.org/10.1074/jbc.M702866200>
- [59] Koch C, Segev I. *Methods in Neuronal Modeling*. Cambridge: The MIT Press; 1999. 671p.
- [60] Berkefeld H, Fakler B. Repolarizing Responses of  $BK_{Ca}$ -Cav Complexes Are Distinctly Shaped by Their Cav Subunits. *J Neurosci* [Internet]. 2008;28(33):8238-45. Available from: <https://doi.org/10.1523/JNEUROSCI.2274-08.2008>
- [61] Hou P, Xiao F, Liu H, Yuchi M, Zhang G, Wu Y, et al. Extrapolating microdomain  $Ca^{2+}$  dynamics using BK channels as a  $Ca^{2+}$  sensor. *Sci Rep* [Internet]. 2016;6:17343. Available from: <https://doi.org/10.1038/srep17343>
- [62] Meyer T, Stryer L. Molecular model for receptor-stimulated calcium spiking. *Proc Natl Acad Sci U S A* [Internet]. 1988;85(14):5051-5. Available from: <https://doi.org/10.1073/pnas.85.14.5051>
- [63] Clements MA, Swapna I, Morikawa H. Inositol 1,4,5-Triphosphate Drives Glutamatergic and Cholinergic Inhibition Selectively in Spiny Projection Neurons in the Striatum. *J Neurosci* [Internet]. 2013;33(6):2697-708. Available from: <https://doi.org/10.1523/JNEUROSCI.4759-12.2013>

## Three-dimensional printing in healthcare

### Impresión 3D en cuidado de la salud

*A. I. Pérez-Sanpablo<sup>1</sup>, E. Romero-Ávila<sup>2</sup>, A. González-Mendoza<sup>1</sup>*

<sup>1</sup>Instituto Nacional de Rehabilitación Luis Guillermo Ibarra Ibarra, Mexico City, Mexico

<sup>2</sup>Department of Rehabilitation and Prevention Engineering, Institute of Applied Medical Engineering - Helmholtz Institute, RWTH Aachen University, Aachen, Germany

#### ABSTRACT

This work aims to briefly present the cutting edge of 3D printing innovation in healthcare. This technology is used for surgical planning, medical education, bioprinting of tissues, and medical equipment spare parts in fields like pharmacology, prosthetics, surgery, and regenerative medicine. A review of the last decade was made in the search engines of PubMed and Espacenet. Three authors reviewed titles, abstracts, and keywords separately to identify studies appropriate to the topic. After the initial examination, complete texts of identified relevant studies were obtained and classified according to the authors. Results were synthesized in a narrative literature review. The revision showed that 3D printing has become of common use in the healthcare system since it allows medical personnel to implement customized solutions for each patient, thus reducing the probability of a false diagnostic or treatment. Major applications among the advantages and disadvantages of 3D printing in healthcare were presented. Nowadays, the main challenge in 3D printing is the cost of the equipment and its manufacturing. In the future, the challenges in cost could be reduced, but processing requirements and limited materials may still need further work.

**KEYWORDS:** 3D printing; stereolithography; medicine

## RESUMEN

Este artículo pretende mostrar breve y rápidamente la vanguardia del empleo de la impresión 3D en salud. La impresión 3D se utiliza para planificación quirúrgica, educación médica, bioimpresión de tejidos e impresión de repuestos de equipos médicos en campos como farmacología, prótesis, cirugía, ingeniería de tejidos y medicina regenerativa. Se realizó una revisión de publicaciones en la última década en los motores de búsqueda PubMed y Espacenet. Tres autores examinaron de forma independiente títulos y resúmenes para identificar estudios relevantes. Se obtuvieron los textos completos y se clasificaron de acuerdo con todos los autores. Los resultados se sintetizaron en una revisión narrativa de la literatura. La revisión mostró que la impresión 3D se ha vuelto de uso común en el sistema de atención médica, ya que permite al personal médico implementar soluciones personalizadas para cada paciente, lo que reduce la probabilidad de un diagnóstico o tratamiento falso. Se presentaron las principales aplicaciones, así como ventajas y desventajas de la impresión 3D en salud. Hoy en día, el principal desafío en la impresión 3D es el costo del equipo y su fabricación. En el futuro, los desafíos en costos podrían reducirse, pero los desafíos de procesamiento y materiales requieren mayor desarrollo.

**PALABRAS CLAVE:** Impresión 3D; estereolitografía; medicina

### Corresponding author

TO: Elisa Romero Avila

INSTITUTION: Institute of Applied Medical  
Engineering - Helmholtz Institute

ADDRESS: Pauwelsstraße 20, 52074, Aachen, Germany

E-MAIL: [romero@ame.rwth-aachen.de](mailto:romero@ame.rwth-aachen.de)

### Received:

26 August 2020

### Accepted:

21 January 2021

## INTRODUCTION

Three-dimensional (3D) printing started as a revolutionizing technology in different fields of healthcare and, at present, has proven to be a useful technology up to a point to become of common use. Clear examples of this are stated in the development of orthotics devices, prostheses, patient-specific implants, Drug Delivery Systems (DDD) <sup>[1][2]</sup>, realistic anatomic models for education or surgical use <sup>[1][2][3]</sup>; the creation of living cells, drugs, protein molecules, that replicate the tissue anatomy, biology, and physiology <sup>[2][4]</sup>. It is forecasted that the 3D printing industry will grow up to 8.4 billion dollars by 2025 <sup>[5]</sup>.

3D printing can be defined as a collection of technologies known as rapid prototyping <sup>[1]</sup> where the conversion of 3D virtual models (models created through Computer-Aided Design (CAD) or image processing) are converted into physical models without the need for specialized tooling, 3D printing includes several established and experimental manufacturing techniques <sup>[1][3][5]</sup>. It is important to mention that any technique used in 3D printing has its limitations and applications. 3D printing is most commonly known as additive manufacturing (AM) <sup>[6]</sup>. The most common way of work of a 3D printing machine is laying one thin layer of material that bonds with another thin layer of material <sup>[3]</sup>. This review aims to identify the latest work and perspectives of 3D printing in healthcare.

## MATERIALS AND METHODS

Searches were carried out in PubMed ([ncbi.nlm.nih.gov](http://ncbi.nlm.nih.gov)) and Espacenet ([worldwide.espacenet.com](http://worldwide.espacenet.com)) in January, 2021. The studies were in English, Spanish, and French, published between 2009 and 2020. No limitation by its publication status was made. Any type of study was included (experimental studies, observational studies, reviews). The following terms were used for the search: "Printing, Three-Dimensional", "Stereolithography", "Health Services", "Medicine", "Biomedical Research", and "Biomedical

Engineering". In PubMed, previous terms were used as MeSH terms. Three authors reviewed titles, abstracts, and keywords separately to identify studies appropriate to the topics of prostheses and implants, operative and surgical procedures, musculoskeletal system, tissue engineering, cardiovascular system, education, regenerative medicine, pharmacology, skin, otolaryngology, orthopedics, urology, gastroenterology, medical device regulation and, neurology. After the initial examination, complete texts of identified relevant studies were obtained. Studies were classified according to all authors, and disagreements as to which articles were suitable for each category included in this work were resolved by discussion. Results were arranged in a conventional literature review.

## RESULTS AND DISCUSSION

3D printing applied to the area of healthcare has progressed rapidly in the past years. As a result, 6,402 papers (see Figure 1) and 31 patents (see Figure 2) were identified.

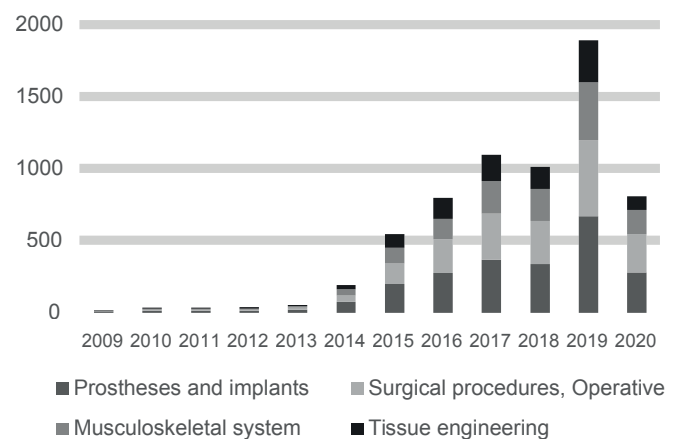


**FIGURE 1. The number of publications per year in PubMed about major 3D printing applications in the healthcare field between 2009 and 2020.**

Major fields of publication of papers about 3D printing in healthcare include prostheses and implants, surgical procedures, and research about the musculo-

skeletal system, see Figure 3. Major fields of publication of patents about 3D printing in healthcare include tissue engineering and regenerative medicine, prostheses and implants and, operative and surgical procedures, see Figure 4. In the next sections, a detailed and selective review of major applications among the advantages and disadvantages of 3D printing in healthcare is presented.

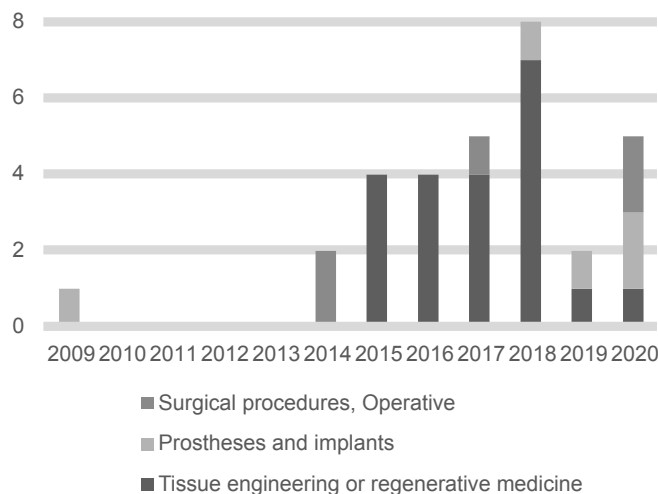


**FIGURE 2.** The number of patents per year in Espacenet about major 3D printing applications in the healthcare field between 2009 and 2020.

### Advantages of 3D printing

It can be said that the main advantage of 3D printing is the personalization of a 3D model that solves a patient-specific problem at a low-cost burden [6] [7]. However, 3D printing technologies also enhance or complement surgical training, research, minimally invasive diagnosis, and disease models [7] [8] [9] [10] [11] [12] [13].

The main advantage of 3D printing is that it can be used in different applications by only changing the printing technique and material. i.e., in tissue engineering using 3D printing techniques, it is commonly the use of hydrogels because hydrogels allow good permeability of nutrients and facilitate cell growth [14]. The use of materials such as metal is used in applications where high mechanical resistance is needed. In

applications such as prosthetics or orthotics, materials using metal can be used. In contrast, in applications such as tissue engineering, materials such as bio-ceramics and bioglass are used since these materials allow the permeability of nutrients [14].

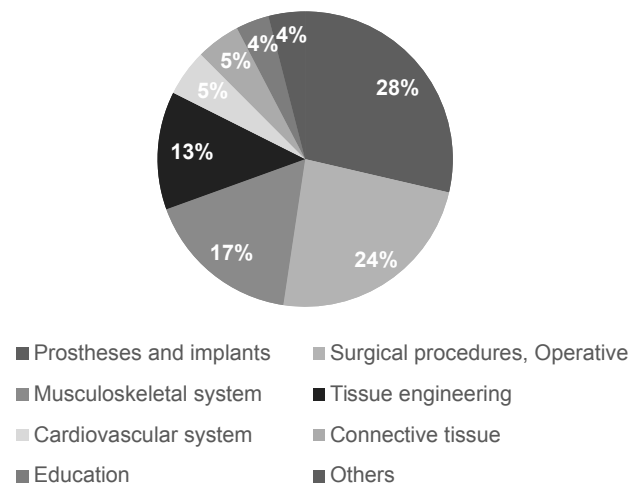


**FIGURE 3.** Major fields of publication of papers about 3D printing in healthcare are based on the number of publications per year in PubMed between 2009 and 2020.

One of the biggest roadblocks in 3D printing technology is that there is no well-established method of the process that validates the quality check in developing 3-D printed medical devices [8] [15].

The main disadvantage in 3D printing is found in its manufacturing, where the two challenges are the negative effects of the blemishes situated in the inner part of the 3D model at sub-millimeter scale, which can result from the feed supply that is damaged or machine failures and the effect of the component's placement amid the print on the execution of the material [2].

Regarding the printing technologies, there are still some limitations such as: narrow color range in stereolithography printing (*STL*), low resolution in fused deposition modeling (*FDM*), and poor quality of the surface finish in selective laser melting technique

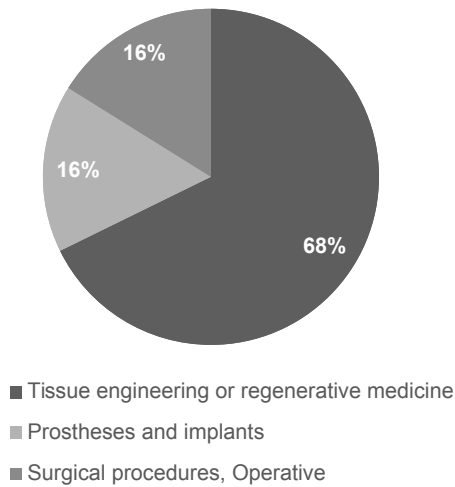


**FIGURE 4. Major fields of publication of patents about 3D printing in healthcare are based on the number of publications per year in PubMed between 2009 and 2020.**

(*SLM*) [16] [17]. Although, inkjet bioprinting represents an optimal printing technology in terms of costs and performance, the printed structures may have an irregular and rough shape due to the hydrogels used as bio-inks [16] [18]. Additionally, the 3D printed material should have specific properties such as flexibility, adaptation, and significant biocompatibility to ensure sufficient vascularization and maturation of the printed tissue [18] [19].

### 3D printing in prosthetics and implants

3D printing in prosthetics can be divided into two types: internal prosthetics and implants and external prosthetics.

Orthoses and splints could be found in external prosthetics. 3D printing has shown various advantages, such as sustainable development and costs reduction. This is particularly relevant in marginalized communities [7] [10] [15] [20]. The most common technique used is additive manufacturing (*AM*). The main advantage of 3D printing is efficiency since this model can be modeled using CAD design, allowing to suit the prosthetics perfectly to human anatomy [11].

Internal prostheses and implants are mainly used in orthopedics. Prostheses and implants must mimic the mechanical properties of bone to maximize its performance in the human body [10]. The selective laser melting (*SLM*) technique is a 3D printed technique used to produce internal prostheses and implants. Another technique is selective electron beam melting (*SEBM*) created by the Swedish company Arcam AB [9]. Both processes work by using high energy beams to disintegrate transversal forms into plies of metal powder melting powder particles into a new structure. The major difference between *SEBM* and *SLM* techniques is their source of power, the former uses electrons, and the later a laser [9]. Enumerated additional requisites of internal prostheses and implants are being biocompatible, allowing cell attachment and expansion, and possess satisfactory porosity [9] [21] [22] [23] [24] [25].

Patents in the field are related to manufacturing devices based on multiple robotic arms and sprayers, manufacturing methods based on the reconstruction of 3D images for facial prosthesis, development of new materials for bone implants, and guiding systems for colocation of dental implants made by stereolithography such as three-dimensional printing devices [26] [27] [28] [29] [30].

### 3D printing in surgical procedures

Surgical procedures request high-quality procedural outcomes in combination with optimal safety outcomes [6]. 3D printing brought into the surgical field as a tool for simulating all surgical steps ahead of time results in a better comprehension of complex underlying anomalies. This can enhance better diagnostics and assist in surgical planning [6] [7]. For example, in craniofacial and maxillofacial surgery where its success has been demonstrated [7]. The key components for surgical 3D printing are (1) analysis (critical thinking for problem-solving solutions), (2) planning (endpoint goals are fixed to formulate a surgical plan), (3) virtual surgery (multiple strategies can be run to determine the most optimal approach for surgery), (4) implant

design and production (biocompatible implants can be printed as an additional complement in surgery), and (5) postoperative analysis (the accuracy of the results can be compared using computed tomography) [6]. 3D models regularly take a day or longer to create. This means that 3D models can be used for surgical procedures where long-term planning is involved.

Success stories of application in surgical training include endoscopic ear surgery (the 3D printed models help the surgeons to reduce time), comparison of planning with 3D imaging techniques vs. 3D printing (3D printing allowed surgeons to create better surgical strategies), endoscopic endonasal (where surgeon accelerate their learning process) [6].

Patents in the field are related to methods for fabrication and collocation of 3D printed materials for facial bone fractures and knee joint replacement [27] [31] [32] [33] [34].

### 3D printing in regenerative medicine

3D printing in regenerative medicine is recognized as an emerging technology that allows the fabrication of biomimetic tissues and organs by cultivating cells on scaffolds. 3D printing in regenerative medicine is made using CAD and computer-aided manufacturing (CAM) methods [18] [35] [36]. Fabricated tissues and organs could be used for medical transplantation in regenerative medicine or drug testing.

To differentiate the specific application of 3D printing within regenerative medicine, it is commonly referred in the literature as 3D bioprinting. As it can be imagined, 3D printing in regenerative medicine has specific challenges, such as the preservation of biological functions of cells and to mimic the architectures and mechanical properties of biological tissues [19]. The 3D printing technology in the field of regenerative medicine had advanced rapidly since its beginning in 2005, when the first cell printing was performed [36].

Patents in the field are related to the fabrication of encapsulated bodies of cells [37] [38] [39], preparation and application of new materials useful as scaffolds [40] [41] [42] [43] [44] [45] [46] [47] [48] [49] [50] [51] [52] [53] [54], or new bioinks with improved printability characteristics [55].

### Bioprinting, biofabrication and bioassembly

Bioprinting in regenerative medicine has been used in literature as a general term, which refers to any biofabrication process. However, Moroni et al. have recommended a classification to distinguish each term [56]. Biofabrication is the production by bioprinting or bioassembly of products that are biologically functional using living cells, biomolecules, or biomaterials [56]. Consequently, bioprinting is only one approach to biofabrication. Bioassembly, which is the other major approach of biofabrication, is the process of biofabrication by the assembly of pre-formed cell-containing building blocks [56].

### Bioprinting techniques

The most widely used bioprinting techniques are inkjet-based printing, laser-based printing, extrusion-based printing, and stereolithography STL [18] [19].

Inkjet-based printers dispense cells or biomaterials as liquid droplets. The first inkjet-based printer was a modification of a commercial desktop inkjet printer where ink cartridge was substituted by a suspension of cells [19]. Inkjet based printers use thermal, piezoelectric, or electromechanical valve mechanisms to print heads to generate the droplets. Thermal printers apply heat to the print head to increase pressure and generate droplets. Piezoelectric printers apply a wave of pressure to split out a droplet of ink. Electromechanical valves printers open and close electromechanical valves to generate droplets. Advantages of inkjet printers are low cost, versatility in managing a wide range of cells and biomaterials with low viscosity (<10 centipoises), high resolution (20-100 micro-meters), high

speed (1-10,000 droplets per second), precise control of droplets parameters such as volume (1-300 pico-liters), pressure and temperature <sup>[19]</sup>. However, one disadvantage of inkjet-based printers is stress, either thermal or mechanical induced to cells, limitation to use high viscosity cells and biomaterials which could result in obstruction of projecting spouts, the high variability of droplet volume, early condensation, and random dispersion of cells within dispensed volume <sup>[19]</sup>.

Extrusion based printers extrude strands of cells and biomaterials by applying constant pressure through a nozzle by pneumatic or mechanical systems. The advantages of inkjet printers are their versatility to manage a wide range of cells and biomaterials, especially with high viscosity, precise control of nozzle pressure, and nozzle moving speed <sup>[19]</sup>. One disadvantage of extrusion-based printers is the shear stress imposed on cells. The survival rate of cells after extrusion-based printing is 40-86% lower than inkjet-based printing <sup>[19]</sup>.

Laser-based printers eject droplets of cells and biomaterials from a ribbon structure into a receiving substrate propelled by the high pressure produced by the energy absorption of the laser by the ribbon structure. The ribbon structure is composed of one energy-absorbing layer made of glass coated with nanofilms of gold or titanium and a second layer with a suspension of cells and materials <sup>[18]</sup>. Advantages of laser-based printers are their versatility in managing a wide range of viscosity of cells and biomaterials (1-300 mili-Pascals per second), high density of cell deposition (<108 cells per mili-liter), high resolution (one cell per drop), high speed and visualization of cells during deposition <sup>[19]</sup>.

*STL* uses a laser of UV light to solidify sections of a photo-sensitive precursor solution layer by layer. The advantages of stereolithography are high resolution (micro-meters). Disadvantages are using only photo-sensitive materials and damage induced to cells and biomaterials for UV exposure <sup>[19]</sup>.

## Bio-inks

Bio-inks are compositions of cells and biomaterials, such as supporting materials and growth factors. Bio-inks are mainly composed of hydrogels, polymers with high water content, and cross-links like extracellular matrix. Bio-ink components could be natural such as agarose, alginate, chitosan, collagen, fibrin, gelatin, gel, and gum, or artificial such as hyaluronic acid, pluronic, polyethylene glycol (*PEG*), and polycaprolactone (*PCL*) <sup>[36]</sup>. Desirable properties of a bio-ink are mechanical stiffness, structural stability, biodegradability, thermic stability, biocompatibility and tissue induction and printability <sup>[36]</sup> <sup>[57]</sup>. The mechanical stiffness of bio-ink should be similar to the mechanical stiffness of healthy tissue, which is important to support loads and maintain the shape of the implant within the body <sup>[36]</sup>. Structural stability and biodegradation denote the maintenance of the structure during printing with a duration of the implant enough to allow tissue remodeling and integration of the cells into the target tissue <sup>[36]</sup>. Thermal stability relates to the property of the bio-ink to remain intact at a relatively high temperature, for example, polymers are solid at 37°C <sup>[57]</sup>. Biocompatibility and tissue induction are related to the biological activity and adherence in agreement with cell-matrix interactions of the target tissue <sup>[36]</sup>. Printability is related to the viscosity and homogeneity of the solution to allow extrusion while maintaining structure after deposition and avoiding high shear stress on cells <sup>[36]</sup>.

## 3D Bioprinting process

The 3D bioprinting process is like a 3D printing process with some particularities, see Figure 5. The bioprinting process is initiated by the formation of a tissue or organ blueprint using *CAD* based on digital images coming from imaging modalities such as Magnetic resonance imaging (*MRI*) or computed tomography (*CT*) and the selection of suitable materials according to histological structure, composition, and tissue and organ topology <sup>[18]</sup>. The bioprinting pro-

cess continues using *CAM* with the selection of the appropriate printer and bio-ink [18]. Finally, the bio-printed tissue or organ is matured in a bioreactor to mimic in vivo environment of the target tissue [18].

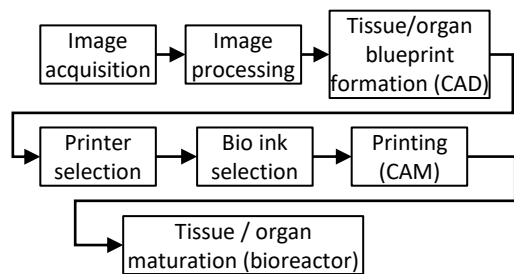


FIGURE 5. 3D bioprinting process.

### 3D printing in research

According to [5], 3D printing opens new opportunities for scientific research activities. 3D printing allows the creation of phantoms that can help understand physiological processes that are not yet fully comprehended alongside a better understanding of complex pathologies. e.g., hemodynamics can be investigated by velocity-encoded *MRI* or by optical flow measurements in transparent models.

### 3D printing in medical education and training

3D printing has proven its value in medical training. As stated in [5] [6] [58], 3D printed models can have a very high value in educational use instead of just images. 3D sections representing a patient with its body structures (bone and vascular) and soft tissues can be printed. To create a 3D model first, an imaging modality is chosen; it can be either through computed tomography or magnetic resonance imaging. From multiple images, volumetric data is acquired. This set of images are put together, and after the noise is smoothed out, a 3D virtual model is created, ready to be printed [2] [3]. The accuracy of these models is enough due to the image processing techniques. Within an educational setting, results show that 3D printing gives a better understanding of anatomy compared to 2D images [6].

### 3D printing in pharmacology

Patient-specific *DDD* is the most common technological development in pharmacology [59]. At present, the FDA has approved 3D printed *DDD* in disintegrating dosage forms such as mini-tablets and films that are suitable for children [60].

3D *DDD* offers favorable circumstances regarding individualized medication conveyance and financial perspective since this is a cheaper alternative to traditional dosage solutions [12] [15] [20] [59] [60] [61]. To print 3D, *DDD* 5 techniques will be reviewed.

Stereolithography (*STL*) in pharmacology is the most commonly used technique. Some examples of materials fabricated using this technique are topical patches and microneedles [59]. This technique has the disadvantage of short dosage delivery [13] [59].

Selective laser sintering is used to build *DDD* using polymers such as Nylon, poly-L-lactic acid (*PLLA*), and *PCL* [59]. This technique gives potential outcomes for controlling the porosity and the medication discharge energy of the 3D printed structures. The fundamental limitations are the absence of reasonable cost printers [2] [13] [59].

Fused filament fabrication (*FFF*) or fused deposition modeling (*FDM*) is the most common technique in the area of pharmacology. The adaptability of *FFF* permits assembling drug conveyance with different geometries and additionally changed medication discharge profiles for patient-explicit medicines at high reproducibility [13] [59].

A pressure-assisted microsyringe is the newest strategy for *DDD*. Pressure-assisted microsyringe produces *DDD* from films of poly-lactide-co-glycolide (*PLGA*) glues, hydrogels, or viscous polymers. However, the amount of medication is limited by the rheological characteristics of the materials [59].

## 3D printing applications

### 3D printing applications - Neurologic Applications

When medical personnel performs neurological surgeries (i.e., Cerebral aneurysm surgery), they can encounter intricate anatomical structures that cannot be seen externally. In order to observe complex anatomical structures, it is commonly used two and three-dimensional images obtained through *CT* or magnetic resonance imaging *MRI* [62]. Although images allow complex anatomical structures to be visualized, they do not allow medical personnel to appreciate these structures physically. By using imaging techniques, 3D printed anatomical forms can be constructed, which allow preoperative planning.

Preoperative planning brings a few advantages, such as reducing surgery time and decreasing the risk of injuring a patient [63]. Neurosurgical models can be printed through FDM, STL, selective laser scintigraphy, and photopolymerization technologies [64]. According to [65] Acrylonitrile Butadiene Styrene (ABS), plastic, and white resin are validated materials to be used in surgical training. Current patents in this field cover the methodology of creating the 3D replica of patient anatomy [66].

3D printing technology can also be used for printing instruments and implants that correspond to individual patient anatomy [67]. In the case of 3D printed implants, advanced materials such as stem cells are used. These methods are considered for either creating new nervous tissue or enhancing the innervation of tissue-engineered constructs [57]. These tissues have basic cellular phenotypes, and previous research shows that their functionality lasts for over two weeks after printing [16]. Current patents using stem cells relate to using inkjet printers to place viable cells in a three-dimensional architecture [68] [69].

### 3D printing applications - Cardiovascular Applications

Cardiovascular disease is one of the most severe illnesses that endanger human health, therefore, the best treatment must be applied [70]. 3D printing offers the possibility of delivering the best diagnostic and cardiovascular treatment since 3D printing has been used for customized individual printing of cardiovascular models, surgery planning, and simulation of intravascular surgery, resulting in improving the success rate of cardiovascular surgeries or treatments [16] [71] [72]. For printing 3D cardiovascular models, photopolymer inkjet printers are recommended since they retain a high resolution and can print complex structures [70] [73]. The polymeric materials perform the best in terms of quality for cardiovascular models and training tools [70]. The current challenge of 3D printing in the cardiovascular field is bio-printing materials used to create functional tissues (stent, valve, tissue-engineered scaffold) that mimic the heart's physiological function [16] [70] [74] [75] [76]. The biomaterials used for tissue are mainly based on hydrogels since it is a very versatile material. The hydrogel material can adjust its cross-linking density, molecular bonding, and swelling degree to customize its mechanical property [70]. The future research of 3D printing cardiovascular disease will focus on bioprinting that can transport blood nutrients [70]. Like in 3D printing in neurologic applications, the methodology for creating a 3D printed cardiovascular model is founded in U.S. Pat. No. 20150025666A1 and its application is being applied at the Children National Medical Center. In 2015 the Guangzhou Hongchang registered a technique for printing a small-caliber bioartificial blood vessel that can be used for coronary artery bypass grafting, hemodialysis, and cerebrovascular replacement (C. N. Pat. No. 104771783A).

### Musculoskeletal Applications

Muscles, ligaments, and connective tissues are used on the body to transfer force and facilitate joint movements. Muscles, ligaments, and connective tissue

might get broken or hurt due to trauma or tumors [77]. Muscle, ligaments, and connective tissue treatment refer to tissue transplantation, which its disadvantage is found in the host tissue mechanical properties [77]. 3D printing using tissue engineering techniques has the purpose of muscle reconstruction [18]. Hydrogels are a common material used in 3D printing tissue engineering techniques. Hydrogels are designed to act as an artificial extracellular matrix and give living cells an environment to grow [14]. Other materials like bioceramics (hydroxyapatite), calcium phosphate, and bio-glass have been used for bone regeneration because they are porous, and like hydrogels, facilitate cell growth [14]. Common 3D printing techniques for tissue engineering are stereolithography, selective laser sintering, FDM. Previous research has shown that these 3D cell printed muscles exhibit bioelectrical mimetic functionality and structural characteristics [35] [16].

### **Bones and Cartilage Applications**

The bones are tissues with the ability to self-regenerate and self-repair, but diseases like cancer, infection, trauma, and congenital deformities can prevent bone regenerates or repairs. To treat bone diseases, the transplantation of artificial bone substitutes promotes bone healing by osteogenesis [77]. Bone substitute transplantation treatment has many disadvantages, such as transplant rejection and transmission of diseases. Like in musculoskeletal 3D applications, 3D printing is used in bones and cartilage, tissue engineering using 3D printing techniques, create scaffolds in combinations of cells, materials to improve or replace biological tissues. The 3D printed scaffolds must use biocompatible materials connected by a porous 3D connected matrix to deliver nutrients [18] [77] [78]. A common technique used for creating bone tissue is the hyaluronic acid bio-inks [35]. A material that has proven to be useful for 3D printing bone applications is the polyethylene glycol (PEG) hydrogel, which is mechanically strong, and porous matrixes can be created with this material [35] [57] [77].

The articular cartilage is a smooth surface. The cartilage surface provides support and facilitates joint movements. Since the articular cartilage is avascular and is subjected to external forces, when it degenerates, it is common to see injuries that can evolve in a disease like joint arthritis [14]. Tissue engineering using 3D printing techniques, and using hydrogels materials, have the purpose of creating cartilage. Currently, the main problem in 3D printing for articular cartilage is a strong form of the inferior 3D printed cartilage tissue [77].

### **Gastroenterology Applications**

Stem cells are also employed in the field of gastroenterology for the 3D bioprinting of liver tissue, in the form of microstructures that show hepatocyte-like phenotypes and high cell viability [16] [71]. This represents a great advantage in the process of liver transplants since there is currently a limited number of donors. Furthermore, the production of hepatic tissue allows a personalized study about the condition of the liver [71]. As seen in other areas, further applications of 3D bioprinting include planning and guidance during surgical operations of the liver for improved screening of the hepatic structures and for medical education, since the 3D bioprinting of these tissues is a preferable alternative to the use of cadavers in terms of costs and sociocultural issues [79]. Patents in this field are related to the methods for 3D printing of liver tissue [80] and modeling methods for pancreatic surgical planning [45].

### **Dermatology Applications**

Applications in the field of dermatology include the fabrication of adipose tissue and skin tissue with its equivalents (sweat glands and hair follicles). In this field, the great advantage of the 3D bioprinted tissues is that they are quickly obtained while having enough accuracy as the natural ones [18] [35]. Stem cells originating from human adipose tissue are used to create 3D grafts that are complex enough to be compared with the natural adipose tissue. Moreover, the 3D printed

adipose tissue has the optimal conditions to be used for transplants and allows a personalized study about the condition of the adipose tissue. A great process in the development of skin tissue has been achieved by using collagen matrices embedded with fibroblasts and keratinocytes as bio-inks. This ensures that there is sufficient vasculature to support the tissue since a poor vascularization may have adverse effects on the 3D bioprinted tissue, including necrosis [16]. For the reproduction of sweat glands, a combination of components taken from the tissue is used, and its initial experiments have been successful [18] [35]. Patents on this field specify the preparation methods for 3D printed skin [44] [81].

### Orthopedic Applications

The obtention of 3D printed models to compensate for the loss of bone and cartilage is the main goal within this area by using the inkjet bioprinting technology [18] [82]. With hydrogels as bioinks, the time needed for the creation of the bone tissue is reduced, and its mechanical properties are enhanced. To ensure vascularization, the pores of the printed structures are around 300  $\mu\text{m}$  [82]. These models are also used in pharmacokinetic studies and for the research of bone-related diseases [82]. Several patents are found in this field related to the methods for bone and cartilage printing [26] [31] [34] [43] [47] [50].

### Otolaryngology Applications

One of the clearest examples of the 3D printing relevance in the field of otorhinolaryngology is the production of hearing aids, as most of the ones available on the market are printed in 3D [83]. Patents in this field include the preparation and manufacturing methods of bones with applications in hospitals [53] [69] [84] [85]. Furthermore, as with the above-mentioned applications, 3D printing is also used for surgical education and training since, by providing accurate and complex models, reconstructive surgeries have proven to have improved outcomes and have even been carried out in a reduced

period of time [83]. The most relevant 3D-printed models/simulators used for surgical education and training in the field of otolaryngology are [17] [83]:

- Temporal bones.
- Auricular reconstruction.
- 3D-printed auricular prosthesis.
- Tissue-engineered trachea.
- Ear, sinonasal, skull base, septoplasty, and laryngeal surgery simulators.

### Urology Applications

Applications of 3D-print in urology include education and surgical planning [86] [88]. Printed models include kidney, liver, prostate, ureters, kidney tumors, and renal pelvicalyceal systems [87] [89]. The materials used for this go from silicone, wax, or polymers for the kidney models and polyvinyl alcohol hydrogels and 3D-printed injection molds for renal systems. These models are used for renal transplantation and treatment of renal masses with suspected renal cell carcinoma. This is possible since the materials used in 3D printing share similar characteristics with the organ in terms of shape, elasticity, and mechanical strength [87]. Renal pelvicalyceal systems are used in the treatment of nephrolithiasis. Other applications of 3D-printing in urology are the creation of equipment such as stents and trochars [86].

### Nutriology Applications

Within food science, 3D-printing has been proposed as a method to obtain personalized functionalized foods [90]. Functional foods (FF) are considered as “foods that supply nutrients and offer potential health benefits that can enhance the well-being of people” [90]. The aim is to offer customized foods that, according to the needs of the user, are supplemented with proteins, sugars, vitamins, and minerals. Examples of ingredients used in 3D-printing are chocolate, pasta, and pork pure, which have been used to produce pizza and enriched cookies [90].

## Radiology Applications

As well as in other fields, applications of 3D-print in radiology include education and surgical planning <sup>[91]</sup>. Specifically, within this field, 3D-printing has been used in vascular radiology with the aim to reduce operating times and complications <sup>[91]</sup>. The production of those 3D printed models follows four steps: image acquisition, image segmentation, creation of a 3D model, and 3D printing <sup>[92]</sup>.

The modality used for the image acquisition in DICOM format (being CT the most common one) depends on the characteristics of the target <sup>[93]</sup>. The segmentation consists of the extraction of regions of interest (ROI) for its 3D reconstruction based on the target tissue and pathophysiology <sup>[93]</sup>. It has been proposed that artificial intelligence can be applied to improve segmentation and also a fusion of multiple imaging modalities <sup>[94]</sup>.

## 3D printing regulations

In America, the Food and Drug Administration (*FDA*) has emitted, through several centers, guidance documents and regulations to be followed according to the type of application <sup>[95]</sup>:

- The Center for Devices and Radiological Health (*CRDH*) supervises medical device applications.
- The Center for Biologics Evaluation and Research controls Biological applications.
- The Center for Drug Evaluation and Research supervises pharmacology applications.

Along with these regulations, the *FDA* also offers descriptions of the 3D printing processes and learning resources for its application in biomedical sciences. The goal is to accelerate the manufacturing process in 3D printing and ensure the correct implementation of this technology.

## 3D printing challenges

The use of 3D printing involves several challenges for its implementation in the healthcare sector. According to a survey made on 700 professional users, the biggest challenges are related to the expenses of the equipment and production, the requirements for its posterior processing, and the short supply of materials <sup>[96]</sup>.

A solution for the cost-related challenges could be the optimization of the manufacturing processes. Another challenge is the resistance to change the guidelines and processes in the healthcare sector <sup>[12]</sup>.

Further challenges are described below. Within the printing process to obtain blueprints of tissues and organs of complex anatomies is a challenge <sup>[97]</sup>. Also, during manufacturing replication of tortuous and thin structures <sup>[97]</sup>, removing negative material from cavities <sup>[98]</sup> are other challenges. Another specific challenge for regenerative medicine is the integration of tissues and various cell types and the assurance of long-term functionality <sup>[4]</sup>.

Specific challenges for applying 3D printing in pharmacology include regulatory aspects such as assurance of safety and quality of materials and final products <sup>[60]</sup>. Ensuring the proper disposal of printed parts when they are no longer required is an additional regulatory challenge.

These and other challenges need to be addressed to ensure advanced and application of 3D printing in healthcare.

## CONCLUSIONS

3D printing started as a revolutionizing technology in the different fields of healthcare and, it has demonstrated to be a useful technology up to the point of becoming of common use. This brief review aimed to identify the latest work rapidly and perspectives of 3D printing in healthcare. Major applications among the

advantages and disadvantages of 3D printing in healthcare were presented. Three-dimensional printing still has challenges that need to be tackled to ensure the progress and application of 3D printing in healthcare.

### **AUTHOR CONTRIBUTIONS**

AIPS, ERA and AGM participated in all the stages of the work together, from conceptualization through all the analyses carried and to the writing of all the manuscript versions.

## REFERENCES

- [1] Hurst EJ. 3D Printing in Healthcare: Emerging Applications. *J Hosp Librariansh* [Internet]. 2016;16(3):255-67. Available from: <https://doi.org/10.1080/15323269.2016.1188042>
- [2] Mukhopadhyay S, Poojary R. A review on 3D printing: Advancement in healthcare technology. In *2018 Advances in Science and Engineering Technology International Conferences (ASET)* [Internet]. Abu Dhabi: IEEE; 2018:1-5. Available from: <https://doi.org/10.1109/ICASET.2018.8376890>
- [3] Mishra S. Application of 3D printing in medicine. *Indian Heart J* [Internet]. 2016;68(1):108-109. Available from: <https://doi.org/10.1016/j.ihj.2016.01.009>
- [4] Ozbolat IT, Peng W, Ozbolat V. Application areas of 3D bioprinting. *Drug Discov Today* [Internet]. 2016;21(8):1257-1271. Available from: <https://doi.org/10.1016/j.drudis.2016.04.006>
- [5] Chen JKC, Do HTT. Perspective of the 3D Printing Technology Applied on Medical Resource Integration and Service Innovation Business Model. In *2017 Portland International Conference on Management of Engineering and Technology (PICMET)* [Internet]. Portland: IEEE; 2017:1-11. Available from: <https://doi.org/10.23919/PICMET.2017.8125298>
- [6] Langridge B, Momin S, Coumbe B, et al. Systematic Review of the Use of 3-Dimensional Printing in Surgical Teaching and Assessment. *J Surg Educ* [Internet]. 2018;75(1):209-221. Available from: <https://doi.org/10.1016/j.jsurg.2017.06.033>
- [7] Vaillant T, Steelandt J, Cordonnier A-L, et al. Revue des guides personnalisés à usage unique dans les prothèses totales de genou. *Ann Pharm Fr* [Internet]. 2018;76(3):228-234. Available from: <https://doi.org/10.1016/j.pharma.2017.12.002>
- [8] Nagarajan NN, Dupret-Bories A, Karabulut E, et al. Enabling personalized implant and controllable biosystem development through 3D printing. *Biotechnol Adv* [Internet]. 2018;36(2):521-533. Available from: <https://doi.org/10.1016/j.biotechadv.2018.02.004>
- [9] Tan XP, Tan YJ, Chow CSL, et al. Metallic powder-bed based 3D printing of cellular scaffolds for orthopaedic implants: A state-of-the-art review on manufacturing, topological design, mechanical properties and biocompatibility. *Mater Sci Eng C Mater Biol Appl* [Internet]. 2017;76(1):1328-1343. Available from: <https://doi.org/10.1016/j.msec.2017.02.094>
- [10] Savonen B, Gershenson J, Bow JK, et al. Open-Source Three-Dimensional Printable Infant Clubfoot Brace. *JPO J Prosthetics Orthot* [Internet]. 2020;32(2):149-158. Available from: <https://doi.org/10.1097/JPO.0000000000000257>
- [11] de Souza MA, Schmitz C, Pinhel MM, et al. Proposal of custom made wrist orthoses based on 3D modelling and 3D printing. In *2017 39th Annual International Conference of the IEEE Engineering in Medicine and Biology Society (EMBC)* [Internet]. Jeju: IEEE; 2017:3789-3792. Available from: <https://doi.org/10.1109/EMBC.2017.8037682>
- [12] Awad A, Trenfield SJ, Gaisford S, et al. 3D printed medicines: A new branch of digital healthcare. *Int J Pharm* [Internet]. 2018;548(1):586-596. Available from: <https://doi.org/10.1016/j.ijpharm.2018.07.024>
- [13] Trenfield SJ, Awad A, Goyanes A, et al. 3D Printing Pharmaceuticals: Drug Development to Frontline Care. *Trends Pharmacol Sci* [Internet]. 2018;39(5):440-451. Available from: <https://doi.org/10.1016/j.tips.2018.02.006>
- [14] Xia R-Z, Zhai Z-J, Chang Y-Y, Li H-W. Clinical Applications of 3-Dimensional Printing Technology in Hip Joint. *Orthop Surg* [Internet]. 2019;11(4):533-544. Available from: <https://doi.org/10.1111/os.12468>
- [15] Liang K, Brambilla D, Leroux J-C. Is 3D Printing of Pharmaceuticals a Disruptor or Enabler? *Adv Mater* [Internet]. 2019;31(5):e1805680. Available from: <https://doi.org/10.1002/adma.201805680>
- [16] Ong CS, Yesanatharao P, Huang CY, et al. 3D bioprinting using stem cells. *Pediatr Res* [Internet]. 2018;83:223-231. Available from: <https://doi.org/10.1038/pr.2017.252>
- [17] VanKoeveering KK, Malloy KM. Emerging Role of Three-Dimensional Printing in Simulation in Otolaryngology. *Otolaryngol Clin North Am* [Internet]. 2017;50(5):947-958. Available from: <https://doi.org/10.1016/j.otc.2017.05.006>
- [18] Huang Y, Zhang X-F, Gao G, et al. 3D bioprinting and the current applications in tissue engineering. *Biotechnol J* [Internet]. 2017;12(8):1600734. Available from: <https://doi.org/10.1002/biot.201600734>
- [19] Lee VK, Dai G. Printing of Three-Dimensional Tissue Analogs for Regenerative Medicine. *Ann Biomed Eng* [Internet]. 2017;45:115-131. Available from: <https://doi.org/10.1007/s10439-016-1613-7>
- [20] Sandler N, Preis M. Printed Drug-Delivery Systems for Improved Patient Treatment. *Trends Pharmacol Sci* [Internet]. 2016;37(12):1070-1080. Available from: <https://doi.org/10.1016/j.tips.2016.10.002>
- [21] Shahar FS, Hameed Sultan MT, Lee SH, et al. A review on the orthotics and prosthetics and the potential of kenaf composites as alternative materials for ankle-foot orthosis. *J Mech Behav Biomed Mater* [Internet]. 2019;99:169-185. Available from: <https://doi.org/10.1016/j.jmbbm.2019.07.020>
- [22] Hooper J, Schwarzkopf R, Fernandez E, et al. Feasibility of single-use 3D-printed instruments for total knee arthroplasty. *Bone Joint J* [Internet]. 2019;101-B(7-C):115-120. Available from: <https://doi.org/10.1302/0301-620X.101B7.BJJ-2018-1506.R1>
- [23] Tang X, Qin Y, Xu X, et al. Fabrication and In Vitro Evaluation of 3D Printed Porous Polyetherimide Scaffolds for Bone Tissue Engineering. *Biomed Res Int* [Internet]. 2019;2019:2076138. Available from: <https://doi.org/10.1155/2019/2076138>
- [24] Theodoridis K, Aggelidou E, Manthou M, et al. Assessment of cartilage regeneration on 3D collagen-polycaprolactone scaffolds: Evaluation of growth media in static and in perfusion bioreactor dynamic culture. *Colloids Surf B Biointerfaces* [Internet]. 2019;183(1):110403. Available from: <https://doi.org/10.1016/j.colsurfb.2019.110403>
- [25] Wu Y-HA, Chiu Y-C, Lin Y-H, et al. 3D-Printed Bioactive Calcium Silicate/Poly-ε-Caprolactone Bioscaffolds Modified with Biomimetic Extracellular Matrices for Bone Regeneration. *Int J Mol Sci* [Internet]. 2019;20(4):942. Available from: <https://doi.org/10.3390/ijms20040942>

- [26] Stanislavovna AO, Mironovich BS, Valerevich SS, et al., inventors; Method of producing ceramic sample based on  $\beta$ -tricalcium phosphate using stereolithography technique for recovering bone tissue [Internet]. RU2729761C1. 2020. Available from: <https://worldwide.espacenet.com/patent/search/family/072086312/publication/RU2729761C1?q=pn%3DRU2729761C1>
- [27] Sergeevich AA, Darchoevich AS, Borisovna AN, et al., inventors; Method of facial prosthesis manufacturing [Internet]. RU2727741C1. 2020. Available from: <https://worldwide.espacenet.com/patent/search/family/071741362/publication/RU2727741C1?q=pn%3DRU2727741C1>
- [28] Yubo F, Wanru F, Xiaoming L, et al., inventors; Multi-arm cooperation type biological three-dimensional printing device [Internet]. CN110435144A. 2019. Available from: <https://worldwide.espacenet.com/patent/search/family/068438558/publication/CN110435144A?q=pn%3DCN110435144A>
- [29] Yubo F, Wenyong L, Baosen T, inventors; Intelligent multisource synchronous orienting three-dimensional printing device [Internet]. CN108891025A. 2018. Available from: <https://worldwide.espacenet.com/patent/search/family/064344415/publication/CN108891025A?q=pn%3DCN108891025A>
- [30] Ayberk Y, inventor; Implant guide system [Internet]. WO2009004526A2. 2009. Available from: <https://worldwide.espacenet.com/patent/search/family/040019402/publication/WO2009004526A2?q=pn%3DWO2009004526A2>
- [31] Vladimirovich PJ, Akhmadovich SS, Evich SAE, inventors; Method for nail osteosynthesis of facial bone fractures [Internet]. RU2523828C1. 2014. Available from: <https://worldwide.espacenet.com/patent/search/family/051265151/publication/RU2523828C1?q=pn%3DRU2523828C1>
- [32] Vladimirovich PJ, Evich SAE, inventors; Method for surgical approach to periapical tissues of jaw [Internet]. RU2523352C1. 2014. Available from: <https://worldwide.espacenet.com/patent/search/family/051217685/publication/RU2523352C1?q=pn%3DRU2523352C1>
- [33] Rui G, Yuyang L, Xiaodong L, et al., inventors; Orbital blow-out fracture titanium mesh prefabrication method [Internet]. CN107374785A. 2018. Available from: <https://worldwide.espacenet.com/patent/search/family/060343715/publication/CN107374785A?q=pn%3DCN107374785A>
- [34] Sergeevich BS, Andreevich CA, Olegovich da, et al., inventors; Method for replacement of defects of proximal tibia when performing knee joint endoprosthesis replacement and device for its implementation [Internet]. RU2730985C1. 2020. Available from: <https://worldwide.espacenet.com/patent/search/family/072238051/publication/RU2730985C1?q=pn%3DRU2730985C1>
- [35] Choi Y-J, Yi H-G, Kim S-W, et al. 3D Cell Printed Tissue Analogues: A New Platform for Theranostics. *Theranostics* [Internet]. 2017;7(12):3118-3137. Available from: <https://doi.org/10.7150/thno.19396>
- [36] Skeldon G, Lucendo-Villarín B, Shu W. Three-dimensional bioprinting of stem-cell derived tissues for human regenerative medicine. *Philos Trans R Soc Lond B Biol Sci* [Internet]. 2018;373(1750): 20170224. Available from: <https://doi.org/10.1098/rstb.2017.0224>
- [37] Yujian K, Xiao Z, inventors; Biobrick used for biological printing and application thereof [Internet]. CN106039419A. 2016. Available from: <https://worldwide.espacenet.com/patent/search/family/057484182/publication/CN106039419A?q=pn%3DCN106039419A>
- [38] James KY, Xiao Z, inventors; Compositions for cell-based three dimensional printing [Internet]. WO2016161944A1. 2016. Available from: <https://worldwide.espacenet.com/patent/search/family/057072284/publication/WO2016161944A1?q=pn%3DWO2016161944A1>
- [39] Yujian K, Xiao Z, inventors; Method for preparing constructed body from biobrick containing endothelial cells [Internet]. CN106039409A. 2016. Available from: <https://worldwide.espacenet.com/patent/search/family/057484197/publication/CN106039409A?q=pn%3DCN106039409A>
- [40] Yuyu H, Shuangshuang M, Wei S, et al., inventors; Frozen gel three-dimensional structural body, preparation method and application thereof [Internet]. CN106178110A. 2016. Available from: <https://worldwide.espacenet.com/patent/search/family/057458617/publication/CN106178110A?q=pn%3DCN106178110A>
- [41] Haiqin D, Liumin H, Huiheng L, et al., inventors; Preparation and application of linear biodegradable polyester elastomer with controllable elasticity and shape memory effect [Internet]. CN105504248A. 2016. Available from: <https://worldwide.espacenet.com/patent/search/family/055712589/publication/CN105504248A?q=pn%3DCN105504248A>
- [42] Yuxiong G, Pan J, Xiaolong W, et al., inventors; 3D (three-dimensional) printing biomedical hydrogel and method for preparing same [Internet]. CN108424533A. 2018. Available from: <https://worldwide.espacenet.com/patent/search/family/063164061/publication/CN108424533A?q=pn%3DCN108424533A>
- [43] Zhi H, Lin M, Qing T, et al., inventors; Photo-thermal chemotherapy bone repair material and preparation method of tissue engineering scaffold [Internet]. CN109010925A. 2018. Available from: <https://worldwide.espacenet.com/patent/search/family/064624217/publication/CN109010925A?q=pn%3DCN109010925A>
- [44] Qianqian D, Jianlong J, Aoqun J, et al., inventors; Biological 3D printed full-custom skin and preparation method thereof [Internet]. CN108392676A. 2018. Available from: <https://worldwide.espacenet.com/patent/search/family/063101298/publication/CN108392676A?q=pn%3DCN108392676A>
- [45] Ming'en X, Rui Y, inventors; Pancreatic-like structural body and construction method and application thereof [Internet]. CN111197024A. 2020. Available from: <https://worldwide.espacenet.com/patent/search/family/070744047/publication/CN111197024A?q=pn%3DCN111197024A>
- [46] Domogatskij, Osidak, inventors; Sterile transparent concentrated solution of biocompatible collagen, method for production and use thereof [Internet]. RU2715715C1. 2020. Available from: <https://worldwide.espacenet.com/patent/search/family/069768223/publication/RU2715715C1?q=RU2715715C1>
- [47] Jintao C, Taiying C, Kang L, inventors; 3D printing bone repairing bracket with antibacterial property and preparation method of 3D printing bone repairing bracket [Internet]. CN106729988A. 2017. Available from: <https://worldwide.espacenet.com/patent/search/family/058947966/publication/CN106729988A?q=pn%3DCN106729988A>
- [48] Jun AM, Woo CD, Jin CY, et al., inventors; 3 Wet 3D cell printing using decellularized extracellular matrix [Internet]. KR20180049712A. 2018. Available from: <https://worldwide.espacenet.com/patent/search/family/062185559/publication/KR20180049712A?q=pn%3DKR20180049712A>

- [49] Peng P, Baoqing Y, Xu Z, et al., inventors; Three-dimensional printing strontium-containing mesoporous bioglass bracket loaded with soy isoflavone and preparation method thereof [Internet]. CN106267375. 2017. Available from: <https://worldwide.espacenet.com/patent/search/family/057673419/publication/CN106267375A?q=pn%3DCN106267375A>
- [50] Yujiang F, Xuan P, Yaning W, et al., inventors; Bionics design bone-line porous bone product and preparation method and purpose thereof [Internet]. CN105877874A. 2016. Available from: <https://worldwide.espacenet.com/patent/search/family/057012628/publication/CN105877874A?q=pn%3DCN105877874A>
- [51] Qi L, Rong W, Weiyi Y, et al., inventors; Three-dimensional biological scaffold, preparation method and applications thereof [Internet]. CN109381739A. 2019. Available from: <https://worldwide.espacenet.com/patent/search/family/065412336/publication/CN109381739A?q=pn%3DCN109381739A>
- [52] Brown A, Chester D, Daniele M, et al., inventor; Three-dimensional printing of colloidal building blocks for wound healing materials [Internet]. WO2019195681A1. 2019. Available from: <https://worldwide.espacenet.com/patent/search/family/068101458/publication/WO2019195681A1?q=pn%3DWO2019195681A1>
- [53] Wenrui C, Cuihai D, Wenbo H, et al., inventors; Multi-pore bionic skull repair material and individualized manufacturing method [Internet]. CN108273137A. 2018. Available from: <https://worldwide.espacenet.com/patent/search/family/062802922/publication/CN108273137A?q=pn%3DCN108273137A>
- [54] Chunyan B, Yujie H, Qiuning L, et al., Preparation, raw material, product and application of photo-coupling co-crosslinking hydrogel material [Internet]. CN109776450A. 2019. Available from: <https://worldwide.espacenet.com/patent/search/family/066495619/publication/CN109776450A?q=pn%3DCN109776450A>
- [55] Yingfang A, Guocheng D, Xiaoqing H, et al., inventors; Preparation method of cell 3D printing bio-ink with good printability [Internet]. CN111544657A. 2020. Available from: <https://worldwide.espacenet.com/patent/search/family/071999658/publication/CN111544657A?q=pn%3DCN111544657A>
- [56] Moroni L, Boland T, Burdick JA, et al. Biofabrication: A Guide to Technology and Terminology. Trends Biotechnol [Internet]. 2018;36(4):384-402. Available from: <https://doi.org/10.1016/j.tibtech.2017.10.015>
- [57] Aljohani W, Ullah MW, Zhang X, et al. Bioprinting and its applications in tissue engineering and regenerative medicine. Int J Biol Macromol [Internet]. 2018;107(Part A): 261-275. Available from: <https://doi.org/10.1016/j.ijbiomac.2017.08.171>
- [58] Zhang YS, Oklu R, Dokmeci MR, et al. Three-Dimensional Bioprinting Strategies for Tissue Engineering. Cold Spring Harb Perspect Med [Internet]. 2017;8(2):a025718. Available from: <https://doi.org/10.1101/cshperspect.a025718>
- [59] Palo M, Holländer J, Suominen J, et al. 3D printed drug delivery devices: perspectives and technical challenges. Expert Rev Med Devices [Internet]. 2017;14(9):685-696. Available from: <https://doi.org/10.1080/17434440.2017.1363647>
- [60] Preis M, Oblom H. 3D-Printed Drugs for Children-Are We Ready Yet? AAPS PharmSciTech [Internet]. 2017;18:303-308. Available from: <https://doi.org/10.1208/s12249-016-0704-y>
- [61] Kaae S, Lind JLM, Genina N, et al. Unintended consequences for patients of future personalized pharmacoprinting. Int J Clin Pharm [Internet]. 2018;40:321-324. Available from: <https://doi.org/10.1007/s11096-018-0596-x>
- [62] Randazzo M, Pisapia JM, Singh N, et al. 3D printing in neurosurgery: A systematic review. Surg Neurol Int [Internet]. 2016;7(S33):S801-S809. Available from: <https://doi.org/10.4103/2152-7806.194059>
- [63] Shah KJ, Peterson JC, Chamoun R. 3D Printed Models in Neurosurgical Training BT - Comprehensive Healthcare Simulation: Neurosurgery. In: Alaraj A (ed). Comprehensive Healthcare Simulation: Neurosurgery. Comprehensive Healthcare Simulation [Internet]. Cham: Springer International Publishing; 2018: 47-64. Available from: [https://doi.org/10.1007/978-3-319-75583-0\\_4](https://doi.org/10.1007/978-3-319-75583-0_4)
- [64] Vakharia VN, Vakharia NN, Hill CS. Review of 3-Dimensional Printing on Cranial Neurosurgery Simulation Training. World Neurosurg [Internet]. 2016;88:188-198. Available from: <https://doi.org/10.1016/j.wneu.2015.12.031>
- [65] McMillan A, Kocharyan A, Dekker SE, et al. Comparison of Materials Used for 3D-Printing Temporal Bone Models to Simulate Surgical Dissection. Ann Otol Rhinol Laryngol [Internet]. 2020;129(12):1168-1173. Available from: <https://doi.org/10.1177/0003489420918273>
- [66] Wu A, inventor; Single-action three-dimensional model printing methods [Internet]. US8579620B2. 2011. Available from: <https://patents.google.com/patent/US8579620B2/en>
- [67] Pucci JU, Christophe BR, Sisti JA, et al. Three-dimensional printing: technologies, applications, and limitations in neurosurgery. Biotechnol Adv [Internet]. 2017;35(5):521-529. Available from: <https://doi.org/10.1016/j.biotechadv.2017.05.007>
- [68] Boland T, Wilson JWC, Xu T, inventors; Ink-jet printing of viable cells [Internet]. US7051654B2. 2003. Available from: <https://patents.google.com/patent/US7051654B2/en>
- [69] Kang H-W, Lee SJ, Atala A, Yoo JJ, inventors; Integrated organ and tissue printing methods, system and apparatus [Internet]. US20120089238A1. 2010. Available from: <https://patents.google.com/patent/US20120089238A1/en>
- [70] Wu Y, Vida VL, Zheng M, Yang J. Progress and Prospects of Cardiovascular 3D Printing BT - Cardiovascular 3D Printing: Techniques and Clinical Application. In: Yang J, Lee AP-W, Vida VL (eds). Cardiovascular 3D Printing [Internet]. Singapore: Springer Singapore; 2021: 179-185. Available from: [https://doi.org/10.1007/978-981-15-6957-9\\_13](https://doi.org/10.1007/978-981-15-6957-9_13)
- [71] Zhang YS, Yue K, Aleman J, et al. 3D Bioprinting for Tissue and Organ Fabrication. Ann Biomed Eng [Internet]. 2017;45:148-163. Available from: <https://doi.org/10.1007/s10439-016-1612-8>
- [72] Ferrari E, Gallo M, Wang C, et al. Three-dimensional printing in adult cardiovascular medicine for surgical and transcatheter procedural planning, teaching and technological innovation. Interact Cardiovasc Thorac Surg [Internet]. 2020;30(2):203-214. Available from: <https://doi.org/10.1093/icvts/ivz250>
- [73] Xu C, Liang J, Yang J. History of Cardiovascular 3D Printing BT - Cardiovascular 3D Printing: Techniques and Clinical Application. In: Yang J, Lee AP-W, Vida VL (eds) Cardiovascular 3D Printing [Internet]. Singapore: Springer Singapore; 2021: 1-2. Available from: [https://doi.org/10.1007/978-981-15-6957-9\\_1](https://doi.org/10.1007/978-981-15-6957-9_1)
- [74] Valverde I. Three-dimensional Printed Cardiac Models: Applications in the Field of Medical Education, Cardiovascular Surgery, and Structural Heart Interventions. Rev Esp Cardiol (Engl Ed) [Internet]. 2017;70(4):282-291. Available from: <https://doi.org/10.1016/j.rec.2017.01.012>

- [75] Baribeau Y, Sharkey A, Mahmood E, et al. Three-Dimensional Printing and Transesophageal Echocardiographic Imaging of Patient-Specific Mitral Valve Models in a Pulsatile Phantom Model. *J Cardiothorac Vasc Anesth* [Internet]. 2019;33(12):3469-3475. Available from: <https://doi.org/10.1053/j.jvca.2019.07.141>
- [76] Wang Z, Mithieux SM, Weiss AS. Fabrication Techniques for Vascular and Vascularized Tissue Engineering. *Adv Healthc Mater* [Internet]. 2019;8(19):1900742. Available from: <https://doi.org/10.1002/adhm.201900742>
- [77] Mok S-W, Nizak R, Fu S-C, et al. From the printer: Potential of three-dimensional printing for orthopaedic applications. *J Orthop Transl* [Internet]. 2016;6:42-49. Available from: <https://doi.org/10.1016/j.jot.2016.04.003>
- [78] Wang Y, Gao M, Wang D, et al. Nanoscale 3D Bioprinting for Osseous Tissue Manufacturing. *Int J Nanomedicine* [Internet]. 2020;15:215-226. Available from: <https://doi.org/10.2147/IJN.S172916>
- [79] Alkhouri N, Zein NN. Three-dimensional printing and pediatric liver disease. *Curr Opin Pediatr* [Internet]. 2016;28(5):626-630. Available from: <https://doi.org/10.1097/MOP.0000000000000395>
- [80] Wei S, Rui Y, inventors; Construction method and application of in-vitro three-dimensional human liver tissue [Internet]. CN106916781A. 2017. Available from: <https://patents.google.com/patent/CN106916781A/en>
- [81] Jintao C, Taiying C, Kang L, inventors; Skin repair material with biological activity and method for preparing skin repair material [Internet]. CN106421931A. 2017. Available from: <https://patents.google.com/patent/CN106421931A/zh>
- [82] Arealis G, Nikolaou VS. Bone printing: new frontiers in the treatment of bone defects. *Injury* [Internet]. 2015;46(S8):S20-2. Available from: [https://doi.org/10.1016/S0020-1383\(15\)30050-4](https://doi.org/10.1016/S0020-1383(15)30050-4)
- [83] Kaye R, Goldstein T, Zeltsman D, et al. Three dimensional printing: A review on the utility within medicine and otolaryngology. *Int J Pediatr Otorhinolaryngol* [Internet]. 2016;89:145-148. Available from: <https://doi.org/10.1016/j.ijporl.2016.08.007>
- [84] Qingzi B, Yunqi B, Jingsong L, et al., inventors; 4D-printing shape-memory-polymer-composite-material tracheal stent and preparing method thereof [Internet]. CN108969165A. 2018. Available from: <https://patents.google.com/patent/CN108969165A/en?q=CN108969165A>
- [85] Valerevich MS, Aleksandrovich PA, inventors; Method for manufacture of individual implant for skull bone defects replacement [Internet]. RU2644275C1. 2018. Available from: [https://yandex.ru/patents/doc/RU2414870C1\\_20110327](https://yandex.ru/patents/doc/RU2414870C1_20110327)
- [86] Chen MY, Skewes J, Desselle M, et al. Current applications of three-dimensional printing in urology. *BJU Int* [Internet]. 2020;125(1):17-27. Available from: <https://doi.org/10.1111/bju.14928>
- [87] Parikh N, Sharma P. Three-Dimensional Printing in Urology: History, Current Applications, and Future Directions. *Urology* [Internet]. 2018;121:3-10. Available from: <https://doi.org/10.1016/j.urology.2018.08.004>
- [88] Childs BS, Manganiello MD, Korets R. Novel Education and Simulation Tools in Urologic Training. *Curr Urol Rep* [Internet]. 2019;20:81. Available from: <https://doi.org/10.1007/s11934-019-0947-8>
- [89] Tatar İ, Huri E, Selçuk İ, et al. Review of the effect of 3D medical printing and virtual reality on urology training with 'MedTRain3DModsim' Erasmus + European Union Project. *Turkish J Med Sci* [Internet]. 2019;49:1257-1270. Available from: <https://doi.org/10.3906/sag-1905-73>
- [90] Severini C, Derossi A. Could the 3D Printing Technology be a Useful Strategy to Obtain Customized Nutrition? *J Clin Gastroenterol* [Internet]. 2016;50:S175-S178. Available from: <https://doi.org/10.1097/MCG.0000000000000705>
- [91] Chang D, Tummala S, Sotero D, et al. Three-Dimensional Printing for Procedure Rehearsal/Simulation/Planning in Interventional Radiology. *Tech Vasc Interv Radiol* [Internet]. 2019;22(1):14-20. Available from: <https://doi.org/10.1053/j.tvir.2018.10.004>
- [92] Hodgdon T, Danrad R, Patel MJ, et al. Logistics of Three-dimensional Printing: Primer for Radiologists. *Acad Radiol* [Internet]. 2018;25(1):40-51. Available from: <https://doi.org/10.1016/j.acra.2017.08.003>
- [93] Mitsouras D, Liacouras P, Imanzadeh A, et al. Medical 3D Printing for the Radiologist. *Radiographics* [Internet]. 2015;35(7):1965-1988. Available from: <https://doi.org/10.1148/rq.2015140320>
- [94] Martín Noguero T, Paulano-Godino F, Martín-Valdivia MT, et al. Strengths, Weaknesses, Opportunities, and Threats Analysis of Artificial Intelligence and Machine Learning Applications in Radiology. *J Am Coll Radiol* [Internet]. 2019;16(9):1239-1247. Available from: <https://doi.org/10.1016/j.jacr.2019.05.047>
- [95] U.S. Food & Drug Administration. 3D Printing of Medical Devices. U.S. Food & Drug Administration [Internet]. 2019. Available from: <https://www.fda.gov/medical-devices/products-and-medical-procedures/3d-printing-medical-devices>
- [96] Stratasys Direct Manufacturing. Top Challenges to Widespread 3D Printing Adoption. *MachineDesign* [Internet]. 2019. Available from: <https://www.machinedesign.com/3d-printing-cad/article/21834436/top-challenges-to-widespread-3d-printing-adoption>
- [97] Abudayyeh I, Gordon B, Ansari MM, et al. A practical guide to cardiovascular 3D printing in clinical practice: Overview and examples. *J Interv Cardiol* [Internet]. 2018;31(3):375-383. Available from: <https://doi.org/10.1111/joic.12446>
- [98] VanKoeveering KK, Hollister SJ, Green GE. Advances in 3-Dimensional Printing in Otolaryngology: A Review. *JAMA Otolaryngol Head Neck Surg* [Internet]. 2017;143(2):178-183. Available from: <https://doi.org/10.1001/jamaoto.2016.3002>

[dx.doi.org/10.17488/RMIB.42.2.4](https://doi.org/10.17488/RMIB.42.2.4)

E-LOCATION ID: 1123

## Antibacterial Activity Analysis of Hydroxyapatite Based Materials with Fluorine and Silver

### Análisis de la Actividad Antibacteriana de Materiales a Base de Hidroxiapatita con Flúor y Plata

V. González-Torres<sup>1</sup>; E. Hernández-Guevara<sup>2</sup>; N. A. Castillo-Martínez<sup>1</sup>; M. Rosales-Aguilar<sup>3</sup>; G. C. Díaz-Trujillo<sup>2</sup>

<sup>1</sup>Facultad de Ciencias de la Salud de la Universidad Autónoma de Baja California

<sup>2</sup>Facultad de Ciencias Químicas e Ingeniería de la Universidad Autónoma de Baja California

<sup>3</sup>Facultad de Medicina y Psicología de la Universidad Autónoma de Baja California

#### ABSTRACT

This investigation aims to evaluate the antibacterial activity of nanostructured hydroxyapatite based materials doped with silver and fluorine, to be used as a biomaterial with antibacterial activity. Four different formulations were prepared by combustion method: hydroxyapatite, hydroxyapatite-fluorine, hydroxyapatite-silver-fluorine and hydroxyapatite-silver, with 2% of the doping agents. X-ray diffraction technique was used to determine the mineralogy, identifying the presence of  $\text{Ca}_5(\text{PO}_4)_3\text{OH}$ ,  $\text{Ca}_2\text{P}_2\text{O}_7$ ,  $\text{Ag}_3\text{PO}_4$ ,  $\text{AgCa}_{10}(\text{PO}_4)_7$ ,  $\text{Ca}_5(\text{PO}_4)_3\text{F}$  and  $\text{CaF}_2$  phases for the studied samples. Scanning electron microscopy was used to study the morphological structure and it showed homogeneous crystallization of the hydroxyapatite and the inclusion of dopant agents. The antibacterial activity was determined using a modified inhibition test zone to observe if the bacteria (*E. faecalis*) was susceptible to the antimicrobial agent by the appearance of the zone of inhibition on the agar plate. Both the hydroxyapatite-silver and the hydroxyapatite-silver-fluorine materials generated an inhibition zone. It was possible to determine the minimum inhibitory concentration needed to kill most viable organisms after 48 hours of incubation using the broth microdilution method, resulting in 75  $\mu\text{g/ml}$  and 200  $\mu\text{g/ml}$  for the hydroxyapatite-silver and the hydroxyapatite-silver-fluorine formulation, respectively. These materials could be used for the development of new biomaterials that can be used in dental applications.

**KEYWORDS:** hydroxyapatite; antibacterial; silver

## RESUMEN

El objetivo de esta investigación es analizar la actividad antibacteriana de materiales nanoestructurados a base de hidroxiapatita con iones de flúor y plata que le confieran características particulares para que pueda ser utilizado como un biomaterial con actividad antimicrobiana. Se realizaron cuatro formulaciones distintas: hidroxiapatita, hidroxiapatita-flúor, hidroxiapatita-plata-flúor e hidroxiapatita-plata con un 2% de los agentes dopantes. La síntesis del material se realizó a través del método de combustión. La caracterización mineral se realizó a través de difracción de rayos X identificando las siguientes fases en las diversas formulaciones:  $\text{Ca}_5(\text{PO}_4)_3\text{OH}$ ,  $\text{Ca}_2\text{P}_2\text{O}_7$ ,  $\text{Ag}_3\text{PO}_4$ ,  $\text{AgCa}_{10}(\text{PO}_4)_7$ ,  $\text{Ca}_5(\text{PO}_4)_3\text{F}$  and  $\text{CaF}_2$ . La estructura morfológica se analizó a través de microscopía electrónica de barrido que muestra la formación de estructuras compactas, presencia de cristales y la incrustación de flúor y plata. Se analizó la actividad antimicrobiana utilizando una prueba modificada para la observación del halo de inhibición, encontrándose solamente que los materiales que contenían plata-flúor y plata generaron dicho halo de inhibición. Por otra parte, usando la prueba de microdilución en pozo se encontró que la concentración mínima inhibitoria para el material de HA-Ag fue de 75  $\mu\text{g/ml}$  y para el material de HA-Ag-F fue de 200  $\mu\text{g/ml}$ , después de 48 horas de incubación utilizando *E. faecalis*.

**PALABRAS CLAVE:** hidroxiapatita; antibacterial; plata

### Corresponding author

TO: Verónica González Torres

INSTITUTION: Facultad de Ciencias de la Salud

de la Universidad Autónoma de Baja California

ADDRESS: Ave. Claridad S/N, Col. Plutarco Elías Calles,

C. P. 21376, Mexicali, Baja California, México

E-MAIL: [vgonzalez@uabc.edu.mx](mailto:vgonzalez@uabc.edu.mx)

### Received:

14 October 2020

### Accepted:

25 January 2021

## INTRODUCTION

Hydroxyapatite (HA),  $\text{Ca}_5(\text{PO}_4)_3(\text{OH})$ , is an inorganic calcium phosphate compound present in nature including the human body [1][2]. Synthetic hydroxyapatite is a biomaterial because it is biocompatible with human tissues and has bioactive properties. Therefore, Nayak [3] says that “it is widely used in various biomedical applications, mainly in orthopedics and dentistry” (p903).

Incorporating dopants into minerals can greatly modify the mineral characteristics related to the crystallization degree or improvement of stability [4]. Adding fluorine to HA produces fluorohydroxyapatite, which is more chemically stable and has a lower solubility than HA alone [5]. HA's cation exchange rate is very high with heavy metals or ions like  $\text{Pb}^{2+}$ ,  $\text{Ca}^{2+}$ ,  $\text{Cu}^{2+}$ ,  $\text{Mn}^{2+}$ ,  $\text{Co}^{2+}$  and  $\text{Ag}^+$  among others [6]. Metallic or ionic silver compounds have been used in a wide variety of products due to their antibacterial activity (including bacteria, viruses and fungi) [4][7][8]. According to Kolmas *et al.* [9], silver has “strong antibacterial properties of an exceptionally broad spectrum” (p3-4).

At low concentrations, silver cations are microcidal and can be used to treat burns, wounds, ulcers or as coatings of medical devices or implants because it delays the microbial biofilm development [10]. It is important to calculate the silver content in doped hydroxyapatite based materials, according to Kolmas *et al.* [9] “since it should be high enough to be able to effectively fight microorganism, while at the same time it should also be limited in order that it does not adversely affect the condition of mammalian tissues” (p5). The antimicrobial effect of silver nanostructures material systems occurs in different ways in the microbial cell, such as damage to the cell membrane by destabilization and cell lysis, damage to the subcellular microbial structure, caused by free  $\text{Ag}^+$  ions and generation of reactive oxygen species (ROS) or inactivation of proteins, enzymes and nucleotides, as well as the modification of microbial signal transduction

pathways [11][12]. The antibacterial effects of silver compounds shows less toxicity in human cells by altering metabolic pathways unique to bacteria and inducing apoptosis dependent on particle size [13].

Among all the methods or techniques used to prepare HA, combustion has its advantages because it produces nanocrystalline powders with specific characteristics depending on the combustion heat and gas evolution [4].

According to Clinical and Laboratory Standards Institute (CLSI) standards for antimicrobial susceptibility test, there are several ways for determining bactericidal activity of antimicrobial agents such a disk diffusion, broth dilution and agar dilution that measures the inhibitory activity (MIC) of an antimicrobial agent [14][15]. For routine determinations, the microdilution method is preferred.

*Enterococcus faecalis* (*E. faecalis*) is a microbial indicator of peri-implantitis and endodontic failure, since the bacteria has been found in the tooth root and the surrounding tissue after implant placement [16][17]. Confocal microscopy studies have demonstrated its persistence in the periapical spaces and the root cementum [18].

The aim of the present study is to investigate the antibacterial activity of hydroxyapatite and hydroxyapatite based materials doped with silver and fluorine against *E. faecalis* since it is the most prominent microorganism involved in persistent infections after root canal therapy [18].

## MATERIALS AND METHODS

### a) Hydroxyapatite based material preparation

In order to prepare the hydroxyapatite based materials with and without silver and fluorine, calcium nitrate ( $\text{Ca}(\text{NO}_3)_2$ ), ammonium phosphate dibasic ( $(\text{NH}_4)_2\text{HPO}_4$ ), silver trifluoroacetate

(CaF<sub>3</sub>O<sub>2</sub>Ag), calcium fluoride (CaF<sub>2</sub>) and silver nitrate (AgNO<sub>3</sub>) were used as precursors. Urea (CO(NH<sub>2</sub>)<sub>2</sub>) was used as fuel.

Four different hydroxyapatite materials were formulated: hydroxyapatite (HA), hydroxyapatite with fluorine (HA-F), hydroxyapatite with silver and fluorine (HA-Ag-F), and hydroxyapatite with silver (HA-Ag). The synthesis of 5 grams of all four HA materials was performed using the combustion method. For all the formulations a 1.67 ratio of Ca/P was used, as for the HA-F, HA-Ag-F and HA-Ag formulations, 2% of the doping agents were used. Every formulation received two thermal treatments, the first one up to 600°C/240 min with a heating speed of 5°C/min, and the second one up to 900°C/240 min at same conditions.

#### b) Characterization

The powder samples obtained were characterized by the X-ray powder diffraction (XDR) method (Bruker X-ray Diffraction D8 Advance diffractometer) with Cu K  $\alpha$ 1. Data were collected over  $\theta$  range of 10-70°. The final materials' surface was observed by using scanning electron microscopy (SEM) (JEOL JSM 7600F microscope).

#### c) Antibacterial evaluation

The materials' antibacterial effects were tested against ATCC reference and clinical microbial strains (*E. faecalis* ATCC 29212). First, a modified inhibition test zone (Kirby-Bauer Test) was performed to observe if the bacteria were susceptible to the antimicrobial agent by the dimension of the inhibition zone on the agar plate. *E. faecalis* ATCC 29212 was grown in pure culture. Using a sterile swab, a suspension of the axenic culture was spread evenly over the surface of a Mueller-Hinton agar plate. Instead of using a paper disk as indicated in the CLSI guide, each material was

applied to the center of a different agar plate. After 24 hours of incubation at 37°C, the plates were observed to see the inhibition around the test product. A control plate was also performed.

The broth microdilution method (Muller-Hinton broth) was used to determine the minimum inhibitory concentration. Dilutions of the materials were prepared freshly for each experiment. Microbial suspensions of 5 x 10<sup>5</sup> colony-forming unit (CFU)/ml obtained from 18 to 20 hours bacterial cultures developed on solid media were used.

## RESULTS AND DISCUSSION

### a) Characterization

All materials obtained were homogeneous powders. The mineralogical XDR analysis of the materials identified hydroxyapatite as a primary phase and various structures and other types of phosphates. Table 1 shows the crystalline phases present in the studied samples and their respective XDR identification card, obtained by XDR.

The XDR patterns of the hydroxyapatite based materials are shown in Figures 1 to 4. All figures present two diffraction patterns, because two different ther-

Formulation	Crystalline phases	XDR card
HA	Ca <sub>5</sub> (PO <sub>4</sub> ) <sub>3</sub> OH	00 009 0432
	$\alpha$ -Ca <sub>2</sub> P <sub>2</sub> O <sub>7</sub>	00 009 0345
	$\beta$ -Ca <sub>2</sub> P <sub>2</sub> O <sub>7</sub>	00 020 0024
HA-F	$\alpha$ Ca <sub>2</sub> P <sub>2</sub> O <sub>7</sub>	00 009 0345
	Ca <sub>5</sub> (PO <sub>4</sub> ) <sub>3</sub> F	00 015 0876
	CaF <sub>2</sub>	00 004 0864
HA-Ag-F	$\beta$ -Ca <sub>2</sub> P <sub>2</sub> O <sub>7</sub>	00 020 0024
	Ag <sub>3</sub> PO <sub>4</sub>	01 089 7399
HA-Ag	Ca <sub>5</sub> (PO <sub>4</sub> ) <sub>3</sub> OH	00 009 0432
	Ag <sub>3</sub> PO <sub>4</sub>	01 089 7399
	Ag <sub>2</sub> P <sub>2</sub> O <sub>7</sub>	00 037 0187
	Ag	01 089 3722
	AgCa <sub>10</sub> (PO <sub>4</sub> ) <sub>7</sub>	00 054 1098

TABLE 1. XDR Crystalline phases.

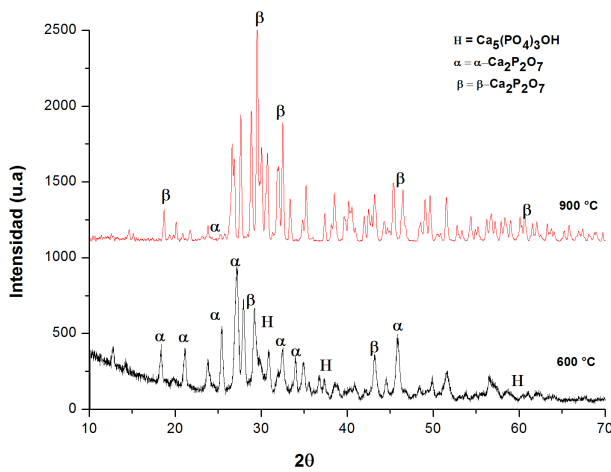


**FIGURE 1. Hydroxyapatite (HA) XDR diffraction pattern.**

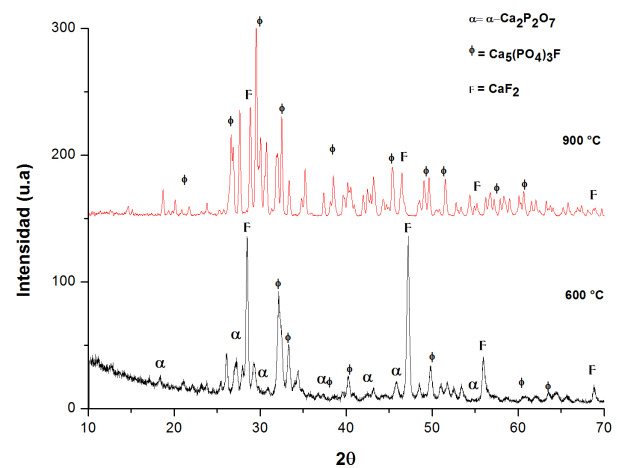


**FIGURE 2. Hydroxyapatite with fluorine (HA-F) XDR diffraction pattern.**

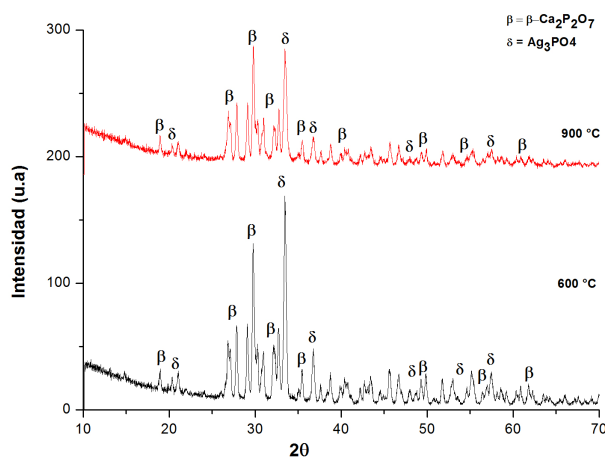


**FIGURE 3. Hydroxyapatite with silver and fluorine (HAAg-F) XDR diffraction pattern.**

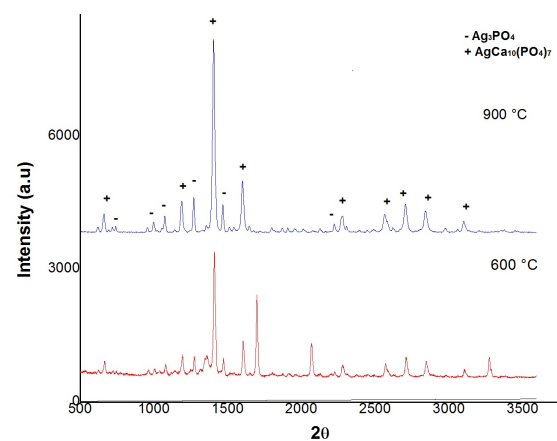


**FIGURE 4. Hydroxyapatite with silver (HA-Ag) XDR diffraction pattern.**

mal treatments were applied, one at 600°C and the other at 900°C. Different heat treatments were applied in order to evaluate the thermal effect on the crystallization phase. All XDR diffraction patterns were obtained from the different materials' powder.

The heat-treated samples at 900°C, show patterns that have better definition, in terms of crystallization.

Figure 1 shows the hydroxyapatite formulation XRD patterns, that closely matches the regular hydroxyapatite pattern. It shows the presence of  $\text{Ca}_5(\text{PO}_4)_3\text{OH}$  as main phase; also  $\alpha\text{-Ca}_2\text{P}_2\text{O}_7$ , and  $\beta\text{-Ca}_2\text{P}_2\text{O}_7$  as second-

ary phases. Figure 2 shows the hydroxyapatite fluorine material diffraction patterns, where fluorapatite ( $\text{Ca}_5(\text{PO}_4)_3\text{F}$ ) is the main phase, and  $\alpha\text{-Ca}_2\text{P}_2\text{O}_7$  and  $\text{CaF}_2$  are secondary phases.

Figure 3 shows the hydroxyapatite with silver and fluorine material diffraction patterns. As can be observed, the peaks correspond to  $\text{Ag}_3\text{PO}_4$  and  $\beta\text{-Ca}_2\text{P}_2\text{O}_7$ , the  $\text{CaF}_2$  peaks are very weak at  $2\theta \sim 29^\circ$ . Figure 4 shows the hydroxyapatite silver diffraction patterns in which  $\text{Ag}$ ,  $\text{Ag}_3\text{PO}_4$ ,  $\text{Ag}_4\text{PO}_7$  and  $\text{AgCa}_{10}(\text{PO}_4)_7$  are present. This material is the one with the highest number of crystalline phases.

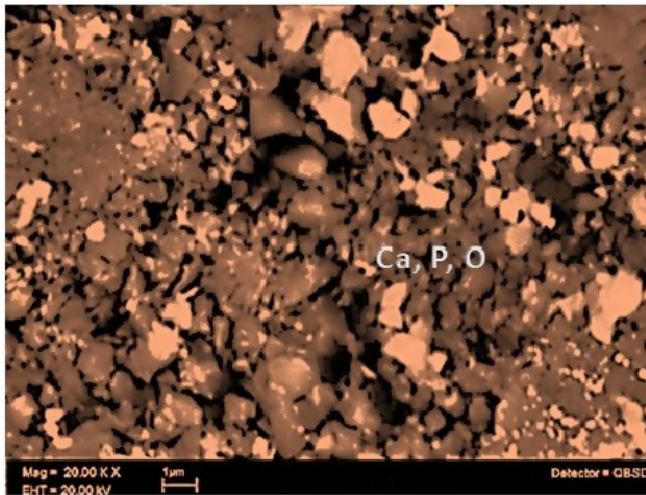


FIGURE 5. SEM micrograph of Hydroxyapatite material (HA).

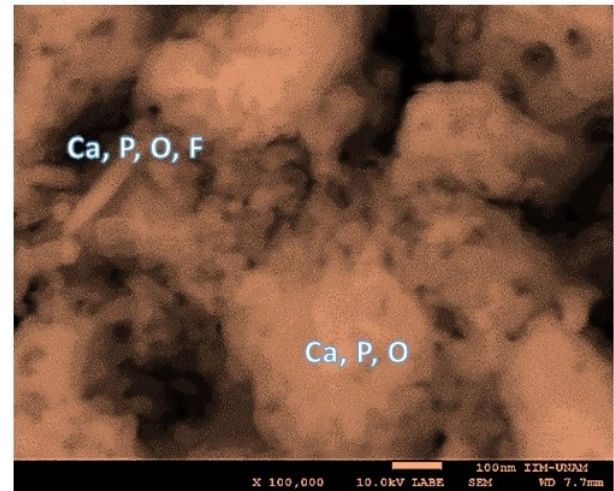


FIGURE 6. SEM micrograph of Hydroxyapatite-fluorine material (HA-F).

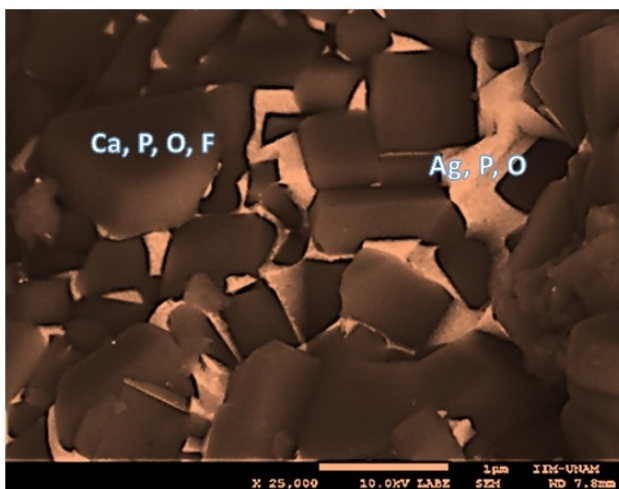


FIGURE 7. SEM micrograph of Hydroxyapatite-silver-fluorine material (HA-Ag-F).

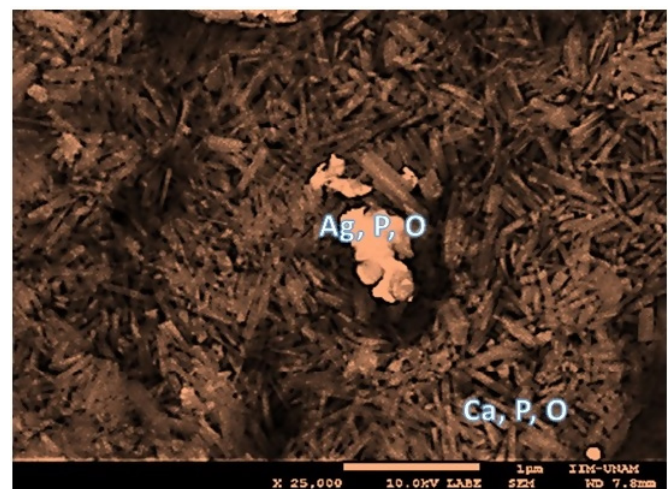


FIGURE 8. SEM micrograph of Hydroxyapatite-silver material (HA-Ag).

Figures 5 to 8 show the scanning electron microscopy (SEM) images of the hydroxyapatite based materials surface structures with and without silver and/or fluorine at 900°C, by microanalysis of secondary electrons of energy dispersive X-ray spectroscopy (EDS).

A homogeneous crystallization is observed for the HA based material with and without silver and/or fluorine. The brighter zones correspond to silver and fluorine [4]. The grain size of each material happens to be in the nanometric scale.

Figure 5 shows the surface analysis of HA material in which a matrix formed mainly by grains composed of Ca, P and O, can be observed. Figure 6 shows the surface of the HA-F material in which two zones can be observed, one containing crystals (Ca, P, O, and F) and the other with circular shaped particles (Ca, P, and O).

The HA-Ag-F material has two defined areas, a crystalline one, composed of Ca, P, O and F, and a second interface, between the grain boundaries, composed of Ag, P and O (Figure 7). Figure 8 shows the surface of

the HA-Ag material in which it is possible to observe a predominant homogeneous crystallization phase (Ca, P and O), and a clearly identifiable secondary phase (Ag, P and O).

b) Antibacterial activity evaluation

After 48 hours of incubation, the modified inhibition test zone showed that HA and HA-F materials did not present antibacterial activity due to the absence of the inhibition zone. Both HA-Ag-F and HA-Ag materials generated an inhibition zone; demonstrating their antibacterial activity. HA-Ag material showed a bigger inhibition zone in comparison to HA-Ag-F. Figure 9 shows the inhibition zones formed by the materials after 48 hours of incubation. After seven days, the HA-Ag inhibition zone grew more than the HA-Ag-F, whereas HA and HA-F did not develop an inhibition zone. Figure 10 shows the inhibition zones maintained after seven days.

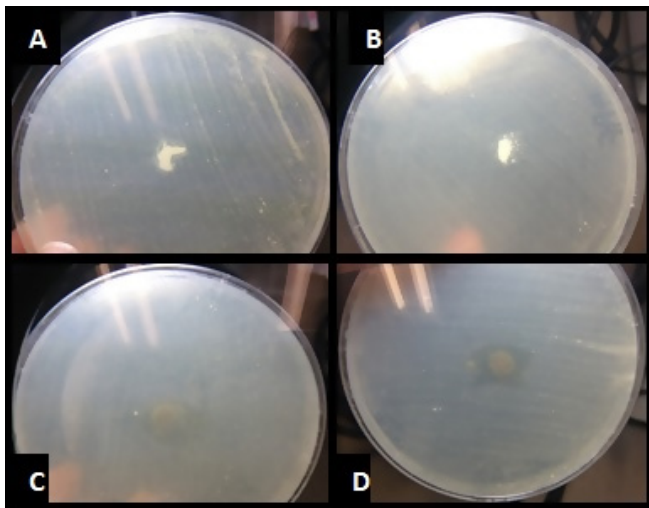


**FIGURE 9.** Inhibition zones formed after 48 hours of incubation of A) HA material, B) HA-F material, C) HA-Ag-F material, D) HA-Ag material in *E. faecalis*.

The minimum inhibitory concentration for the silver-doped hydroxyapatite (HA-Ag) material needed to kill most of the viable organism (*E. faecalis*) after 24

hours of incubation was 75 µg/ml, and 200 µg/ml for the silver and fluorine-doped hydroxyapatite (HA-Ag-F) respectively. Figure 11 shows the microdilution trays for the HA-Ag formulation and Figure 12 shows the results for the HA-Ag-F formulation.

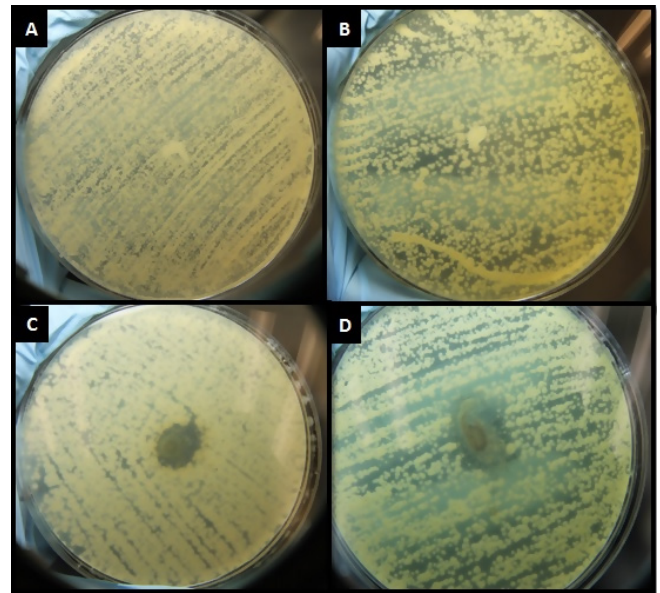


**FIGURE 10.** Inhibition zones after seven days of incubation of A) HA material, B) HA-F material, C) HA-Ag-F material, D) HA-Ag material in *E. faecalis*.

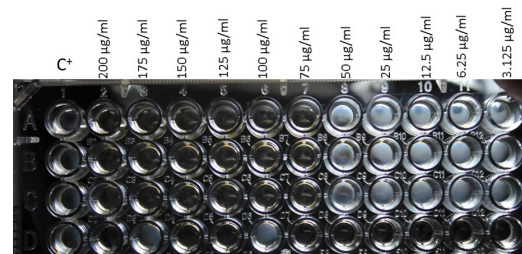


**FIGURE 11.** HA-Ag minimum inhibitory concentration results in *E. faecalis*.

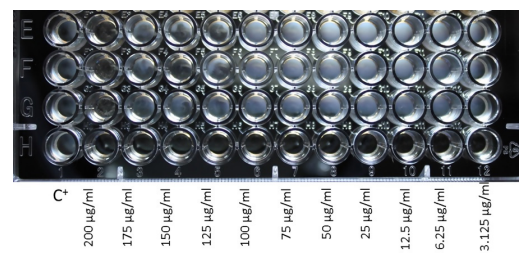


**FIGURE 12.** HA-Ag-F minimum inhibitory concentration results in *E. faecalis*.

## CONCLUSIONS

The aim of this investigation was to evaluate the antibacterial activity of nanostructured hydroxyapatite based materials doped with silver and/or fluorine. It was demonstrated that the hydroxyapatite and hydroxyapatite with fluorine formulations did not form an inhibition zone due to its lack of antibacterial properties, as it was expected because neither of these formulations contained antibacterial dopant agents. It was demonstrated that the hydroxyapatite with silver and the hydroxyapatite with silver and fluorine formulations have antibacterial properties; they inhibited the *E. faecalis* bacteria's growth. The minimum inhibitory concentration of the hydroxyapatite with silver formulation needed to kill most viable organism after 24 hours of incubation was 75 µg/ml, and 200 µg/ml for the silver and fluorine-doped hydroxyapatite formulation. It is recommended to perform more tests to determine if the materials have a bacteriostatic or bactericidal effect.

The hydroxyapatite with silver formulation had the highest antibacterial activity when compared to the silver and fluorine-doped hydroxyapatite formulation, possibly due to the lower amount of silver contained in this last formulation. This is why, new formulations are recommended, where the amount of silver is higher, all the while maintaining the presence of fluorine in the hydroxyapatite matrix since its presence lower the hydroxyapatite solubility and therefore its deionization, which in turn allows the tooth to not demineralize.

HA-Ag formulation shows activity in *E. faecalis* and a potential use in the treatment for root canals or in other dental applications due to its antibacterial activity.

According to the available literature, these materials could be used to develop new biomaterials that in effect can be use in the health field, particularly in dentistry.

## AUTHOR CONTRIBUTIONS

V.G.T. conceived the idea, carried out the formulation and synthesis of the hydroxyapatite based materials doped with silver and fluorine, contributed; Contributed to perform the materials physical and chemical properties analysis by X-ray Diffraction and Scanning Electron Microscopy. Contributed to carry out the antibacterial evaluation experiments. Took the lead in writing the manuscript. E.H.G. designed and performed the antibacterial evaluation experiments. N.A.C.M. contributed to carry out the antibacterial evaluation experiments and to the interpretation of the antibacterial evaluation experiments results and writing of the manuscript. M.R.A. contributed to perform data processing and writing of the manuscript. G.C.D.T. contributed to carry out the formulation and synthesis of the materials; performed the hydroxyapatite based materials physical and chemical properties analysis by X-ray Diffraction and Scanning Electron Microscopy. Performed data processing and writing of the manuscript.

## REFERENCES

- [1] Tas AC. Combustion synthesis of calcium phosphate bioceramic powders. *J Eur Ceram Soc* [Internet]. 2000;20(14-15):2389-2394. Available from: [https://doi.org/10.1016/S0955-2219\(00\)00129-1](https://doi.org/10.1016/S0955-2219(00)00129-1)
- [2] Markovic M, Fowler BO, Tung MS. Preparation and Comprehensive Characterization of a Calcium Hydroxyapatite Reference Material. *J Res Natl Inst Stand Technol* [Internet]. 2004;109(6):553-68. Available from: <http://dx.doi.org/10.6028/jres.109.042>
- [3] Nayak AK. Hydroxyapatite synthesis methodologies: an overview. *Int J ChemTech Res.* 2010; 2(2): 903-907.
- [4] González-Torres V, Méndez-Sánchez ER, Gaitán-Cepeda LA, et al. Characterization and Biocompatibility Evaluation of Hydroxyapatite Doped with Silver and/or Fluorine. *Adv Sci Tech* [Internet]. 2014;96:27-32. Available from: <https://doi.org/10.4028/www.scientific.net/AST.96.27>
- [5] Robinson C, Shore RC, Brookes SJ, et al. The Chemistry of Enamel Caries. *Crit Rev Oral Bio Med* [Internet]. 2000;11(4):481-495. Available from: <https://doi.org/10.1177/10454411000110040601>
- [6] Kim TN, Feng QL, Kim JO, et al. Antimicrobial effects of metal ions (Ag<sup>+</sup>, Cu<sup>2+</sup>, Zn<sup>2+</sup>) in hydroxyapatite. *J Mater Sci Mater Med* [Internet]. 1998;9(3):129-34. Available from: <https://doi.org/10.1023/A:1008811501734>
- [7] Kawashita M, Tsuneyama S, Miyaji F, et al. Antibacterial silver-containing silica glass prepared by sol-gel method. *Biomaterials* [Internet]. 2000;21(4):393-98. Available from: [https://doi.org/10.1016/S0142-9612\(99\)00201-X](https://doi.org/10.1016/S0142-9612(99)00201-X)
- [8] Bai X, More K, Rouleau CM, Rabiei A. Functionally graded hydroxyapatite coatings doped with antibacterial components. *Acta Biomater* [Internet]. 2010;6(6):2264-2273. Available from: <https://doi.org/10.1016/j.actbio.2009.12.002>
- [9] Kolmas J, Groszyk E, Kwiatkowska-Różycka D. Substituted Hydroxyapatites with Antibacterial Properties. *BioMed Res Int* [Internet]. 2014;2014:1-15. Available from: <https://doi.org/10.1155/2014/178123>
- [10] Silver S. Bacterial silver resistance: molecular biology and uses and misuses of silver compounds. *FEMS Microbiol Rev* [Internet]. 2006;27(2-3):341-53. Available from: [https://doi.org/10.1016/S0168-6445\(03\)00047-0](https://doi.org/10.1016/S0168-6445(03)00047-0)
- [11] Burdusel, A-C, Gherasim O, Grumezescu AM, et al. Biomedical Applications of Silver Nanoparticles: An Up-to-Date Overview. *Nanomaterials* [Internet]. 2018; 8(9):681. Available from: <https://doi.org/10.3390/nano8090681>
- [12] Durán N, Durán M, de Jesús MB, et al. Silver nanoparticles: A new vie won mechanistic aspects on antimicrobial activity. *NMB* [Internet]. 2016;12(3):789-799. Available from: <https://doi.org/10.1016/j.nano.2015.11.016>
- [13] Salleh A, Naomi R, Utami ND, et al. The Potential of Silver Nanoparticles for Antiviral and Antibacterial Applications: A Mechanism of Action. *Nanomaterials* [Internet]. 2020;10(8): 1566. Available from: <https://doi.org/10.3390/nano10081566>
- [14] National Committee for Clinical Laboratory Standards. Methods for determining bactericidal activity of antimicrobial agents: approved guideline. Wayne, PA: National Committee for Clinical Laboratory Standards; 1999.
- [15] Clinical and Laboratory Standards Institute. Performance standards for antimicrobial disk susceptibility tests. 13th ed. Wayne, PA: National Committee for Clinical Laboratory Standards; 2018. 92p.
- [16] Flanagan D. Enterococcus faecalis and Dental Implants. *J Oral Implantol* [Internet]. 2017; 43(1):8-11. Available from: <https://doi.org/10.1563/aaid-joi-D-16-00069>
- [17] Prad I, Micó-Muñoz P, Giner-Lluesma T, Collado-Castellano N, Manzano-Saiz A. Influence of microbiology of endodontic failure. Literature review. *Med Oral* [Internet]. 2019;24(3):e364-72. Available from: <https://doi.org/10.4317/medoral.22907>
- [18] Halkai R, Hedge MN, Halkai K. Evaluation of the presence of Enterococcus Faecalis in root cementum: A confocal laser scanning microscope analysis. *J Conserv Dent* [Internet]. 2014;17(2):119-23. Available from: <https://doi.org/10.4103/0972-0707.128039>

[dx.doi.org/10.17488/RMIB.42.2.5](https://dx.doi.org/10.17488/RMIB.42.2.5)

E-LOCATION ID: 1116

## Biomechanical Evaluation of Hemiarthroplasty in the First Proximal Phalanx. A Finite Element Study

M. A. Madrid-Pérez<sup>1</sup>, R. Becerro de Bengoa-Vallejo<sup>2</sup>, J. Bayod-López<sup>3</sup>

<sup>1</sup>Escuela de Ingeniería y Arquitectura, Universidad de Zaragoza. Facultad de Ingeniería, Universidad Autónoma de Chihuahua

<sup>2</sup>Escuela de Enfermería, Fisioterapia y Podología, Universidad Complutense de Madrid

<sup>3</sup>Escuela de Ingeniería y Arquitectura, Universidad de Zaragoza

### ABSTRACT

Hallux rigidus produces a decrease in the dorsiflexion of the first metatarsophalangeal joint and is usually associated with the appearance of osteophytes. Hemiarthroplasty in the first proximal phalanx is a recommended surgical procedure in patients with advanced grade of hallux rigidus. Finite element analysis allows us to understand the biomechanical behavior of the foot. The objective of this work is to evaluate the biomechanical effects of an hemi implant placed in first proximal phalanx. Two models of finite elements are going to be compared, one free of pathologies and the other with a hemiarthroplasty in the first ray of the foot. We detected after inserting the prosthesis in the model that passive windlass mechanism is lost, and the lesser toes become overloaded, which leads to a loss of efficiency in gait as well as being able to cause postsurgical medical complications.

**KEYWORDS:** Hemiarthroplasty; Hallux Rigidus; Finite Element Analysis; First Metatarsophalangeal Joint

### Corresponding author

TO: Mario Alberto Madrid Pérez

INSTITUTION: Facultad de Ingeniería, Universidad Autónoma de Chihuahua

ADDRESS: Circuito Número I S/N, Nuevo Campus Universitario II, C. P. 31125, Chihuahua, Chihuahua, México

E-MAIL: 715181@unizar.es; mmadrid@uach.mx

### Received:

22 September 2020

### Accepted:

11 February 2021

## INTRODUCTION

Hallux Rigidus (HR) is characterized by permanent pain with joint crunches when performing the mobilization of the great toe. The pain is increased when walking and standing up. HR is usually associated with a decrease in joint function, as well as the appearance of a lump or excrescence in the metatarsophalangeal dorsal region of the First Ray of the Foot (FRotF)<sup>[1]</sup>. This pathology is usually associated with a limitation of the movement of the FRotF, especially in dorsiflexion, medically called osteoarthritis of the metatarsophalangeal joint of the great toe<sup>[2]</sup>. The mobility arc of the First Metatarsophalangeal Joint (FMJ) is 110 degrees, with a plantar flexion of 35 degrees and dorsal flexion of 75 degrees. In HR the range of mobility decreases, with a decrease in dorsiflexion<sup>[3]</sup>.

To date, there is no technique that can be applied to all the different grades of HR. The treatments against HR have had considerable advances in recent years. The destructive surgical techniques include arthrodesis, arthroplasty, and cheilectomy, while the nondestructive surgical techniques include many kinds of osteotomies<sup>[2]</sup>. Arthroplasty is a surgical procedure where the skeletal muscle's surface of an articular joint is remodeled, replaced, or realigned. There are three different types of arthroplasty: The interposition arthroplasty where some tissue is interposed, such as a muscle or a tendon to keep some distance between the bones. The resection arthroplasty where the resected bone is removed and the implant arthroplasty where the bony surfaces of proximal phalanx and/or head of first metatarsal bone are removed and replaced by an implant<sup>[4]</sup>. The surgical treatment and the type of technique to be used depend on the stage in which it is found and the morphological type of the forefoot. However, all methods should be aimed at supplying the function of the first phalanx during the moment of toe-off in walking<sup>[1]</sup>. As mentioned above, there are many treatments for the described pathology, but it is not yet clear which treatments are better than others.

The present work focuses on implant arthroplasty. This surgical technique remains controversial. Implant arthroplasty has the advantage of being a technique that can alleviate pain and restore the mobility of the FMJ but also has the disadvantage of being a destructive procedure, which is why it is considered one of the last options<sup>[5]</sup>. This project presents a biomechanical evaluation of an implant arthroplasty using the AnaToemics®Phalangeal Prosthesis by Arthrex. The implant researched in this paper is recommended to be used in patients with HR in grade III or IV and with patients with moderate hallux valgus (HV)<sup>[5][6]</sup>.

To date, no scientific articles have been presented that display a biomechanical evaluation for this type of hemi-implant. Finite element models are a good technique to understand these effects<sup>[4][7][8][9]</sup> and are more economical and easier to carry out than experimental ones (either in vivo or on cadavers). Reference<sup>[4]</sup> discusses a foot model after an arthroplasty has been developed using two types of implants, Swanson and Tornier joint implants. Reference<sup>[7]</sup> makes an analysis of the foot varying the size of the first proximal phalanx. Reference<sup>[8]</sup> researches the load distribution in first metatarsal bone and reference<sup>[10]</sup> makes an analysis of the foot when hemiarthroplasty in the first metatarsal bone has been developed using the hemi-implant HemiCAP®Toe DF by Arthrosurface. The objective of this work is to understand the biomechanical effect generated by a hemiarthroplasty of the FRotF using the hemi-implant AnaToemics®Phalangeal by Arthrex. To do this, displacements and tensions will be compared in two computational models, one healthy and the other one with a hemiarthroplasty.

The hemiarthroplasty process consists in aligning the first ray of the foot, if there are osteophytes they are removed, first proximal phalanx is resected, the implant is inserted and some muscles and tendons are disconnected<sup>[10]</sup>. By making this process in a finite element model of the foot with the aim to understand the impact

of the first proximal phalanx hemiarthroplasty on the gait biomechanics. The stresses and displacements of both healthy and hemiarthroplasty models are analysed during toe-off in order to evaluate the effects of the implant on the gait biomechanics, specifically on the first ray of the foot. The healthy model induces stresses and displacements that must correspond with the biomechanics of the foot in the literature of the toe-off phase and the hemiarthroplasty model induces displacements and stresses that let us know how the implant works and how the biomechanics of the human gait changes with the process of hemiarthroplasty, especially to know if there are or there are not any consequences in the biomechanics of the first ray of the foot.

## MATERIALS AND METHODS

### Healthy model

The healthy model presented was developed by the University of Zaragoza (Spain). 93 computed tomography scans were necessary for the foot scan. The creation of volumes was done considering cortical and trabecular bone. The maximum and minimum size element was of 3 mm and 0.31 mm respectively with an average of 1.78 mm solving in that way the model convergence problem. The foot is modelled during toe-off since at this phase the maximum stresses occur in the FRotF [7]. For bones and cartilage, we use tetrahedral elements due is a good type of element to mesh complicated geometries, for muscles and tendons we use beam elements because they experiment directly a pretension force due to the position of toe-off and for thin ligaments, plantar ligaments, and plantar fascia we use bar elements due they only suffer small displacements in their extreme nodes when the model is loaded [4] [7] [9] [15] [16] [17] [18] [24]. Fig. 1 shows the elements that this model contains. All bones, cartilage, and soft tissues were considered as homogeneous, isotropic, and linearly deformable bodies. This model (without an implant) contains 150,594 nodes and 802,294 elements. More details about this model can be found in [4] [9].

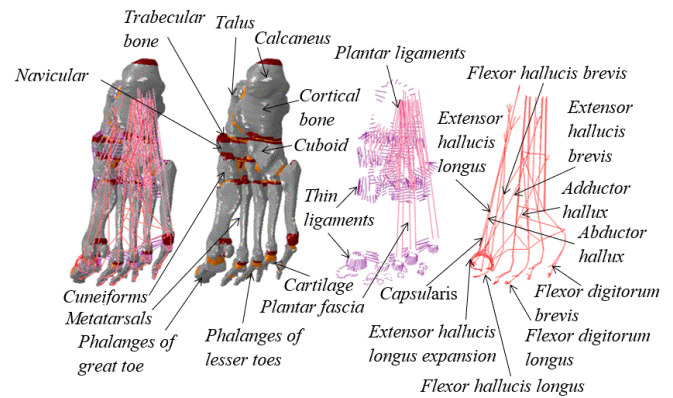


FIGURE 1. Elements of the model without an implant.

### Hemiarthroplasty model

The second model presented in this article contains the insertion of the hemi-implant AnaToemics® Phalangeal Prosthesis by Arthrex in the proximal phalanx of the great toe. To obtain the volume of the implant, we used a 3D scanner provided by the University of Zaragoza. According to the surgical procedure, the first proximal phalanx is resected to later introduce the implant. To make this cut in the proximal phalanx, Mimics 10.0 was used after the prosthesis was placed with the help of Softimage 2015 and exporting the entire model in the .STL format. The mesh for hemiarthroplasty model was creating with ICM CFD 17.2 of ANSYS having in the entire model a maximum and minimum element size of 3.8 mm and 0.18 mm respectively with an average of 1.13 mm, in the implant the maximum and minimum size of element was 3 mm and 0.42 mm respectively with an average of 1 mm preserving in that way the geometry of the first ray after having developed the surgical procedure, in addition to solving the model convergence problem. When the maximum element size in the implant is 5 mm, the minimum size is 0.7 mm and the average size is 1.7 mm, there are no significant changes in the calculations of stresses and deformations in the implant. Hemiarthroplasty model has a more refined mesh than healthy model due to the surgical procedure. To maintain the geometry of the soft tissues MATLAB R2013b programming was used to insert

muscles, tendons, and ligaments calculating the minimum distance of the nodes of healthy model with the nodes of hemiarthroplasty model.

For this model with implant, some muscles and tendons have been removed as well as some ligaments of the first metatarsophalangeal joint as part of the hemiarthroplasty process [10]. Fig. 2 shows the elements of the model with the implant and Fig. 3 shows the hemi implant and its mesh, it is worth to note that in the part of the implant (spikes) inserted in the trabecular bone of the first proximal phalanx, the stresses and deformations are small values, so the mesh size adequately solves the model convergence problem. Hemiarthroplasty model contains 1,836,607 elements and 329,159 nodes.

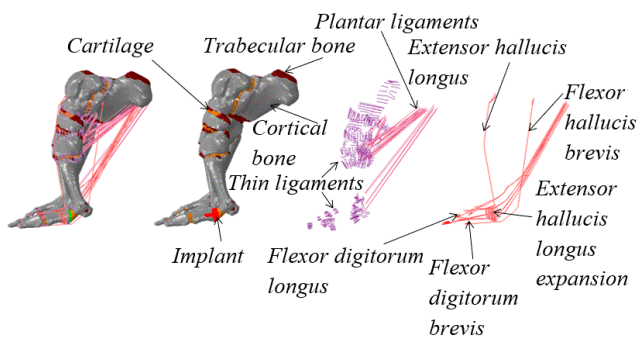


FIGURE 2. Elements of the model with the implant.

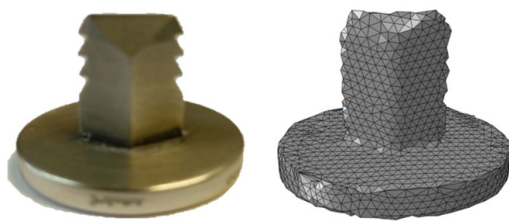


FIGURE 3. The implant and mesh from the implant.

### Mechanical properties and boundary conditions

The mechanical properties, as well as boundary and load conditions that are used in the two models presented in this paper, are the same, so they will only be defined once [4] [7]. All elements were considered as

homogeneous, isotropic, and linearly deformable elastic because there are only small displacements and small deformations. For cortical bone, trabecular bone, muscles, thin ligaments and plantar ligaments, a modulus of elasticity of 17000, 700, 450, 260 and 350 MPa respectively has been used, all the elements mentioned above have a Poisson coefficient of 0.3. For cartilage a Young's modulus of 10 MPa and a Poisson's ratio of 0.4 were used and for the cobalt-chrome hemi implant a Poisson's ratio of 0.29 and an elastic modulus of 210 GPa have been used [11] [12] [13] [14].

Some authors divide the human gait cycle into three stages, while others define six or eight stages [15]. Regardless of the classification of the human gait that is taken, it is well-documented that the maximum efforts at the FROT occur in the position of the toe-off [7].

The models presented are in the toe-off stage and correspond to a person weighing 60 kg. The analysis was performed in the Abaqus 6.13-5 software. For the analysis, two steps were used. In the first step, a pretension force of 2 % is added to the muscles as consequence of the toe-off phase. This pretension force has been obtained by measuring the elongation of the muscles during toe-off with cadavers [16] [17] [18]. All displacements of some nodes on the attachment surface of the Achilles tendon are restricted. All degrees of freedom were constrained at the base of the first two proximal phalanges. Vertical translations and rotations in the distal phalanges of the lesser toes are restricted. In the second step, the pretension force is maintained, and the weight of the person is added, considering a force of 1805 N [15]. A contact pair frictionless was used between the outer surface of the tetrahedral elements with the muscles and tendons. The master surface is made up of triangular elements while the slave surface is made up of the nodes of the muscles and tendons. Fig. 4 shows how the body weight acts on the model; this load was applied in the area where the fibula and the tibia meet the talus.

With the aim to understand how the implant functions when it is overloaded, we simulate the foot during toe-off loading 2 and 2.5 times the weight of the person.

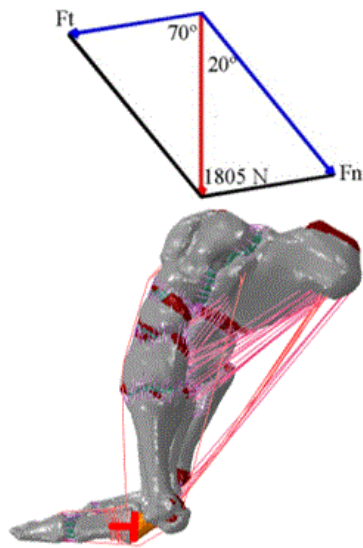


FIGURE 4. Loads due to the person's own weight.

## RESULTS AND DISCUSSION

### Results for model without an implant

In the healthy model the first distal phalanx acquires a movement in the sagittal plane. This movement is due to the force reaction that the ground exerts on the person and produces a forward impulse, giving directionality to the gait [19]. In Fig. 5, we can see this movement, which is commonly known as the passive windlass mechanism, and we can see too the principal stresses for the model. For the first distal phalanx, the maximum concentration of principal stresses occurs in the dorsal area, where the tendons of extensor hallucis longus muscle act. Concentrations of principal stresses at the support points appear for the second and third ray of the foot. The maximum displacement occurs in the phalanges of the fifth ray of the foot.

### Results for model with the implant

For the second model presented in this article, concentrations of principal stresses appear in the second ray of the foot and calcaneus. For the FRotF, the great-

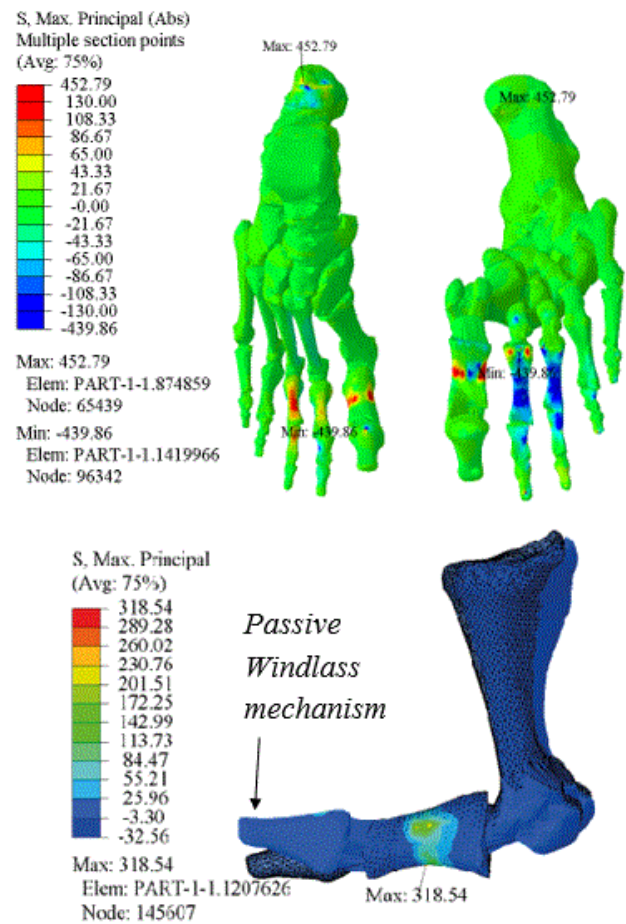


FIGURE 5. Principal stresses in the model without an implant.

est concentration of principal stresses appears in the support points. For the second and third rays, the highest stress concentration occurs in the proximal phalanges. For the second and third rays of the foot, the greatest concentration of major stress occurs in the proximal plantar area of the proximal phalanges. The greatest displacement occurs in the third and fifth rays of the foot in the phalangeal area. The function of the passive windlass mechanism is lost. The stresses and displacements mentioned previously can be contemplated in Fig. 6. In upper part of Fig. 7 the displacements for the healthy model in the three loading conditions are shown. In the lower part, appear the displacements for the three loading conditions in the model with the implant. The units of the displacements are millimeters.

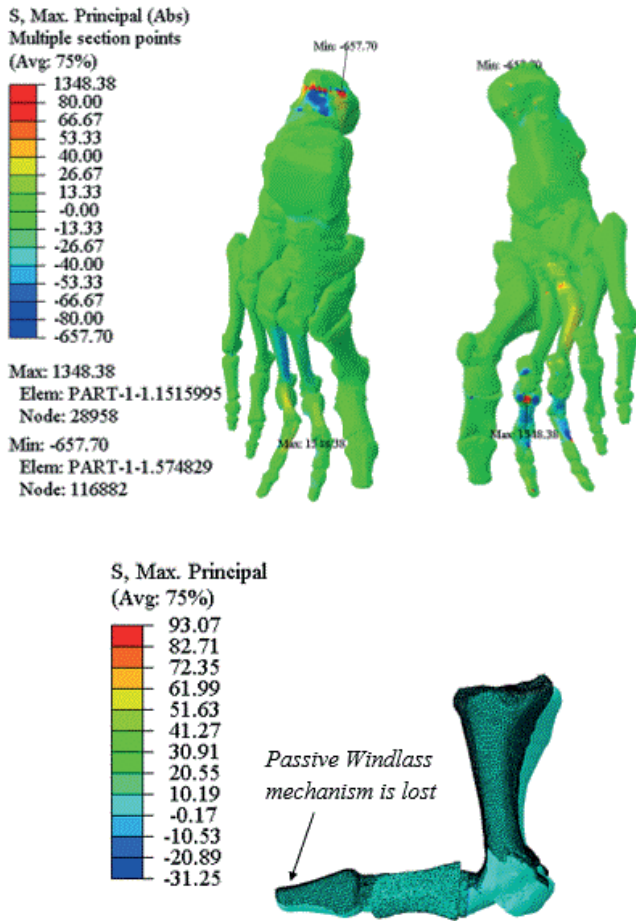


FIGURE 6. Principal stresses in the model with implant.

The maximum von Mises stress on the implant is 27 MPa (Fig. 8). The maximum principal stress registered in the implant is 29 MPa, and this occurs in the joint of the oval part with the pilot pin. The highest absolute value of the minimum principal stress in the implant is 27 MPa (compression stress), and it appears in the oval part. Table 1 presents a comparison of the maximum Von Mises stresses developed in the implant when loading condition is 1.0, 2.0 and 2.5 the body weight.

**Discussion**

Arthroplasty using the AnaToemics®Phalangeal Prosthesis by Arthrex is a recommended procedure for patients with HR grade 3 and 4 who have failed conservative treatment for at least 6 months. This proce-

TABLE 1. Comparison of maximum equivalent Von Mises stress in implant.

Loading condition	Von Mises Stress (MPa)
1.0 times the person's own weight	27.47
2.0 times the person's own weight	61.60
2.5 times the person's own weight	78.63

dure requires that the patient has a well-aligned and stable FMJ [5]. Despite the fact that the use of implants is becoming more and more common, no studies have been carried out using Finite Element Analysis to know the consequences that these types of implants produce in the foot [20].

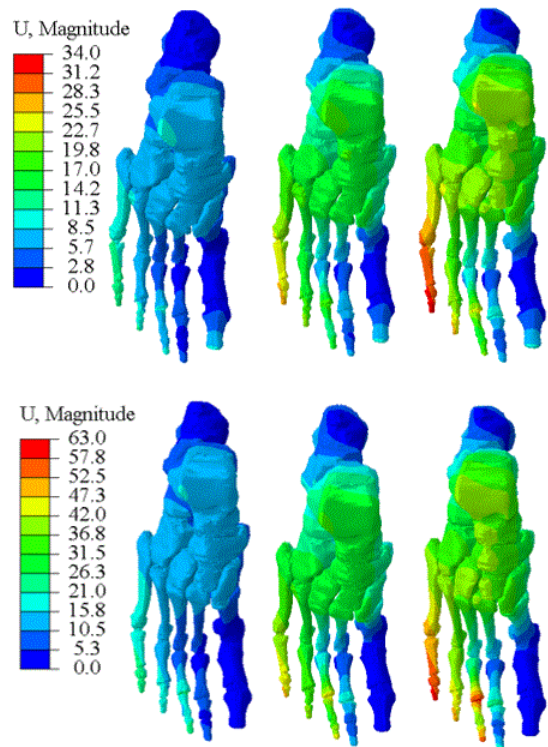
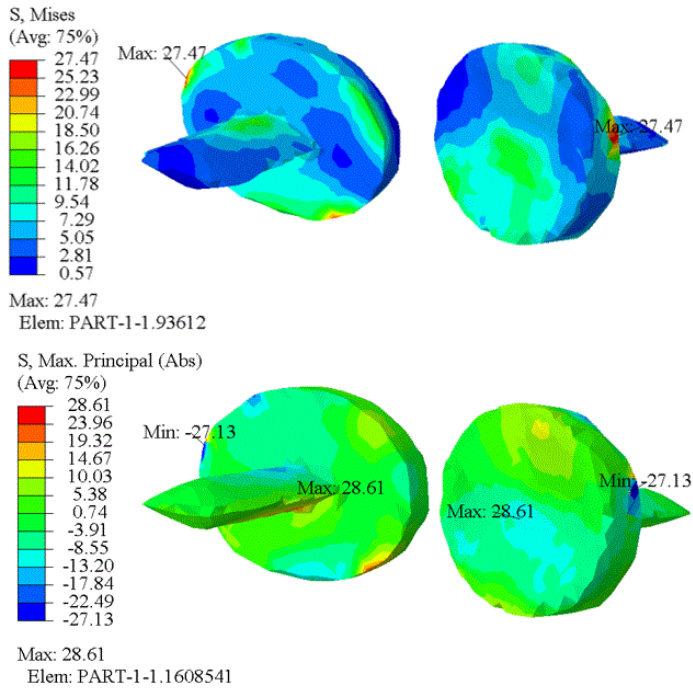


FIGURE 7. Displacements values for healthy model (upper part) and hemiarthroplasty model (lower part) for all load conditions.

Eric Eric Giza et al. [21] report 22 Hemiarthroplasties in the First Proximal Phalanx (HitFPP) in 20 patients. Preoperative radiographs revealed 14 cases of grade 3 and 8 cases of grade 4 HR, according to the classifica-



**FIGURE 8. Von Mises stresses and absolute maximum principal stresses.**

tion of Coughlin and Shurnas. The average dorsiflexion of the FMJ improved from 41 with a Standard Deviation (SD) of 11 degrees to 49 with a SD of 10 degrees in 1 year. The average score of the AOFAS scale improved from 61 points (range: 35-80) to 86 points (range: 75-95). The VAS pain scale improved from 4.7 with a SD of 2.6 points to 2.5 with a SD of 1.9 points. One patient developed metatarsalgia in the second metatarsophalangeal joint and only required conservative treatment. Konkel et al. followed up 23 patients for 72 months (17 had HR grade 3, and 6 had HR grade 4). The average age was 62 years. There were two patients with mild clawing of the great toe and two of mild transfer metatarsalgia. The average plantar flexion increased from 1 degree with a range of (-15 to 15) to 13 degrees with a range of (-20 to 30). For dorsiflexion, there was an average improvement from 16 (5 to 50) to 60 (20 to 85) degrees. In the score of the AOFAS scale the change was from 19 (17 to 50) to 89 (40 to 100) points.

At the end of the follow-up there was a 68% of recurrent dorsal osteophytes, the recurrence was mild in 10 patients, moderate in 4, and severe in 6, while 8 patients had no recurrence. There were three unsatisfied patients; a hard-working man in the construction industry, a woman who worked in a marketing industry and had to wear designer shoes, and another man who worked as a machinist in a factory and had to stand all day [22].

In this paper two finite element models of the foot have been presented. The first model analyses a healthy foot and the second model analyses the same foot having released a HitFPP. We found that when the hemiarthroplasty is performed the rays 2 and 3 become overloaded. In the first model, it was also observed that thin ligaments between first metatarsal and proximal phalanx, the pedio muscle, capsularis, flexor hallucis brevis, hallux adductor, and hallux abductor muscles transmit the most loads to the first proximal phalanx in the toe-off stage; these muscles and ligaments are disconnected in the surgical procedure. When performing the arthroplasty, it was also observed that passive windlass mechanism is lost despite not having disconnected the extensor hallucis longus muscle in the surgical procedure. The FRotF gives the ability to walk on uneven terrain [23]. This capacity could be affected after having developed an HitFPP. We recommend further work to evaluate the mechanism of active windlass in patients during postsurgical follow-up. The tensile strength yield for CrCo alloy is 410 MPa and this value is higher than the von Mises stresses reported in this paper (27.47 MPa). This indicates that failure for this implant may be due to fatigue problem [25].

## CONCLUSIONS

Some authors have reported metatarsalgia in the second toe as a side effect of the first phalangeal arthroplasty [21] [22] and Garcia-Aznar et al. have shown that when the FRotF is unloaded, the others are overloaded, thus increasing the risk of metatarsalgia [24] [17].

For the healthy model, the results have a good correlation with a similar models presented by Enrique Morales et al. [15], Marco A. Martinez et al. [4] and Mario Alberto Madrid et al. [9]. These are the same model with minor modifications through various researches, while for the implant model there is no experimental validation because nobody has done it before, however there are clinical results that coincide with the results obtained in the implant model [21] [22]. This study makes a comparison of a foot free of any pathology with a foot that undergoes a HitFPP. It is worth to note that most people who undergo this procedure feel great relief after the postsurgical rehabilitation because, before the operation, they could not walk, jump, run, or wear shoes as normal.

The results shown in Figs. 5, 6 and 8 correspond to the condition loading of 1.0 times the person's own weight. Since the implant is made from metal, we use the von Mises stresses, while for hard and soft tissues we use the principal stresses. The distribution of stress in the three analysed loading conditions was similar. The higher value of load condition the higher values of stress and strain in the model. The values of the displacements in the lesser toes increased when the load condition increased, but for the healthy model the displacements of the distal phalanx of the great toe, because of the windlass mechanism, obtained the same value in the three load conditions. In the hemiarthroplasty model the values of the displacements in first distal phalanx are null in all load conditions. The maximum von Mises stress obtained in this study is 6.7% of the yield strength [25], thus failure for this implant could be due to fatigue problem.

Because it is a destructive procedure, the HitFPP is usually one of the last options for patients with HR in advanced stages of the pathology. Many authors have compared this procedure with other procedures, such as Keller's arthroplasty, hemiarthroplasty of the first metatarsal or implant arthroplasty that replace the entire FMJ [5] [6].

On the other hand, the use of finite element analysis has helped to understand the changes in foot biomechanics after having been developed an HitFPP. Despite these efforts, there is still much work to be done to find an effective and efficient way to return a comfortable and painless life to people suffering from these pathologies that continue to have no cure.

#### **AUTHOR CONTRIBUTIONS**

M.A.M.P. Contributed to elaboration of models, writing the manuscript and interpretation of results.

R.B.B.V. Contributed to review the anatomy and the arthroplasty process of the models, interpretation of results, writing and reviewing the manuscript.

J.B.L. Contributed to software licenses, interpretation of results, reviewed and writing the manuscript.

#### **ACKNOWLEDGEMENTS**

The authors gratefully acknowledge the support of the Ministry of Economy and competitiveness of the Government of Spain through the project DPI2016-77016-R.

## REFERENCES

- [1] Núñez-Samper M, Llanos Alcázar LF. Biomecánica, medicina y cirugía del pie. Barcelona: Masson, S. A; 2000.
- [2] Polzer H, Polzer S, Brumann M, et al. Hallux rigidus: Joint preserving alternatives to arthrodesis - a review of the literature. *World J Orthop* [Internet]. 2014;5(1):6-13. Available from: <https://dx.doi.org/10.5312/wjo.v5.i1.6>
- [3] Asunción Márquez J, Martín Oliva X. Hallux rígido: Etiología, diagnóstico, clasificación y tratamiento. *Rev Esp Cir Ortop Traumatol* [Internet]. 2010;54(5):321-328. Available from: <https://doi.org/10.1016/j.recot.2010.05.005>
- [4] Martínez Bocanegra MA, Bayod Lopez J, Vidal-Lesso A, et al. Structural interaction between bone and implants due to arthroplasty of the first metatarsophalangeal joint. *Foot Ankle Surg* [Internet]. 2019;25(2):150-157. Available from: <https://doi.org/10.1016/j.fas.2017.10.002>
- [5] Delman C, Kreulen C, Sullivan M, et al. Proximal Phalanx Hemiarthroplasty for the Treatment of Advanced Hallux Rigidus. *Foot Ankle Clin* [Internet]. 2015;20(3):503-512. Available from: <https://doi.org/10.1016/j.fcl.2015.05.002>
- [6] Perler AD, Nwosu V, Christie D, et al. End-Stage Osteoarthritis of the Great Toe/Hallux Rigidus. A Review of the Alternatives to Arthrodesis: Implant Versus Osteotomies and Arthroplasty Techniques. *Clin Podiatr Med Surg* [Internet]. 2013;30(3):351-395. Available from: <https://doi.org/10.1016/j.cpm.2013.04.011>
- [7] Morales-Orcajo E, Bayod J, Becerro-de-Bengoa-Vallejo R, et al. Influence of first proximal phalanx geometry on hallux valgus deformity: a finite element analysis. *Med Biol Eng Comput* [Internet]. 2015;53:645-653. Available from: <https://doi.org/10.1007/s11517-015-1260-4>
- [8] Kristen K-H, Berger K, Berger C, et al. The First Metatarsal Bone Under Loading Conditions : A Finite Element Analysis. *Foot Ankle Clin* [Internet]. 2005;10(1):1-14. Available from: <https://doi.org/10.1016/j.fcl.2004.11.003>
- [9] Madrid MA, de Bengoa Vallejo RB, López JB. Biomechanical Evaluation of Hemiarthroplasty in First Metatarsal Bone. In: González Díaz C, et al. (eds). VIII Latin American Conference on Biomedical Engineering and XLII National Conference on Biomedical Engineering CLAIB 2019 [Internet]. Cancún: IFMBE Proceedings; 2019:831-840. Available from: [https://doi.org/10.1007/978-3-030-30648-9\\_109](https://doi.org/10.1007/978-3-030-30648-9_109)
- [10] Becerro de Bengoa Vallejo R, Losa Iglesias ME, Jules KT. Tendon Insertion at the Base of the Proximal Phalanx of the Hallux: Surgical Implications. *J Foot Ankle Surg* [Internet]. 2012;51(6):729-733. Available from: <https://doi.org/10.1053/j.jfas.2012.06.004>
- [11] Ramos AR. Estudio por elementos finitos del comportamiento del pie [dissertation]. [Zaragoza]: Universidad de Zaragoza; 2006. Spanish.
- [12] Moharrami N, Langton DJ, Sayginer O, et al. Why does titanium alloy wear cobalt chrome alloy despite lower bulk hardness: A nanoindentation study? *Thin Solid Films* [Internet]. 2013;549(31):79-86. Available from: <https://doi.org/10.1016/j.tsf.2013.06.020>
- [13] Çelik I. Influence of CrN Coating on Electrochemical Behavior of Plasma Nitrided Pure Titanium in Bio-simulated Environment. *J Bionic Eng* [Internet]. 2016;13:150-155. Available from: [https://doi.org/10.1016/S1672-6529\(14\)60169-4](https://doi.org/10.1016/S1672-6529(14)60169-4)
- [14] Tanner KE. Titanium in Medicine. *Proc Inst Mech Eng H* [Internet]. 2002;216(3):215-215. Available from: <https://doi.org/10.1243/0954411021536432>
- [15] Morales Orcajo E.. Influencia de la geometría de la falange proximal en la formación de juanetes [master's thesis]. [Zaragoza]: Universidad de Zaragoza; 2012. Spanish.
- [16] Bayod J, Losa-Iglesias M, Becerro de Bengoa-Vallejo R, et al. Advantages and Drawbacks of Proximal Interphalangeal Joint Fusion Versus Flexor Tendon Transfer in the Correction of Hammer and Claw Toe Deformity. A Finite-Element Study. *J Biomech Eng* [Internet]. 2010;132(5):51002. Available from: <https://doi.org/10.1115/1.4001115>
- [17] Bayod J, Becerro de Bengoa Vallejo R, Losa Iglesias ME, et al. Stress at the Second Metatarsal Bone After Correction of Hammertoe and Claw Toe Deformity: A Finite Element Analysis Using an Anatomical Model. *J Am Podiatr Med Assoc* [Internet]. 2013;103(4):260-73. Available from: <https://doi.org/10.7547/1030260>
- [18] García-González A, Bayod J, Prados-Frutos JC, et al. Finite-element simulation of flexor digitorum longus or flexor digitorum brevis tendon transfer for the treatment of claw toe deformity. *J Biomech* [Internet]. 2009;42(11):1697-1704. Available from: <https://doi.org/10.1016/j.jbiomech.2009.04.031>
- [19] Marco Sanz C. Cinesiología de la marcha humana normal [Internet]. Universidad de Zaragoza; 2011. Available from: <http://wzar.unizar.es/acad/cinesio/MaterialDidactico.html>
- [20] DeHeer PA. The Case Against First Metatarsal Phalangeal Joint Implant Arthroplasty. *Clin Podiatr Med Surg* [Internet]. 2006;23(4):709-723. Available from: <https://doi.org/10.1016/j.cpm.2006.08.001>
- [21] Giza E, Sullivan M, Ocel D, et al. First metatarsophalangeal hemiarthroplasty for hallux rigidus. *Int Orthop* [Internet]. 2010;34:1193-1198. Available from: <https://doi.org/10.1007/s00264-010-1012-x>
- [22] Konkel KF, Menger AG, Retzlaff SA. Results of Metallic Hemi-Great Toe Implant for Grade III and Early Grade IV Hallux Rigidus. *Foot Ankle Int* [Internet]. 2009;30(7):653-660. Available from: <https://doi.org/10.3113/FAI.2009.0653>
- [23] Kirby K. Foot and lower extremity biomechanics, Vol. IV. Payson: Precision Intracast Newsletter ;1997. 142p.
- [24] García-Aznar JM, Bayod J, Rosas A, et al. Load Transfer Mechanism for Different Metatarsal Geometries: A Finite Element Study. *J Biomech Eng* [Internet]. 2008;131(2):021011. Available from: <https://doi.org/10.1115/1.3005174>
- [25] Dolgov, N A, Dikova T, Dzhendov D, et al. Mechanical Properties of Dental Co-Cr Alloys Fabricated via Casting and Selective Laser Melting. *Int Sci J Materials Science. Non-Equilibrium Phase Transformation*. 2016;2(3):29-33.

[dx.doi.org/10.17488/RMIB.42.2.6](https://doi.org/10.17488/RMIB.42.2.6)

E-LOCATION ID: 1136

## Detection of Exudates and Microaneurysms in the Retina by Segmentation in Fundus Images

### Detección de Exudados y Microaneurismas en la Retina por Segmentación en Imágenes de Fondo

*E. Bernal-Catalán<sup>1</sup>, E. De la Cruz-Gómez<sup>1</sup>, J. A. Montero-Valverde<sup>1</sup>, R. Hernández Reyna<sup>1</sup>, J. L. Hernandez-Hernández<sup>2</sup>*

<sup>1</sup>Tecnológico Nacional de México/Instituto Tecnológico de Acapulco

<sup>2</sup>Tecnológico Nacional de México/Instituto Tecnológico de Chilpancingo

#### ABSTRACT

This article proposes two methodologies for the detection of lesions in the retina, which may indicate the presence of diabetic retinopathy (DR). Through the use of digital image processing techniques, it is possible to isolate the pixels that correspond to a lesion of RD, to achieve segmenting microaneurysms, the edges of the objects contained in the image are highlighted in order to detect the contours of the objects to select by size those that meet an area of 15 to 25 pixels in the case of 512x512 images and identify the objects as possible microaneurysms, while for the detection of exudates the green channel is selected to contrast the luminous objects in the retinography and from the conversion to gray scale, a histogram is graphed to identify the ideal threshold for the segmentation of the pixels that belong to the exudates at the end of the optical disk previously identified by a specialist. A confusion matrix supervised by an ophthalmologist was created to quantify the results obtained by the two methodologies, obtaining a specificity of 0.94 and a sensitivity of 0.97, values that are outstanding to proceed with the classification stage.

**KEYWORDS:** Diabetic Retinopathy; Exudates; Microaneurysms; Image Processing; Segmentation

## RESUMEN

Este artículo propone dos metodologías para la detección de lesiones en la retina, que pueden significar la presencia de retinopatía diabética (RD). Mediante el uso de técnicas de procesamiento de imágenes digitales se logra aislar los píxeles que corresponden a una lesión propia de RD, para lograr segmentar microaneurismas se resaltan los bordes de los objetos contenido en la imagen con la finalidad de detectar los contornos de los objetos para seleccionar por tamaño los que cumplan con un área de 15 a 25 píxeles en el caso de imágenes de 512x512 y se identifiquen los objetos como posibles microaneurismas, mientras que para la detección de exudados se selecciona el canal verde para contrastar los objetos luminosos en la retinografía y a partir de la conversión a escala de grises se grafica un histograma para identificar el umbral idóneo para la segmentación de los píxeles que pertenecen a los exudados al final eliminar el disco óptico previamente identificado por un especialista. Se creó una matriz de confusión supervisada por un oftalmólogo para cuantificar los resultados obtenidos por las dos metodologías obteniendo una especificidad del 0.94 y una sensibilidad del 0.97, unos valores que son sobresalientes para proceder con la etapa de clasificación.

**PALABRAS CLAVE:** Retinopatía Diabética; Exudados; Microaneurismas, Procesamiento de imágenes; Segmentación

### Corresponding author

TO: Eduardo Bernal Catalán

INSTITUTION: Tecnológico Nacional de México/Instituto  
Tecnológico de Acapulco

ADDRESS: Sauces #13, Col. Los Arcos, C. P. 40188,  
Zumpango del Río, Guerrero, México

E-MAIL: MG18320003@acapulco.tecnm.mx

### Received:

13 November 2020

### Accepted:

1 March 2021

## INTRODUCTION

The analysis of medical images is a recurring process in the medical branch in order to obtain correct results on the detection and location of objects that determine a diagnosis or the course of a treatment to monitor changes obtained by medical methods depending on the disease, the success of a diagnosis depends significantly on the ability of a professional to visualize the object of study.

In the methodology of an artificial vision system, the segmentation stage is carried out in order to locate the objects of interest to determine the existence of any disease or results of surgery or treatment. The digital images obtained from the photographs taken to the fundus of the eye (Retinographies) give the opportunity to search for lesions that obstruct the patient's vision that leads to total loss of sight or even to be able to observe the results of a treatment applied to prevent the damage from expanding and see the positive results of medication or any surgical intervention.

Diabetes mellitus is a major health problem worldwide that is estimated to reach 592 million in 2035 [1]. In different specialized magazines, DR is the most frequent complication of long-term diabetes mellitus [2].

In the “Encuesta Nacional de Enfermedades Crónicas” (ENEC) or The National Survey of Chronic Diseases (NSCD) reports that, in Mexico, diabetes mellitus has been identified as a serious public health problem with alarming numbers that rank from 12 to 14 million people with this disease, of which it stands out that approximately 40% suffer from retinopathy [3].

DR is the third leading cause of irreversible blindness in Mexico and is presented as the main disease in people of productive age between 14 and 64 years in developing countries. The patients with Diabetes Mellitus, 10% have visual limitation and 2% suffer from total and irreversible blindness [4].

This visual complication is becoming more and more frequent among the young population and that brings with it the increase in cases of disability pensions, due to the partial or total loss of the sense of sight that results in a significant economic expense. See figure 1.

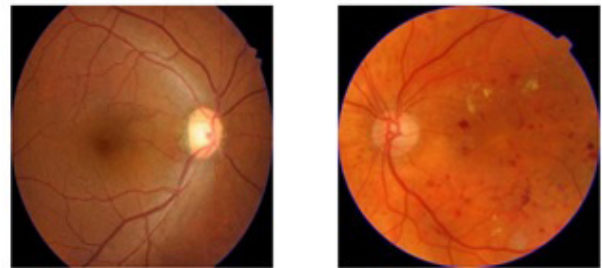


**FIGURE 1. Healthy retina and retina with diabetic retinopathy.**

The lesions that occur with DR vary in size and color; this is a relevant feature that allows classifying one from the other. The present work covers the most common types of lesions that allow early detection of DR: Exudates and Microaneurysms. See figure 2.

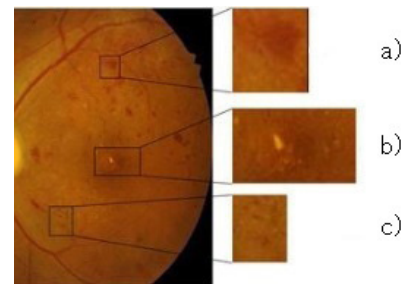


**FIGURE 1. Healthy retina and retina with diabetic retinopathy.**

Computer-aided programs exist for the detection of glaucoma, macular degeneration, and the detection of retinopathy of prematurity; however, the main screening application focuses on the early detection of diabetic retinopathy.

Computer-aided diagnosis is one of the most common and essential tools today, where medical images play an important role in the creation of image processing

techniques. Usman M. Akram <sup>[5]</sup> developed a proposal to detect dark and bright lesions within a retinography, taking these two as the main descriptors of the objects of interest.

As an antecedent, the method proposed by Balazs Harangi and Andras Hajdu <sup>[6]</sup> is taken into consideration, which creates an algorithm divided into 3 stages, which are the extraction of candidates, precise segmentation of contours and labeling of candidates with true or false values, which is based on grayscale morphology that allows to identify the bright regions and then extract the precise limit of the objects presenting a method based on active contours to increase the precision of the segmentation. Then, a regional classifier is applied to eliminate false positives considering the characteristics based on regions and thus obtain the appropriate descriptors to train a Naive-Bayes classifier with which they obtained a sensitivity of 0.92, a specificity of 0.68 and an accuracy of 0.82.

Microaneurysms are a lesion to which several investigations have been assigned for the automatic detection of these, researchers from the University of Guadalajara in conjunction with researchers from the merida technology <sup>[7]</sup> developed a methodology based on the creation of masks that allowed to separate and identify the objects of a digital retinography and using the area size descriptor according to the number of pixels of each object.

There are segmentation algorithms <sup>[8]</sup> in order to identify objects that are not part of the disease, such as blood vessels, since they are present in all retinographies in order to eliminate objects that do not represent an injury to the eye, a semi-automatic method developed to measure and quantify the geometric and topological properties of vascular trees in which 3 stages are proposed: thinning, branching and crossing, where the insertion points are identified to segment the union between them, labelling and storing

a code chain. This method recognizes areas and angles, obtaining geometric data and connectivity information.

There are computer-assisted diagnostic systems such as RISA <sup>[9]</sup> that, using the morphology of the vascular tree, allow the detection of veins and arteries, allowing the rest of the scene to be isolated and separated, leaving only foreign objects on the retina. It is a scalable system that can be nourished by this type of research and more robust methods. RISA transforms a retinography into a binary image, obtaining the objects of interest to obtain information from their characteristics using morphological changes of the images.

The objective of this type of methodologies is to generate the necessary information to carry out training of learning algorithms, if the quality of segmentation and certainty are high, better results are obtained during training.

## MATERIALS AND METHODS

The data set used for the experimentation of the two proposed methodologies is MESSIDOR, which is a database established to facilitate studies on the computer-assisted diagnosis of diabetic retinopathy. The database contains 1200 color images obtained by ophthalmology departments using a non-mydratic TRC NW6 ophthalmoscope with a 45-degree field of view, of which 800 photographs were taken of patients with dilated pupils and 400 without dilatation. The images were captured using 8 bits per color and with the following sizes: 1440x960 pixels, 2240x1488 pixels and 2304x1536 pixels <sup>[10]</sup>. Derived from the variation in sizes, a standard resize is applied to 512x512 to avoid variations in the results.

A methodology is proposed for the detection and extraction of shiny lesions that signify the presence of exudates in the retina, due to the color and intensity of

brightness, these objects can be highlighted over the others to achieve an extraction of the objects in question, the proposed methodology includes by 3 stages: Preprocessing, Exudate extraction and Elimination of false positives (FP).

### a) Preprocessing

Because the retina does not have any type of internal illumination, the little or no illumination can be uniform and with a low contrast, which is why preprocessing is used to highlight and contrast the objects that exist in the scene <sup>[11]</sup>.

The image preprocessing consists of three steps on the original image, in a specific order to enhance the objects and give more probability of success to the next phase, the steps are: Elimination of noise, Extraction of the green channel and Conversion to scale of gray.

Noise is an effect that appears in all existing digital images, it is the random appearance of signals captured by an acquisition device, which do not belong to the original scene <sup>[12]</sup>. It is a very noticeable effect in the images that are taken in places with low luminosity, such as the back of the eye. For this case, the Gaussian smoothing filter was chosen since it is the most effective in eliminating noise in medical images due to the noise inherently generated by the capture sensor due to the low level of illumination and its own temperature, and even more. due to the circuits of the devices that cause their own noise of the electronic circuit and to blur the image in such a way that the gradient of the shiny objects is more uniform and thus distinguish from their soft edge to their hard shape. The Gaussian filter is a low-pass filter whose coefficients are assigned by the Gaussian distribution function <sup>[13]</sup>.

Figure 3 shows the transformation that results when applying the Gaussian filter to an image.

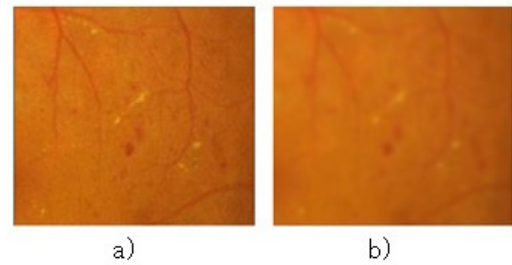


**FIGURE 3. Gaussian Filter a) Original Image b) Noise Elimination.**

One element that serves as a powerful descriptor is color, which greatly simplifies the task of detecting and extracting objects from any scene. The colors that exist in the taking of a scene are the combination of the primary colors Red, Green and Blue in different intensities to cover the great variety of colors of the RGB Model.

With the opinion of Konstantinos Rapantzikos <sup>[14]</sup>, for this methodology it was selected to choose the green channel (G for RGB) because it enhances and contrasts the shiny objects over the image background, facilitating the segmentation of the objects of interest more effectively.

Computer programs use a simple method of converting a color image to grayscale. An addition of the three RGB channels is made to obtain a single shade of gray taking different percentages of intensity of each one, for Red use 30%, Green 59% and Blue 11%, which, according to expert studies, this it is the closest way in which the human eye captures the intensity of light according to its color <sup>[15]</sup>.

The function for the conversion to grayscale from the RGB color model is a mathematical expression that is applied to each one of the pixels of the image to obtain a new gray palette with different ranges of clarity. The equation 1, is as follows:

$$Y = R * 0.3 + G * 0.59 + B * 0.11 \quad (1)$$

Finally, the result of the preprocessing is shown in Figure 4, with each of its steps so that the details of the shiny objects are highlighted and the stage of obtaining characteristics can be advanced.

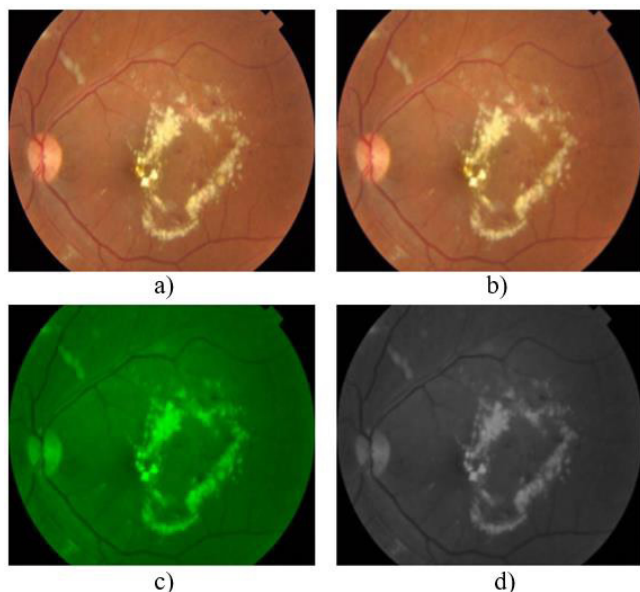


**FIGURE 4. Preprocessing Steps. a) Original image, b) Noise removal, c) Green channel extraction, d) Grayscale conversion.**

### **b) Extraction of exudates**

In this second stage, the processes that lead to the identification of the shiny objects that are of interest are proposed, for this, two steps are used, which are Calculation of the histogram and Binarization to obtain all the potential candidates for shiny lesions (Exudates).

Histograms are one of the most important techniques applied for representation and management of information in a digital image and is relevant for the enhancement or segmentation tasks. There is a wide variety of software that performs this function and due to its low consumption of resources and speed it has made it essential in real-time processing tasks [16].

The group of biomedical engineers from the University of Valladolid [17] propose the use of the histogram to identify exudates in retinographies after normalizing

the image to a gray scale where the exudates are transformed into objects with high gray intensities, using the average quantity of 200 pixels to identify lesions with greater intensity, the disadvantage of a fixed value is that they depend on external lighting and the ophthalmoscope focus may not perceive exudates that are captured with little lighting detail, even ignoring those that are find a recent appearance on the retina.

The resulting statistics from the histogram calculation is a graph with two axes (horizontal and vertical) in which the horizontal axis represents the gray levels that can be found in a left grayscale image where the darkest value is black at right where the maximum value is white. The rest of the clarity levels are uniformly distributed according to the number of pixels that contain the same level of gray and that set of pixels of the same tone corresponds to some object in the image.

In Figure 5 the graph that results from the grayscale image obtained in the preprocessing stage is shown in which a range of pixels that tend more to a light color is chosen because the lesions we are looking for are bright and clear.

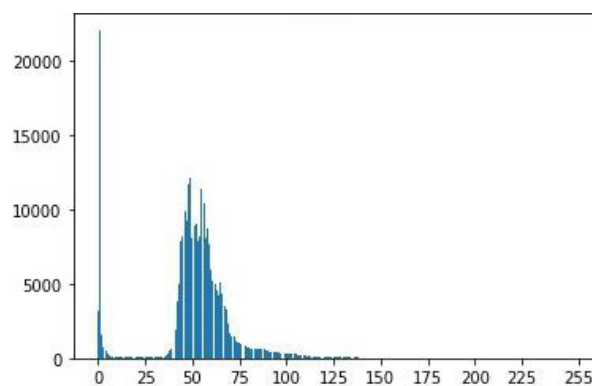


**FIGURE 5. Histogram.**

Binarization is one of the most basic techniques of segmentation [18] with which the background of an image and the different objects that constitute it are divided. Binarization selects the pixels that have a

specific value that is interpreted from the histogram calculation and thus be able to identify the objects in the image according to their brightness.

### c) Elimination of false positives

Due to the similarity of brightness intensity between the exudates and the optic disc (OD), it can become confusing at the time of binarization, therefore, after performing the feature extraction stage, the OD is previously removed identified. In figure 6 the result of the extraction step is observed, and the elimination of false positives is carried out.

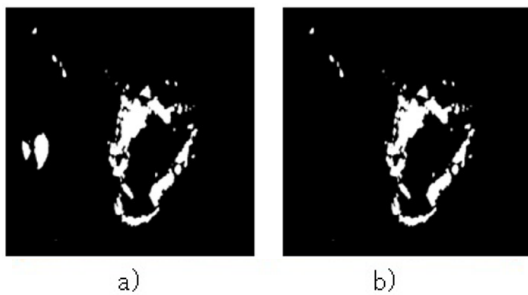


**FIGURE 6. Elimination of false positives.**  
a) Binarization, b) Elimination of OD.

Hard and soft exudates were uniformly detected, looking for the particularity of being shiny objects and thus facilitating their detection. In Figure 7 are shown examples of original retinographies, detection of exudates in binary image and the superposition of the images as a sample of the results obtained.

The proposed methodology for the detection and extraction of microaneurysm lesions by means of digital retinographies has three stages to carry out the detection of the objects that interest us: Preprocessing, Microaneurysm extraction and Elimination of FP.

### a) Preprocessing

Due to the contrast and great variety of red tones in the images, this stage is of great importance to be able to carry out the detection of microaneurysms and discuss.

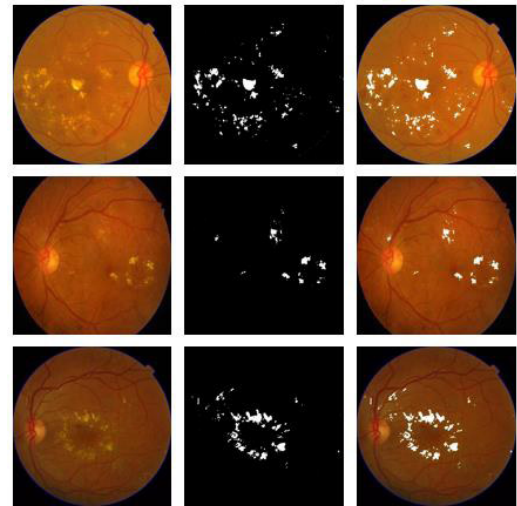


**FIGURE 7. Detection of exudates.**

The LAB color model [19] is a system that measures the three colors of RGB light in the context of specific lighting, combining lighting, color and reflective surface. Each LAB acronym includes a spatial axis in which L is light in a range from white to black, A occupies the colors between green and red, and B for the colors that are between blue and yellow [20].

After obtaining the Luminosity channel of the LAB model, an inverse or negative operator is applied that creates an inverse image from the LAB input image, being of great help in the medical field since it optimally contrasts inconspicuous objects. The transformation function is given by equation 2.

$$(i,j) = 255 - (i) \quad (2)$$

A median filter is applied to the resulting image to remove noise. Finally, an enhanced edge enhancement is made to highlight the changes in image intensities and to be able to detect the location of the lesions more accurately. In Figure 8 the result of each step and end of the preprocessing stage is shown.

The detection of microaneurysms has been studied for a long time since it is the main lesion that, if detected in time, would allow a rapid medical response

to start with the pertinent treatment that can prevent vision loss. Various articles develop different types of methods for their localization, some use mathematical morphology [21] [22], some others opt for an analysis based on the characteristics of the lesions [17] [24] size, perimeter, intensity, etc. And other methods based on eigenvalues.

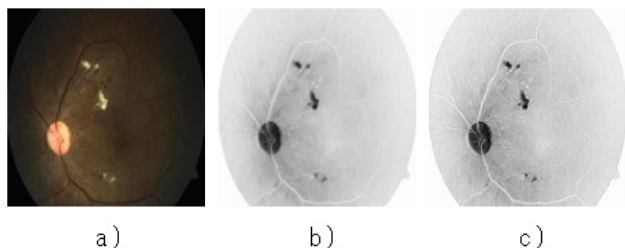


**FIGURE 8. Preprocessing stage.**

**a) Original image, b) Inverted L, c) Noise removal and increased edge enhancement.**

The purpose of these steps is to normalize the contrast of the image to have a greater range of success in the detection of microaneurysms, a suggestion proposed by Alan D. Fleming [23].

### **b) Extraction of microaneurysm**

Based on the method proposed by J. H. Hipwell [24], the elimination of background variations is of great importance to highlight the characteristics of small round objects and classify them based on their size and intensity.

After applying an increased edge enhancement in the preprocessing stage, it is helpful at the beginning of the extraction stage as applying the Canny edge detection algorithm greatly improves the detection of the contours of objects of interest in the field.

The next process consists of filling in the identified contours and subtracting the image resulting from the Canny algorithm to eliminate the edges, leaving only a binary image with the detected lesions as shown in Figure 9.

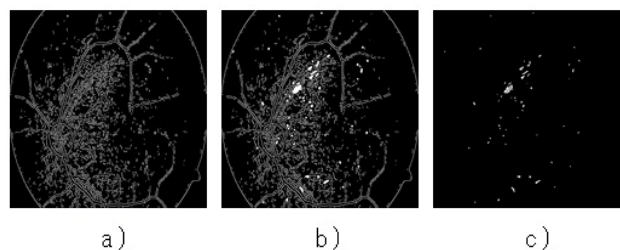


**FIGURE 9. Object extraction. a) Edge detection, b) Contour fill, b) Lesions detected.**

### **c) Elimination of false positives**

The similarity of shapes between lesions can cause the detection of objects that are not microaneurysms, even the OD can become confused and appear in the final binary image to eliminate FP of this type, a function is carried out that detects the size in pixels of the detected objects, in this case retinographies of a size of 512x512 were used and the established value was no greater than 20 and the objects of greater size are eliminated.

In some cases, it was possible to identify hard exudates that coincided with the size and shape of the microaneurysms, for the elimination of these FP the first mentioned methodology was applied and with the two final images of the methodologies a subtraction of the exudates was applied to the resulting from the microaneurysms that eliminated the shiny lesions.

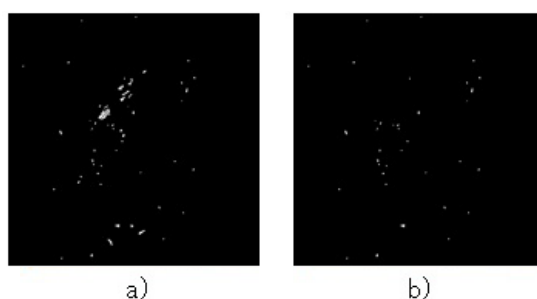


**FIGURE 10. Results of the methodology. a) Detected objects, b) Elimination of false positives**

### **d) Microaneurysm detection results**

The detection of microaneurysms was based on the shape of the objects, locating their edges by changing the intensities of the gray levels.

The algorithm was conceived for automatic execution, speeding up the obtaining of results from several images in a reduced time. Through the support of a specialist ophthalmologist, he verified the result of the methodology and resolved a general precision value of 0.92, number that was obtained from the division of the correct detections and the total of images processed.

In Figure 11 the result is shown, compared to the original image.

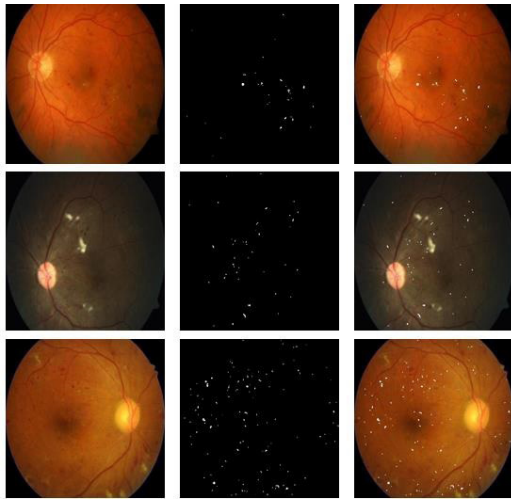


FIGURE 11. Detection of microaneurysms.

## RESULTS AND DISCUSSION

For the evaluation of both lesion segmentation methodologies, a confusion matrix is made as shown in Table 1, to calculate the specificity and sensitivity of said detection algorithms and thus verify their efficacy against healthy and diseased retinographies.

**True Positives (TP):** It is the type of result that indicates when the algorithm has detected a lesion in a retinography where it is known that the lesion exists.

**False Positives (FP):** It is the type of result that indicates when the algorithm has detected a lesion in a retinography where it is known that the lesion does not exist.

**True Negatives (TN):** It is the type of result that indicates when the algorithm has not detected a lesion in a retinography in which it is known that there is no lesion.

**False Negatives (FN):** It is the type of result that indicates when the algorithm has not detected any lesion in a retinography in which it is known that there is any injury.

TABLE 1. Confusion matrix

	WITH LESION	NO LESIÓN	TOTAL
POSITIVE DETECTION	TP = 237	FP = 12	249
NEGATIVE DETECTION	FN = 6	TN = 189	195
TOTAL	243	201	444

Specificity indicates the efficiency of the algorithm to detect cases that are negative, and its formula is as follows:

$$E = \frac{TN}{TN + FP}$$

Interpreting the specificity formula with the data from the confusion matrix we obtain that  $E = 189 / (189 + 12)$  gives a result of **0.94**.

To calculate the sensitivity to obtain the efficiency of the algorithms when correctly detecting the lesions as positive, the formula is the following:

$$S = \frac{TP}{TP + FN}$$

Where applying the results of the confusion matrix gives us the operation of  $S = 237 / (237 + 6)$ , and we obtain a sensitivity level of **0.975**.

## CONCLUSIONS

This article proposes two methodologies for the arrest of two types of lesions in the fundus of the eye from retinographies taken by an ophthalmoscope at low cost, making use of free use technologies. These processes, divided into 3 stages, are part of the development of an artificial vision system for the early detection of diabetic retinopathy to support ophthalmologists for the primary detection of the disease and to be able to treat and prevent loss of sight.

The principle of each methodology consists of enhancing the details and characteristics of the objects of interest from a first pre-processing stage to facilitate the extraction of lesions and eliminate false positives and perform the correct segmentation of the lesions.

For the detection of exudates, one of the main steps was the choice of the green channel of the RGB color model that enhances the bright objects in the scene to facilitate the localization of lesions using the data provided by the histogram and thus find the ideal threshold to terminate the binarized and segmented image. On the other hand, in the methodology for the detection of microaneurysms, the enhancement of the image edges in the preprocessing stage and its smoothing was prioritized to improve the efficiency of the Canny edge detection algorithm, which serves as the main detector of lesions and then apply the filling of the detected contours that results in the microaneurysms.

The running time of the microaneurysm detection algorithm is 0.10504865400000085 seconds per image of a size of 512x512 on a computer with a 7th generation Intel Core i7 processor, with 16 GB of RAM and solid-state disk for higher speed of writing, while the exudate algorithm was not measured because the threshold in each image varies and an average value does not give the desired results when generated automatically and they are processed individually to obtain optimal results.

Although the techniques used in both methodologies are basic, they have shown good results and a low consumption of resources, being able to execute them on computers with basic characteristics.

The results of both methodologies demonstrate a better performance than that of previously published research <sup>[6]</sup> <sup>[7]</sup> comparing specificity and sensitivity, taking specificity as the most important value when checking the efficiency of the algorithm, being able to quantify the capacity to correctly identify negative cases. Other objects that can be found in the retina such as blood vessels, optic disc, macula, and haemorrhages must be detected to proceed to the training stage to classify them by normal and abnormal objects and be successful in the stage of classification that several authors recommend the creation of a vector support machine. This article is part of a series of documents published on each stage of development of a complete machine vision system.

## AUTHOR CONTRIBUTIONS

E.B.C. contributed to the development and programming of the algorithms for the proposed methodologies. E.C.G. contributed to obtain quantitative results (sensitivity and specificity) of the used methodologies. J.A.M.V. analyzed the image processing algorithm. R.H.R. developed a state-of-the-art bibliographical search. J.L.H.H. contributed to processing image analysis.

## ACKNOWLEDGMENTS

Authors are grateful to the National Technological Institute of Mexico/Technological Institute of Acapulco, for supporting this work.

## CONFLICTS OF INTEREST

The authors declare no conflicts of interest. The funders had no role in the design of the study; in the collection, analyses, or interpretation of data; in the writing of the manuscript, or in the decision to publish the results.

## REFERENCES

- [1] Basto-Abreu A, Barrientos-Gutiérrez T, Rojas Martínez R, et al. Prevalencia de diabetes y descontrol glucémico en México: resultados de la Ensanut 2016. *Salud Publica Mex* [Internet]. 2020;62(1):50-59. Available from: <https://doi.org/10.21149/10752>
- [2] Martínez Rubio M, Moya Moya M, Bellot Bernabé A, et al. Cribado de retinopatía diabética y teleoftalmología. *Arch Soc Esp Oftalmol* [Internet]. 2012;87(12):392-395. Available from: <http://dx.doi.org/10.1016/j.oftal.2012.04.004>
- [3] Instituto Nacional de Salud Pública. Encuesta Nacional de Salud y Nutrición de Medio Camino 2016 [Internet]. Secretaría de Salud; 2016. Available from: <https://ensanut.insp.mx/encuestas/ensanut2016/informes.php>
- [4] Federación Mexicana de Diabetes A. C. Retinopatía diabética [Internet]. Federación Mexicana de Diabetes A. C; 2017. Available: <http://fmd diabetes.org/retinopatia-diabetica-estadisticas>
- [5] Akram UM, Khan SA. Automated Detection of Dark and Bright Lesions in Retinal Images for Early Detection of Diabetic Retinopathy. *J Med Syst* [Internet]. 2012;36(5):3151-3162. Available from: <https://doi.org/10.1007/s10916-011-9802-2>
- [6] Harangi B, Hajdu A. Automatic exudate detection by fusing multiple active contours and regionwise classification. *Comput Biol Med* [Internet]. 2014;54(1):156-171. Available from: <https://doi.org/10.1016/j.compbiomed.2014.09.001>
- [7] Norma RH, Janet MP, Miguel MU, et al. Detección de microaneurismas en la retina. XXXVIII Congreso Nacional de Ingeniería Biomédica. Ingeniería Biomédica. Mazatlán: SOMIB; 2015;92-95.
- [8] Martinez-Perez ME, Highes AD, Stanton, AV, et al. Retinal vascular tree morphology: A Semi-Automatic Quantification. *IEEE Trans Biomed Eng* [Internet]. 2002;49(8):912-917. Available from: <https://doi.org/10.1109/tbme.2002.800789>
- [9] Gelman R, Martínez Pérez ME, Vanderveen DK, et al. Diagnosis of Plus Disease in Retinopathy of Prematurity Using Retinal Image multiScale Analysis. *Investig Ophthalmol Vis Sci* [Internet]. 2005;46(12):4734-4738. Available from: <https://doi.org/10.1167/iovs.05-0646>
- [10] Decencièrre E, Zhang X, Cazuguel G, et al. FEEDBACK ON A PUBLICLY DISTRIBUTED IMAGE DATABASE: THE MESSIDOR DATABASE. *Image Anal Stereol* [Internet]. 2014;33(3):231-234. Available from: <https://doi.org/10.5566/ias.1155>
- [11] Uribe Valencia LJ. Detección automática de exudados en imágenes a color del fondo del ojo para el pre-diagnóstico de la retinopatía diabética [master's thesis]. [Tonantzintla]: Instituto Nacional de Astrofísica, Óptica y Electrónica, 2014. 99p. Spanish.
- [12] Flores Mamani O. Sistema de diagnóstico de la retinopatía diabética mediante imágenes digitales [dissertation]. [Ciudad de la Paz]: Universidad Mayor de San Andrés, 2014. 108p. Spanish.
- [13] Vivanco LMQ, Sánchez FH, Marañoón DCE. Optimización de los filtros mediana-gaussiano para una mejor convergencia del snake en la segmentación de imágenes médicas. In: XV Convención y Feria Internacional Informática 2013 - I Congreso Integracionista de las Ciencias y las Tecnologías Informáticas. La Habana: Ministerio de Informática y Comunicaciones; 2013. Spanish.
- [14] Rapantzikos K, Zervakis M, Balas, K. Detection and segmentation of drusen deposits on human retina: Potential in the diagnosis of age-related macular degeneration. *Med Image Anal* [Internet]. 2003;7(1):95-108. Available from: [https://doi.org/10.1016/s1361-8415\(02\)00093-2](https://doi.org/10.1016/s1361-8415(02)00093-2)
- [15] Flores Eraña JG. Síntesis digital de color utilizando tonos de gris [master's thesis]. [San Luis Potosí]: Universidad Autónoma de San Luis Potosí, 2009. 49p. Spanish.
- [16] Sepulveda Giraldo A. Procesamiento de imágenes por medio de filtros acusto-ópticos [master's thesis]. [Pereira]: Universidad Tecnológica de Pereira, 2007. 80p.
- [17] García M, Sánchez, CI, Poza J, et al. Detection of Hard Exudates in Retinal Images Using a Radial Basis Function Classifier. *Ann Biomed Eng* [Internet]. 2009;37(7):1448-1463. Available from: <https://doi.org/10.1007/s10439-009-9707-0>
- [18] La Serna Palomino S, Román Concha UN. Técnicas de segmentación en procesamiento digital de imágenes. *RISI* [Internet]. 2009;6(2):9-16. Available from: <https://revistasinvestigacion.unmsm.edu.pe/index.php/sistem/article/view/3299>
- [19] Schwarz MW, Cowan WB, Beatty JC. An experimental comparison of RGB, YIQ, LAB, HSV, and opponent color models. *ACM Trans Graph* [Internet]. 1987;6(2):123-158. Available from: <https://doi.org/10.1145/31336.31338>
- [20] Mokrzycki WS, Tatol M. Perceptual difference in Lab Colour space as the base for object colour identification. In: Burduk R, Kurzynski M, Wozniak M, Zolnierek A (eds). *Computer Recognition Systems 4* [Internet]. Berlin: Springer-Verlag Berlin Heidelberg; 2009. Available from: <https://doi.org/10.13140/2.1.3650.5927>
- [21] Wisaeng K, Sa-Ngiamvibool W. Exudates Detection Using Morphology Mean Shift Algorithm in Retinal Images. *IEEE Access* [Internet]. 2019;7:11946-11958. Available from: <https://doi.org/10.1109/ACCESS.2018.2890426>
- [22] Akter, M, Uddin MS, Khan MH. Morphology-Based Exudates Detection from Color Fundus Images in Diabetic Retinopathy. In 2014 International Conference on Electrical Engineering and Information & Communication Technology [Internet]. Dhaka: IEEE; 2014:1-4. Available from: <https://doi.org/10.1109/ICEEICT.2014.6919124>
- [23] Fleming AD, Philip S, Goatman KA, et al. Automated microaneurysm detection using local contrast normalization and local vessel detection. *IEEE Trans Med Imag* [Internet]. 2006;25(9):1223-1232. Available from: <https://doi.org/10.1109/TMI.2006.879953>
- [24] Hipwell JH, Strachan F, Olson JA, et al. Automated detection of microaneurysms in digital red-free photographs: a diabetic retinopathy screening tool. *Diabet Med* [Internet]. 2000;17(8):588-594. Available from: <https://doi.org/10.1046/j.1464-5491.2000.00338.x>

[dx.doi.org/10.17488/RMIB.42.2.7](https://dx.doi.org/10.17488/RMIB.42.2.7)

E-LOCATION ID: 1140

## Feature Extraction from Distributions of Phase Synchronization Values of EEG Recordings

J. A. Quirarte-Tejeda<sup>1</sup>, J. L. Flores<sup>1</sup>, R. Romo-Vázquez<sup>2</sup>

<sup>1</sup>Departamento de Electrónica, CUCEI, Universidad de Guadalajara

<sup>2</sup>Departamento de Ciencias Computacionales, CUCEI, Universidad de Guadalajara

### ABSTRACT

Epilepsy is the most common neurological pathology. Despite treatments available to patients, only 58% to 73% will be free of seizures. This uncertainty in treatment outcomes can lead to other psychiatric affectations in cases where treatment success may be in doubt. Seizure prediction models (SPMs) emerged as a measure to help determine when patients may be susceptible to an imminent crisis. These models are based on the continuous monitoring of patient's EEG signals and subsequent continuous analysis to identify features that differentiate ictal from interictal states. This is an ongoing field of research whose aim is to establish a robust set of features to feed the SPM and obtain a high degree of certainty regarding when the next seizure will occur. In this work we propose the analysis of phase differences of EEG as a method to extract features capable of discriminating ictal and preictal states in patients; specifically, the numeric distance between Q1 and Q3 of the distribution of phase differences. We compared this values to other phase synchronization methods and tested our hypothesis getting a  $p < 0.0009$  with our proposed method.

**KEYWORDS:** Epilepsy; Phase analysis; Synchronization; Phase differences

### Corresponding author

TO: Rebeca del Carmen Romo Vázquez

INSTITUTION: Universidad de Guadalajara

ADDRESS: Blvd. Gral. Marcelino García Barragán #1421,

Col. Olímpica, C. P. 44430, Guadalajara, Jalisco, México

E-MAIL: [rebeca.romo@academicos.udg.mx](mailto:rebeca.romo@academicos.udg.mx)

### Received:

2 December 2020

### Accepted:

11 March 2021

## INTRODUCTION

Epilepsy is the most common neurological disorder, affecting around 30 million people worldwide <sup>[1]</sup>. At a neurological level, epilepsy manifests itself as electrical discharges in neuron populations, that can produce muscular contractions and loss of consciousness <sup>[2] [3] [4] [5] [6]</sup>. These disorders affect the daily life of patients and impedes them from performing certain tasks at work, driving, and swimming when unsupervised; hence, the interest in researching new ways to diagnose and treat epilepsy.

Current treatments for epilepsy involve drugs that can reduce the incidence and/or intensity of seizures up to a 70% of patients. For the remaining 30%, who have drug-resistant epilepsy, other treatments are being tested. Of these, brain surgery has been the most successful <sup>[4]</sup>. Brain surgery, however, is not a viable treatment in all cases, and even when performed, only 58% to 73% of patients will be free of impairing seizures <sup>[7] [8]</sup>.

Despite the ratio of success of surgical procedures and drug treatments, patients who suffer impairing epileptic seizures are also prone to suffering other psychiatric affections, such as anxiety and depression <sup>[7] [8]</sup>, both caused by the uncertainty as to when the next seizure will occur. The unpredictable nature of epilepsy and the lack of understanding of how *epileptogenic* conditions emerge in the brain, have led to the development of several techniques for estimating the beginning or *onset* of an epileptic seizure <sup>[8]</sup>. The aim is to understand the conditions that lead to seizures and use this information in seizure prediction models in order to prevent the *onset* of epileptic crises in patients.

Most seizure prediction models (SPMs) are based on the analyses of recorded electroencephalographic signals (EEG), a common diagnostic procedure. SPMs derived from analyses of EEG signals are constrained to physiological and mathematical assumptions <sup>[9]</sup>: the former holds that changes in brain activity and its

associated electrical signals appear before seizures and can be acquired by EEG, while the mathematical assumption refers to a commonly implicit, but not well understood, statistical relationship between past and future observations of the EEG signals. These two assumptions lead to consider that is possible to predict seizures based on EEG recordings <sup>[9]</sup>.

In general, SPMs based on EEG signal processing, consist of three stages <sup>[10, 11]</sup>: preprocessing the EEG signals, extracting features from them, and classifying of brain electrical activity. One current challenge in this approach is to successfully discriminate the different epileptic seizure stages such as *interictal*, *pre-ictal*, *ictal* and *post-ictal* stages <sup>[9] [10] [11] [12] [13] [14]</sup>.

Depending on the method used in feature extraction, SPMs can be classified as: time-frequency methods, nonlinear measures, or statistical parameters of the signals <sup>[8] [10] [14]</sup>. Most of the time-frequency methods -e.g. as spectral power and connectivity- only function under certain limitations related to a limited temporal resolution. Additionally they assume linear interactions of the signals and disregard non-stationary properties <sup>[15]</sup>. Nonlinear methods are preferred since it is assumed that they preserve the nonlinear nature of EEG signals <sup>[10]</sup> which is closer to their real behavior <sup>[16]</sup>.

Phase synchronization analysis of EEG signals is now a promising approach for understanding brain dynamics because it has shown that some changes occur in the synchronization and connectivity of brain networks during seizures <sup>[17]</sup>. The premise is that different areas of the brain may come to be connected between each other during an epileptic seizure <sup>[6]</sup>; that is. two distinct brain regions with oscillatory electrical activity will show phase synchronization though they are not anatomically adjacent. This phenomenon is known as *functional connectivity*. It has been widely reported that *functional connectivity* can be affected by brain pathologies, such as epilepsy <sup>[21]</sup>.

In the past decade, synchronization indexes have been used in epilepsy analyses during *preictal/ictal* stages, Haitao *et al.* for example, showed that synchronization between distant areas of the brain increases in epileptic patients [18]. While Alaei *et al.* [19] proposed the mean phase coherence index as a feature to determine the preictal stage in patients, and Detti *et al.* [12] proposed an SPM whose features, obtained from synchronization measurements in ictal and preictal stages, was able to predict the *onset* of seizures with high accuracy. These features were obtained by analyzing phase synchronization between each pair of EEG channels and selecting the most appropriate pair by inspection.

In this work, we propose the instantaneous phase difference index (PDI) as an alternative approach for analyzing EEG signals to discriminate the *preictal/post ictal* and ictal stages. To this end we compared the performance of our index against *Phase Locking Value* (PLV), *Phase Lag Index* (PLI) and *Phase Linearity Measurements* (PLM) in two EEG databases and applied a Kruskal-Wallis test based on characteristics of their phase differences or synchronization value distributions in each epileptic stage.

## MATERIALS AND METHODS

### Databases

In this work we analyzed two databases. The first consists of EEG recordings and the second of intracranial EEG recordings (iEEG).

#### Database 1

These EEG signals were obtained from Zenodo “A dataset of neonatal EEG recordings with seizure annotations” [20]. This dataset contains 79 recordings of neonates acquired by a clinical team due to suspicions of seizure activity. The EEG recordings have an average recording time of 74 min, and were recorded with a NicOne EEG amplifier using a sample frequency of

256Hz, with 19 electrodes positioned according to the 10-20 International System with referential montage. Two additional channels were included in the recording, which contain ECG and respiratory signals from the patients. Three experts (identified as A, B and C) were asked to individually annotate seizures with a clear *onset* of abnormal electrical activity. Seizures were defined by a duration of over 10 seconds

Of the 79 initial recordings of patients in database 1, 29 were chosen for further analysis because they showed lateralized epileptic seizure annotations. However, based on the criterion that at least two of the experts had to agree on the starting times, only 20 seizure events were chosen.

A window containing 15 seconds before and 15 seconds after the starting time of the seizure was cropped from the original recording and preprocessed for further analysis.

#### Database 2

Database 2 consists of iEEG signals, obtained from the “American Epilepsy Society Seizure Prediction Challenge”. It contains a variable number of interictal/ ictal test samples of one second iEEG recordings for each subject. For our work only the first 20 interictal samples and the first 20 ictal samples per subject were chosen for further analysis. The number of channels also varied from subject-to-subject, but all channels available from each subject were used in the subsequent analysis.

### Methods

Phase synchrony metrics has been proposed as a way to estimate the degrees of functional connectivity [2]. Most of the approaches proposed to analyze connectivity are based on the frequency domain and operate under certain assumptions such as: stationary signals and limited temporal resolution. These techniques also assume linear behavior and interactions between

signals [15]. But these considerations are not always consistent with the real behavior and properties of EEG signals.

We consider EEG to be the result of nonlinear dynamic processes in the brain, and seizure events as a non-stationary process [16] that may be evidenced by changes in phase synchrony indexes before and after the *onset*.

### Phase Locking Value (PLV)

In literature, several phase-based indexes have been proposed, one of which is the *Phase Locking Value* (PLV), proposed in [15]. PLV was the first synchronization index approach to determine the synchronization between two signals in terms of their phase,  $\varphi_1$  and  $\varphi_2$  as:

$$PLV = \frac{1}{N} \sum_1^N e^{j(\Delta\varphi)} \quad (1)$$

where  $\Delta_\varphi$  is the phase difference between two signals whose synchronization is being estimated.

In this sense, PLV has a range of 0-1, where 0 corresponds to no synchrony and 1 represents total synchrony between signals. Lachaux *et al.* introduced the  $N$  term in order to test the synchrony of both signals against  $N$  trials, expecting a reduction of spontaneous synchronization.

### Phase Lag Index (PLI)

Another approach to determining the synchrony between two signals is the *Phase Lag Index*, (PLI), proposed in [22]. In this case, synchrony is analyzed in terms of phase difference,  $\Delta_\varphi$ , as

$$PLI = |\langle \text{sign}[\Delta_\varphi] \rangle| \quad (2)$$

where  $\text{sign}[]$  is the sign function and  $\langle \cdot \rangle$  is the mean operator. PLI returns an index of synchronization in a range of 0-1. A PLI index equal to 1, means that the

phase difference between two signals modulus  $\pi$  is equal to zero, i. e. both signals contain information from the same brain source, and this value does not represent true synchronization.

### Phase Linearity Measurement (PLM)

A third method is *Phase Linearity Measurement* (PLM), proposed by Baseline *et al.* [23]. PLM analyzes phase differences as a function of time in narrow frequency bands, from  $-B$  to  $B$ , that can be determined as

$$PLM = \frac{\int_{-B}^B \left| \int_0^T e^{j(\Delta\varphi(t))} e^{-j2\pi ft} dt \right|^2 df}{\int_{-\infty}^{\infty} \left| \int_0^T e^{j(\Delta\varphi(t))} e^{-j2\pi ft} dt \right|^2 df} \quad (3)$$

This approach introduces a first order model phase differences that is dependent on the instantaneous frequency of the signal, instead of a constant one, as in the PLV and PLM indexes.

### Phase Difference Index (PDI)

From Equations (1), (2), and (3) we can observe that the PLV, PLI and PLM indexes are surjective functions over the  $\Delta_\varphi$  set. However, the use of surjective functions does not preserve the full relationships between the elements of the set applied to, resulting in information loss.

Phase difference  $\Delta_\varphi$  is a discrete variable, with values in a range of  $\pi$  to  $-\pi$ , whereas the PLV, PLI and PLM functions all have a range of 0-1. This limited range also results in information loss that can be demonstrated by calculating the probability of any outcome  $\delta_1$  for the  $\Delta_\varphi$  and the probability of the outcome  $x_1$  for any variable  $X$  in a range from 0-1; thus  $P(\delta_1) < P(x_1)$ . Through Shannon's entropy definition [24], we can show that:

$$P(\delta_1) < P(x_1) \quad (4)$$

so variable  $\Delta_\varphi$  has greater entropy than  $X$ .

This difference in entropy from  $\Delta_\varphi$  to  $X$  led us to consider that this reduced range of the codomain of the PLV, PLI and PLM functions might be hiding part of the chaotic behavior of the EEG recordings. Hence, to avoid surjective functions we propose the *Phase Difference Index (PDI)*, as an adequate means of analyzing the phase synchronization of EEG signals:

$$PDI = \frac{\varphi_1 - \varphi_2}{k} \quad (5)$$

where  $\varphi_1$  and  $\varphi_2$  are two phase vectors of  $k$  length.

The use of phase differences to analyze EEG scalp signals could lead to the detection of spurious phenomena caused mainly by volume conduction [22] [23]. In order to test whether this phenomenon affects the ability of phase differences to discriminate preictal/ ictal signals, we calculated the phase differences: PLV, PLI and PLM indexes for database 2, which consists of intracranial EEG recordings (iEEG), where volume conduction effects are not present.

Figure 1 depicts a block diagram of proposed algorithms, where we can see the different stages in the processing of EEG signals.

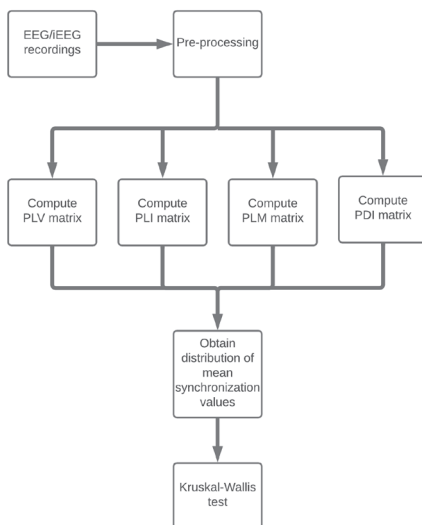


FIGURE 1. Data processing scheme.

## Database pre-processing

In both databases a band-pass filter was applied with a bandwidth of 4Hz-6Hz (i. e. *theta* range). Specifically, we applied a zero phase FIR filter of 20th order, due zero padding and floating-point values of the FIR filter which results in non-zero DC gain. In this way, the DC component in the filtered signals was removed. Additionally, since the EEG signals in database 2 had a sampling frequency of 500Hz to 5000Hz, all recordings were downsampled to 500Hz.

## Instantaneous phase calculation

As our aim was to obtain phase values from each sample of the signal, we considered each recording as an array of  $N$  signals obtained from electrodes placed on the brain according to the 10-20 International System.

In order to retrieve the instantaneous phase for each EEG signals ( $s(k)_n$  for  $n = 1,2...N$ ), we constructed an analytic signal as

$$x_n(k) = s_n(k) + j\hat{s}_n(k) \quad (6)$$

where  $\hat{s}_n(k)$  is the *Hilbert Transform* of  $s_n(k)$ . From the Eq. (6) we can retrieve the phase value  $\varphi(k)$  for each EEG sequence as

$$\varphi_n(k) = \arctan \frac{\hat{s}_n(k)}{s_n(k)} \quad (7)$$

For each phase vector  $\varphi_n(k)$  obtained from the EEG signal, we can compute the degree of phase synchronization between these EEG signals. PLV, PLI, PLM and PDI were calculated using a window of half-second or 128 samples, sliding one sample at a time. The size of the window was selected as a trade-off between the capacity to observe brain network reorganization on the sub-second time scale, as reported in [25] and to detect synchronization on the second-scale, as described in [15] [16] [17] [18] [19] [20] [21] [22].

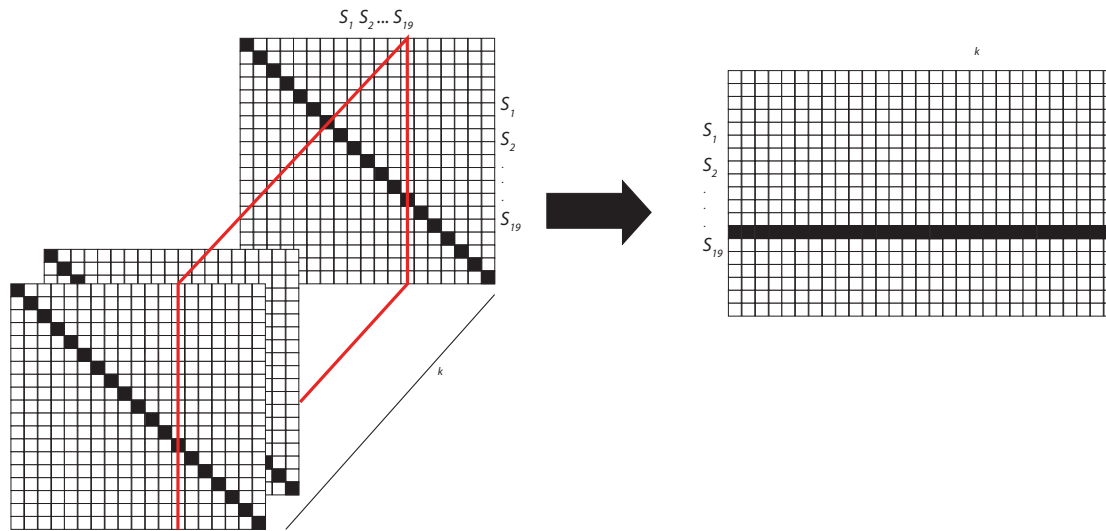


**FIGURE 2. Synchronization/phase difference matrix structure. The red slice can be extracted to visualize changes in synchronization/phase differences over time.**

### Synchronization and phase difference matrices

For database 1, the synchronization values for PLV, PLI, PLM and PDI were obtained from  $s(k)_n$  for  $k = 0$  and stored in a  $19 \times 19$  matrix. Each cell corresponds to a possible combination of the  $n$  available channels. Since Eqs. (1), (2) and (3) do not preserve the sign of the phase difference, therefore PLV, PLI and PLM are commutative between a pair of signals. As a result, the synchronization matrix will be symmetrical, with the main diagonal representing the synchronization of a given signal with itself. The diagonal of the PDI matrix will have a value of zero since it corresponds to the difference between signals from the same source. The same procedure was applied to the next sample of each sequence  $s(k)_n$  for  $k = 1$  and the resulting new  $19 \times 19$  matrix was stacked behind the previous one until the sliding window reached the last sample  $s(k)_n$  for  $k = 7554$ . This resulted in a 3D matrix with  $19 \times 19 \times 7554$  elements for each synchronization index PLV, PLI, PLM and PDI for each seizure event selected from database 1.

The matrices obtained can be used to show how synchronization or phase differences change over time when sliced them along the  $k$  dimension, see Figure 2.

The column index from which the slice is extracted defines the reference signal to determine the temporal evolution of the synchronization or phase difference, respectively.

Since each matrix contains information pre- and post- seizure onset, the onset information will be in the center, along the  $k$  length, as Figure 2 shows. We can split each matrix in two along the  $k$  length to separate the information from preictal to ictal stages (see Figure 3).

For the database 2 recordings, the data processed by means of PLV, PLI, PLM and PDI were stored in matrices with the same structure as before. The only difference was in their dimensions, since each of the subjects' recordings had distinct number of available channels.

### Distributions of synchrony/phase difference values

Each matrix has dimension  $N \times N \times k$ , to analyze how the synchrony indexes and phase difference change as a function of time during the different epilepsy stages, we took a  $N \times N$  matrix along the  $k$  dimension and gen-

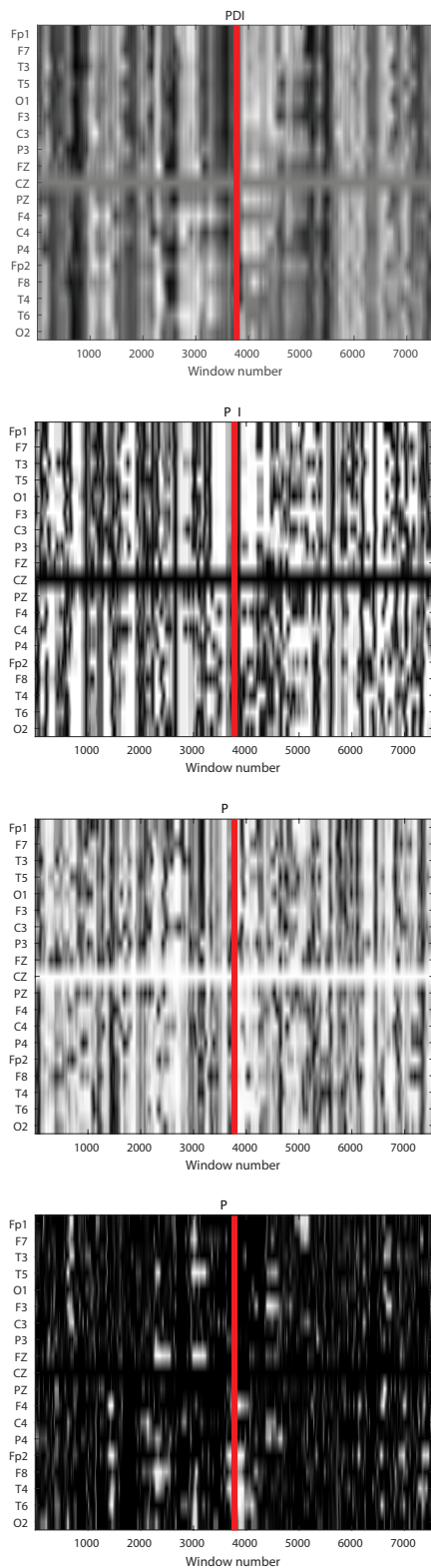


**FIGURE 3. Grayscale map of slices along the Cz channel of the PDI, PLV, PLI and PLM matrices. A darker shade indicates a lower synchronization level. The line indicates the onset of the seizure.**

erated a vector of length  $N$  with the average synchrony or phase difference values of each channel. The first element of the vector corresponds to the average value of the channel 1 in the first  $N \times N$  matrix. We then proceeded to the following  $N \times N$  matrices until reaching the last one. At the end we obtained  $k$  number of vectors of  $N$  length. Finally, we plotted the histogram of values of all the resulting vectors and then repeated the process with all the matrices.

Given that the *ictal* matrices were separated from the *preictal/interictal* ones, we displayed the histograms from between the *ictal* and *preictal* events. For both database 1 and database 2 recordings. We compared the *ictal* histograms to the corresponding *interictal* histograms.

Finally, we averaged the histograms per subject and analyzed how the distribution varied from the *ictal* stages to the *interictal/preictal* stages. We observed that the histograms corresponding to the *interictal/preictal* stages tended to have greater dispersion than the *ictal* ones, these changes in dispersion led us to choose the numeric distance between the first,  $Q1$  and the third quartiles,  $Q3$ , as a discriminator for the *ictal* and *interictal/preictal* stages of an epileptic event. A Kruskal-Wallis test was performed to probe our hypothesis.

## RESULTS AND DISCUSSION

Figures 4 and 5 show box plots of the mean phase differences and mean values of the PLV, PLI and PLM histograms for the *ictal* and *preictal/interictal* states, retrieved from an EEG recordings in databases 1 and 2. We observed that changes in the distribution of the mean values of the histograms between the *ictal* and *interictal* stages of the seizure were more evident when the recordings were analyzed by PDI, whereas the distribution of the mean values of the histograms for PLV, PLI and PLM indexes showed only small changes between seizure stages.

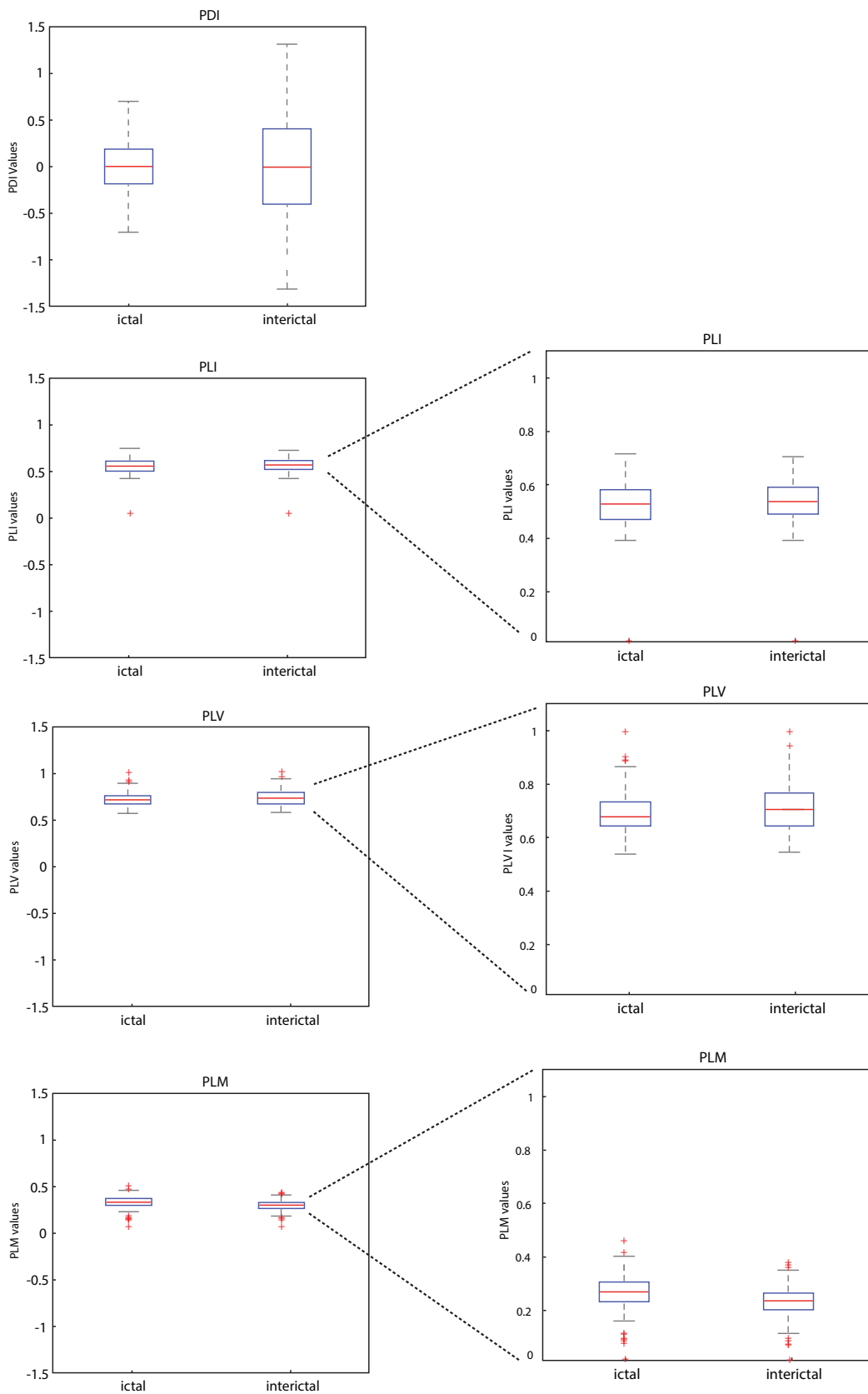


**FIGURE 4.** Grayscale map of slices along the Cz channel of the PDI, PLV, PLI and PLM matrices. A darker shade indicates a lower synchronization level. The line indicates the *onset* of the seizure.

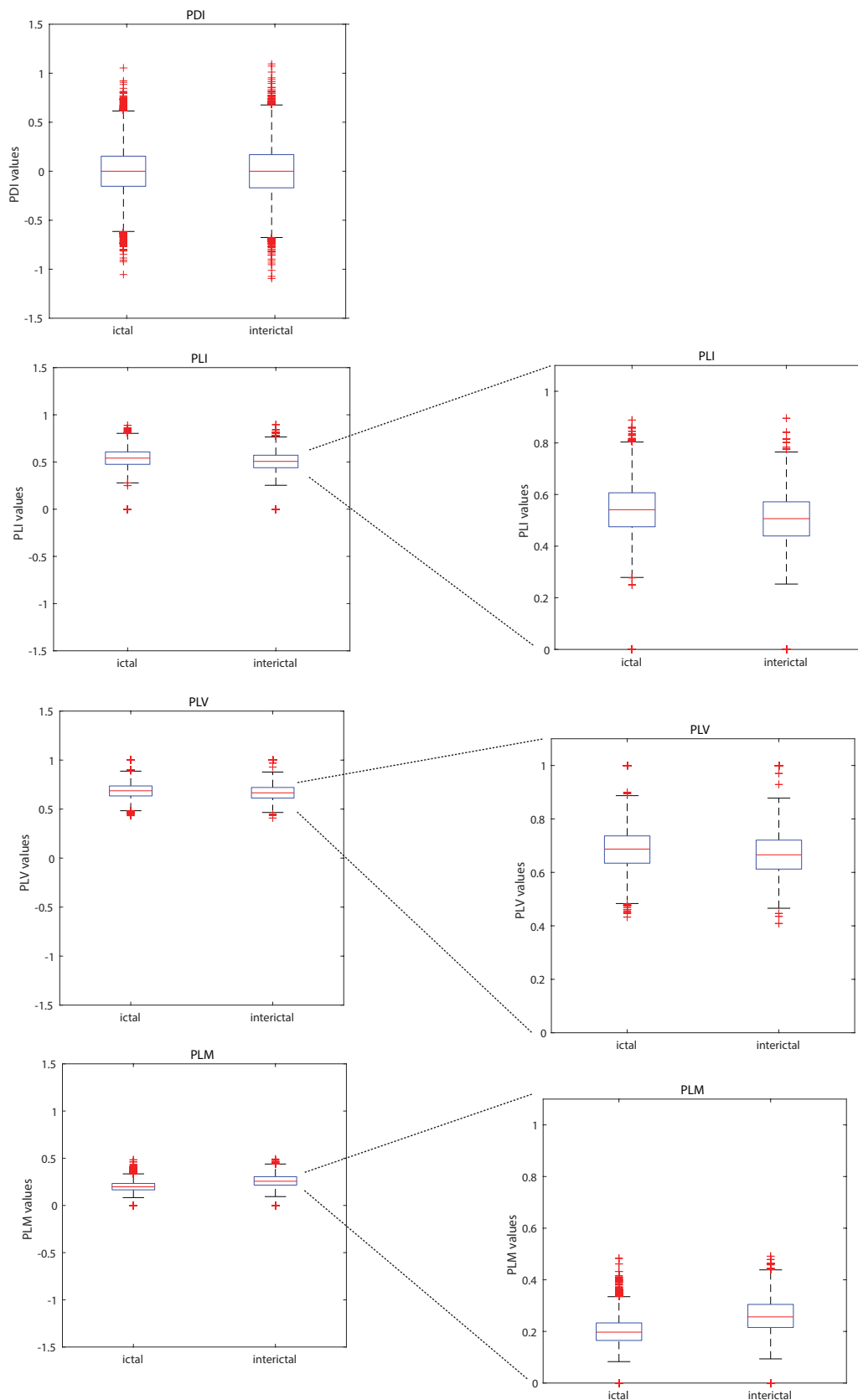


**FIGURE 5.** Distributions of the mean PDI, PLV, PLI and PLM values for a crisis selected from database 2. The left column shows the distributions at the same scale; the right column shows the zoomed-in distributions of PLI, PLV and PLM.

Tables 1 and 2 summarize the results of the Kruskal-Wallis test applied to the indexes computed from the recordings in databases 1 and 2, respectively. In both cases, the PDI performed better than PLV, PLI and PLM

indexes under our testing conditions. Tables 3 and 4 summarize the Q1, Q2 and Q3 values of the distributions of the mean histograms for the PLV, PLI, PLM and PDI indexes for the *ictal* and *preictal* stages.

**TABLE 1. Kruskal-Wallis test results for each index of the database 1 EEG recordings**

Index	p-value
PLV	0.2235
PLI	0.3169
PLM	0.6263
PDI	0.0008

**TABLE 2. Kruskal-Wallis test results for each index of the database 2 EEG recordings**

Index	p-value
PLV	0.0615
PLI	0.4132
PLM	0.0086
PDI	0.0013

A similar performance was observed for the recordings from database 2. As the PLI and PLM indexes were developed to reduce spurious synchronization values caused by volume conduction, but PLV and PDI are susceptible to this, database 2 provided a scenario with no advantage to any index. In this case it was evident that under no volume conduction effects, PDI also performed better than the other three indexes, suggesting that PDI preserves information that is useful for discriminating the stages of epileptic seizures. This results are consistent with the results reported

previously in [26] where the authors found no significant changes in the PLI mean value between the *preictal* and *ictal* stages.

Overall, our proposed index, PDI, showed a better performance in feature extraction based on the distribution analysis of phase synchronization values than other indexes developed previously. Implementing our proposed index in the processing stages of SPMs offers a feature that was not previously revealed by existing phase synchronization indexes.

**TABLE 3. Q1, Q2 and Q3 values for the mean histograms of the for PLV, PLI, PLM and PDI values computed for Database 1.**

Index	Q1 <i>preictal</i>	Q2 <i>preictal</i>	Q3 <i>preictal</i>	Q1 <i>ictal</i>	Q2 <i>ictal</i>	Q3 <i>ictal</i>
PLV	0.091618	0.11099	0.12004	0.083648	0.098677	0.11634
PLI	0.08535	0.10345	0.12568	0.080434	0.094336	0.10965
PLM	0.061742	0.077533	0.10111	0.068173	0.083978	0.11099
PDI	0.40871	0.74746	0.94231	0.26251	0.36316	0.52263

**TABLE 4. Q1, Q2 and Q3 values for the mean histograms of the for PLV, PLI, PLM and PDI values computed for Database 2.**

Index	Q1 <i>preictal</i>	Q2 <i>preictal</i>	Q3 <i>preictal</i>	Q1 <i>ictal</i>	Q2 <i>ictal</i>	Q3 <i>ictal</i>
PLV	0.2369	0.31682	0.37125	0.15321	0.28253	0.37855
PLI	0.58824	0.66667	0.70588	0.58824	0.64706	0.70588
PLM	0.32242	0.38348	0.45536	0.2595	0.35476	0.4189
PDI	2.3803	2.8566	3.2211	2.0286	2.5791	3.0129

## CONCLUSIONS

We found that changes in synchrony occur during the onset of a seizure and could be detected by phase analysis of EEG signals. The changes in the distribution of synchronization values before and after onset identified with the proposed PDI index suggest non-stationary behavior of EEG signals as reported in [16].

The phase difference index (PDI) can be used as a feature to discriminate *ictal* and *preictal/interictal* stages with good accuracy. It offers the advantage of using a simple algorithm that results in less intensive computational tasks and has potential applications in the development of SPMs which can operate in almost real time, and be implemented in portable devices. Further development of feature extraction using PDI can be extended using of broadband phase estimation methods.

The main limitations of the PDI approach is the need for a narrow frequency band in order to obtain interpretable results, this means that a priori knowledge of the spectral distribution of energy of the seizure events is required. We recognize that this approach neglects interactions that may occur between differ-

ent frequency bands. Although approaches to calculating broadband synchronization between signals have been developed [26] [27], they still have the limitation of being surjective functions that, as the presented work shows, can obfuscate information contained in the EEG recording.

## AUTHOR CONTRIBUTIONS

J.A.Q.T., J.L.F and R.R.V. conceived and designed the analysis, validation and writing-review and editing; J.A.Q.T. and R.R.V. performed the analysis; J.A.Q.T. investigation and writing original draft preparation; J.F.L. and R.R.V. supervision. All authors have read and agreed to the published version of the manuscript.

## ACKNOWLEDGEMENTS

The authors thank Francisco J. Alvarado Rodríguez for his valuable assistance and suggestions during this work.

## FUNDING

J.A. Quirarte-Tejeda was supported by CONACYT scholarship No. 716724. This research received no additional external funding.

## REFERENCES

- [1] Acharya UR, Sree SV, Swapna G, et al. Automated EEG analysis of epilepsy: A review. *Knowl-Based Syst* [Internet]. 2013;45:147-65. Available from: <https://doi.org/10.1016/j.knosys.2013.02.014>
- [2] Bruña R, Maestú F, Pereda E. Phase locking value revisited: teaching new tricks to an old dog. *J Neural Eng* [Internet]. 2018;15(5):056011. Available from: <https://doi.org/10.1088/1741-2552/aacfe4>
- [3] Fisher RS, Acevedo C, Arzimanoglou A, et al. ILAE Official Report: A practical clinical definition of epilepsy. *Epilepsia* [Internet]. 2014; 55(4):475-82. Available from: <https://doi.org/10.1111/epi.12550>
- [4] Nair DR. Management of Drug-Resistant Epilepsy. *Continuum (Minneapolis)* [Internet]. 2016;22(1):157-72. Available from: <https://doi.org/10.1212/con.0000000000000297>
- [5] Sejnowski TJ, Churchland PS, Movshon JA. Putting big data to good use in neuroscience. *Nat Neurosci* [Internet]. 2014;17:1440-1. Available from: <https://doi.org/10.1038/nn.3839>
- [6] van Mierlo P, Papadopoulou M, Carrette E, et al. Functional brain connectivity from EEG in epilepsy: Seizure prediction and epileptogenic focus localization. *Prog Neurobiol* [Internet]. 2014;121:19-35. Available from: <https://doi.org/10.1016/j.pneurobio.2014.06.004>
- [7] Camfield P, Camfield C. Idiopathic generalized epilepsy with generalized tonic-clonic seizures (IGE-GTC): a population-based cohort with >20 year follow up for medical and social outcome. *Epilepsy Behav* [Internet]. 2010;18(1-2):61-3. Available from: <https://doi.org/10.1016/j.yebeh.2010.02.014>
- [8] Ramgopal S, Thome-Souza S, Jackson M, et al. Seizure detection, seizure prediction, and closed-loop warning systems in epilepsy. *Epilepsy Behav* [Internet]. 2014;37:291-307. Available from: <https://doi.org/10.1016/j.yebeh.2014.06.023>
- [9] Chen H-H, Cherkassky V. Performance metrics for online seizure prediction. *Neural Netw* [Internet]. 2020;128:22-32. Available from: <https://doi.org/10.1016/j.neunet.2020.04.022>
- [10] Acharya UR, Hagiwara Y, Adeli H. Automated seizure prediction. *Epilepsy Behav* [Internet]. 2018;88:251-61. Available from: <https://doi.org/10.1016/j.yebeh.2018.09.030>
- [11] Kuhlmann L, Lehnertz K, Richardson MP, et al. Seizure prediction –ready for a new era. *Nat Rev Neurol* [Internet]. 2018;14(10):618-30. Available from: <https://doi.org/10.1038/s41582-018-0055-2>
- [12] Detti P, Vatti G, Zabalo Manrique de Lara G. EEG Synchronization Analysis for Seizure Prediction: A Study on Data of Noninvasive Recordings. *Processes* [Internet]. 2020;8(7):846. Available from: <https://doi.org/10.3390/pr8070846>
- [13] Espinoza-Valdez A, González-Garrido A, Luna B, et al. Epileptic brain reorganization dynamics on the basis of the probability of connections. *NeuroReport* [Internet]. 2015;27(1):1-5. Available from: <https://doi.org/10.1097/WNR.0000000000000472>
- [14] Mormann F, Andrzejak RG, Elger CE, Lehnertz K. Seizure prediction: the long and winding road. *Brain* [Internet]. 2007;130(2):314-33. Available from: <https://doi.org/10.1093/brain/awl241>
- [15] Lachaux J-P, Rodriguez E, Martinerie J, Varela FJ. Measuring phase synchrony in brain signals. *Hum Brain Mapp* [Internet]. 1999;8(4):194-208. Available from: [https://doi.org/10.1002/\(SICI\)1097-0193\(1999\)8:4<194::AID-HBM4>3.0.CO;2-C](https://doi.org/10.1002/(SICI)1097-0193(1999)8:4<194::AID-HBM4>3.0.CO;2-C)
- [16] Klonowski W. Everything you wanted to ask about EEG but were afraid to get the right answer. *Nonlinear Biomed Phys* [Internet]. 2009;3(1):2. Available from: <https://doi.org/10.1186/1753-4631-3-2>
- [17] Fan M, Chou C-A. Detecting Abnormal Pattern of Epileptic Seizures via Temporal Synchronization of EEG Signals. *IEEE Trans Biomed Eng* [Internet]. 2019;66(3):601-8. Available from: <https://doi.org/10.1109/TBME.2018.2850959>
- [18] Yu H, Cai L, Wu X, et al. Investigation of phase synchronization of interictal EEG in right temporal lobe epilepsy. *Physica A* [Internet]. 2018;492:931-40. Available from: <https://doi.org/10.1016/j.physa.2017.11.023>
- [19] Alaei HS, Khalilzadeh MA, Gorji A. Online Epileptic Seizure Prediction Using Phase Synchronization and Two Time Characteristics: SOP and SPH. *Int Clin Neurosci J* [Internet]. 2019;7(1):16-25. Available from: <https://doi.org/10.15171/icnj.2020.03>
- [20] Stevenson N, Tapani K, Lauronen L, Vanhatalo S. A dataset of neonatal EEG recordings with seizure annotations. *Sci Data* [Internet]. 2019;6:190039. Available from: <https://doi.org/10.1038/sdata.2019.39>
- [21] Alducin Castillo J, Yanez Suárez O, Brust Carmona H. Electroencephalographic analysis of the functional connectivity in habituation by graphics theory. *RMIB* [Internet]. 2016;37(3):181-200. Available from: <https://doi.org/10.17488/RMIB.37.3.3>
- [22] Stam CJ, Nolte G, Daffertshofer A. Phase lag index: assessment of functional connectivity from multi channel EEG and MEG with diminished bias from common sources. *Hum Brain Mapp* [Internet]. 2007;28(11):1178-93. Available from: <https://doi.org/10.1002/hbm.20346>
- [23] Baseliçe F, Sorriso A, Rucco R, Sorrentino P. Phase Linearity Measurement: A Novel Index for Brain Functional Connectivity. *IEEE Trans Med Imag* [Internet]. 2019;38(4):873-82. Available from: <https://doi.org/10.1109/TMI.2018.2873423>
- [24] Shannon CE. 1 Shannon's Measure of Information. In: Aczél J, Daróczy Z (eds). *Mathematics in Science and Engineering* [Internet]. New York: Academic Press; Elsevier; 1975. 26-49p. Available from: [https://doi.org/10.1016/S0076-5392\(08\)62730-7](https://doi.org/10.1016/S0076-5392(08)62730-7)
- [25] Michel CM, Koenig T. EEG microstates as a tool for studying the temporal dynamics of whole-brain neuronal networks: A review. *NeuroImage* [Internet]. 2018;180:577-93. Available from: <https://doi.org/10.1016/j.neuroimage.2017.11.062>
- [26] Wang L, Long X, Aarts R, et al. A broadband method of quantifying phase synchronization for discriminating seizure EEG signals. *Biomed Signal Process Control* [Internet]. 2018;52:371-83. Available from: <https://doi.org/10.1016/j.bspc.2018.10.019>
- [27] Sorrentino P, Ambrosanio M, Rucco R, Baseliçe F. An extension of Phase Linearity Measurement for revealing cross frequency coupling among brain areas. *J Neuroeng Rehabil* [Internet]. 2019;16(1):135. Available from: <https://doi.org/10.1186/s12984-019-0615-8>

[dx.doi.org/10.17488/RMIB.42.2.8](https://doi.org/10.17488/RMIB.42.2.8)

E-LOCATION ID: 1141

## Efficacy of Virtual Reality in Neurorehabilitation of Spinal Cord Injury Patients: A Systematic Review

### Eficacia de la Realidad Virtual en la Neurorrehabilitación de Pacientes con Lesión de Médula Espinal: una Revisión Sistemática

B. A. Orsatti-Sánchez<sup>1</sup>, O. Diaz-Hernandez<sup>2</sup>

<sup>1</sup>Universidad Nacional Autónoma de México, División de Ingeniería Mecánica e Industrial

<sup>2</sup>Universidad Nacional Autónoma de México, ENES Juriquilla

#### ABSTRACT

This systematic review (SR) analyzed the effectiveness of interventions using virtual reality (VR) technology as a neurorehabilitation therapy in people with spinal cord injury (SCI). The SR was developed under the guidelines of the PRISMA statement and the recommendations of the Cochrane Collaboration, along with the PEDro and National Institute of Health scales to assess the risk of bias and methodological quality. The Cochrane, IEEE, BVS/LILACS, MEDLINE/PubMed, and Web of Science databases were browsed to identify studies that, between 2010 and 2020, evaluated the efficacy of these therapies. Out of 353 retrieved studies, 11 were finally selected after the application of the defined inclusion and exclusion criteria. These articles presented good methodological quality as they were mostly controlled clinical trials that analyzed mixed therapies with conventional therapies. Interventions based on non-immersive or immersive VR technology that achieved functional motor, balance, and psycho-emotional health improvement with positive effects on motivation, self-confidence, commitment, and active participation were identified in a total sample of 155 SCI patients. It was concluded that such VR technology is an effective tool of neurorehabilitation complementary to conventional therapies, which promotes functional improvement in SCI patients both in the clinic and at home.

**KEYWORDS:** Spinal cord injury; virtual reality; neurorehabilitation; systematic review

## RESUMEN

Esta revisión sistemática (RS) analizó la eficacia de las intervenciones que utilizan la tecnología de realidad virtual (RV) como terapia de neurorrehabilitación en personas con lesión de médula espinal (LME). La RS fue desarrollada bajo los lineamientos de la declaración *PRISMA* y las recomendaciones de la Colaboración Cochrane, junto con las escalas de *PEDro* y del *National Institute of Health* para evaluar el riesgo de sesgo y la calidad metodológica. Se revisaron las bases de Cochrane, *IEEE*, *BVS/LILACS*, *MEDLINE/PubMed* y *Web of Science* para identificar estudios que, entre 2010 y 2020, evaluaron la eficacia de dichas terapias. De 353 estudios recuperados, 11 fueron finalmente seleccionados tras la aplicación de los criterios de inclusión y exclusión definidos. Dichos artículos presentaron una buena calidad metodológica, al ser mayormente ensayos clínicos controlados que analizaron terapias mixtas con terapias convencionales. Se identificaron intervenciones basadas en tecnología de RV no inmersiva o inmersiva que lograron una mejora funcional motora, de equilibrio y de salud psico-emocional con efectos positivos de motivación, seguridad, compromiso y activa participación en una muestra total de 155 pacientes con LME. Se concluyó que dicha tecnología de RV es una herramienta eficaz de neurorrehabilitación complementaria a las terapias convencionales, al promover una mejora funcional en pacientes con LME tanto en la clínica como en casa.

**PALABRAS CLAVE:** Lesión de medula espinal; realidad virtual; rehabilitación neurológica; revisión sistemática

### Corresponding author

TO: Bruno Alejandro Orsatti Sánchez  
INSTITUTION: Universidad Nacional Autónoma de México, División de Ingeniería Mecánica e Industrial  
ADDRESS: Circuito Exterior S/N, Col. Ciudad Universitaria, C. P. 04510, Coyoacán, CDMX, México  
E-MAIL: orsattisba@gmail.com

### Received:

21 December 2020

### Accepted:

25 March 2021

## INTRODUCTION

*Spinal cord injury* (SCI) is related to damage to the spinal cord resulting from traumatic (external force) or non-traumatic (disease or degeneration) causes. As the spinal cord (SC) is the main information conduit connecting the brain to the rest of the body, an SCI can have significant physiological consequences below the level of injury, ranging from no or mild neurological deficit to a more serious loss of motor, sensory, and autonomic functions, or even death, mainly depending on the number of surviving axons <sup>[1] [2] [3]</sup>.

The World Health Organization highlights that the incidence of both traumatic and non-traumatic SCI ranges from 40 to 80 cases per million inhabitants per year, with 90% of them caused by trauma <sup>[1]</sup>. Men in the 20-29 age group and over 70 are at a higher risk of suffering an SCI, whereas the risk for women appears between the ages of 15 and 19 and over 60. The male-to-female ratio is usually 2:1 <sup>[1]</sup>.

The increased life expectancy in high-income countries accounts for a higher SCI prevalence of around 70% for people with quadriplegia and 88% for people with complete paraplegia as compared to low- and middle-income countries <sup>[1]</sup>. By 2020, SCI is expected to be one leading causes of disability globally <sup>[4]</sup>.

SCI is often associated with various psychological and social consequences including low rates of school enrollment, difficulty with schoolwork, work barriers as reflected in an overall unemployment rate in excess of 60%, and the fact that 20% to 30% of these patients show signs of depression <sup>[1]</sup>.

Injuries may be traumatic in the case of fracture, dislocation, or compression of one or more vertebrae, mainly as a result of road accidents, falls, or gunshot wounds. There are also non-traumatic injuries caused by arthritis, cancer, inflammation, infections, degenerative disc disease, or congenital conditions <sup>[1] [2] [3] [4]</sup>.

The degree of paralysis caused by an SCI depends on the location of the injury, which will determine whether it is paraplegia or quadriplegia. The latter is more serious as it causes a partial or total loss of motor and/or sensory function in all four extremities, trunk, and pelvic organs when the injury is located in the C1-C7 segments. In contrast, there is paraplegia when the injury is located in the T1-S5 segments, causing functional disorders in the legs, pelvic organs, and part of the trunk <sup>[1] [2] [3] [4] [5] [6]</sup>.

The neurological condition of an SCI patient is determined by the American Spinal Injury Association (ASIA) Impairment Scale, which defines 5 levels of impairment based on the absence or preservation of motor and sensory function. In a complete injury (grade A), these functions are not present below the level of injury up to the S4-S5 sacral segments. In contrast, when some signals can still be transmitted below the level of injury, then the injury is incomplete (grades B, C, and D) with some preserved motor and/or sensory function. Grade E describes normal function of all segments <sup>[3] [6] [7]</sup>.

Although, so far, the consequences of an SCI are considered to be irreversible given the SC's inability to regenerate, the development of new surgical procedures and the technological advances in the last few decades have contributed to the design of new rehabilitation programs aimed at improving patients' prognosis and quality of life <sup>[1] [2] [8]</sup>.

Comprehensive, conventional rehabilitation programs combine physical therapy with occupational therapy activities. While the former focuses on maintaining and strengthening muscle function, improving balance and coordination in both standing and seating positions, training gait and weight shifting, and learning adaptation techniques in order to perform daily tasks, the latter aims to recover fine motor skills in order to achieve greater biopsychosocial well-

being and independence to perform personal care activities and adapt the impaired abilities to professional or academic life <sup>[1] [2] [5]</sup>.

Against this backdrop, the introduction of virtual reality (VR) in rehabilitation therapies after SCI seeks to contribute to motor and cognitive relearning processes by arousing patients' interest in rehabilitation programs. This is done through a series of game-based exercises that also instill higher levels of self-confidence and self-improvement through the use of new stimuli to enhance the effectiveness of patients' physical and cognitive abilities and functions in controlled virtual environments. These game-based exercises stimulate the patient to perform a greater number of repetitions and therefore the intensity of the rehabilitation activities increases, which stimulates neuroplasticity promoting motor relearning in SCI patients. Some literature highlights the importance of using VR as a complement to traditional rehabilitation programs to improve them, since these usually involve simple and repetitive movements which causes a feeling of boredom, thus reducing the motivation of SCI patients. Moreover, the capturing patients' movements enables therapists to plan, supervise, and adapt exercises in an individualized manner <sup>[1] [9] [10]</sup>.

VR or a virtual environment is an IT-based structure that creates a simulated or artificial, three-dimensional (3D) environment that mimics the real environment where a person is located. The application of VR devices depends on the level of technological advancement, the level of platform complexity, costs, and the ability to adapt them to different VR environments <sup>[9] [10]</sup>.

VR systems fall into three categories according to the sense of reality of the created virtual environment: 1) in fully-immersive VR, the user wears a headset or goggles, earphones, and other special peripherals (gloves, haptic hand controllers, etc.); 2) in semi-im-

mersive VR, the user places himself or herself among four aligned screens on which the virtual environment is projected and uses peripherals to interact with the environment with head movements; 3) in non-immersive VR, the user needs a screen monitor, a keyboard, a mouse, or other peripherals to place himself or herself in the VR environment and interact with it <sup>[10]</sup>. There is also the so-called "augmented reality," which requires the use of a device that enables users to visualize virtual objects overlaid in the real world; this is often mixed up with semi-immersive VR.

Since VR technology is an innovative tool that has been applied in the medical field of rehabilitation and should be followed up in terms of its most recent development over the last few years <sup>[1]</sup>, it is important to compile, synthesize and analyze the evidence achieved on the advances, effects and level of acceptance of VR in the rehabilitation of motor and cognitive functions after SCI.

The objective was to conduct a systematic review (SR) with the aim of analyzing the efficacy of VR technology in the neurorehabilitation of SCI patients based on evidence gathered by the studies included in the review, with an emphasis on: 1) whether VR was integrated into conventional rehabilitation therapies and the resulting benefits; 2) whether the results of the use of VR have been compared with those of conventional rehabilitation therapies; 3) how VR was applied; 4) the types of SCI analyzed; 5) patients' acceptability; 6) main limitations observed; and 7) future work.

## MATERIALS AND METHODS

### Protocol

This SR was conducted following the 27 guidelines and the flow diagram structure provided by the PRISMA statement <sup>[11] [12] [13]</sup> as well as the recommendations of the Cochrane Collaboration to perform an orderly selection of papers according to the proposed

protocol [14]. All this enhanced the quality and presentation of the analysis and brought transparency to the paper selection process.

### Search strategy

Between 1 May and 19 June 2020, an electronic search was carried out in the COCHRANE, IEEE, BVS/LILACS, MEDLINE/PUBMED, and WEB OF SCIENCE databases in order to find any papers published in the January 2010-June 2020 period, when most of the development and research work around the use of VR technology applied to motor and cognitive rehabilitation [9] took place. Additionally, the search was performed in English and Spanish, without a geographic delimitation with the purpose of obtaining a global overview.

The search terms in Spanish consisted of combinations of keywords found in the Descriptores en Ciencias de la Salud (DeCS) thesaurus: lesión de médula espinal, traumatismo de médula espinal, tetraplejía, cuadriplejía, paraplejía, realidad virtual, realidad aumentada, terapia de exposición mediante realidad virtual, juego de video, rehabilitación, and rehabilitación neurológica. The search terms in English included terms found in the Medical Subject Headings (MeSH) thesaurus: spinal cord injury, spinal cord trauma, tetraplegia, quadriplegia, paraplegia, virtual reality, augmented reality, virtual reality immersion therapy, virtual reality exposure therapy, video game, rehabilitation, and neurorehabilitation. The final structure of each database search strategy was adjusted based on syntax, logical operators, tags, and relevant qualifiers [15] [16] [17] [18].

### Eligibility criteria

The inclusion criteria were defined based on the PICOS model (Participants, Interventions, Comparators, Outcomes, Study Design) [13]. The review took into account both controlled and randomized controlled clinical trials [14] [19] conducted on human sub-

jects that provided empirical evidence of the efficacy of neurorehabilitation of motor and cognitive functions through virtual reality therapies (VRT) applied as a complement or not to physical, occupational, or mixed therapies, and that allowed for a comparison of an intervention group with a control group. Quasi-experimental (before-and-after) studies were also considered. The patient population included both male and female subjects with SCI in the 18 to 85 age range, with traumatic and non-traumatic, complete and incomplete injuries, regardless of their ASIA grades or time since injury.

The studies were required to contain this information: population sample, assisted limbs and SCI characteristics, objectives, and aspects of the rehabilitation intervention; VR technology type, effects, and application method; duration, frequency, and acceptability; assessment of the effect of the intervention compared to conventional therapies; validation or development of VR software or devices; and intervention efficacy indicators.

Any systematic reviews, meta-analyses, lectures, abstracts, or studies that were duplicated or not designed to assess the clinical efficacy of motor or cognitive rehabilitation on SCI, that did not focus on VR as a therapeutic intervention, or that used electrical stimulation that could have influenced its own results of the technology under study were excluded. Similarly, studies that did not fit the defined study time period and were not written in English or Spanish were also excluded.

The selection of potentially relevant studies was performed in three stages. The first stage focused on eliminating duplicate records; the second stage centered on exclusion of papers according to their title and abstract; finally, the third stage consisted of a full-text analysis. The last two stages were guided by inclusion and exclusion criteria [14].

## Data extraction

Two electronic worksheets were created in order to obtain detailed information from the studies selected in an organized manner. The first worksheet contained demographic and clinical information about the patient population: mean age, sex, cause and level of SCI, ASIA impairment grade, type of injury, time since injury, sample distribution across study groups, and their respective dropout rates. The second worksheet summarized the characteristics of the selected studies: authors' names, country and year of publication, study design, and characteristics of the VR technology used, information on interventions, sessions, outcome measures, and conclusions.

## Risk of bias assessment

The internal validity of the controlled clinical trials was assessed using the PEDro scale criteria [20]. For before-and-after studies without a control group, the National Institute of Health Quality Assessment Tool was applied [21].

Taking the registered level of evidence as a reference, the internal validity was rated as poor, fair, good, or excellent for scores in the 0-4, 5-6, 7-8, and 9-10 ranges, respectively, for PEDro. Comparatively, for the before-and-after studies, it was rated as poor, fair, or good in the 0-4, 5-6, and 7-10 ranges, respectively. Studies rated as with good methodological quality and low risk of bias were identified with a score higher than the mean of 5, while those with scores lower than the mean of 5 were rated as with poor methodological quality and high risk of bias.

## RESULTS AND DISCUSSION

### Paper search and selection process

A total of 353 papers were found, 218 of which remained after eliminating duplicates. Of these, only 207 could be downloaded. During the second stage of the selection process, 179 papers were ruled out based

on their title and abstract, and only 28 moved forward to the final stage for full-text analysis, where another 17 were excluded, resulting in 11 papers finally selected for the SR. Figure 1 depicts the paper selection process listing the exclusion criteria in each stage based on the PRISMA statement [12].

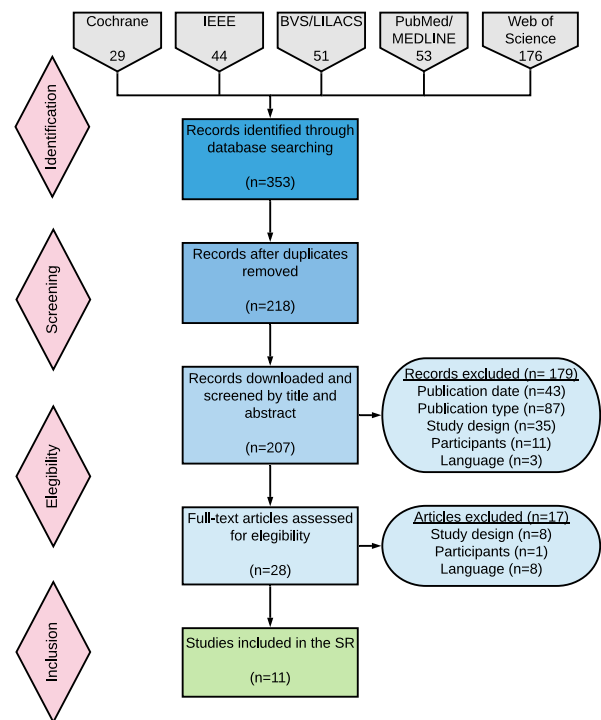


FIGURE 1. PRISMA flow diagram of the paper search strategy and selection process.

A larger number of papers were found from India and Spain, each represented 27.27% of the studies selected, while Italy, South Korea, Switzerland, Taiwan, and Australia each represented only 9.09% of these. Over the entire search time period, no papers were found for the years 2013 and 2019. English was the main language used in 90.91% of the studies selected.

### Risk of bias assessment of selected papers

The results of the controlled clinical trials [22] [23] [24] [25] [26] [27] [28] [29] [30] and the before-and-after studies [31] [32] are presented in Tables 1 and 2, respectively. According to the PEDro scale, the score for the risk of bias of the controlled clinical trials was  $7.22 \pm 1.30$ , and in the case

TABLE 1. Assessment of the risk of bias of controlled clinical trials according to the PEDro scale.

STUDY CRITERION	D'Addio G, et. al. (2014) [22]	Dimbwadyo Terrer I, et. al. (2016) [23]	Dimbwadyo Terrer I, et. al. (2015) [24]	Gil Agudo A, et. al. (2011) [25]	Khurana M, et. al. (2017) [26]	Lakhani A, et. al. (2020) [27]	Tak S, et. al. (2015) [28]	Prasad S, et. al. (2018) [29]	Sengupta M, et. al. (2019) [30]
Randomization	✓	✓	✓	✓	✓	✓	✓	✓	X
Allocation concealed	X	✓	X	X	✓	✓	✓	✓	X
Groups were similar at baseline	✓	✓	✓	✓	✓	✓	✓	✓	✓
Blinding of all subjects	X	✓	X	X	X	X	X	X	✓
Blinding of all therapists	X	X	X	X	✓	X	X	X	X
Blinding of all assessors	X	✓	X	X	✓	X	✓	✓	✓
Key outcomes in 85% of the allocated subjects	✓	✓	✓	✓	✓	✓	✓	✓	✓
Groups received planned treatment or "intention to treat"	✓	✓	✓	✓	✓	X	✓	✓	✓
Statistical comparisons between groups	✓	✓	✓	✓	✓	✓	✓	✓	✓
Point and variability measures of treatment effects	✓	✓	✓	✓	✓	✓	✓	✓	✓
Total	6	9	6	6	9	6	8	8	7
Level of evidence	Fair	Excellent	Fair	Fair	Excellent	Fair	Good	Good	Good
Risk of bias	Low	Low	Low	Low	Low	Low	Low	Low	Low

Note. ✓: yes; X: no.

of the before-and-after studies, the National Institute of Health score was  $7.5 \pm 0.7$ . This indicates that the selected papers have a low risk of bias and a high methodological quality associated with the evidence they provide.

### Ethical statement

All studies reported that, before the start of the intervention, patients were asked to sign an informed consent letter after they were informed, in writing and verbally, of the experimental procedures in the study protocol. The interventions were authorized by the ethics committees of the participating hospitals [23] [24] [25], universities [27] [28], sites [26] [27] [29] [30] [31] or state agency [32], with the exception of one [22], which did not report anything in this regard. Only 3 studies [23] [25] [32] adapted their protocols to the Helsinki Declaration of the World Medical Association.

### Design of selected studies

Of the 11 selected papers, 9 were controlled clinical trials (8 randomized [22] [23] [24] [25] [26] [27] [28] [29] and 1 non-randomized [30]), and 2 were before-and-after studies [31] [32].

Controlled clinical trials were those in which the subjects had been allocated to a control group (CG) or an intervention group (IG) and which conducted a prospective analysis. If such allocation had been made through randomization, then the trial was considered a randomized, controlled clinical trial. Additionally, the design of before-and-after studies included subjects that received the same treatment without a control group [14].

Out of the 9 controlled clinical trials, 8 worked with parallel groups, and only 1 [27] worked with crossover groups. Only 5 of the 8 randomized controlled clinical

**TABLE 2. Assessment of the risk of bias of before-and-after studies according to the National Institute of Health.**

STUDY	Sung W, et. al. (2012) [31]	Villiger M, et. al. (2017) [32]
CRITERION		
Stated study question or objective	✓	✓
Eligibility criteria (subjects)	✓	✓
Representative participants	✓	✓
Enrollment of all eligible participants	✓	NR
Sample size sufficiently large	✗	✗
Intervention clearly described and delivered	✓	✓
Clearly define outcome measures	✗	✗
Blinding of all assessors	NR	✗
More than 20% of participants followed-up after baseline.	✓	✓
Statistical analysis (p)	✓	✓
Outcome measures taken multiple times	✓	✓
Group level statistical analysis	NA	NA
Total	8	7
Level of evidence	Good	Good
Risk of bias	Low	Low

Note. ✓: yes; ✗: no; NR: not reported; NA: not applicable.

trials were blinded and reported the randomization technique used: opaque envelopes containing sequential numbers [23], computer-generated random numbers [26], the “randbetween” function in Excel [27], Random Allocation 2.0 software [28], and an unspecified fixed randomization method [29]. In the case of the non-randomized study [30], patients were assigned to the IG and CG based on their demographic characteristics, which is not considered an adequate randomization method by PEDro [20] and the Cochrane Collaboration [14].

As far as blinding is concerned, 4 controlled clinical trials and 2 before-and-after studies had no blinding [22] [24] [25] [27] [31] [32]. Moreover, of the 5 controlled clinical tri-

als, 2 were single-blinded to the assessors [28] [29], and 3 were double-blinded to both the subjects and the assessors [23] [30] or to the therapists and the assessors [26].

It should be noted that only 3 papers [23] [29] [32] included a long-term follow-up on the effects of VRT on subjects over time.

### Population characteristics

All papers reported their inclusion and exclusion criteria for subject eligibility, and only 9 [23] [25] [26] [27] [28] [29] [30] [31] [32] indicated their recruitment sources.

The total population sample analyzed was made up of 243 patients with SCI, with 4 studies [22] [25] [26] [28] having a 1:1 distribution between the IG and the CG. Only 2 randomized controlled trials [27] [29], 1 controlled clinical trial [30], and 1 before-and-after study [32] reported 1 or 4 dropouts in both groups [27] [29] or only in the intervention group [30] [32], with a total of 15 patient dropouts. The mean age of the total population analyzed was 40.25 years for both groups, with a majority of men (78.68%) in the reported population (n=197) in 9 studies (see Table 3).

Traumatic injuries were found in 86% of the population analyzed (n=150) by 8 studies [23] [24] [25] [26] [27] [29] [31] [32] and only 1 study [30] reported both traumatic and non-traumatic injuries without providing precise data. As to the level of injury, all studies (n=209) but one [22] observed that 50.72% of injuries were located in the cervical spine, 44.97% at the thoracic level, and 4.31% in the lumbar spine. Most studies worked with recently injured patients (< 6 months), and 4 other studies [28] [29] [31] [32] worked with patients who had had their injuries for more than one year.

Most SCI were incomplete (58.37%) in the reported population (n=209), and only 1 study [26] did not report on this. Regarding the level of impairment of all patients (n=167), according to the ASIA scale, most had

**TABLE 3. Demographic characteristics of patients included in the studies.**

STUDY	SAMPLE/DROPOUT		AGE (YEARS) <sup>#</sup>		SEX			
	IG	CG	IG	CG	IG		CG	
					M	F	M	F
D'Addio G, et. al. [22]	15/0	15/0	43±18.7		X			
Dimbwadyo Terror I, et. al. [23]	16/0	15/0	34.53±13.71	40.27±13.61	10	6	12	3
Dimbwadyo Terror I, et. al. [24]	6/0	3/0	54.3±9.86	44.17±22.92	5	1	2	1
Gil Agudo A, et. al. [25]	5/0	5/0	36.20±10.41	49±6.11	1	4	3	2
Khurana M, et. al. [26]	15/0	15/0	29.47±7.48	29.8±7.32	14	1	14	1
Lakhani A, et. al. * [27]	10/4	14/4	56.20±20.74	48±16.21	10	0	6	8
Tak S, et. al. [28]	13/0	13/0	49.54±8.25	43.08±11.23	10	3	10	3
Prasad S, et. al. * [29]	12/1	10/1	23.7±5.2	33.9±7.1	11	1	10	0
Sengupta M, et. al.** [30]	25/4	12/0	28	30.5	17	4	10	2
Sung W, et. al.*** [31]	12	NA	28.5	NA	10	2	NA	
Villiger M., et. al.*/*** [32]	12/1	NA	60±10.2	NA	X		NA	

Note. IG: intervention group; CG: control group; M: male; F: female; X: information not provided; NA: not applicable.  
\*Data before dropout. \*\*Data after dropout. \*\*\*No control group. #The values are represented as mean ± standard deviation.

grade A injuries (47.31%), followed by grade B (23.35%), grade D (15.57%), and grade C (13.77%). Two studies [22] [26] reported, with no details, that they had worked with certain ASIA grades, and one [31] did not address this issue.

The clinical characteristics of each population group analyzed are presented in Table 4.

### Characteristics of virtual reality

The studies used different types of commercial VR technologies, including video game consoles, specialized VR peripherals and systems designed for rehabilitation, as well as devices developed by the research teams (see Table 5).

Only one study used a commercial, fully-immersive VR system (Oculus Go VR headset) [27], while the other 10 studies used non-immersive VR systems [22] [23] [24] [25] [26] [28] [29] [30] [31] [32]. Four of them [22] [26] [28] [29] were based on Nintendo and Sony commercial consoles, with their video games (mainly sports and recreational) and compatible peripherals that, in few cases, were reported to be adapted for use in rehabilitation of certain impairment grades (for instance, only one men-

tioned attaching the Wiimote controller to the hand with bandages or a glove in cases of weak grip [29]). Additionally, Rhetoric system [30] only used Microsoft Kinect peripheral. Other studies used motion sensing devices for rehabilitation such as YouKicker (with four wireless accelerometers) [32], TOyRA [23] [25] (based on five wireless inertial sensors), and CyberGlove [24] (with 22 resistive bend sensing technology and vibrotactile stimulators). One study developed a driving simulator [31] using an adapted real car mounted on a one-axle tiltable platform to virtually control acceleration and braking.

Regarding those studies where their VRT used commercial consoles along with their video games, only one [26] explicitly mentioned the adaptation of their virtual environments for rehabilitation purposes without providing further details. On the other hand, those studies where commercial video games were not used as virtual environment, two of them were developed by the research teams [24] [32] and only one specified the use of Unity 3D [32] as graphic engine for its development. In the case of the Rhetoric [30] and TOyRA [23] [25] systems, their games were designed for neurorehabilitation purposes by specialized teams of Rehametrics



TABLE 5. Characteristics of included studies.

STUDY	DESIGN	VR	INTERVENTIONS	FREQUENCY DURATION FOLLOW- UP	OUTCOME MEASURES	MAIN FINDINGS
D'Addio G, et. al. (2014) Italy [22]	Randomized controlled clinical trial, nonblinded.	Nintendo Wii Fit + Balance board + Games ("Table Tilt", "Balance Bubble" and "Deep Breathing").	<b>IG(n:15):</b> VRT (multidirectional balance and static postural control training) + TRT. <b>CG(n:15):</b> TRT (balance training with active/passive UL and LL stretching and exercises to increase strength and improve posture).	<b>Total period</b> = 12 weeks. <b>IG:</b> 3 VRT sessions + TRT for 60 [min] per week. <b>CG:</b> 3 TRT sessions of 60[min] per week.	BBS (Berg Balance Scale), SCIM (Spinal Cord Independence Measure), COP EO and EC (Posturographic Index: Center of Pressure) and Romberg Index.	An improvement in balance control was observed in both IG and CG. However, the improvement was greater in the IG, particularly in balance and self-confidence to perform tasks without external support. The Wii Fit system was potentially acceptable as an adjunct to TRT. Given its low cost and intuitive use, it could be used as a rehabilitation tool at home under supervision.
Dimbwadyo Terrer I, et. al. (2016) Spain [23]	Pilot randomized controlled clinical trial, double-blinded.	TOyRA wireless system (LCD monitor + inertial sensors Xsens + Virtual environment with 3D interactive objects and personalized avatar.	<b>IG(n:16):</b> VRT (ADL training with dominant UL) + CT. <b>CG(n:15):</b> CT (OT: ADL training + PT: strengthening exercise and active/passive mobilizations of UL).	<b>Total period</b> = 5 weeks. <b>IG:</b> 3 VRT sessions of 30 [min] + 5 CT sessions of 90 [min] per week. <b>CG:</b> 5 CT sessions of 90 [min] per week. <b>Follow-up (n=22: 11 per group):</b> Only CT 3 months after treatment for both groups.	SCIM III (self-care subscore), MI (Motricity Index), BI (Barthel Index), MB (Muscle Balance), FIM (Functional Independence Measure), QUEST 2.0 (Quebec User Evaluation of Satisfaction with Assistive Technology) and Satisfaction Survey (Likert scale).	The effects of an intensive and repetitive VRT + CT compared to those of CT alone produced similar functional changes in the IG and CG in UL performance in patients with complete tetraplegia. A high level of patient satisfaction was observed as a result of the gaming aspects. The TOyRA system as a complement to CT can be useful to increase duration of therapy, as well as engagement and motivation during the rehabilitation process. There were no reports of vertigo, motion sickness or muscle pain.
Dimbwadyo Terrer I, et. al. (2015) Spain [24]	Pilot randomized controlled clinical trial, nonblinded.	CyberGlove (resistive bend-sensors and vibrotactile feedback) + LCD Philips monitor (autostereoscopic 3D) + First-person virtual environment with 3D objects	<b>IG(n:6):</b> VRT (reach and release movements with UL in ADL and trunk balance control) + CT. <b>CG(n:3):</b> CT (OT: ADL training and UL Functional exercises + PT: assisted/active mobilizations of UL and trunk balance exercises).	<b>Total period</b> = 2 weeks. <b>IG:</b> 2 VRT sessions of 30 [min] + 2 CT sessions of 30 [min] per week. <b>CG:</b> 2 CT sessions of 30 [min] per week.	MB, BI, SCIM (self-care subscore), NHPT (Nine Hole Peg Test) with JHFT (Jebson Taylor Hand Function Test) + two implemented parameters: "Repeatability" and "Normalized Trajectory Length".	The results between the groups were similar, although the IG improved in dexterity, coordination and fine finger movement during reaching movements. The results showed the usefulness of VRT in ADLs rehabilitation as a complement to CT. VRT (CyberGlove) based on functional parameters, such as normalized trajectory length and repeatability, adapted the level of difficulty of the tasks to patients' individual abilities. Prolonged repetitive movements led to functional improvement. There were no reports of vertigo, motion sickness or muscle pain.

<p>Gil Agudo A, et. al. (2011) Spain [25]</p>	<p>Randomized controlled clinical trial, nonblinded.</p>	<p>TOyRA system.</p>	<p><b>IG(n:5):</b> VRT (ADL training with UL) + CT. <b>CG(n:5):</b> CT (OT: ADL training + PT: active-assisted-resistive mobilizations of UL joints).</p>	<p><b>Total period</b> = 5 weeks. <b>IG:</b> 15 VRT sessions of 30 [min] on alternated days + 7 OT sessions of 30[min] and 30[min] of PT per week. <b>CG:</b> 7 OT sessions of 30[min] and 30[min] of PT per week.</p>	<p>ROM (Range of Motion), BI, FIM, SCIM II, NHPT, JTHFT and MI.</p>	<p>The use of VRT + CT produced similar results in both groups with tetraplegic patients, although an improvement in UL function was observed in the IG vis-à-vis CT alone, with improved dexterity, pincer grasp, and coordination as well as a slight improved ROM for shoulder flexion-extension and forearm pronation. The TOyRA system can be used as a complementary therapeutic tool with CT.</p>
<p>Khurana M, et. al. (2017) India [26]</p>	<p>Randomized controlled clinical trial, double-blinded.</p>	<p>Sony PlayStation 2 + Eye Toy + 3 adapted games ("Birds and balls", "Soccer" and "Snowboard").</p>	<p><b>IG(n:15):</b> VRT (sitting balance in ADL with UL and trunk) + CT. <b>CG(n:15):</b> CT (OT: balance in ADL moving upper body over/outside support base + PT: stretching of LL, mat and range of motion exercises).</p>	<p><b>Total period</b> = 4 weeks. <b>IG:</b> 5 VRT sessions of 25 [min] + 5 PT sessions of 20 [min] per week. <b>CG:</b> 5 OT sessions of 25 [min] + 5 PT sessions of 20 [min] per week.</p>	<p>mFRT (modified Functional Reach Test), t-shirt test and SCIM III (self-care subscore).</p>	<p>Game-based (PlayStation 2) VRT + CT improved sitting balance and functional performance in patients with low paraplegia in the IG vis-à-vis CT alone. Increasing the level of difficulty of the activities and making them more intense contributed to motor function recovery by promoting neuroplasticity. Patients' motivation was not measured, but participants showed interest and enthusiasm for VRT.</p>
<p>Lakhani A, et. al. (2020) Australia [27]</p>	<p>Randomized controlled clinical trial, nonblinded.</p>	<p>Oculus Go headset + 9 real natural landscapes 360 [°] videos (London's Natural History Museum and National Geographic).</p>	<p><b>IG(n:10):</b> VRT (videos for psycho-emotional health) + CT <b>CG(n:14):</b> CT (OT + PT based on each participant's goals and level of injury + psychological leisure therapy) + VRT.</p>	<p><b>Total period</b> = 2 weeks. <b>IG:</b> Week 1: 3 VRT sessions of 20 [min]. Week 2: 7 OT sessions + 20 [min] of PT. <b>CG:</b> Same as IG but in reversed per week.</p>	<p>PHQ-8 (Patient Health Questionnaire 8) and Feeling Intensity Evaluation (adapted Depression Intensity Scale Circles).</p>	<p>VRT (real landscape projection) + CT promoted inpatients' short-term psycho-emotional health as reflected in high levels of happiness, relaxation and feeling good, even when performed at the hospital. This had a positive impact on patients' engagement with rehabilitation. VRT can have a favorable impact as a complement to CT. Signs of depression were observed in the IG after VRT, possibly given that they were the first ones to experience it during the first week and not during the second one.</p>
<p>Tak S, et. al. (2015) South Korea [28]</p>	<p>Randomized controlled clinical trial, single-blinded.</p>	<p>Nintendo Wii + Wiimote + Wii Sports and Wii Sports Resort games with avatar (tennis, ping pong, box, golf, bowling, frisbee, canoeing and swordplay).</p>	<p><b>IG(n:13):</b> VRT (static and dynamic sitting balance training with UL and trunk) + CT. <b>CG(n:13):</b> CT (OT: sitting balance training, transfer to toilet and positioning + PT: stretching and strengthening).</p>	<p><b>Total period</b> = 6 weeks. <b>IG:</b> 3 VRT sessions of 30 [min] + 5 CT sessions of 90 [min] per week. <b>CG:</b> 5 CT sessions of 90 [min] per week.</p>	<p>mFRT, t-shirt test and the use of a forceplate for static balance ability, postural sway distance and velocity.</p>	<p>Game-based VRT (Nintendo Wii) + CT improved static and dynamic sitting balance for IG. It helped with raising the arms out to the sides and the head, improved balance in SCI, and had a positive effect on sitting postural balance. VRT can be used as a complement to CT both in hospital or home-based programs as it is an accessible system that can arouse patients' motivation and interest.</p>

Prasad S, et. al. (2018) India [29]	Pilot randomized controlled clinical trial, single-blinded.	Nintendo Wii + Wiimote + Wii Sports Resort games (ping pong, bowling, cycling and swordplay speed slice).	<p><b>IG(n:12):</b> VRT (dominant hand movements depending on the game) + CT.</p> <p><b>CG(n:10):</b> CT (OT: functional tasks for handling objects + PT: strength training with active or active-assisted movements of the target UL).</p>	<p><b>Total period</b> = 4 weeks.</p> <p><b>IG:</b> 3 VRT sessions of 30 [min] + 3 CT sessions of 30 [min] per week.</p> <p><b>CG:</b> 3 CT sessions of 30 [min] per week. Follow-up (IG=11, CG=9): 6 weeks after treatment.</p> <p><b>Follow-up (IG=11, CG=9):</b> 6 weeks after treatment.</p>	CUE (Capabilities of Upper Extremity questionnaire), BBT (Box and Block Test), SCIM-SR (self-report), WHOWOL-BREF (World Health Organization Quality of Life-BREF) and Satisfaction Evaluation based on VAS (Visual Analog Scale).	An intensive and repetitive VRT + CT improved UL motor function, similar as did CT alone. However, the IG had higher scores. A high level of satisfaction and adherence to treatment was reported, along with a drive for finding new self-improvement strategies based on game scoring and level of difficulty. VRT (Nintendo Wii) was considered as an adjunct to CT that could be used to develop home-based therapies and increase therapy duration. The improvements achieved were maintained during the follow-up period. No adverse effects were reported.
Sengupta M, et. al. (2020) India [30]	Controlled clinical trial, nonrandomized, double-blinded.	Rhetoric system (Microsoft Kinect + Rehametrics' neurological rehabilitation games + monitor).	<p><b>IG(n:25):</b> VRT (static and dynamic balance control training with UL and trunk, and static gait with LL) + CT.</p> <p><b>CG(n:12):</b> CT (based on patient needs and goals).</p>	<p><b>Total period</b> = 3 weeks.</p> <p><b>IG:</b> 5 VRT sessions of 30 [min] with 5 [min] of warm-up per week. CT time was not reported.</p> <p><b>CG:</b> Not reported.</p>	BBS, POMA-B (Performance-Oriented Mobility Assessment-Balance) and FRS (Functional Reach Score).	The improvements produced were similar in both groups, although the IG achieved a significant improvement in all outcome measures. The completeness of motor injury did not influence the effects of intervention on balance VR training. VRT is an enjoyable adjunct to CT that can be used for rehabilitation of balance control in SCI patients. Virtual objectives promoted full-body reach movements of the joints similar to those of ADLs. Neck and back pain were reported during the initial training sessions.
Sung W, et. al. (2012) Taiwan [31]	Before-and-after study, noncontrolled, nonrandomized, nonblinded.	Driving simulator (5 virtual driving routes and a single-axis tilting platform) developed by the authors.	<b>IG(n:12):</b> VRT (recovery and enhancement of driving skills with UL and LL).	<p><b>Total period</b> = 6 weeks.</p> <p><b>IG:</b> 2 VRT sessions of 30[min] or a bit more per week.</p>	Total driving time, average speed, center-line violation, stop-line violation, collisions, and steering or breaking stability	After five VRT sessions, improvements were observed in driving skills. The VR driving simulator had a positive effect on SCI driver training rehabilitation programs as a result of the challenges posed by the simulator's tilt effect in sitting posture and balance.
Villiger M, et. al. (2017) Switzerland [32]	Before-and-after study, noncontrolled, nonrandomized, nonblinded.	YouKicker (accelerometers) + 5 virtual environments created with Unity 3D ("Footbag", "Hamster Splash", "Get to the Game", "Star Kick" and "Planet Drive") + computer monitor.	<b>IG(n:12):</b> VRT (balance training and sitting/standing LL mobility with ADL: ankle dorsal flexion, knee extension and leg ad-/abduction).	<p><b>Total period</b> = 4 weeks.</p> <p><b>IG:</b> 16-20 VRT sessions of 30-45 [min] per week. (VRT with supervision by a physical therapist in the first session).</p> <p><b>Follow-up (IG=11):</b> 1-2 months after treatment.</p>	LEMS (Lower Extremity Motor Score), BBS, TUG (Timed Up and Go), WISCI II (Walking Index for Spinal Cord Injury), SCIM III, 10m and 6min Walking Test, Motivation Evaluation scored by 11-point NRS (Numeric Rating Scale) and the Patients' Global Impression of Change (PGIC).	Unsupervised home-based VRT improved muscle strength, balance and LL functional mobility promoted by structural brain plasticity due to intensive and repetitive movements. In addition, high levels of motivation were reported for all participants. It was noted that having trained with specific isolated movements, there was an overall motor functional improvement. The system is a useful tool for neurorehabilitation follow-up during or after supervised therapy in home-based training programs reducing cost and time of transportation. The presence of a therapist during VRT may help with motivation. There were no reports of pain or spasticity.

Note. IG: intervention group; CG: control group; VRT: Virtual Reality Therapy; TRT: Traditional Rehabilitation Therapy; OT: Occupational Therapy; PT: Physiotherapy; CT: Conventional Therapy (OT + PT); n: number of patients; ADL: Activities of Daily Living; UL: Upper Limb; LL: Lower Limb; EO: Eyes open; EC: Eyes closed; SCI: Spinal Cord Injury.

**TABLE 6. VRT effects achieved based on rehabilitation goal.**

STUDY	BALANCE CONTROL	MOTOR FUNCTION	PSYCHOLOGICAL ASPECTS	MOTIVATION/SATISFACTION
D'Addio G, et. al. [22]	✓*			
Dimbwadyo Terror I, et. al. [23]		X		✓
Dimbwadyo Terror I, et. al. [24]	✓	✓		
Gil Agudo A, et. al. [25]		✓*		
Khurana M, et. al. [26]	✓*	✓*		
Lakhani A, et. al. [27]			✓*	
Tak S, et. al. [28]	✓*			
Prasad S, et. al. [29]		✓*		✓
Sengupta M, et. al. [30]	✓*			
Sung W, et. al. [31]		✓*		
Villiger M, et. al. [32]	✓*	✓*		✓

Note. ✓: at least one relevant effect; X: no relevant effect achieved. \*statistically significant ( $p < 0.05$ ).

same treatment as those in the IG but without the VR component. The before-and-after study protocols only had one group of subjects on which they experimented with VRT independently [31] [32].

Most VRT, TRT, or CT activities focused on balance control [22] [24] [26] [28] [30] [32], ADL autonomy [23] [24] [25], other functional limb movements [29] [32], psycho-emotional health [27], and driving skills [31]. Only 2 studies based their CT on each subject's goals or needs [27] [30].

It should be highlighted that in 5 studies, VRT aimed at improving upper limb (UL) function [23] [24] [25] [28] [29]; in 1 study, VRT aimed at improving lower limb (LL) [32] function, and in 4 studies, VRT aimed at improving both UL and LL [22] [26] [30] [31] function. Some therapies also included trunk movements [22] [24] [26] [28] [30].

In most cases, VRT was supervised by an occupational therapist [23] [30], a physical therapist [22] [28] [30] [31], or several therapists [26] [32].

The number of VRT sessions varied from 3 to 80, with a frequency between 2 and 20 times per week over a total VRT period of 2 to 12 weeks, mostly with 30-minute sessions. Most of the studies were conducted at

specialized centers or hospital departments [23] [24] [25] [27] [28], or rehabilitation centers [22] [26] [29] [30] [31], while only 1 study [32] reported that VRT was administered at the patient's home and set up by a therapist.

It should be pointed out that in 7 studies [23] [24] [25] [26] [29] [30] [32], the level of difficulty of the virtual games or activities was adjusted (increasing/reducing speed or number of repetitions, changing object appearance, and interaction parameters) depending on the level of progress achieved by patients in the various VRT exercises. It is worth noting that one intervention [31], instead of including gradually increasing levels of difficulty according to the patient's progress, created a more challenging scenario that brought together all the isolated activities done in previous scenarios. The details of the interventions analyzed are included in Table 5.

## Outcome measures

The various scales, indices, or instruments used to evaluate the effects of interventions on UL and LL motor function, balance, functional independence in ADL, and psycho-emotional health associated with depression are presented in Table 5 according to the VRT applied in each study and where at least two or

more combinations were used. Only 3 studies [23] [29] [32] assessed the level of acceptance and motivation using patient satisfaction scales after the intervention.

Other studies came up with new outcome measures, such as the normalized trajectory length to measure movement trajectory precision improvement, and repeatability to measure movement precision improvement [24]. Similarly, kinematic variables [25] or the simulator's own aspects [31] were used to evaluate the effects of VRT.

### Effects of virtual reality therapy

There were 7 controlled clinical trials [23] [24] [25] [26] [27] [28] [30] that did not report significant differences between both intervention groups at baseline, which means that at the start of the studies, patients were in similar functional conditions. The effects of VRT are consolidated in Table 6. From then onwards, VRT was understood as being a mixed or as an individual therapy.

Only 9 papers reported a statistically significant difference in VRT ( $p < 0.05$ ) in balance control [22] [26] [28] [30] [32], motor function [25] [26] [29] [31] [32], and psychological aspects [27]. Furthermore, 3 studies assessed the effect size of the interventions, which was found to be between medium and large, with Cohen's  $d$  values between 0.41 and 0.84, and an  $\eta^2$  between 0.21 and 0.95 [23] [26] [27]. Similarly, the level of satisfaction [23] [29] and motivation [32] were assessed, and one study [26] subjectively observed a high level of interest and enthusiasm in patients during VRT.

### Side effects of virtual reality

There were no adverse or side effects reported, such as motion sickness, vertigo, muscle pain, or spasticity [23] [24] [29] [30] [32]. Only one study [27] reported significant signs of depression in its IG immediately after VRT. Another study [29] reported difficulty in holding the Wii-mote controller due to weak grip in seven patients, and another one mentioned [30] that during the inter-

vention there were some cases of back pain and orthostatic hypotension that were controlled and subsided with medication, allowing the therapy to continue as they were not deemed serious side effects.

### Limitation of the studies

Some of the controlled clinical trials indicated that their design did not include any type of blinding [22] [24] [25] [27], concealed allocation [22] [24] [25] [30], or even randomization [30]. In the before-and-after studies [31] [32], it was clear that there was no blinding as they did not include a CG in their design, which implied certain bias in the results.

Regarding subjects and protocols, it was not possible to generalize results given the limitations observed, such as small sample size [23] [24] [25] [28] [29] [30] [32], with particular SCI characteristics [23] [26] [28] [29] [32] and very few variations in demographic data [27], as well as the fact of having single selection sources [26].

As far as interventions are concerned, the identified limitations included: the short duration of intervention [23] [24] [27] [29] [31]; most studies did not follow-up on the results, except for 3 of them [23] [29] [32]; only 1 study explicitly recognized having included a small set of virtual exercises as a limitation [30]; the weight of any other health condition that could have influenced the results was not considered [27]; and the diversity of interventions did not make it possible to set guidelines on intensity, dosage, and duration of VRT [30].

As to the limitations derived from the VR technology, the need to have more sophisticated and modern software (commercial or especially designed games) and hardware (consoles, controllers, headsets, sensors, graphic cards) was identified for VRT to be more effective [26] [30]. The Wii Fit system especially stood out, because as it is a black box system, it was not possible to monitor several game parameters included in the VRT, thus limiting its contribution to improving balance control [22].

Three studies pointed out limitations in terms of interaction with VR devices, which could have affected the obtained results. Such was the case with the Nintendo Wii console [28] [29], where the patient required some prior training before using it.

Patients with acute SCI could not use it because they could not maintain balance, hold the controller, or even generate motion, especially in the case of higher cervical injuries. The third study identified predefined VR scenarios (360° recordings) as a limitation since patients could not interact with them [27].

### Future development

Based on the above-mentioned limitations, the subjects' profiles, and the intervention protocol, a suggestion was made to use a broader patient sample [23] [24] [25] [26] [27] [29] [30] [31] [32], with different SCI characteristics than the ones included in the studies [26] [29] [31] [32], involving several recruitment sites [30], and including more VRT sessions [23] [24] to better identify VRT benefits, the system's critical characteristics, and the virtual exercises that achieved better results [24].

The before-and-after studies [31] [32] along with one controlled clinical trial [30] proposed to carry out future interventions based on a blinded, randomized, controlled clinical trial with long-term follow-up design [30] [31] [32] to reduce the risk of bias and monitor the sustainability of the intervention by means of a longitudinal study to validate the level of skill improvement achieved [31].

Regarding types of VR devices, a proposal was made to conduct studies that combine VRT (such as TOyRA) with robotic devices (Amadeo) for telerehabilitation based on VR motion capture systems [25] and develop new VR devices for rehabilitation with a focus on ADL or relevant exercises/skills designed to simulate more realistic situations with higher levels of difficulty according to different SCI levels [31].

For interventions that used mixed VRT [22] [24] [29] [30], a proposal was raised to conduct new studies to assess the impact of VRT individually, compare the results of home-based therapies with those achieved at the clinic [32], and develop methods to exercise systematized balance control with a focus on SCI level and sitting balance control [28].

### Main findings, quality of evidence and potential application

This SR included a total sample of 243 subjects from the 11 papers analyzed, out of which 155 experimented with VRT (63.78%). There was a similar number of paraplegic (69) and tetraplegic (67) patients, and 14 patients did not complete the intervention. Patients treated with VRT mostly had ASIA grade A/B impairment (42.20% and 20.18%), followed by ASIA grades C/D (16.51% and 21.10%), with an absence of motor function and little or no sensory perception below the neurological level of injury, with a major focus on UL.

Three types of studies were taken into consideration: randomized controlled clinical trials [22] [23] [24] [25] [26] [27] [28] [29], one non-randomized controlled clinical trial [30], and before-and-after studies [31] [32]. Over half of the studies [23] [26] [28] [29] [30] [31] [32] had a good or excellent level of evidence with low risk of bias and achieved statistically significant results [26] [28] [29] [30] [31] [32] with regard to VRT.

The controlled clinical trials exhibited an adequate level of evidence given that they were mostly randomized [22] [23] [24] [25] [26] [27] [28] [29], with 6 of them having an adequate sample size [22] [23] [26] [27] [28] [29]. Seven [23] [24] [25] [26] [27] [28] [30] did not show any confounding bias upon observing a similar baseline functional condition among patients. Regarding blinding, half of them did not describe any blinding method [22] [24] [25] [27], while the remaining half that reported having used a double-blind [23] [26] or single-blind [28] [29] method reduced their detection bias upon including blinded assessors.

Given their methodological limitations, the before-and-after studies and the controlled clinical trials had to be considered with caution as they had a certain selection bias for not presenting any randomization method [30] or control groups [31] [32], which could have affected the VRT evidence obtained.

Most trials aimed at a non-immersive use [22] [23] [24] [25] [26] [28] [29] [30] [31] [32] of VR, and only 1 was fully-immersive [27]. All of them showed a statistically significant improvement with VRT ( $p < 0.05$ ) in balance control [22] [26] [28] [30] [32], motor function [25] [26] [29] [31] [32], and psychological aspects [27]. The effect size of the interventions [23] [26] [27] was determined to be between medium and large.

Regarding the type of VRT, although in some controlled clinical trials [23] [24] [25] [29] [30] no statistically significant differences were observed between the VRT + CT intervention compared to the CT, significant improvements were found in the IG in different functional parameters (Table 6). Additionally, in the remaining 4 trials [22] [26] [27] [28], statistically significant differences were observed in the IG that were reflected in a greater improvement compared to the CG. The sum of both results suggests that VRT can be an important adjunct/complementary instrument for CT when considering the benefits derived from the different protocols, particularly in terms of balance control, motor function, and patients' moods.

Moreover, even though the evidence was methodologically limited, it could be added that the before-and-after studies [31] [32] also showed positive effects of VRT when applied individually to improve LL motor function and driving skills, which speaks to the convenience of using VRT along with CT.

Furthermore, the findings [23] [25] [29] [32] suggest considering VRT as a complement to CT that can be used at home and not just in a hospital setting to extend the time of therapy sessions and to monitor and/or main-

tain the results achieved after rehabilitation. In this regard, the need for future studies to compare the effects of VRT in both settings was highlighted.

Comparatively, 4 controlled clinical trials [22] [24] [29] [30] underlined that it was not possible to visualize the effect of VRT separately, because it was applied together with CT. Thus, a proposal was made to conduct studies with the same methodological quality focused on interventions centered on VRT alone, with a broader and more diverse sample of SCI patients.

### **Efficacy of virtual reality therapy**

Most studies showed a good level of evidence for the use of VR technology applied to the rehabilitation of SCI patients based on a detailed description of its application, movements made, and patient interaction with the virtual environment. There was only one exception, where information was inferred from the system used [29].

Non-immersive VR was the most commonly implemented type of VR based on games with a scoring system and a set duration, whose level of difficulty was determined based on the progress recorded [22] [23] [25] [26] [28] [29] [30] [32].

Other study [32] mentioned that the type of VR used was augmented reality, which would require virtual objects to be projected onto real world surfaces. However, when the VR technological description was analyzed, it was clear that they had used a non-immersive system that displayed the virtual environment and objects on a screen.

It was interesting to see how fully-immersive VR technology [27] used to study patients' moods only focused on projecting videos of real landscapes without any means of interaction with the virtual environment, given the technological capabilities of the device. Although an improvement was achieved in patients'

psycho-emotional health, it will be necessary to gather more evidence on the effects of fully-immersive technology on VRT, related with physiotherapy and occupational therapy exercises, to analyze and determine the impact of this type of VR on the rehabilitation of SCI patients. Despite the technological differences inherent to each VR technology, such as the degree of immersivity and sensorimotor interaction, previous literature has shown different benefits of the use of the full-immersive VR and some of them points that full-immersive VR outperforms non-immersive [33] [34] [35].

Although all the interventions applied different immersive and non-immersive VR, some significant benefits were identified that can be generalized as follows: VR stimulated a wide set of functional movements similar to those of the real world; it promoted independence and self-confidence; it improved psycho-emotional health; it increased patient motivation and engagement with the rehabilitation process; and it promoted VRT with no side effects. Such evidence made it possible to confirm the potential use of VR technology as an effective tool for rehabilitation of SCI patients.

The efficacy of VR was confirmed based on a number of indicators reported by the studies. Firstly, there was positive feedback (visual and auditory) about therapeutic sessions designed around games that included a scoring system to help patients come up with new self-improvement strategies within certain timeframes and levels of difficulty established by the devices and/or adjusted by therapists, which made it possible to follow-up on the progress made.

In this regard, it was observed that the level of difficulty in each round prompted patients to make specific movements in an intensive and repetitive manner, which stimulated the subsequent recovery of motor function as a result of triggering neuroplasticity mostly in the motor cortex of the brain [23] [24] [26] [28] [29] [32].

Secondly, real-time visual feedback was another indicator of efficacy of VR environments for motor function recovery [26] [28] [29], that is, there was visual feedback of the patient's proper movement execution within the game's virtual environment with the use of an avatar through activation of certain areas of the motor cortex, leading to improved recovery [32]. There was also activation of the mirror neuron system and motor cortex of the brain by enabling recovery in spatial orientation and balance [30]. Furthermore, visualizing the patient's movements in real-time made by the avatar through mirror vision produced a feeling of control and realism with a similar positive effect on motor function [23].

Thirdly, given the importance of patients' motivation as an indicator of efficacy, it is interesting to see that this factor was assessed only by 3 studies [23] [29] [32], with high levels of satisfaction and motivation achieved during VRT. However, even when such an evaluation was not considered, another study [26] indicated that patients showed a high level of interest and enthusiasm towards VRT, and another one [30] observed that patients were open to develop new self-improvement strategies as a result of their experience with VRT. In summary, given the limited evidence on the level of patient acceptance of VRT, it is suggested that future research should include instruments to evaluate this aspect as well.

The findings from the above-mentioned evaluations showed that patients' satisfaction and motivation with VRT promoted a higher level of commitment, adherence, active engagement, and dedication to the rehabilitation process. Personal motivation due to VR was promoted by feelings of increased curiosity, self-confidence, self-driven exploration, and imagination which led to a greater enjoyment of the CT in addition to functional improvements [23] [29] [32]. Moreover, social motivation that led to the development of self-improvement and self-esteem were promoted through

competition as a result of the social interaction of patients based on the level of difficulty and scoring of VR games <sup>[23] [29]</sup>.

As it was confirmed in other studies <sup>[33] [34] [36]</sup>, these key elements are not induced by CT, which limits their level of effectiveness by showing low level of attendance and adherence to the training exercises, thus limiting the level of intensity necessary to achieve patient recovery.

This increase in motivation may be related to the influence of the video games used in VRT with a scoring and reward system (positive feedback) <sup>[29] [34]</sup>, and that it decreases the perception of effort <sup>[37]</sup>, which boost active patient participation and therefore increases adherence and commitment to the rehabilitation therapy.

In addition, some studies <sup>[35] [38]</sup> have confirmed that VRT promotes a deep motivation in patients, which improves their subjective initiative and commitment to actively complete various rehabilitation exercises, thus creating a virtuous circle that improves their functional recovery.

Some studies included in the SR underlined that the VRT was the most effective tool for improving neuroplasticity and subsequent recovery of motor function in SCI patients through intense and repetitive task-oriented practice by increasing exercise therapy time expressed as time dedicated to practice (dosage) compared to CT <sup>[36] [38]</sup>, which may enhance functional recovery <sup>[23] [26] [29] [30] [32] [34]</sup>. However, it is important to point out that other studies report that the evidence of neuroplasticity as a result of training in VR is currently modest and more research it is needed <sup>[38]</sup>. Also, it should be noted that the relation between dosage and achieving functional recovery is currently an unsolved issue in rehabilitation studies <sup>[30] [32] [36]</sup>, where the need for further evidence is highlighted.

There is some additional evidence resulting from the authors' perceptions during the interventions. For instance, when patients immersed themselves in VRT game activities, they forgot about certain fears that could have affected their performance vis-à-vis the objectives of the CT activities <sup>[26]</sup>. The projected images had a positive impact on the patients' moods and reduced the perception of pain from the SCI <sup>[27]</sup>, which reaffirmed the convenience of using VRT in conjunction with CT <sup>[28] [30]</sup>.

The importance of the familiarization process between the patient and the VR technology is a key element to achieve the objectives of the rehabilitation programs as it allows the patients to be engaged with the VRT and to perform the training exercises in a more effective way, thus promoting their active participation and motivation. In this regard, some studies have highlighted <sup>[26] [28] [33] [37]</sup> the limitations of commercial VR systems to fit the needs of SCI patients, since these are designed to be used by people without motor or cognitive impairments. Additionally, previous studies <sup>[34] [38] [39]</sup> have confirmed the importance of patients perceiving a greater immersion in the virtual environment rather than in the real world, which is related to the software and hardware characteristics.

Therefore, it is necessary that research teams seek to adapt existing devices to provide better grip and manipulation of the peripherals of VR systems <sup>[29] [33]</sup>, or still better to design new devices that allow an improved handling and capture of the movements made by patients according to their motor and cognitive skills, along with an appropriate calibration according to their neurological conditions <sup>[29]</sup>, which will increasing their interaction with the virtual environment, thus a better immersive experience.

On the other hand, another important element that allows patient familiarization is the sense of presence, which is related to the patients' subjective experience

of feeling inside the virtual environment and is able to activate brain mechanisms underlying sensorimotor integration as well cerebral networks regulating focused attention promoting patients to perform rehabilitation programs and patients' movement recovery [34] [37]. Since this also depends on the characteristics of the VR system itself [37], it is important that the games are able to imitate both in execution and visually the task-oriented activities and the virtual scenario, as well as to increase the sensory feedback through the peripherals, which allows a higher level of realism when interacting with 3D objects in real-time, for instance the realistic haptic feedback achieved by the CyberGlove compared to the simple feedback offered by most commercial consoles [24] [33]. In addition, as already pointed out by some studies included in this review, the patient's embodiment in the virtual avatar, either in one part (first person) or the whole body (third person), has a key role in developing a sense of presence in the virtual environment, as it allows the sensation that the actions performed belong to the patient [34]. In this sense the non-commercial devices achieved better results, especially TOyRA system [23] [25] by achieving an avatar based on the patients' anthropometric data.

In addition, it would be important to include induction training programs [30] [32] that make it possible to be familiar with the VR system and interact with greater confidence within the virtual environment. Therefore, all the elements that allow familiarization increase the acceptance of the system by the patient as he/she feels that real world movements are performed within the virtual environment, which allows to obtain adequate functional improvements by providing a better transfer of skills to the real world and open the possibility of continuing rehabilitation programs at home [23] [33].

Fourthly, another efficacy indicator was the ability to gradually reduce the help required from the therapist as therapy progressed, leading to more patient inde-

pendence to choose the VRT activities designed in accordance with the rehabilitation goals [23] [29]. Nevertheless, some authors reported that VRT had been more effective with the help of a therapist [32].

Fifthly, potential home-based rehabilitation and telerehabilitation were other key efficacy indicators of the use of VR technology based on commercial consoles and other devices. Having more intuitive, smaller sized, home-based systems could possibly increase the amount of time devoted to rehabilitation following therapy administered at the hospital or rehabilitation center. In this context, it should be stressed [23] that patients stated their interest in using the virtual system at home and would suggest its use to other patients with the aim of potentially creating an online gaming network to promote more socializing among patients and to extend therapy time.

Moreover, home-based VR rehabilitation could have a positive impact on reducing costs, time, effort, and travel of patients to the clinics, with systems being adapted to patients' needs, particularly those with a high SCI level [29] [32]. Based on the aforesaid, it would be necessary to have data capture systems imbedded in the consoles or in future rehabilitation dedicated devices that are capable of sending information of the activities performed at home to the therapist for analysis [25] [32].

It is important to emphasize that some features of the VR devices posed some potential limitations to the efficacy of VRT, for instance: the virtual environment used by the TOyRA system did not represent execution of ADL in a realistic fashion [23]; the commercial consoles or peripherals used in the interventions were relatively obsolete given the ongoing technological advances seeking to make VR more efficient and easy to use in rehabilitation; and the consoles or peripherals could not be easily modified (black box), thus preventing adaptation to patients' functional needs [22] [26] [28] [29] [30].

It should be noted that only one paper reported having used a graphic engine (Unity 3D) [32], given its relevance to the creation of virtual environments and the effect of VR on rehabilitation. Using a graphic engine implied a significant investment in terms of time and practice in order to create an appealing virtual environment where the patient can properly interact. Therapists collaborated on this design effort [23] [25] [32].

Finally, this SR identified some evidence of the impact of VRT in other neurological disorders, which confirms some of the findings for SCI, since the impaired motor function is one of its common consequences. For instance, some reviews have been identified concerning the use of VR technology applied to Stroke [38] [39] [40] [41], Parkinson's Disease [35] [42] [43], Multiple Sclerosis [37] [44], Cerebral Palsy [45] and Traumatic Brain Injury [46], which have reported positive effects of VRT improving balance control [35] [40] [42] [43] [44] [45] [46], UL or LL motor function [37] [38] [39] [40] [41] [45], gait [35] [40] [42] [43] [44] [46] and cognitive function [37] [42] [46]. A systematic review [47] showed positive impacts in the treatment of phantom limb pain due to a greater immersive experience based on the use of the mirror therapy which induces the perception that the amputated limb is performing the tasks. However, the authors are inconclusive regarding the efficacy of VR and Augmented Reality therapy and continues to need further research with higher quality evidence.

As is the case of the interventions with SCI patients, the role of VR as rehabilitation tool in these neurological disorders is still under discussion, although some studies reported positive results when VR was used as a complementary therapy which improved ADL performance and quality of life. These studies provided evidence points toward the advantages of increased motivation, confidence, engagement, and increase the intensity of movement based in repetitive and task-oriented with multisensory feedback which is needed for promoting neuroplasticity [35] [37] [39] [40] [43] [45] [46].

These results align with the main findings on the use of TRV in patients with SCI and for future development could be important to follow research on how the VR devices had been designed to these pathologies, including the greater use of VR full immersive and multisensory feedback [33].

In this regard, an interesting feature showed in a study applied to Stroke [40] was the introduction of a specific type of rehabilitation visual feedback named "virtual teacher", which can be displayed during every task repetition and that shows the correct execution movement of the training exercise so that the patient can imitate it allowing real-time visual comparison between a patient's execution and the virtual teacher's execution of a movement. The incorporation of this characteristic into the VR systems for SCI could improve the motor performance quality promoting motor adaptation via supervised learning mechanism.

### **Limitations and future work of the systematic review**

One of the main limitations was not having a larger number of papers providing evidence on the use of augmented reality and fully-immersive VR technology as a rehabilitation tool.

Patient sample heterogeneity as well as the application of different types of VR technology and VRT protocols made it impossible to generalize the results and applied therapies, and since this SR was guided by the Cochrane recommendations [14], it was deemed advisable not to do a meta-analysis.

Moreover, no controlled clinical trials were found to focus on the use of VRT individually in the IG compared only with the CT. This could be based on the fact that there is not much research on this, and it was not possible to access a more specialized, fee-based database.

The authors of this SR consider it necessary to update this SR in the future to largely include blinded, randomized, controlled clinical trials with long-term follow-up to reduce the risk of bias and follow-up on the sustained effects of the intervention.

### **CONCLUSIONS**

Given the evidence obtained from the papers included in the review, this SR concludes that non-immersive VR technology is an effective tool for use in neurorehabilitation as a complement to CT. It has positive effects by promoting motivation, self-confidence, commitment, and active engagement of patients, leading to improvements in motor function, and balance control, both in a clinical setting and at home, and it also increases rehabilitation time. No side effects were observed throughout the interventions.

Positive effects of VRT were identified when it was applied alone, although more evidence is needed to determine its contribution. Furthermore, there were psycho-emotional benefits reported with a decrease in depression in SCI patients when fully-immersive VR was used, although more research is needed to conclude its level of efficacy as a complementary tool to CT.

However, the high cost and the complexity of the new VR technology is a key limitation to extend the use for rehabilitation which may explain why the therapy based on video games consoles and non-immersion VR systems are playing an important role in rehabilitation programs even considering that these devices are not suitable to the needs of the SCI patients.

This SR suggest further development of VR systems customized to the motor and cognitive skills of SCI patients that achieves increased immersion with a higher level of realism of the rehabilitation activities, multisensory stimuli, and patient interaction, while trying to keep low-cost in order to increase accessibility.

### **AUTHOR CONTRIBUTIONS**

Both authors formulate and designed the systematic review; collected, selected, and extracted the data; assessed the risk of bias and methodological quality of included papers, and summarized the results. B.A.O.S. drafted the first version of the manuscript. Both authors reviewed the manuscript in depth and wrote the final version. Both authors analyzed and included the reviewers suggested comments.

## REFERENCES

- [1] World Health Organization. International perspectives on spinal cord injury [Internet]. Geneva: WHO; 2013. Available from: [https://www.who.int/disabilities/policies/spinal\\_cord\\_injury/en/](https://www.who.int/disabilities/policies/spinal_cord_injury/en/)
- [2] Latham R. Lesión de la médula espinal: Esperanza en la investigación [Internet]. Bethesda: National Institute of Neurological Disorders and Stroke; 2005. Spanish. Available from: [https://espanol.ninds.nih.gov/trastornos/lesion\\_de\\_la\\_medula\\_espinal.htm#:~:text=Las%20personas%20con%20lesiones%20de%20la%20m%C3%A9dula%20espinal%20tienen%20un,anticoagulante%20como%20medida%20de%20prevenci%C3%B3n](https://espanol.ninds.nih.gov/trastornos/lesion_de_la_medula_espinal.htm#:~:text=Las%20personas%20con%20lesiones%20de%20la%20m%C3%A9dula%20espinal%20tienen%20un,anticoagulante%20como%20medida%20de%20prevenci%C3%B3n)
- [3] Tortora GJ, Derrickson B. Principles of Anatomy and Physiology. 13th edition. Hoboken (NJ): J. Wiley & Sons; 2012.
- [4] Strassburguer-Lona K, Hernández-Porras Y, Barquín Santos E. Lesión Medular: guía para el manejo del paciente con LM crónica [Internet]. Madrid: Aspayam-Madrid; 2013. Spanish. Available from: <https://www.codem.es/guias/lesion-medular-guia-para-manejo-integral-del-paciente-con-lm-cronica>
- [5] Northwestern Medicine. Spinal Cord Injury [Internet] Chicago: Northwestern Medicine; 2020. Available from: <https://www.nm.org/conditions-and-care-areas/orthopaedics/acute-spinal-cord-injury>
- [6] Huete-García A, Díaz-Velázquez E. Análisis sobre la lesión medular en España [Internet]. Madrid: Aspaym; 2012. Available from: <http://riberdis.cedd.net/handle/11181/5510>
- [7] National Institute of Child Health and Human Development. How is SCI diagnosed? [Internet]. Bethesda: NICHD; 2016. Available from: <https://www.nichd.nih.gov/health/topics/spinalinjury/conditioninfo/diagnosed>
- [8] Pérez-Estudillo CA, Sánchez-Alonso D, López-Meraz ML, Morgado-Valle C, et al. Aplicaciones terapéuticas para la lesión de médula espinal. *Eneurobiología*. 2018; 9(21):141118. Spanish.
- [9] Navarrete JM. La realidad virtual como arma terapéutica en rehabilitación. *Rehabil Integral*. 2010;5(1):40-45. Spanish.
- [10] Navarro Araujo GMK. Realidad virtual en la terapia física [dissertation]. [Lima]: Universidad Inca Garcilaso de la Vega; 2017. Spanish.
- [11] Urrútia G, Bonfill X. PRISMA declaration: A proposal to improve the publication of systematic reviews and meta-analyses. *Med Clin [Internet]*. 2010; 135(11):507-511. Available from: <https://doi.org/10.1016/j.medcli.2010.01.015>
- [12] Moher D, Liberati A, Tetzlaff J, et al. Preferred Reporting Items for Systematic Reviews and Meta-Analyses: The PRISMA Statement. *PLoS Med [Internet]*. 2009; 6(7):e1000097. Available from: <https://doi.org/10.1371/journal.pmed.1000097>
- [13] Liberati A, Altman DG, Tetzlaff J, Mulrow C, et al. The PRISMA statement for reporting systematic reviews and meta-analyses of studies that evaluate healthcare interventions: explanation and elaboration. *BMJ [Internet]*. 2009;339:b2700. Available from: <https://doi.org/10.1136/bmj.b2700>
- [14] Centro Cochrane Iberoamericano. Manual Cochrane de Revisiones Sistemáticas de Intervenciones, versión 5.1.0 [Internet]. Barcelona: Centro Cochrane Iberoamericano; 2012. Available from: <http://www.cochrane.es/?q=es/node/269>
- [15] Silvera Iturrioz C. Algunas orientaciones prácticas para la búsqueda de información en LILACS y PUBMED [Internet]. Montevideo: e-prints in library & information science; 2013. Available from: <http://eprints.rclis.org/24012>
- [16] Clarivate Analytics. Web of Science Core Collection Help [Internet]. Web of Knowledge; 2020. Available from: [https://images.webofknowledge.com/WOKRS533JR18/help/WOS/hp\\_database.html](https://images.webofknowledge.com/WOKRS533JR18/help/WOS/hp_database.html)
- [17] National Center for Biotechnology Information. PubMed User Guide [Internet]. NCBI; 2020. Available from: <https://pubmed.ncbi.nlm.nih.gov/help>
- [18] BIREME. Tutorial de búsqueda LILACS [Internet]. BIREME; 2019. Available from: [https://wiki.bireme.org/es/index.php/Tutorial\\_de\\_b%C3%BAsqueda\\_LILACS](https://wiki.bireme.org/es/index.php/Tutorial_de_b%C3%BAsqueda_LILACS)
- [19] Zurita-Cruz JN, Márquez-González H, Miranda-Novales G, Villasis-Keever MA. Estudios experimentales: diseños de investigación para la evaluación de intervenciones en la clínica. *Rev Alerg Mex [Internet]*. 2018;65(2):178-186. Spanish. Available from: <https://doi.org/10.29262/ram.v65i2.376>
- [20] PEDro. PEDro scale [Internet]. Physiotherapy Evidence Database; 1999. Available from: <https://pedro.org.au/english/resources/pedro-scale>
- [21] National Institute of Health. Study Quality Assessment Tools [Internet]. NIH. Available from: <https://www.nhlbi.nih.gov/health-topics/study-quality-assessment-tools>
- [22] D'Addio G, Iuppariello L, Gallo F, Bifulco P, et al. Comparison between clinical and instrumental assessing using Wii Fit System on balance control. 2014 IEEE International Symposium on Medical Measurements and Applications (MeMeA) IEEE MeMeA [Internet]. Lisboa: IEEE; 2014:1-5. Available from: <https://doi.org/10.1109/MeMeA.2014.6860124>
- [23] Dimbwadyo-Terrer I, Gil-Agudo A, Segura-Fragoso A, de los Reyes-Guzmán A, et al. Effectiveness of the Virtual Reality System Toyra on Upper Limb Function in People with Tetraplegia: A pilot Randomized Clinical Trial. *Biomed Res Int [Internet]*. 2016;2016(6):6397828. Available from: <https://doi.org/10.1155/2016/6397828>
- [24] Dimbwadyo-Terrer I, Trincado-Alonso F, de los Reyes-Guzmán A, Aznar MA, et al. Upper limb rehabilitation after spinal cord injury: a treatment based on a data glove and an immersive virtual reality environment. *Disabil Rehabil Assist Technol [Internet]*. 2016;11(6):462-467. Available from: <https://doi.org/10.3109/17483107.2015.1027293>
- [25] Gil-Agudo A, Dimbwadyo-Terrer I, Peñasco-Martin B, de los Reyes-Guzmán A, et al. Experiencia clínica de la aplicación del sistema de realidad TOYRA en la neuro-rehabilitación de pacientes con lesión medular. *Rehabilitación [Internet]*. 2012;46(1):41-48. Spanish. Available from: <https://doi.org/10.1016/j.rh.2011.10.005>
- [26] Khurana M, Walia S, Noohu M. Study on the Effectiveness of Virtual Reality Game-Based Training on Balance and Functional Performance in Individuals with Paraplegia. *Top Spinal Cord Inj Rehabil [Internet]*. 2017;23(3):263-270. Available from: <https://doi.org/10.1310/sci16-00003>

- [27] Lakhani A, Martin K, Gray L, Mallison J, et al. What is the impact of engaging with natural environments delivered via virtual reality on the psycho-emotional health of people with spinal cord injury receiving rehabilitation in hospital? Findings from a pilot randomized controlled trial. *Arch Phys Med Rehabil* [Internet]. 2020;101(9):1532-1540. Available from: <https://doi.org/10.1016/j.apmr.2020.05.013>
- [28] Tak S, Choi W, Lee S. Game-Based Virtual Reality Training Improves Sitting Balance after Spinal Cord Injury: A Single-Blinded, Randomized Controlled Trial. *J Med Sci Technol* [Internet]. 2015;56:53-59. Available from: <https://doi.org/10.12659/MST.894514>
- [29] Prasad S, Aikat R, Labani S, Khanna N. Efficacy of Virtual Reality in Upper Limb Rehabilitation in Patients with Spinal Cord Injury: A Pilot Randomized Controlled Trial. *Asian Spine J* [Internet]. 2018;12(5):927-934. Available from: <https://doi.org/10.31616/asj.2018.12.5.927>
- [30] Sengupta M, Gupta A, Khanna M, Krishnan UKR, et al. Role of Virtual Reality in Balance Training in Patients with Spinal Cord Injury: A Prospective Comparative Pre-Post Study. *Asian Spine J* [Internet]. 2019;14(1):51-58. Available from: <https://doi.org/10.31616/asj.2019.0013>
- [31] Wen-Hsu S, Ting-Ying C, Wen-Wei T, Cheng H, Jin-Jong C. The effect of virtual reality-enhanced driving protocol in patients following spinal cord injury. *J Chin Med Assoc* [Internet]. 2012;75(11):600-605. Available from: <https://doi.org/10.1016/j.jcma.2012.08.004>
- [32] Villiger M, Liviero J, Awai L, Stoop R, et al. Home-Based Virtual Reality-Augmented Training Improves Lower Limb Muscle Strength, Balance, and Functional Mobility following Chronic Incomplete Spinal Cord Injury. *Front Neurol* [Internet]. 2017;8:635. Available from: <https://doi.org/10.3389/fneur.2017.00635>
- [33] Massetti T, Dias-da-Silva T, Brusque Crocetta T, Guarnieri R, et al. The Clinical Utility of Virtual Reality in Neurorehabilitation: A Systematic Review. *J Cent Nerv Syst Dis* [Internet]. 2018;10:1-18. Available from: <https://doi.org/10.1177/1179573518813541>
- [34] Tieri G, Morone G, Paolucci S, Iosa M. Virtual reality in cognitive and motor rehabilitation: facts, fiction and fallacies. *Expert Rev Med Devices* [Internet]. 2018; 15(2):107-117. Available from: <https://doi.org/10.1080/17434440.2018.1425613>
- [35] Cheng L, Kejimu S, Fengling D, Xiaoqin L, et al. Effects of virtual reality rehabilitation training on gait and balance in patients with Parkinson's disease: A systematic review. *PLoS One* [Internet]. 2019; 14(11):e0224819. Available from: <https://doi.org/10.1371/journal.pone.0224819>
- [36] Kwakkel G. Impact of intensity of practice after stroke: Issues for consideration. *Disabil Rehabil*. 2006;28(13-14):823-830. Available from: <https://doi.org/10.1080/09638280500534861>
- [37] Grazia Maggio M, Russo M, Foti Cuzzola M, Destro M, et al. Virtual reality in multiple sclerosis rehabilitation: A review on cognitive and motor outcomes. *J Clin Neurosci* [Internet]. 2019;65:106-111. Available from: <https://doi.org/10.1016/j.jocn.2019.03.017>
- [38] Laver KE, Lange B, George S, Deutsch JE, et al. Virtual Reality for stroke rehabilitation (Review). *Cochrane Database Syst Rev* [Internet]. 2017;11(11):CD008349. Available from: <https://doi.org/10.1002/14651858.CD008349.pub4>
- [39] Sin HH, Lee GC. Additional virtual reality training using Xbox Kinect in stroke survivors with hemiplegia. *Am J Phys Med Rehabil* [Internet]. 2013;92(10):871-880. Available from: <https://doi.org/10.1097/PHM.0b013e3182a38e40>
- [40] Kiper P, Luque-Moreno C, Pernice S, Maistrello L, et al. Functional changes in the lower extremity after non-immersive virtual reality and physiotherapy following stroke. *J Rehabil Med* [Internet]. 2020;52(11):jrm00122. Available from: <https://doi.org/10.2340/16501977-2763>
- [41] Norouzi-Gheidari N, Hernandez A, Archambault PS, Higgins J, et al. Feasibility, Safety and Efficacy of a Virtual Reality Exergame System to Supplement Upper Extremity Rehabilitation Post-Stroke: A Pilot Randomized Clinical Trial and Proof of Principle. *Int J Environ Res Public Health* [Internet]. 2019;17(1):113. Available from: <https://doi.org/10.3390/ijerph17010113>
- [42] Triegaardt J, Han TS, Sada C, Sharma S, et al. The role of virtual reality on outcomes in rehabilitation of Parkinson's disease: meta-analysis and systematic review in 1031 participants. *Neurol Sci* [Internet]. 2020;41(3):529-536. Available from: <https://doi.org/10.1007/s10072-019-04144-3>
- [43] Feng H, Li C, Liu J, Wang L, et al. Virtual Reality Rehabilitation Versus Conventional Physical Therapy for Improving Balance and Gait in Parkinson's Disease Patients: A Randomized Controlled Trial. *Med Sci Monit* [Internet]. 2019;25:4186-4192. Available from: <https://doi.org/10.12659/MSM.916455>
- [44] Casuso-Holgado MJ, Martín-Valero R, Carazo AF, Medrano-Sánchez EM, et al. Effectiveness of virtual reality training for balance and gait rehabilitation in people with multiple sclerosis: a systematic review and meta-analysis. *Clin Rehabil* [Internet]. 2018;32(9):1220-1234. Available from: <https://doi.org/10.1177/0269215518768084>
- [45] Ravi DK, Kumar N, Singhi P. Effectiveness of virtual reality rehabilitation for children and adolescents with cerebral palsy: an updated evidence-based systematic review. *Physiotherapy* [Internet]. 2017;103(3):245-258. Available from: <https://doi.org/10.1016/j.physio.2016.08.004>
- [46] Aida J, Chau B, Dunn J. Immersive virtual reality in traumatic brain injury rehabilitation: A literature review. *NeuroRehabilitation* [Internet]. 2018;42(4):441-448. Available from: <https://doi.org/10.3233/NRE-172361>
- [47] Dunn J, Yeo E, Moghaddampour P, et al. Virtual and augmented reality in the treatment of phantom limb pain: A literature review. *NeuroRehabilitation* [Internet]. 2017;40(4):595-601. Available from: <https://doi.org/10.3233/NRE-171447>

[dx.doi.org/10.17488/RMIB.42.2.9](https://doi.org/10.17488/RMIB.42.2.9)

E-LOCATION ID: 1156

## Numerical Simulation of a Physiological Mathematical Model of Energy Consumption in a Sarcomere

### Simulación Numérica de un Modelo Matemático Fisiológico de Consumo de Energía en un Sarcómero

K. G. Flores-Rodríguez<sup>1</sup>, D. E. Pérez-Garza<sup>2</sup>, G. Quiroz-Compeán<sup>3</sup>

<sup>1</sup>Departamento de Medicina Preventiva y Salud Pública. Facultad de Medicina, Universidad Autónoma de Nuevo León

<sup>2</sup>Dirección de Hospitales, Servicios de Salud de Nuevo León

<sup>3</sup>Facultad de Ingeniería Mecánica y Eléctrica, Universidad Autónoma de Nuevo León

#### ABSTRACT

The paradigm of biological systems provides a framework to quantify the behavior of biological processes. Mathematical modeling is one of the analytical tools of biological systems used to reproduce the variables of a system for prediction. This article presents the analysis of muscular contraction, the physiological process responsible of generating force in skeletal muscle, from the point of view of mathematical modeling. The aim is to provide numerical evidences about the force generated by the sarcomere, and the energy required to produce such a force. The proposed scheme includes a model to activate the contractile cycle, based on the action potential that reaches the neuromuscular junction, the calcium release into the sarcoplasm, the contraction response, and the quantification of the energy that the sarcomere requires to perform mechanical work. The results shows that the proposed scheme is acceptable because it reproduces experimental data of force, velocity, and energy reported in the literature. The results of the proposed scheme are encouraging to scale the model at the muscle or muscle group level, in such a way that the quantification of energy can be an alternative to the indirect estimation methods of energy consumption that currently exist.

**KEYWORDS:** Mathematical modeling; sarcomere; skeletal muscle; energy consumption

#### Corresponding author

TO: Griselda Quiroz Compeán

INSTITUTION: Universidad Autónoma de Nuevo León

ADDRESS: Av. Universidad S/N, Col. Ciudad

Universitaria, C. P. 66455, San Nicolás de los Garza,

Nuevo León, México

E-MAIL: [griselda.quirozcm@uanl.edu.mx](mailto:griselda.quirozcm@uanl.edu.mx)

#### Received:

28 January 2021

#### Accepted:

16 April 2021

## INTRODUCTION

Biological systems deal with the understanding of biological processes at the systems level. The initial ideas were established by Dr. Norbert Wiener in his book published in the 1940s [1]. However, the execution and confirmation of these ideas did not flourish due to technological (low availability of sensors, actuators, and computer systems), and scientific limitations (for example, the theory of nonlinear systems was in its infancy). It was not until early in this century that these ideas were taken up by the scientific community encouraged, primarily, by advances in molecular biology. The current availability of high-performance computer systems capable of processing copious amounts of data and of information-processing methods like machine learning, as well as the development of sensors capable of measuring biological variables in real time, have all fostered advances in biological systems. In addition, modern systems theory provides a broad platform of methodologies for the analysis, mathematical modeling, and control synthesis of highly-complex processes, including linear, nonlinear, continuous, discontinuous, and interconnected behaviors, to name a few [2].

The study of biological systems proposes a four-part paradigm for understanding a biological process at the systems level [3]. (1) System structure: identifying the elements of a process that interact and modify its physical properties. (2) System dynamics: understanding under what conditions certain properties of the process change in time and the repercussions of those changes for the functioning of the process. (3) Control method: once the natural dynamics of the biological process are known, it may be interesting to modify specific properties so that, depending on its structure and dynamics, it may become possible to propose a method for the systematic manipulation of a property. (4) Design method: strategies for the physical implementation of the resulting control scheme according to the first three points. The advantage of this paradigm

over the qualitative trial-and-error method used so widely in the biological sciences, is that it provides quantitative descriptions of the process that make it possible to predict the behavior of the properties of interest. Thus, it generates quantitative information, or design parameters, for experimental protocols that help optimize characterization methods and/or design and, more generally, our understanding of the biological process involved. Examples of applications of this paradigm can be consulted in the pioneering papers reported by Kitano [2][3]. The area of biological systems devoted specifically to human health is called systems medicine, a field that studies physiological processes, pathological conditions, and recommended treatments with the goal of providing quantitative elements to optimize medical treatments [4].

This article discusses a specific case of analysis of a biological process from the perspective of biological systems: energy consumption in a sarcomere, the basic functional unit of the contraction of skeletal muscle. The expenditure of energy is defined as the number of calories that people utilize to perform their basic vital functions, and to participate in physical activities [5]. Total energy expenditure depends on the total energy acquired from food. It is expended, approximately, in the percentages depicted in Figure 1 [6].

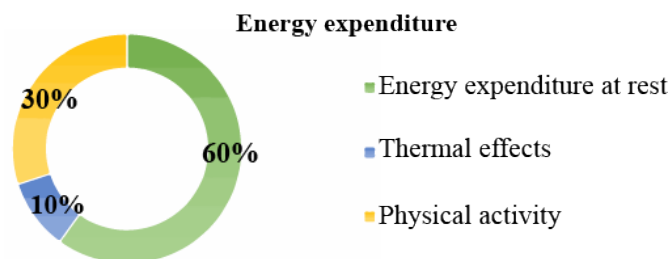


**FIGURE 1. Percentages of energy expenditure in the human body [6].**

Today, energy expenditure is measured by indirect calorimetry, a method that estimates the number of calories the human body consumes while performing

a physical activity like walking or running by measuring oxygen consumption ( $VO_2$ ) and carbon dioxide production ( $VCO_2$ ). This allows researchers to calculate the total energy expenditure of an entire human body [6]. Regarding knowledge of the structure of the human body, biological systems conceptualizes this as a system of systems, that can be analyzed on different scales of organization: molecular, cellular, tissue, or organ and, finally, as an integrated organism [4]. Indirect calorimetry gathers data on energy consumption at the level of the organism; that is, the highest level of analysis of the structure of a biological process, but in certain cases it may be important to determine the functioning of this process on another scale. For this reason, this article focuses on the question of the amount of energy consumed by a sarcomere during muscular contraction. To this end, we proposed a methodology of analysis centered on the structure and function of the process at the cellular level. The approach consist of a mathematical model of the contraction cycle of a sarcomere of skeletal muscle, which represents the dynamic behavior of the troponin units during the contraction cycle. Such dynamics determines the force generated and the velocity of the sarcomere, which are the elements to quantify the energy consumed by the sarcomere during contraction. Moreover, an activation scheme is presented in this paper, to model the voluntary activation of contraction cycle after the arrival of an action potential to the neuromuscular junction. The content of this article is as follows. The next section describes the physiological principles that lead a sarcomere to contract, a physiological function that provides muscular force and the energy required to generate such force. The section that follows outlines the methodology of mathematical modeling used to calculate the energy that a sarcomere requires to execute the contraction, and the conditions of the numerical implementation of the model utilized. The final part presents the results, discussion, and conclusions of the study.

## MATERIALS AND METHODS

### Muscular contraction

A skeletal muscle is a tissue that specializes in producing contractions. It is made up of cells called muscle fibers that have the capacity to contract individually. It is the synchronized contraction of the muscle fibers of a skeletal muscle that generates the force required to produce movement of the articulations to which it is joined. The movement produced by the skeletal muscle system is voluntary and results from the contraction and relaxation of these cells. To achieve movement, the muscle performs a series of functions that include generating force, transmitting the force, consuming, and storing energy, and producing heat.

During embryonic development, a series of myoblasts fuse to form a muscle fiber, so each fiber is a cell with multiple nuclei. The sarcolemma is cell membrane of the muscle fiber and the cytoplasm is known as the sarcoplasm. The organelles that provide muscle fibers with their contractile structure are called myofibrils. They are made of proteins that extend over the entire length of the muscle fiber. Myofibrils are formed by two elements denominated thick and thin filaments, which are organized in compartments called sarcomeres. Because contraction occurs in the sarcomeres, they are known as the basic functional units of the myofibrils [7]. Figure 2 illustrates the organization of a skeletal muscle, from the complete muscle down to the sarcomere.

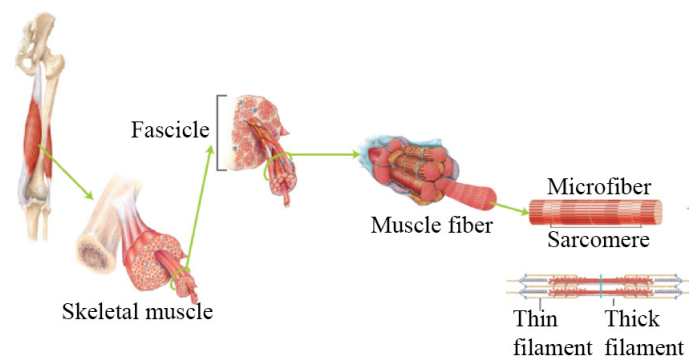
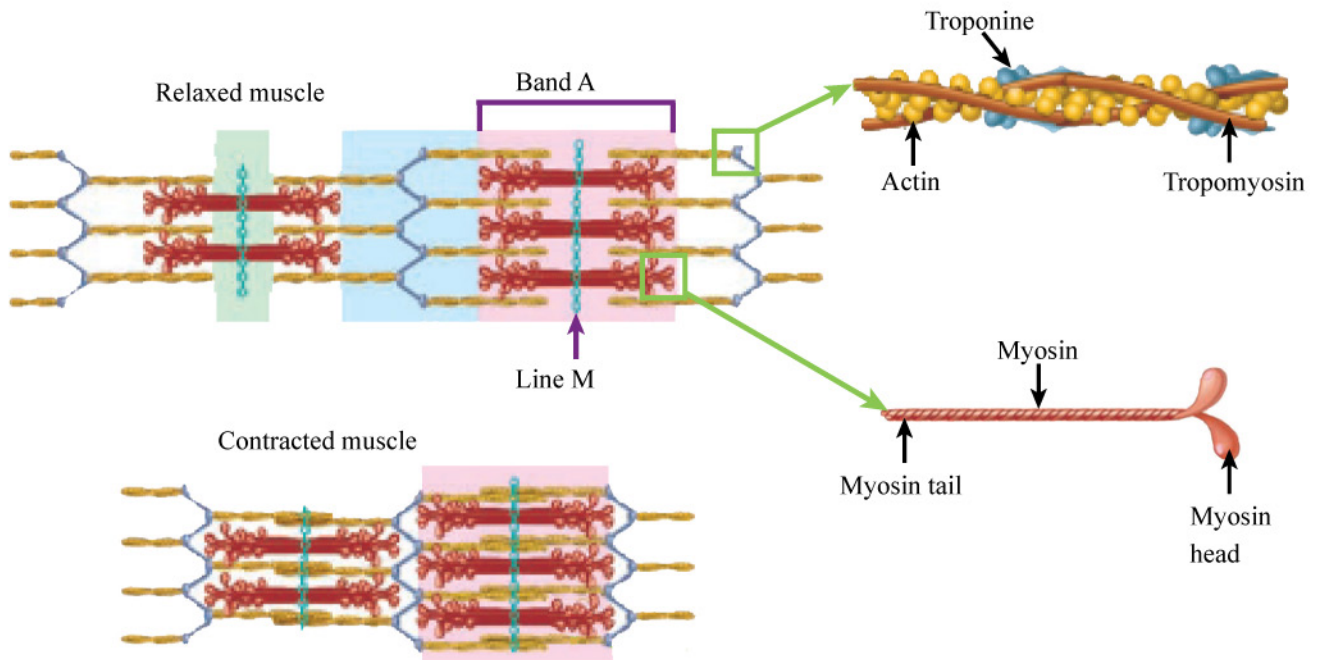


FIGURE 2. Organization of skeletal muscle tissue.

Edited from Tortora *et al.* [7].



**FIGURE 3. Thick and thin filaments in relaxation and contraction. Figure edited from Tortora et al.<sup>[7]</sup>.**

Three types of proteins define the structure and function of the sarcomere: (1) *Contractile proteins* are responsible for generating force during contraction. (2) *Regulator proteins* are in charge of activating and deactivating the contraction process. (3) *Structural proteins* form the thick and thin filaments that give the myofibrils their elasticity, extensibility, and ability to bond to the sarcolemma. The structure of the sarcomere is shown in Figure 3. The thin filaments (yellow) are composed mainly of a contractile protein called actin, while the thick filament (red) is formed by the contractile protein myosin. When a muscle is relaxed, the thick and thin filaments are superimposed in an area of the sarcomere called band A. The central part of band A contains the line M, formed by myomesin, a structural protein <sup>[7]</sup>. The regulator proteins, troponin and tropomyosin, form part of the thin filament, together they make up the troponin-tropomyosin complex. The structure of the sarcomere allows it to contract; that is, to shorten itself by overlapping the thick and thin filaments by through the transformation of energy, from chemical into mechanical <sup>[5] [6]</sup>.

The contractile cycle is activated when an action potential reaches the neuromuscular union and depolarizes the sarcolemma of the muscle fiber, releasing calcium ( $Ca^{2+}$ ) into the sarcoplasm.  $Ca^{2+}$  prepares the thin filament so that the thick filament can bond to it through the association of actin proteins with the heads of the myosin. Actin occupies a site related to myosin that is protected by tropomyosin during relaxation. When  $Ca^{2+}$  is available in the sarcoplasm, it associates with troponin such that the tropomyosin exposes the sites of the myosin-related actin sites to allow the heads of myosin to bond to that protein. These unions are called crossbridges. The troponin-tropomyosin complex is recognized as the regulator proteins of muscular contraction due to its function of preparing the thin filament to associate with the thick filament <sup>[7]</sup>.

The contractile cycle refers to the sequence of events that takes place during the movement of the filaments. It consists of four stages (see Figure 4). In the first stage (1), myosin becomes charged with energy

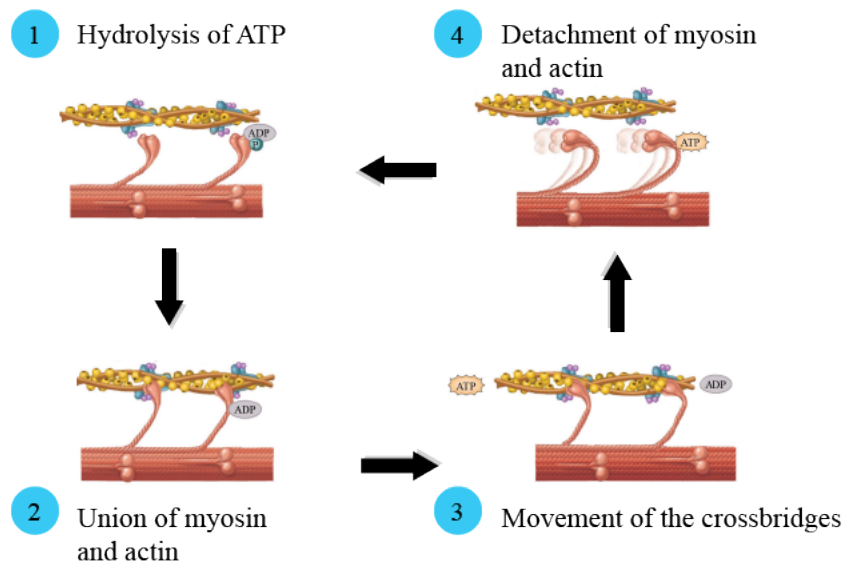


**FIGURE 4. Stages of the contractile cycle: (1) hydrolysis of ATP, (2) formation of crossbridges, (3) movement phase, and (4) detachment of myosin and actin. Figure edited from Tortora *et al.* [7].**

through the hydrolysis of adenosine triphosphate (ATP) molecules in its head. In this stage, the heads of the myosin are oriented towards the thin filaments. In the second stage (2), the energy-charged myosins adhere to the actin in the thin filaments to form crossbridges. In the third (3), the thick filament generates the traction necessary to move the thin filaments towards the line M, causing them to overlap and produce force in the sarcomere. When this movement concludes, in stage four (4), the myosin uncouples from the actin, ending the cycle. The contractile cycle is repeated as long as ATP molecules are available and the concentration of  $Ca^{2+}$  in the sarcoplasm remains high. The shortening of the sarcomeres in the myofibrils causes the muscle fiber -and then the complete muscle- to contract [7].

Muscular contractions are classified as either isotonic or isometric. In the former, the force of contraction developed by the muscle is constant, and the length of the muscle changes. This type of contraction generates movement of the joints and the force required to move loads or objects. In the latter, the force of contraction is insufficient to move a load or object; it only

generates sufficient force to sustain it, not move it. In this type of contraction, the muscle does not change its size [7]. Next, the mathematical modeling of muscular contraction is revised.

### Mathematical model of contraction

Most of the mathematical models proposed in the literature to emulate the mechanical behavior of skeletal muscles are based on the one posited by Hill *et al.* [8], that is, addressing the mechanical response of muscle at the tissue level [9] [10]. Mathematical modeling of the mechanical response of the muscle, in contrast, is based on the physiological principles of the origin of muscular contraction in the sarcomere of the skeletal muscle. This physiological approach has been used in mathematical modeling of cardiac muscle; the approaches range from initial models proposing the mechanical response of a single sarcomere of cardiac muscle [11], multi-scale mathematical modeling of the heart mechanics [12] [13] to current *in silico* models used in preclinical trials to assess drugs for cardiac diseases [14]. While our approach sets out from current physiological models of the sarcomere of cardiac muscle, it proposes an adaptation to represent the contractile

response of the sarcomere of skeletal muscle. The main function of both types of tissue is to generate muscular contraction, but their activation mechanisms differ: the heart muscle is activated involuntarily, while activation of skeletal muscle is voluntary, triggered by the emission of an action potential from the motor cortex to the neuromuscular union. This permits control of the onset of the contractile cycle through the release of  $Ca^{2+}$  into the sarcoplasm. The model proposed herein includes the effect of the voluntary activation of muscular contraction through the signal generated in the neuromuscular union while also quantifying the energy consumption that this process requires.

Landesberg *et al.* proposed a physiological model of the contraction of the sarcomere based on an analysis of the dynamics of the regulator protein troponin during the contractile cycle<sup>[11]</sup>. They called the relaxation stage the phase of ATP hydrolysis. Here, the sarcomere is relaxed, the crossbridges are in a weak conformation (not force-generating), and  $Ca^{2+}$  is not bonded to troponin. They defined the parameter  $R$  (in  $\mu\text{M}$ ) as the number of units of troponin available in this stage. The bonding of  $Ca^{2+}$  to troponin defines the activation stage, when the crossbridges prepare to generate force. The variable that measures the number of troponin units associated with  $Ca^{2+}$  is  $A(t)$  (in  $\mu\text{M}$ ). The time variation of  $A$  is defined by the next differential equation:

$$\frac{dA}{dt} = k_L R C a^{2+} - (k_{-l} + f)A + gT, \quad (1)$$

where the left-side of the Equation (1) stands for the accumulation of  $A$  (number of troponin units per unit of time), and the right side stands that such accumulation is directly proportional to  $Ca^{2+}$  concentration in sarcoplasm and the number of troponin units available in the relaxation stage. The rate of association of troponin units with  $Ca^{2+}$  is represented by  $k_L$  (in  $\mu\text{M}^{-1}\text{s}^{-1}$ ). Accumulation of  $A$  could decrease by the disposition of troponin units, the rate of  $Ca^{2+}$  dissociation ( $k_{-l}$  in  $\text{s}^{-1}$ ),

and the transition rate of the crossbridges between conformations ( $f$  in  $\text{s}^{-1}$ ).  $f$  is defined by  $f = f_0 + f_1 V(t)$ , where  $f_0$  (in  $\text{s}^{-1}$ ) is the transition rate in isometric state, and  $f_1$  (in  $\mu\text{m}^{-1}$ ) is the rate of dependence on the velocity of the shortening of the sarcomere ( $V(t)$  in  $\mu\text{m}/\text{s}$ ). Accumulation of  $A$  are also promoted by the number of troponin units defining the strong crossbridges  $T(t)$  (in  $\mu\text{M}$ ). This relation is proportional to the transition rate of the crossbridges from strong to weak conformation ( $g$  in  $\text{s}^{-1}$ ), defined as  $g = g_0 + g_1 V(t)$ , where  $g_0$  (in  $\text{s}^{-1}$ ) is the rate of the weakening of the crossbridges during isometric contraction, and  $g_1$  (in  $\mu\text{m}^{-1}$ ) defines the velocity on the rate of the crossbridges in the weak conformation.

The traction of the thick filaments over the thin filaments through the available crossbridges results in the movement of the latter, generating force in the sarcomere. This is the stage where the crossbridges change from their weak (not force-generating) to strong (force-generating) conformation. The accumulation of troponin units in this stage is defined by the next differential equation:

$$\frac{dT}{dt} = fA - (g + k_{-l})T + k_L U C a^{2+}. \quad (2)$$

Such accumulation is directly proportional the number of troponin units associated to  $Ca^{2+}$  at the transition rate of the crossbridges between conformations. The accumulation of  $T$  can be decreased by the number of troponin units in this stage at the rate defined by the addition of the transition rate of the crossbridges from strong to weak conformation and the rate of  $Ca^{2+}$  dissociation. Nevertheless, accumulation of  $T$  is also promote by the number of troponin units that regulate crossbridges still in the stage of strong conformation, but in which the  $Ca^{2+}$  has not been disassociated, defined by  $U(t)$  (in  $\mu\text{M}$ ). This last promotion is proportional to the  $Ca^{2+}$  concentration and the rate of association of troponin units with  $Ca^{2+}$ . Regarding the accumulation of  $U$ , it is defined by the next differential equation:

$$\frac{dU}{dt} = k_{-l}T - (k_LCa^{2+} + g)U. \quad (3)$$

This equation represents the time variation of  $U$ , in which the accumulation is defined by a function directly proportional to the units of troponin in the strong crossbridges and the rate of  $Ca^{2+}$  dissociation. The accumulation of  $U$  can be decreased by the unit  $U$  available in this stage at a rate defined by the addition of the association rate of troponin units with  $Ca^{2+}$  and the transition rate of the crossbridges from strong to weak conformation.

Finally, the dynamical behavior of the troponin units in all stages of the contractile cycle is determined by the concentration of  $Ca^{2+}$  in the sarcoplasm, which accumulation is defined as:

$$\frac{dCa^{2+}}{dt} = (I_{in} - I_{out}) + k_{-l}(A + T) - k_LCa^{2+}(R + U), \quad (4)$$

where  $I_{in}$  e  $I_{out}$  (both in  $\mu Ms^{-1}$ ) are the flow currents of  $Ca^{2+}$  through the sarcoplasm and the sarcoplasmic reticulum, activated by the depolarization of the sarcolemma when an action potential reaches the neuromuscular union.  $Tro$  (in  $\mu M$ ) represents the number of troponin molecules present in the entire contractile cycle:  $Tro=R(t)+A(t)+T(t)+U(t)$ . Equations (1)-(4) define the mathematical model of the contraction of a sarcomere [11]. In the next subsection, the equations to compute the force generated by the sarcomere are presented. Force is related to the velocity of the shortening of the sarcomere,  $V(t)$ , as well as the troponin units  $T$  and  $U$  defined in Equation (2) and (3).

### Force-velocity relation

Setting out from the assumption that each crossbridge is a pseudoviscous Newtonian element, the force generated by the sarcomere is defined as (Assumption 5 in Landesberg *et al.* [15]):

$$F(t) = L_s(T + U)(\bar{F} - \eta V(t)) \quad (5)$$

where  $L_s$  (in  $\mu M$ ) is the length of the overlap between the thin and thick filaments,  $(T+U)$  is the total number of crossbridges in the strong conformation, and  $(\bar{F} - \eta V(t))$  is the force generated in each crossbridge.

$\bar{F}$  (in  $\mu Nm$ ) is the unitary force supplied by each crossbridge in the isometric condition,  $\eta$  (in  $Ns$ ) is the coefficient of pseudoviscosity of the crossbridges, defined as

$$\eta = \frac{\bar{F}}{V_u} \quad (6)$$

and  $V_u$  (in  $\mu m/s$ ) is the maximum velocity of the shortening of the sarcomere [16].

The sarcomere at rest constitutes the stationary state of the system of differential Equations (1)-(4), so  $A^*$ ,  $T^*$ ,  $U^*$  and  $Ca^{2+*}$  are the values of the equilibrium point -or stationary state- that satisfy the system of algebraic equations which emerges upon setting the derivatives of the system (1)-(4) to zero; that is:

$$k_LCa^{2+*}R - (k_{-l} + f)A^* + gT^* = 0, \quad (7)$$

$$A^* - (g + k_{-l})T^* + k_LCa^{2+*}U^* = 0, \quad (8)$$

$$k_{-l}T^* - (k_LCa^{2+*} + g)U^* = 0, \quad (9)$$

$$(I_{in} - I_{out}) + k_{-l}(A^* + T^*) - k_LCa^{2+*}(R + U^*) = 0. \quad (10)$$

Calculating the force-velocity ratio requires Equation (5) and the substitution of  $T^*$  and  $U^*$  from the system defined by Equations (1)-(4). This produces the following equation:

$$(F_h + a_h)(V(t) + b_h) = (F_m + a_h) b_h. \quad (11)$$

Landesberg *et al.* [17] accommodated the terms such that Equation (11) is expressed in the form of Hill's force-velocity ratio equation [18], where  $F_h$  is the force in the stationary state:

$$F_h = \frac{g_0 F_m \left(1 - \frac{V(t)}{V_u}\right)}{(g_0 + g_1 V_u)} \quad (12)$$

and  $F_m$  is the force generated by the muscle during isometric contraction:

$$F_m = L_s Tro^* \bar{F} \left(\frac{k_l}{k_l + k_{-l}}\right) \left(\frac{f}{g_0 + f}\right), \quad (13)$$

with  $Tro^* = R + A^* + T^* + U^*$ ,  $k_l = k_l Ca^{2+}$ , where  $a_h$  and  $b_h$  are Hill's parameters, defined as follows:

$$a_h = \frac{\eta F_m b_h}{\bar{F}} \quad (14)$$

and

$$b_h = \frac{g_0 + f}{g_1} \quad (15)$$

Upon initiating a movement, the muscle passes from the relaxed to the contracted state, where the muscle fibers change their length by contracting, thus producing movement (isotonic contraction).

The velocity generated by the sarcomere in the isotonic state is given by the expression [17]:

$$V(t) = V_h \frac{1 + \frac{V_u(V_0 - V_h)}{V_h(V_u - V_0)} e^{-(g_0 + g_1 V_u)t}}{1 + \frac{V_0 - V_h}{V_u - V_0} e^{-(g_0 + g_1 V_u)t}} \quad (16)$$

where  $V_h$  is the velocity in the stationary state, defined as:

$$V_h = \frac{g_0(F_m - F)}{(g_1 + L_s^{-1})F + g_0 F_m V_u^{-1}} \quad (17)$$

$V_0 = V(0)$  (in  $\mu\text{m/s}$ ) is the initial condition (in  $t=0$ ) of the velocity of the shortening of the sarcomere. Upon integrating Equation (16), we obtain the change in the length of the shortening of the sarcomere, given by the expression [17]:

$$L(t) = V_h t + \frac{V_0 + V_h}{g_0 + g_1 V_u} \left(1 - e^{-(g_0 + g_1 V_u)t}\right) \quad (18)$$

This equation makes it possible to obtain the length of a sarcomere ( $SL$ ) at a certain time as:  $SL(t) = SL(0) + L(t)$ , where  $SL(0)$  is the initial length of the sarcomere. In addition, the length of the overlap required to calculate the force generated by the sarcomere, defined in Equation (5), is obtained from the length of the sarcomere, given by the following ratio [19]:

$$L_s = \frac{SL - L_\varphi}{2} \quad (19)$$

where  $L_\varphi$  is the length of the filaments of actin and myosin in a simple overlap during contraction. Likewise, the force generated by the sarcomere due to isotonic contraction at a certain moment (also called transitory force) is given by the expression [17]:

$$F(t) = F_h + (F_0 - F_h) e^{-(g_0 + g_1 V_u)t} \quad (20)$$

where  $F_0 = F(0)$  is the initial condition (at  $t=0$ ) of the force generated by the sarcomere.

## Energy consumed

As mentioned in the description mathematical model of contraction of a sarcomere defined by Equations (1)-(4), the number of crossbridges that pass from the weak to the strong conformation is represented by the variable  $A(t)$ ; that is, the troponin molecule linked to  $Ca^{2+}(t)$  each one of which corresponds to a crossbridge.

The crossbridges in the strong (force-generating) conformation are represented by the variable  $T(t)$ . Each crossbridge in the strong conformation requires a unit of ATP hydrolysis and the release of phosphate, in order to pass from the weak to the strong conformation [20] [21]. Hence, the rate of energy consumption ( $\frac{dE}{dt}$ ) is determined by three elements: (1) the variable  $A(t)$ ; (2) the transition rate of the crossbridges from the weak to the strong conformation ( $f$ ); and (3) the length of the overlap ( $L_s$ ). This process is modeled by the next differential Equation (15):

$$\frac{dE}{dt} = E_{ATP} f L_s A(t) \quad (21)$$

where  $E_{ATP}$  is the free energy released from the hydrolysis of a simple ATP molecule, given by [15]

$$E_{ATP} = \frac{\bar{F}V_u}{\rho(g_0 + g_1V_u)} \quad (22)$$

where  $\rho = 1/g_1$ .

### Model of $Ca^{2+}$ release

Finally, we propose an adaptation of the contraction model defined by Landesberg *et al.* and represented by Equations (1)-(4) [11]. As it was mentioned before, the model proposed by Landesberg reproduces the dynamics of contraction of a sarcomere of cardiac muscle; although both cardiac and skeletal produce contraction, their activation mechanisms are different. In the cardiac muscle, the contraction is carried out automatically as long as there is  $Ca^{2+}$  in the sarcoplasm; this is, there exist a constant influx of  $Ca^{2+}$  currents, then the term  $(I_{in} - I_{out})$  in Equation (4) is constant. The activation mechanism changes in skeletal muscle, where the contraction is activated when an action potential pulse arrives at the neuromuscular junction and this generates a variation of  $Ca^{2+}$  currents, that is, the term  $(I_{in} - I_{out})$  in Equation (4) is a time-varying function depending on the action potential. For this reason, to reproduce

the contraction in a sarcomere of skeletal muscle, the force that it generates and, finally, the energy that it consumes during contraction, it is necessary to have a mathematical model to emulate the dynamic response of  $Ca^{2+}$  currents ( $I_{in} - I_{out}$ ) caused by the depolarization of the sarcolemma in response to the arrival of the action potential (AP) at the neuromuscular junction, and then producing voluntary contraction of skeletal muscle.

For this end, we propose an activation scheme based on a mathematical model to reproduce the input-output response of the dynamics of calcium release in the sarcoplasm. Figure 5 shows this proposal in which the objective is to have a dynamic model based on a transfer function, called model of  $Ca^{2+}$  release, whose output is the calcium currents through the membrane, this term  $(I_{in} - I_{out})$ .

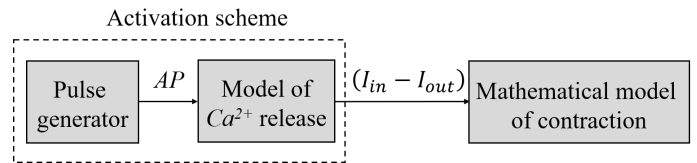


**FIGURE 5. Activation scheme of the mathematical model of contraction of a sarcomere of skeletal muscle. The scheme is based on a transfer function with input data form a train of pulses (AP), the output data correspond to the total  $Ca^{2+}$  current  $(I_{in} - I_{out})$  reported by Beuckelmann *et al.* [22].**

In turn, this term is the one that initiates the contraction cycle defined by the model defined in Equations (1)-(4) represented by the right block of Figure 5 (mathematical model of contraction). The input of the model of  $Ca^{2+}$  release is a pulse generator emulating the AP, illustrated by the left block of Figure 5. Thus, the problem is to compute an input-output model of  $Ca^{2+}$  release based on available data of AP and  $(I_{in} - I_{out})$ .

The input data of the model of  $Ca^{2+}$  release is represented by a train of pulses that emulates the AP which reaches the neuromuscular junction. Regarding output

data, existing literature has no separate measurements of the currents of  $Ca^{2+}$  entering ( $I_{in}$ ) or leaving ( $I_{out}$ ) the sarcoplasm, but experimental studies have measured the total influx of  $Ca^{2+}$  current, that is ( $I_{in}-I_{out}$ ). Thus, the output data used to compute the model of  $Ca^{2+}$  release are experimental measurements of the total  $Ca^{2+}$  current ( $I_{in}-I_{out}$ ) reported by Beuckelmann *et al.* [22].

## RESULTS AND DISCUSSION

To devise the model that reproduces the dynamics of total  $Ca^{2+}$  current in the sarcoplasm, the diagram in Figure 5 posits a problem of system identification. To resolve it, we set out from the disposition of input and output data from the process analyzed. Thus, we propose that the input data take the form of a train of pulses of unitary amplitude with a work cycle of 0.5, to emulate the wave form of the AP that reaches the terminal of the neuromuscular union. The output data ( $I_{in}-I_{out}$ ) are taken from Beuckelmann *et al.* (see Figure 5 in [22]). Based on a set of points in the referenced figure, we obtained a sufficient series of data (1000 samples) by adjusting a polynomic curve using MATLAB's® polyfit library. Based on observations of the input and output data, we propose that the mathematical model take the form of a transference function. To define the order of the polynomials of the function, and their parameters, we employed MATLAB's® ident systems identification tool, which resulted in a second-order transference function that defines the dynamics of the total  $Ca^{2+}$  current in the sarcoplasm after the arrival of the stimulus of the action potential at the neuromuscular union:

$$\frac{(I_{in} - I_{out})}{AP} = \frac{-0.9916s + 406.4}{s^2 + 7.71s + 1055} \quad (23)$$

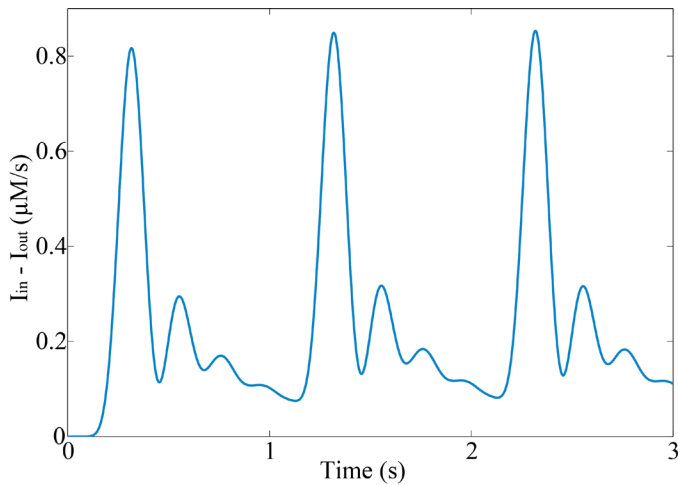
The percentage of fit between the proposed model and the experimental data was 84%. Using Equation (23) we can calculate ( $I_{in}-I_{out}$ ) and substitute it in Equation (4) of the mathematical model of contraction to obtain the elements required to numerically simulate the dynam-

ics of contraction of the sarcomere defined by the system of Equations (1)-(4). The numerical solution was elaborated using MATLAB® and Simulink®. Initial conditions were:  $A(0)=0$ ,  $T(0)=0$ ,  $U(0)=0$  and  $Ca^{2+}(0)=0$ . The numerical method applied to solve the differential equations was the Runge-Kutta approach, available in MATLAB's® ode45 library. The solution interval was 0-3 seconds, and the integration step was 0.0001 s. The nominal parameters used to solve the system of the dynamics of muscular contraction, to calculate the force-velocity relation, and to obtain the energy consumed during contraction, are summarized in Table 1.

**TABLE 1. Values of the nominal parameters used in the numerical simulations.**

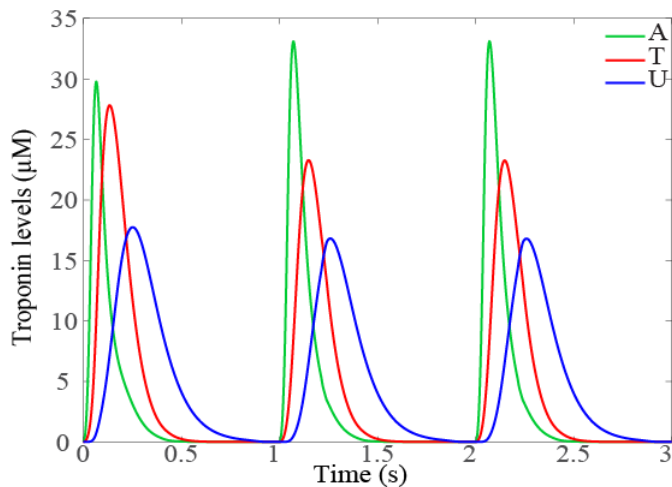
Parameter	Value	Reference
<b>Dynamics of contraction of the sarcomere</b>		
$k_L$	200 $\mu M^{-1}s^{-1}$	[15]
$k_{-L}$	20 $s^{-1}$	[19]
$f_0$	50 $s^{-1}$	[15]
$f_i$	2.5 $\mu M^{-1}s^{-1}$	[15]
$g_0$	10 $s^{-1}$	[15]
$g_i$	35 $\mu M^{-1}s^{-1}$	[15]
<b>Force-velocity ratio</b>		
$\bar{F}$	2 pN	[23]
$\eta$	0.28 pNs/ $\mu m$	[17]
$Tr_0$	53 mM	[15]
$V_u$	7 $\mu m/s$	[19]
$V_0$	0 $\mu m/s$	[19]
$SL(0)$	2.2 $\mu m$	[15]
$L_\varphi$	0.8 $\mu m$	[19]
<b>Energy consumed</b>		
$E_{ATP}$	1.92 mM	[17]

Figure 6 presents the results of the current of  $Ca^{2+}$  in the sarcoplasm in response to three nervous impulses that reached the neuromuscular junction. These results are considered reliable for simulating the input of  $Ca^{2+}(t)$  to the model (1)-(4) since the basal  $Ca^{2+}$  concentration in the cells is approximately 0.1  $\mu M$  [20].



**FIGURE 6.** Currents of  $Ca^{2+}$  in the sarcoplasm ( $I_{in} - I_{out}$ ) when three impulses of AP are generated in the activation scheme of Figure 5 considering the model of  $Ca^{2+}$  release in Equation (23).

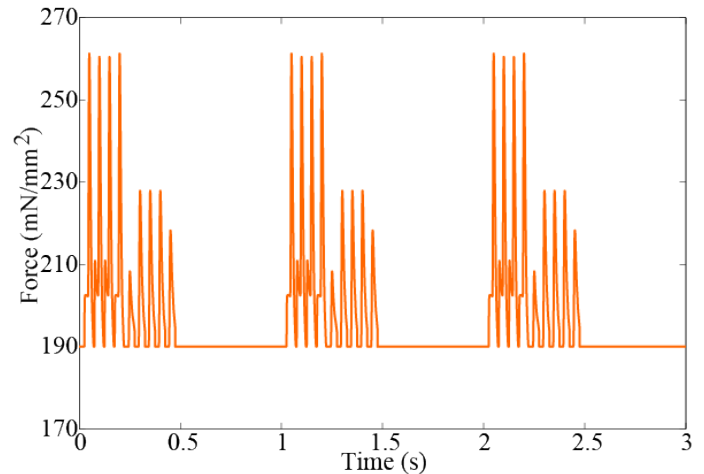
Figure 7 shows the solution of the dynamic model of muscular contraction of the system of Equations (1)-(4) using the  $Ca^{2+}$  current ( $I_{in} - I_{out}$ ) obtained from Equation (23).



**FIGURE 7.** Numerical solution of the mathematical model of troponin units in the activation stage of the crossbridges of the contraction cycle.

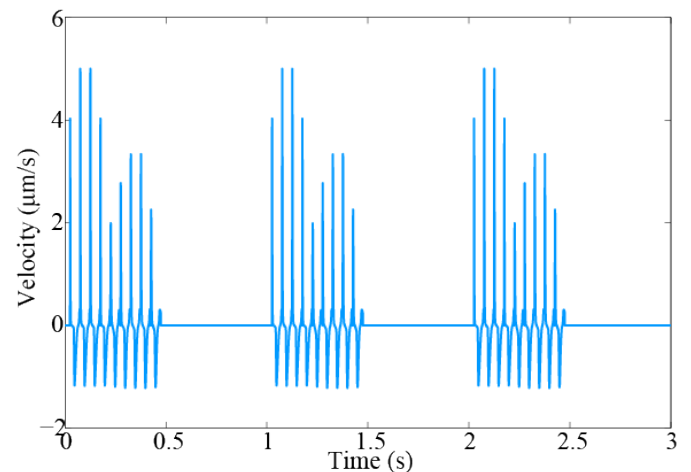
$A(t)$  and  $T(t)$  are the troponin units during the strong conformation of crossbridges;  $U(t)$  are the troponin units in the strong conformation of crossbridges without associated  $Ca^{2+}$ .

Figure 8 presents the force generated by the sarcomere during a 3-second period, determined by Equation (20).



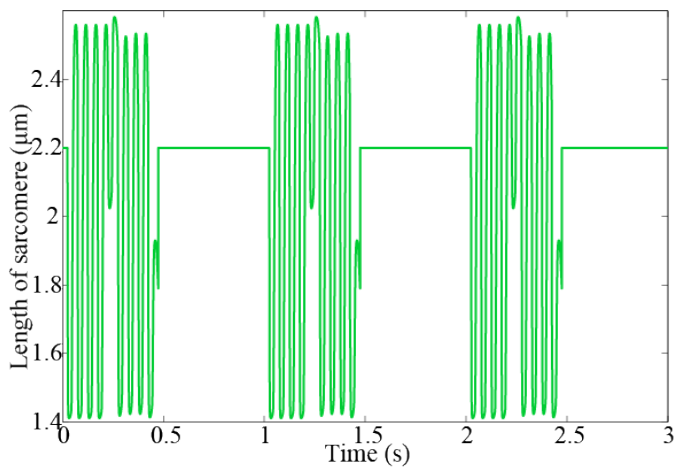
**FIGURE 8.** Force generated by the sarcomere of skeletal muscle during activation of three action potentials.

Figure 8 shows that when  $Ca^{2+}$  levels are high (see Figure 6), the force is greater and remains constant during the 0.5-second period in which  $Ca^{2+}$  is  $0.1 \mu M$ . Likewise, the variables  $A(t)$ ,  $T(t)$  and  $U(t)$  tend to return to their initial values in that period, as Figure 7 shows. Figure 9 indicates the shortening velocity obtained from the simulation of Equation (16).



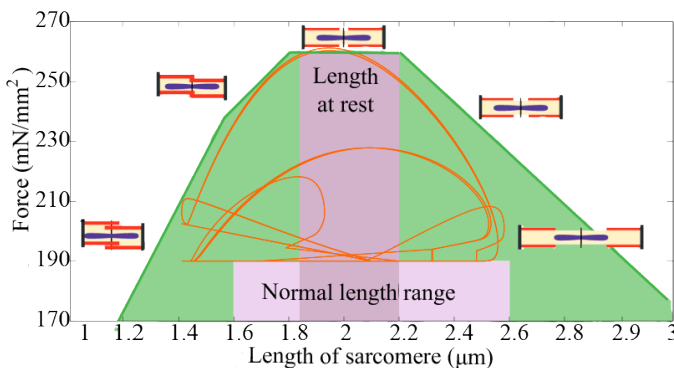
**FIGURE 9.** Shortening velocity of the sarcomere of skeletal muscle calculated by Equation (7) and considering three action potentials for the activation of muscular contraction.

Figure 10 displays the variation in the length of the sarcomere during each contraction. Shortening depends on the input of  $Ca^{2+}$ , since the greater the concentration of  $Ca^{2+}$  the greater the shortening in the overlap region. During the period from 0.5-1 s, no shortening is produced, and the sarcomere remains in its resting position because during that period  $Ca^{2+}$  is at its basal value.



**FIGURE 10. Shortening of the sarcomere of skeletal muscle during contraction.**

Figure 11 shows the force-length ratio of the shortening of the sarcomere; that is, the muscle’s capacity to generate force regardless of the degree of shortening [24] [25]. The amount of tension generated by the muscle depends on how much it can contract or shorten during stimulation.



**FIGURE 11. Force-length ratio of the shortening of the sarcomere of skeletal muscle (orange line).**

The orange line represents the result of the simulation by Equations (17) and (18). Figure 11 compares the results to the simulation reported in Tortora *et al.* [7], who proposed only minimum and maximum values of the force generated by the sarcomere (image in green). A sarcomere in a relaxed state measures 2-2.2  $\mu\text{m}$ . Figure 11 shows that the maximum force occurs when the sarcomere returns to its normal position (at rest). The normal length range of the sarcomere during the contractile cycle runs from 1.6-2.6  $\mu\text{m}$ . Figure 11 also reveals that the force which decreases the length of the sarcomere is outside the normal range; that is, the length exceeds the value at rest (eccentric contraction), as occurs in extreme contractions.

Figure 12 presents the force-velocity ratio. Clearly, during the velocity of shortening ( $V(t)>0$ ) -that is, contraction- the force tends to remain at its initial or minimum value, before increasing during relaxation.

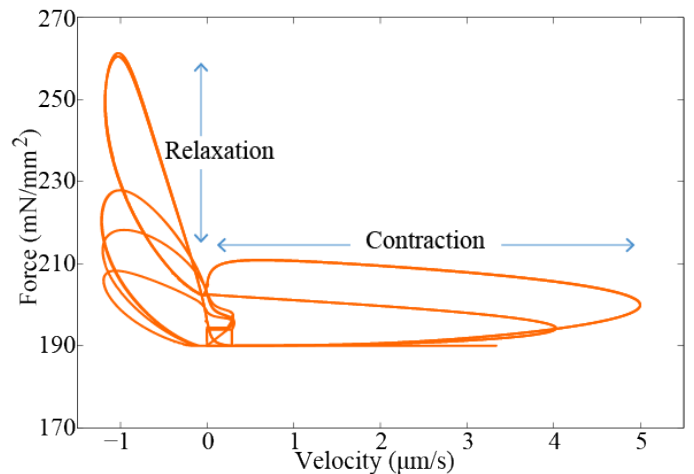


**FIGURE 12. Force-velocity ratio of the sarcomere of skeletal muscle. The orange line represents the force generated during contraction, in terms of the velocity of the shortening of the sarcomere.**

This is because the force is generated in the stage of the change from the strong to weak conformation of the crossbridges when the union and separation of the molecules of myosin and actin is strong. This coincides with the force-shortening ratio.

Finally, the energy consumed by the sarcomere can be seen in Figure 13. The negative results are due to the sign of the velocity of shortening. Here, after 0.5 s, the rate of consumption is small and does not vary, since in this period the  $Ca^{2+}$  remains in its basal state, and there is no contraction.

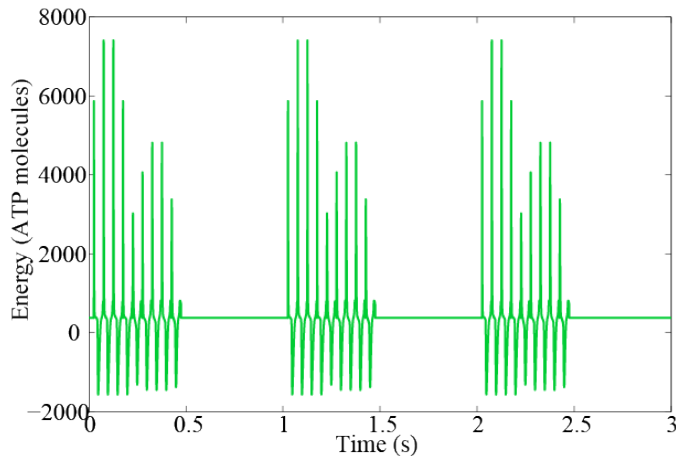


**FIGURE 13. Total energy consumed by a sarcomere of skeletal muscle upon receiving three action potentials at the neuromuscular union to activate the contraction cycle and, hence, the performance of mechanical work.**

### CONCLUSIONS

The study of the mechanical properties of the sarcomere of skeletal muscle based on the biological systems paradigm is interesting for characterizing and quantifying the dynamic behavior of muscle cells.

Moreover, the ratio between the mechanical response and the energy consumed by the sarcomere can provide valuable information on the efficient use of energy in cells. The results obtained from the numerical simulations of force are considered acceptable since they coincide with the maximum and minimum ranges of force generated by a sarcomere, according to experimental values reported in the literature [26] [27]. The availability of experimental data on the maximum and minimum force that the sarcomere can perform is a disadvantage for the validation of the dynamic response of the proposed model.

Therefore, to overcome this disadvantage, experimental studies at sarcomere level must be carried out to account with data to validate the dynamical behavior of force generated by the sarcomere. The findings on the length of the sarcomere during the contractile cycle are also deemed acceptable. Experimental reports indicate that the length of a sarcomere at rest phase is 2-4  $\mu\text{m}$ , but when this exceeds the normal state of relaxation, during an extreme contraction, length may decrease to just 1  $\mu\text{m}$  [7].

Figures 6, 7 and 8 show that when the levels of  $Ca^{2+}$  input are high, the force generated is greater, but that when  $Ca^{2+}$  is at its basal value, the force remains at its minimum value. Once the model of energy consumption at the level of sarcomere is fully resolved, future work will focus on modeling the coupling rules between sarcomeres that allows the mechanical response of a complete muscle fiber, and on proposing rules for the recruitment of fibers to model the mechanical response and energy consumption of a complete muscle. The challenge seems achievable, since currently studies have been reported addressing this problem of inter-scale modeling, for example, the one reported by Marcucci *et al.* [28], where they propose a scaling from muscle fiber to full muscle just considering the mechanical response, without considering energy consumption.

The significance of solving the mathematical modeling of energy consumption by skeletal muscle would be to have quantitative methods, rather than indirect estimations, of a person's energy consumption. This could be of relevant importance in pathologies related to energy management in the human body, from overweight, obesity, metabolic syndrome and diabetes. In addition to the representation in mathematical models of energy consumption, it would allow the design of patient-oriented energy consumption optimization schemes that could be useful, for example, for high-performance athletes.

### **AUTHOR CONTRIBUTIONS**

All authors participate equally in the writing, reviewing, and editing of the present manuscript. K. G. F. R. oversaw the methodology, software, and validation analyses, carried out the investigation and wrote the original draft. D. E. P. G. carried out software analysis and visualization of results. G. Q. C. developed con-

ceptualization of the study as well as formal analysis, obtained resources for the study and oversaw the project.

### **DECLARATION OF INTERESTS**

The authors declare that they have no conflict of interests.

## REFERENCES

- [1] Wiener N. Cybernetics: or control and communication in the animal and the machine. Cambridge: The MIT Press; 1961. 352 p.
- [2] Kitano H. Computational systems biology. Nature [Internet]. 2002;420(6912):206-10. Available from: <https://doi.org/10.1038/nature01254>
- [3] Kitano H. Systems Biology: A Brief Overview. Science [Internet]. 2002;295(5560):1662-4. Available from: <https://doi.org/10.1126/science.1069492>
- [4] Vogt H, Hofmann B, Getz L. The new holism: P4 systems medicine and the medicalization of health and life itself. Med Health Care Philos [Internet]. 2016;19(2):307-23. Available from: <https://doi.org/10.1007/s11019-016-9683-8>
- [5] Verboven K, Hansen D. Critical Reappraisal of the Role and Importance of Exercise Intervention in the Treatment of Obesity in Adults. Sport Med [Internet]. 2021;51(3):379-89. Available from: <https://doi.org/10.1007/s40279-020-01392-8>
- [6] Brychta R, Wohlers E, Moon J, Chen K. Energy Expenditure: Measurement of Human Metabolism. IEEE Eng Med Biol [Internet]. 2010; 29(1):42-7. Available from: <https://doi.org/10.1109/EMEM.2009.935463>
- [7] Tortora GJ, Derrickson BH. Principles of Anatomy and Physiology. 12th ed. NJ: John Wiley & Sons; 2009. 299 p.
- [8] Dao TT, Ho Ba Tho M-C. A Systematic Review of Continuum Modeling of Skeletal Muscles: Current Trends, Limitations, and Recommendations. Appl Bionics Biomech [Internet]. 2018;2018: 7631818. Available from: <https://doi.org/10.1155/2018/7631818>
- [9] Rodrigo S, García I, Franco M, Alonso-Vázquez A, et al. Energy expenditure during human gait. I-An optimized model. In: 2010 Annual International Conference of the IEEE Engineering in Medicine and Biology [Internet]. Buenos Aires: IEEE; 2010: 4254-7. Available from: <https://doi.org/10.1109/IEMBS.2010.5627174>
- [10] Böl M, Reese S. Micromechanical modelling of skeletal muscles based on the finite element method. Comput Methods Biomech Biomed Engin [Internet]. 2008;11(5):489-504. Available from: <https://doi.org/10.1080/10255840701771750>
- [11] Landesberg A, Sideman S. Mechanical regulation of cardiac muscle by coupling calcium kinetics with cross-bridge cycling: a dynamic model. Am J Physiol Circ Physiol [Internet]. 1994;267(2):H779-95. Available from: <https://doi.org/10.1152/ajpheart.1994.267.2.h779>
- [12] Sugiura S, Washio T, Hatano A, Okada J, et al. Multi-scale simulations of cardiac electrophysiology and mechanics using the University of Tokyo heart simulator. Prog Biophys Mol Biol [Internet]. 2012;110(2-3):380-9. Available from: <https://doi.org/10.1016/j.pbiomolbio.2012.07.001>
- [13] Regazzoni F, Dedè L, Quarteroni A. Biophysically detailed mathematical models of multiscale cardiac active mechanics. PLoS Comput Biol [Internet]. 2020;16(10):e1008294. Available from: <https://doi.org/10.1371/journal.pcbi.1008294>
- [14] Kügler P. Modelling and Simulation for Preclinical Cardiac Safety Assessment of Drugs with Human iPSC-Derived Cardiomyocytes. Jahresber Dtsch Math Ver [Internet]. 2020;122(4):209-57. Available from: <https://doi.org/10.1365/s13291-020-00218-w>
- [15] Tchaicheeyan O, Landesberg A. Regulation of energy liberation during steady sarcomere shortening. Am J Physiol Heart Circ Physiol [Internet]. 2005;289(5):2176-82. Available from: <https://doi.org/10.1152/ajpheart.00124.2005>
- [16] Gams A, Petric T, Debevec T, Babic J. Effects of robotic knee exoskeleton on human energy expenditure. IEEE Trans Biomed Eng [Internet]. 2013;60(6): 1636-44. Available from: <https://doi.org/10.1109/tbme.2013.2240682>
- [17] Landesberg A, Sideman S. Force-velocity relationship and biochemical-to-mechanical energy conversion by the sarcomere. Am J Physiol Heart Circ Physiol [Internet]. 2000;278(4):H1274-84. Available from: <https://doi.org/10.1152/ajpheart.2000.278.4.h1274>
- [18] Hill AV. The heat of shortening and the dynamic constants of muscle. Proc. R. Soc. Lond. B [Internet]. 1938;126(843):136-95. Available from: <https://doi.org/10.1098/rspb.1938.0050>
- [19] Yaniv Y, Sivan R, Landesberg A. Stability, controllability, and observability of the "four state" model for the sarcomeric control of contraction. Ann Biomed Eng [Internet]. 2006;34(5):778-89. Available from: <https://doi.org/10.1007/s10439-006-9093-9>
- [20] Brenner B, Eisenberg E. Rate of force generation in muscle: correlation with actomyosin ATPase activity in solution. Proc Natl Acad Sci U S A [Internet]. 1986;83(10):3542-6. Available from: <https://doi.org/10.1073/pnas.83.10.3542>
- [21] Chalovich JM, Eisenberg E. The effect of troponin-tropomyosin on the binding of heavy meromyosin to actin in the presence of ATP. J Biol Chem [Internet]. 1986;261(11):5088-93. Available from: <https://www.ncbi.nlm.nih.gov/pubmed/2937784>
- [22] Beuckelmann DJ, Näbauer M, Erdmann E. Intracellular calcium handling in isolated ventricular myocytes from patients with terminal heart failure. Circulation [Internet]. 1992;85(3):1046-55. Available from: <https://doi.org/10.1161/01.cir.85.3.1046>
- [23] Yaniv Y, Sivan R, Landesberg A. Analysis of hystereses in force length and force calcium relations. Am J Physiol Circ Physiol [Internet]. 2005;288(1):H389-99. Available from: <https://doi.org/10.1152/ajpheart.00722.2003>
- [24] Edman KAP. Contractile properties of mouse single muscle fibers, a comparison with amphibian muscle fibers. J Exp Biol [Internet]. 2005;208(10):1905-13. Available from: <https://doi.org/10.1242/jeb.01573>
- [25] Ma S, Zahalak GI. Activation dynamics for a distribution-moment model of skeletal muscle. Math Comput Model [Internet]. 1988;11:778-82. Available from: [https://doi.org/10.1016/0895-7177\(88\)90599-7](https://doi.org/10.1016/0895-7177(88)90599-7)
- [26] Gollapudi SK. Modeling temperature dependent dynamic contractile properties in human skeletal muscle fibers using crossbridge models [Ph.D.'s thesis]. [Washington]: Washington State University, 2011.
- [27] Stienen GJ, Kiers JL, Bottinelli R, Reggiani C. Myofibrillar ATPase activity in skinned human skeletal muscle fibres: Fibre type and temperature dependence. J Physiol [Internet]. 1996;493(2):299-307. Available from: <https://doi.org/10.1113/jphysiol.1996.sp021384>
- [28] Marcucci L, Reggiani C, Natali AN, Pavan PG. From single muscle fiber to whole muscle mechanics: a finite element model of a muscle bundle with fast and slow fibers. Biomech Model Mechanobiol [Internet]. 2017;16(6):1833-43. Available from: <https://doi.org/10.1007/s10237-017-0922-6>

[dx.doi.org/10.17488/RMIB.42.2.10](https://doi.org/10.17488/RMIB.42.2.10)

E-LOCATION ID: 1171

## Development of Films, Based on Oxidized *Ipomea Batatas* Starch, with Protein Encapsulation

### Desarrollo de Películas, Basadas en Almidón Oxidado de *Ipomea Batatas*, con Encapsulación de Proteínas

J. F. Alvarez-Barreto, D. Viteri-Narvaez, J. S. Proano, A. Caicedo, M. Grunauer, L. Eguiguren, M. Vargas

Universidad San Francisco de Quito, USFQ

#### ABSTRACT

Dialdehyde starches (DAS) have been used as biomaterials due to their biocompatibility and biodegradability; nonetheless, sweet potato (*Ipomea batatas* L.) starch has not been researched. Films based on sweet potato DAS, mixed with native starch (NS), poly-vinyl alcohol (PVA) and glycerin have been developed with protein encapsulation, using central composite design (CCD) and response surface methodology (RSM). Input variables were oxidation degree, NS concentration and polymeric mixture volume, while output variables were film's thickness, equilibrium swelling and BSA (Bovine serum albumin) release. DAS was obtained through hydrogen peroxide ( $H_2O_2$ ) oxidation, and the oxidation degree is referred to as  $H_2O_2$  concentration. Films presented rough surfaces, and formulations containing 10%  $H_2O_2$  DAS presented micropores. Water uptake was greater with higher DAS content. Film thickness depended on the volume of the polymeric suspension and influenced swelling capacity. According to RSM, the optimal formulation was DAS with 5%  $H_2O_2$  and 35% NS. These results demonstrate that oxidized sweet potato starch has potential for protein encapsulation and delivery.

**KEYWORDS:** Scaffolds, Oxidation, Starch, Biomaterial, Biomedical Applications

## RESUMEN

Almidones dialdehído (DAS) se han utilizado como biomateriales por su biocompatibilidad y biodegradabilidad; sin embargo, el almidón de camote (*Ipomea batatas L.*) no ha sido investigado. Se han desarrollado películas de DAS de camote, con almidón nativo (NS), alcohol polivinílico (PVA) y glicerina con encapsulación de proteínas, utilizando un diseño central compuesto (CCD) y metodología de superficie de respuesta (RSM). Las variables de entrada fueron: grado de oxidación, concentración de NS y volumen de la mezcla polimérica, mientras que las variables de salida fueron: espesor de la película, hinchamiento y liberación de BSA (Albúmina de Suero Bovino) en equilibrio. DAS se obtuvo mediante oxidación con peróxido de hidrógeno ( $H_2O_2$ ), y el grado de oxidación se define como concentración de  $H_2O_2$ . Las películas presentaron superficies rugosas y las formulaciones con 10%  $H_2O_2$  DAS presentaron microporos. La absorción de agua fue mayor con mayor contenido de DAS. El espesor de la película dependió del volumen de la mezcla polimérica e influyó en la capacidad de hinchamiento. Según RSM, la formulación óptima fue DAS con 5%  $H_2O_2$  y 35% NS. Estos resultados demuestran que el almidón de camote oxidado tiene potencial para aplicaciones en la encapsulación y liberación de proteínas.

**KEYWORDS:** Andamios, Oxidación, Almidón, Biomaterial, Aplicaciones Biomédicas

### Corresponding author

TO: Jose Francisco Alvarez-Barreto

INSTITUTION: Universidad San Francisco de Quito

ADDRESS: Diego de Robles y Vía Interoceánica S/N,

Edif. Hayek, Ofic. H320, P. O. BOX 170901, Quito,

Pichincha, Ecuador

E-MAIL: jalvarezb@usfq.edu.ec

### Received:

12 February 2021

### Accepted:

26 April 2021

## INTRODUCTION

In recent years, macromolecular drugs have been the focus of many therapeutic technologies. Examples include insulin, antibodies, enzymes and other proteins. Extensive research has been carried out also on drug delivery systems for these agents, and the transdermal route has been considered as a possible way to mitigate limitations, such as first passage metabolism, posed by other delivery ways <sup>[1]</sup>.

Protein delivery is also important in tissue engineering. Particularly, the encapsulation and release of growth and differentiation factors can enhance the regeneration process. Chronic skin wounds, genetic skin disorders, burns and diseases, such as diabetes mellitus, may result in important skin damage <sup>[2]</sup>. Epidermal and fibroblast growth factors are some of the proteins that potentiate skin regeneration <sup>[3] [4]</sup>. Moreover, traditional medicine has also been used to create optimal conditions for skin growth using natural extracts that have been combined with biopolymers for their effective use <sup>[2] [5] [6] [7]</sup>.

Biopolymeric materials traditionally used in these applications include polylactic-acid (PLA), polycaprolactone (PCL), polyacrylonitrile (PAN). However, naturally derived polysaccharides, such as chitosan, alginate, carboxymethyl cellulose, pectin and starch present different advantages like wide availability, certain degree of biomimicry, and many are inherently biocompatible <sup>[8] [9]</sup>. These materials have been used to generate different delivery structures, most commonly hydrogels, films and patches, and have demonstrated great potential for the encapsulation of macromolecular agents <sup>[10] [11] [12]</sup>. These structures meet the requirements for wound dressings, and transdermal delivery systems, including absorbing exudates and keeping a moist environment that enhances the growth of new granulation tissue, so as to make the wound healing process efficient <sup>[2] [13]</sup>. Examples of biomaterial formulations in this area

include gelatin-starch hydrogels <sup>[14]</sup>, carboxymethyl cellulose-PEG hydrogels <sup>[15]</sup>, nanofibrous scaffolds <sup>[6]</sup>, polyvinyl alcohol (PVA)-carboxymethyl cellulose and tamarind gum based films <sup>[16]</sup>.

One of the most abundant natural polymers is starch, and it has been extensively studied due to its compatibility, availability, low cost, and biodegradability. Starch can decompose without producing toxic residues, and it is like the native cellular milieu. Thus, starches have been used in the pharmaceutical industry, where they have applications in the manufacturing of soft capsules without gelatin, as bone wax, porous scaffolds and as bio-absorbable materials, such as hydrogels to cure wounds <sup>[17] [18]</sup>.

One of the most common problems with starch, however, is its instability in water, and there are two ways to address this issue. One is the use of cross-linking methods with plasticizers like vinyl monomers, glycerol or polyvinyl alcohol (PVA) <sup>[19] [20]</sup>. The other mechanism is chemical modification, with oxidation being one of the most widely applied in the biomaterials field. Dialdehyde starch (DAS), resulting from oxidation has improved mechanical properties, greater stability in water, and carbonyl groups that can interact with other macromolecules, and thereby, regulate their delivery <sup>[21] [22] [23]</sup>. DAS has been used as a component in systems for encapsulation and delivery of insulin, different proteins and non-steroidal anti-inflammatory drugs <sup>[24] [25]</sup>. Nonetheless, the combination of both approaches is also feasible, and hydrogels composed of DAS and PVA have shown potential for the controlled delivery of ibuprofen.

Most drug delivery studies involving DAS have used corn, cassava, or potato as original starch sources, but very little has been done with *Ipomea batatas* L, a purple tuber from the Convolvaceae family. After potato, sweet potato is the second most cultivated tuber in the world, and it is a great source of starches <sup>[26]</sup>. Therefore,

the aim of this research was to elaborate a film composed of oxidized *Ipomea batatas L.* starch, for protein encapsulation and delivery. Sweet potato DAS was obtained through hydrogen peroxide oxidation, and it was later mixed with PVA and glycerol. A surface response methodology was used to optimize certain film parameters, such as polymer concentration, thickness, and native starch to DAS ratio.

## MATERIALS AND METHODS

### Starch Extraction

*Ipomea batatas L.*, or sweet potato, was used to extract the starch. Briefly, tubers without the skin were cut into 2-cm pieces, and homogenized in a blender, using distilled water at 250 grams per 100 mL. The homogenate was filtered, and the starch could precipitate. Starch was thoroughly washed, discarding the supernatant, and following the same precipitation procedure. After the third wash, rinsing with 70% v/v ethanol was carried out, and the purified starch was dried at 40 °C.

### Starch modification

Starch modification was performed through hydrogen peroxide (H<sub>2</sub>O<sub>2</sub>) oxidation, based on the methodology proposed by Zhang [23]. Three aqueous hydrogen peroxide solutions, at 3, 5 and 10% v/v, were prepared. At the same time, starch was washed with ethanol 70% v/v and twice with distilled water.

A 2% w/v starch suspension was heated until gelatinization at 80°C for 30 min, under mild agitation. Then, it was cooled to 25°C. The oxidation process was carried out under moderate agitation, at a constant pH value of 7. For every 100 mL of the starch suspension, 6.25 mL of the H<sub>2</sub>O<sub>2</sub> solution, at a given concentration, were added dropwise, in a period of 1h. The resulting dialdehyde starch (DAS) was centrifuged at 400g for 5 min, thoroughly washed with distilled water, and dried at 40°C.

## Starch characterization

### Optical Microscopy

Starch granules were analyzed in a LEICA DM500 microscope. Granule size was calculated using the LAS EZ microscope software. For every picture, 100 measurements were collected, and an average was reported.

### Carbonyl and carboxyl group content

Modified starch was characterized estimating the amount of carbonyl and carboxyl groups. For carbonyl groups, an adaptation of the protocol proposed by Smith in 1967 was carried out [27], using 1g of modified starch with 25mL of distilled water. The mixture was heated until gelatinization, cooled to 25 °C, and the pH was corrected to 3.2. After that, 3.75 mL of hydroxylamine hydrochloride solution (25g of hydroxylamine hydrochloride and 100 mL of NaOH 0.5M in a 500mL) were incorporated, and the mixture was incubated at 40°C for 4h. Then, it was titrated potentiometrically with 0.1M HCl until pH of 3.2. The amount of carbonyl groups was calculated through Equation 1:

$$\frac{CO}{100GU} = \frac{(V_b - V_s) \times M \times 0.028 \times 100}{W} \quad (1)$$

Where  $V_b$  is the blank titration volume (NS),  $V_s$  the titration volume of the sample,  $M$  is HCl molarity, and  $W$  the dry sample weight.

In a similar procedure, carboxyl group content was determined using the protocol proposed by Parovouri, et. al., in 1995 [28], using 1g of oxidized starch in 60mL of distilled water, gelatinized and titrated to a value of pH 8.2 with NaOH 0.01M. Carboxyl groups were determined with Equation 2:

$$\frac{COOH}{100GU} = \frac{(V_s - V_b) \times M \times 0.045 \times 100}{W} \quad (2)$$

Where  $V_b$  is the blank titration volume (NS),  $V_s$  the sample titration volume,  $M$  HCl molarity and  $W$  the weight of the sample dry basis.

### Fourier Transformed Infrared Spectroscopy (FT-IR) analysis

Samples of native starch (NS), oxidized starch at 5%  $H_2O_2$  (DAS5), oxidized starch at 10%  $H_2O_2$  (DAS10) and different film formulations (CCD) were analyzed with a Cary 630 FTIR Spectrometer from Agilent Technologies.

Square samples of 0.5 cm per side were analyzed with diamond ATR accessory, and spectra were acquired in the region of 4000-500  $cm^{-1}$ .

### Design of Experiments (DOE) and Film Preparation

A statistically designed set of experiments was carried out using response surface methodology (RSM) to minimize the number of experiments and maximize the amount of data generated. Through this analysis, the effect of each parameter/input variable in the film formulation could be evaluated [29].

**TABLE 1. Design of experiments to study the effect of the oxidation degree, amount of native starch and volume of polymeric suspension in the composition of each film considering the constant variables to be 2% wt/v PVA, 2% v/v glycerin and 5% wt/wt BSA of the total amount of starch. Design based on the face centered composite design.**

Face centered Central Composite Design					
Factor	Levels				
	a	-	0	+	A
	-a	-1	0	1	a
Oxidation degree [%H <sub>2</sub> O <sub>2</sub> ]*	0	0	5	10	10
NS [wt%]**	0	0	50	100	100
Volume [mL]	12	12	18.5	25	25

\* Oxidation degree is expressed as the concentration of  $H_2O_2$  (%v/v) used in the process of modification

\*\* NS: percentage of native starch

Using the software JMP, the model was prepared with 34 experiments using a composite design method with a 5-center point model described in Table 1. The input variables were volume of the polymeric suspension, oxidation degree and amount of native starch; the outputs were film thickness, protein release at equilibrium and swelling at equilibrium.

Bovine serum albumin (BSA), Sigma-Aldrich, acted as model protein for encapsulation. Poly (vinylalcohol), PVA, (Mowiol® 18-88,  $M_w$ ~130,00, Sigma-Aldrich) was dissolved in distilled water. Each film was made according to Table 1 (DOE). Constant parameters were PVA concentration (2%wt/v), glycerin concentration (2%v/v) and BSA content (5 %wt of the total starch amount).

First, the amounts of native and oxidized starch were weighed and gelatinized in distilled water and cooled to room temperature. The slurry was transferred to a 50 mL conical tube, and the PVA, glycerin and BSA solutions were incorporated to the polymeric mixture. Vortex homogenization followed for 30 seconds, and the resulting mixture was placed in polystyrene petri dishes, stored in a freezer at -14°C for 24h, and subsequently dried at 40°C overnight according to preliminary experimentation (data not shown). Once dried, films were stored in the refrigerator at 4°C.

## Film characterization

### Film Thickness

Film thickness ( $\mu m$ ) was determined using a micrometer (Mitutoyo, Tokyo, Japan). The film was dried at 37°C overnight, and the thickness was determined as the average of measurements in 8 random locations.

### Film swelling and protein release

Films were dried at 37°C overnight. They were then weighed, and 4 squares of 0.7x0.7cm were cut from each film. These squares were placed in 24 well-plates,

filled with Phosphate Buffer Saline (PBS at pH 7.2). During the first hour of the experiment the film was weighted every 15 minutes, and a known volume of the supernatant was collected and replaced with fresh PBS. After that, samples were weighed at 5, 24, 48, and 72h, and supernatant was collected. According to previous analyses, equilibrium was already reached at 72h (data not shown).

The swelling ratio was calculated by Equation 3 [17]:

$$SW = \frac{M_t - M_0}{M_0} \times 100\% \quad (3)$$

Where  $SW$  is the swelling percentage,  $M_t$  is sample weight at equilibrium, and  $M_0$  is the initial sample.

Protein release was determined by the Bradford method, through the collected supernatant aliquots. A calibration curve was made with BSA solutions of known concentrations in PBS [30].

### Scanning Electron Microscopy (SEM)

Samples were analyzed in a JEOL JSM-IT300 scanning electron microscope, using the program MP-96040EXCS External Control Software. Starch samples were observed at 50 Pa and 5 kV, while films were analyzed at 30 Pa and 5 kV to avoid sample damage by the electron beam.

## RESULTS AND DISCUSSION

### Starch extraction and modification

#### Yield, size and morphology

The process of starch extraction from *ipomea batatas* L. presented a yield of 14.44%, with respect to the total mass of the tuber processed. Starch granule had an average size of  $(23.18 \pm 7.25) \mu m$ . Sweet potato starch presented a spherical bell form, as seen in previous studies where this unusual shape is described [31] [32].

### Carbonyl and carboxyl group content

Chemical modification is generally practiced in food and non-food industry as it gives functional groups to the starch, changing its properties and thereby, its functionality [22]. Functional groups resulting from hydroxyl group oxidation are carbonyl and carboxyl; their quantification values in this work are shown in Table 2. Carbonyl and carboxyl group content depends on the pH value, temperature, and reaction time, among others; therefore, it is described as a complex reaction by Salmi, *et al.* [33]. In the present study, the oxidation with  $H_2O_2$  at 5 and 10% v/v yields carbonyl and carboxyl groups comparable to the study made by Zhang, *et al.*, where the highest carbonyl and aldehyde groups were reached in the oxidation with molar ratio of  $H_2O_2$ /starch  $< 0.7$  which is equivalent to a 10%  $H_2O_2$  percentage [23].

The amount of carboxyl groups is smaller than carbonyl groups (Table 2), which is appropriate since the purpose of the oxidation is to obtain carbonyl groups as they are responsible for providing greater stability in water, and they can form Schiff bases with the amine groups from proteins.

**TABLE 2. Carbonyl and carboxyl group content in the dialdehyde sweet potato starch.**

H <sub>2</sub> O <sub>2</sub> Percent [%v/v]	Carbonyl [CO/100GU]	Carboxyl [COOH/100GU]	Total oxidation [CO+COOH/100GU]
3	0.157 ± 0.040	0.023 ± 0.001	0.220 ± 0.327
5	0.432 ± 0.010	0.066 ± 0.003	0.508 ± 0.013
10	0.534 ± 0.022	0.070 ± 0.002	0.627 ± 0.021

#### Design of Experiments (DOE)

Experimental factors were analyzed according to the important responses for the development of films for potential protein encapsulation and delivery. In this work, films were developed using a methodology previously established in the laboratory. The response variables were protein release, swelling at equilibrium,

and thickness of the films. These responses are important as it is not expected that all the protein is released completely. It is possible that amine groups in the protein form Schiff's bases with DAS carbonyl groups. Swelling is an important response as the wound needs humidity to heal and it would exudate fluids in the process; thus, the film needs to absorb a great amount of those exudates [34]. Additionally, swelling capacity is directly related to protein delivery [35].

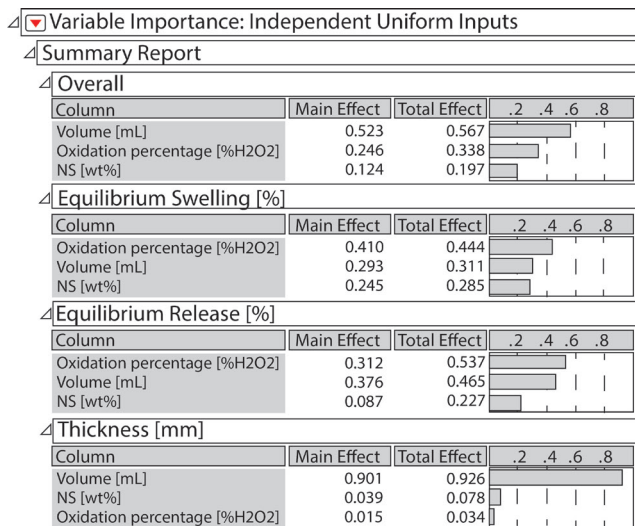


**FIGURE 1. Importance of each input variable depending on the output obtained in the experimentation process.**

Great deviations in central points can be seen for protein release response, giving a great experimental error as data from the central point variates greatly from one another; nevertheless, for thickness and swelling, variations were low in central points, with small experimental errors. According to Figure 1, in the overall analysis, the volume of the polymeric suspension had a greater effect, followed by the degree of oxidation, and lastly, the amount of native starch in the formulation. The parameters with greater effects on each response are also described; for swelling and protein release in equilibrium it was the oxidation degree; in the release, the effect of the degree of oxidation and volume of polymeric suspension are close, so both are important in the response. Finally, and as

expected, the thickness of the film depends on the volume of the polymeric suspension almost in its entirety.

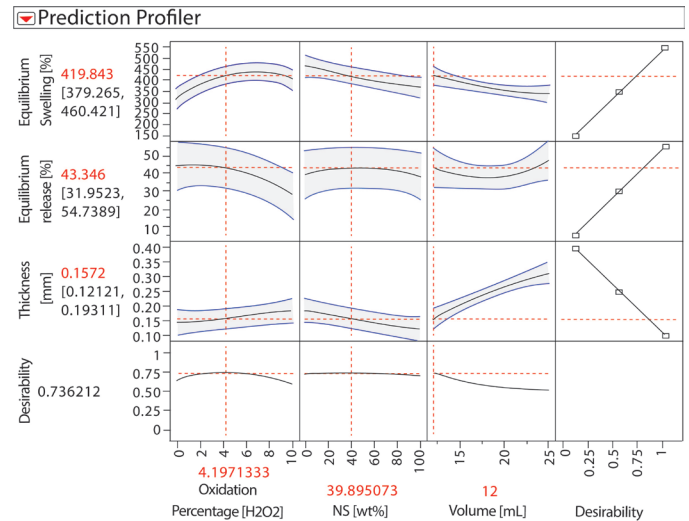


**FIGURE 2. DOE prediction profiles for output variables: thickness, equilibrium swelling and equilibrium release, dependent on oxidation degree, NS content and polymeric mixture volume.**

In Figure 2, influences of each parameter in the responses are described. For equilibrium swelling, the degree of oxidation shows a maximum around 7%. NS content also influences the release, and it presents a maximum when no NS is added to the formulation. For protein release at equilibrium, as the degree of oxidation and volume of polymeric suspension are important parameters, this figure shows the model with each predicted response. Release decreased at greater degree of oxidation, which is consistent with the hypothesis that proteins could be immobilized through Schiff bases with the carbonyl groups of the oxidized starch. The prediction of the model shows, in red lines, the values of the input variables needed to maximize swelling and protein release at equilibrium, while minimizing the film thickness. The model has predicted that the amount of NS should be approximately 35%, oxidation degree approximately 4% and volume 12mL. The available DAS, how-

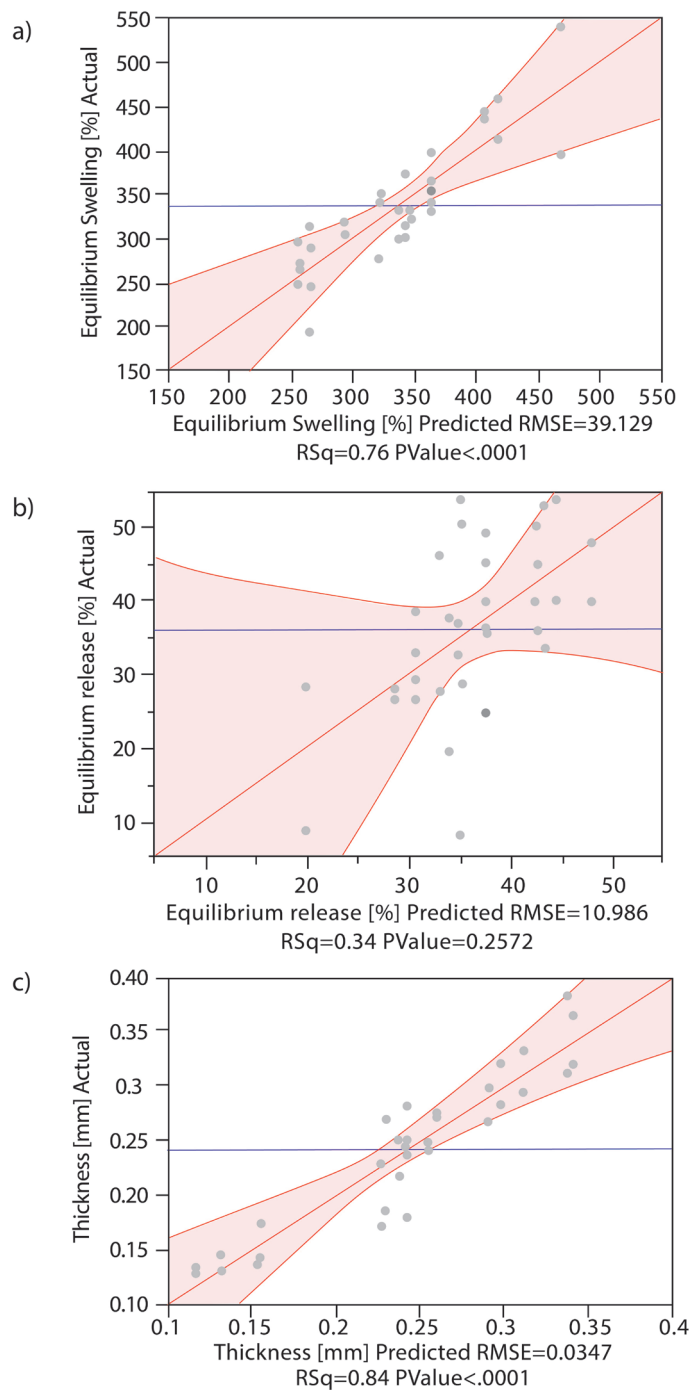


**FIGURE 3. Variability of the responses according to the variables. Actual (grey dots) and predicted data for the model. a) Equilibrium Swelling, b) Equilibrium release, c) Thickness.**

ever, were oxidized at 5 and 10%  $H_2O_2$ , so it was decided to use 5% degree of oxidation for model testing, since it was closest to the optimal value.

Differences between the predicted model and experimental data are showed in Figure 3. It can be seen that the experimental data fits the swelling predicted model as it has a  $P < 0.0001$ , and the confidence level was established at 95% ( $P < 0.05$ ). For the thickness model, experimental data also fits with a  $P < 0.0001$ ; however, the model does not fit the experimental data for the protein release, with  $P = 0.22$ .

According to the literature, the levels of oxidation reached in this work were low, as no catalyst was used. Thus, some hydroxyl groups were still present and those are responsible for water absorption; when starches have a high degree of oxidation, most of these groups are used so it decreases the swelling [22]. These results are comparable to those reported by Nourmohammadi, et al., where they developed bioactive composite scaffolds with polycaprolactone, chitosan and oxidized starch; as more DAS was included in the formulations, swelling rates increased because of greater starch hydroxyl group content [36].

To corroborate the generated prediction model, two more experiments were carried out: one with a formulation close to the optimum predicted by the program, using DAS5 and 35% of NS in a 12mL volume of polymeric mix, and one with no NS with the same conditions. In Table 3, the results of this set of experiments are shown.

**TABLE 3. Results from de corroboration of the DOE.**

Film's Composition		Model deviation [%]		
NS [%]	DAS5 [%]	Thickness [mm]	Swelling [%]	Release [%]
35	65	10.151	7.8766	37.152
0	100	16.949	9.7800	55.072

Thickness and swelling in equilibrium are parameters that were adjusted to the model prediction, as they displayed a deviation from the model of less than 17%, and the equilibrium release does not fit the

model as its deviation for the model is about 37% using DAS5 and 35% of NS, which is comparable with the other results where equilibrium release showed a big variability. These differences were expected, as equilibrium release presented the largest dispersion of the data, and the model did not fit the experimental results (as seen in Figure 3).

### Fourier Transform Infrared Spectroscopy (FT-IR) of the films

Figure 4 shows the spectra for a film containing PVA, glycerin and BSA, compared to a film containing NS, PVA, glycerin and BSA. Around  $1539\text{ cm}^{-1}$ , it can be observed that there is a difference in the wavenumber which corresponds to N-H bending and C-H stretching vibration of amine II present in the planar peptidic bond vibrational modes of BSA molecules [35] [37].

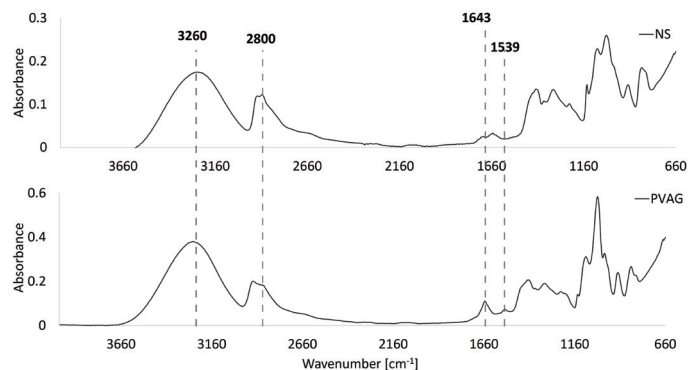


**FIGURE 4.** FT-IR spectra of film formulations: a) with native starch, and b) without starch (only PVA and glycerin).

The same pattern is observed in Figure 5 for DAS5 and similar patterns in DAS10, as the peak intensity decreases when using more NS. At  $1643\text{ cm}^{-1}$  a peak corresponding to C-N bonds that are assumed to correspond to Schiff bases (C=O bending vibrations and C-N stretching) is seen [38]. This wavenumber shows a bigger peak when no NS is used, thereby corroborating that it corresponds to Schiff bases formed between the protein and DAS. In Figure 5, when NS is used at 50%, the interactions C-N decrease; this could be as less car-

bonyl groups are present Schiff base cannot form with amines from the BSA. Nevertheless, when using the optimal composition with NS 35% these interactions are similar as using no starch (PVAG). This could be due to the availability of carbonyl groups.

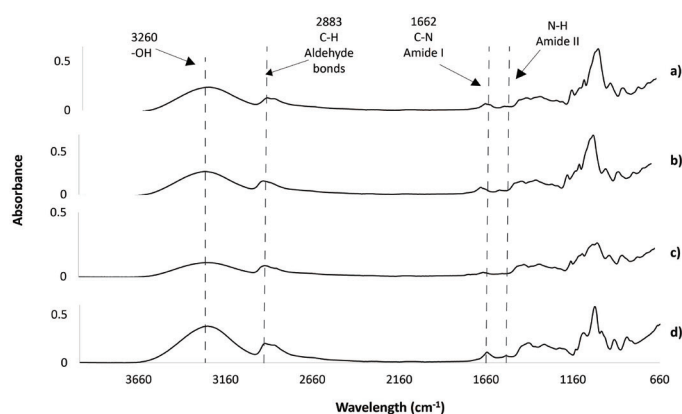


**FIGURE 5.** FT-IR spectra of films formulations with:

- a) DAS5 + 2% wt/v PVA + 2%v/v Glycerin + BSA,
- b) DAS5 with 50% NS + 2% wt/v PVA + 2%v/v Glycerin + BSA (DAS5NS50), and c) the optimal composition with DAS5 with 35% NS + 2% wt/v PVA + 2%v/v Glycerin + BSA (DAS5NS35), compared with d) without starch (only PVA and glycerin. PVAG).

Peaks around  $3260\text{ cm}^{-1}$  correspond to hydroxyl groups (-OH), those are from PVA, glycerin and the starches. Hydroxyl groups are responsible for the water absorption in the films [22]. Here, there could be a confirmation for the model as less quantity of NS is present more hydroxyl groups are present in the films, so they can uptake more water and the swelling rates increases.

Finally, peaks around  $1000\text{ cm}^{-1}$  are characteristic for NS, glycerin and PVA, in the three figures below the same pattern is present, when NS is present the peaks are smaller, this could be that the NS is not interacting with PVA or glycerin. Some of the characteristic peaks from glycerin and PVA shift when in the presence of starch, probably indicating important interactions between the plasticizers and the polysaccharide.

## Film Morphology

Film surfaces were assessed through SEM for morphological analyses. A sample for five different formulations were analyzed. Surfaces of the films are uniform, with important rugosity, as seen in Figure 6.

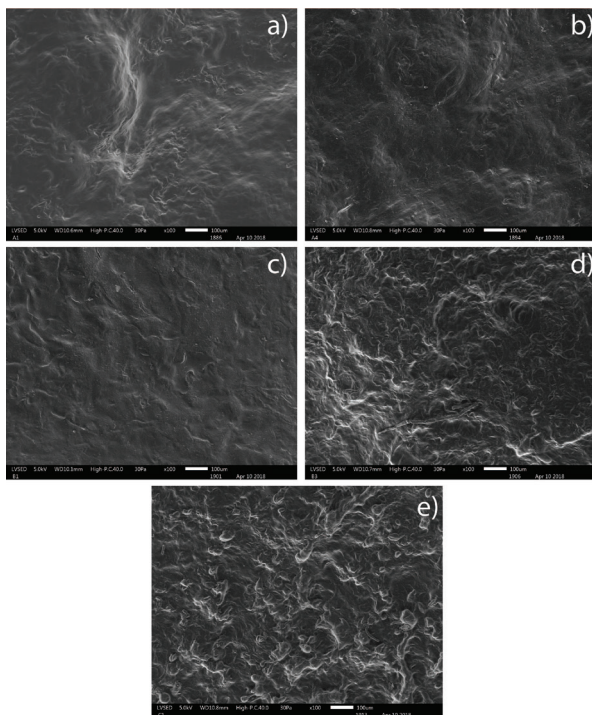


**FIGURE 6.** Scanning Electron Microscopy for samples with different compositions at 100X. a) DAS10 + 2% wt/v PVA + 2%v/v Glycerin + BSA; b) DAS10 with 50% NS + 2% wt/v PVA + 2%v/v Glycerin + BSA; c) DAS5 + 2% wt/v PVA + 2%v/v Glycerin + BSA; d) DAS5 with 50% NS + 2% wt/v PVA + 2%v/v Glycerin + BSA; e) 100% NS + 2% wt/v PVA + 2%v/v Glycerin + BSA.

Samples with DAS10 present micropores which can be seen in Figure 6, a), and micropores are also present for samples with DAS10 and 50% NS in Figure 6, b). These can influence water absorption, and help oxygen exchange, corroborating the results from swelling at equilibrium [39]. Formulations with DAS10, DAS10 50% NS and DAS5 (a, b, c), respectively, present smoother surfaces, according to previous studies for films with gelatin and oxidized starch gelatin, film smoothness represent the crosslinking ability of oxi-

dized starch and a great integration between all the components of the films [40]. Formulations with DAS5 50%NS and 100% NS in Figure 6, d), and Figure 6, e), respectively, present more rugosity than the films described previously. This could be due to insufficient homogenization between all components and caused by the high viscosity of gelatinized NS. For tissue engineering, pores are important as they allow permeability of oxygen and essential nutrients [35], also they allow more water uptake which is beneficial in early healing stages since cells will depend completely on nearby tissue fluids [41][42]. Another important fact with this type of scaffolds is that the roughness is necessary for cell adhesion. Some studies revealed that for osteoblasts rough surfaces shows great cell adhesion and proliferation [43][44]; for fibroblasts studies demonstrate that this type of cells prefer rough surfaces instead of smooth ones, as the studies showed more cells in rough surfaces than in smoother ones [35].

## CONCLUSIONS

The response surface methodology (RSM) for this work gives a model that fits for thickness and swelling parameters; however, protein release was poorly predicted. According to the DOE, the parameter with the greatest effect on the overall system was the volume followed by the degree of oxidation and percentage of NS. Swelling and protein release are responses that mostly depend on the degree of oxidation and are correlated; as swelling rates increases the release increases, this is also a good fact as these films need to absorb exudates from the wound and promote its healing. FT-IR spectra for the films show that some Schiff bases may be formed when less NS is used, and the peaks for hydroxyl groups may confirm the swelling rates for the films, when they have less NS they absorb more water which is beneficial for wound healing. Nevertheless, the films compositions performed showed properties that may be useful for protein encapsulation and release for different applications, such as transdermal delivery or skin regeneration

Studies on cytocompatibility, cytotoxicity, cell adhesion, biocompatibility, biodegradability, and in vivo studies must be performed.

### **AUTHOR CONTRIBUTIONS**

J.A.B. designed the experimental planning, carried out data analyses and FTIR; participated in the manuscript preparation. D.V.N. did the film preparation and characterization, carried out data analyses and participated in the manuscript preparation. J.S.P.A. generated SRM and carried out the subsequent analysis. A.C. contributed with the protein entrapment and release characterization. M.G. did the material charac-

terization and participated in writing the manuscript. L.E. participated in the protein entrapment and in vitro release and participated in the manuscript preparation. M. V. did the scanning electron microscopy.

### **ACKNOWLEDGEMENT**

Funding for this work was provided by the POLIGRANT and MedGrant Funds, as well as Collaboration Grant Program from USFQ.

### **COMPETING INTERESTS STATEMENT**

The authors declare no competing interests regarding the present study.

## REFERENCES

- [1] Chaulagain B, Jain A, Tiwari A, Verma A, et al. Passive delivery of protein drugs through transdermal route. *Artif Cells Nanomed Biotechnol* [Internet]. 2018;46(sup1):472-87. Available from: <https://doi.org/10.1080/21691401.2018.1430695>
- [2] López Angulo DE, do Amaral Sobral PJ. Characterization of gelatin/chitosan scaffold blended with aloe vera and snail mucus for biomedical purpose. *Int J Biol Macromol* [Internet]. 2016;92:645-53. Available from: <https://doi.org/10.1016/j.ijbiomac.2016.07.029>
- [3] Sharma P, Kumar P, Sharma R, Bhatt VD, et al. Tissue Engineering: Current Status & Futuristic Scope. *J Med Life* [Internet]. 2019;12(3):225-9. Available from: <https://doi.org/10.25122/jml-2019-0032>
- [4] Augustine R, Hasan A, Dalvi YB, Rehman U, et al. Growth factor loaded in situ photocrosslinkable poly(3-hydroxybutyrate-co-3-hydroxyvalerate)/gelatin methacryloyl hybrid patch for diabetic wound healing. *Mater Sci Eng C* [Internet]. 2021;118:111519. Available from: <https://doi.org/10.1016/j.msec.2020.111519>
- [5] Wu D, Bäckström E, Hakkarainen M. Starch Derived Nanosized Graphene Oxide Functionalized Bioactive Porous Starch Scaffolds. *Macromol Biosci* [Internet]. 2017;17(6):1600397. Available from: <https://doi.org/10.1002/mabi.201600397>
- [6] Unnithan AR, Pichiah T, Gnanasekaran G, Seenivasan K, et al. Emu oil-based electrospun nanofibrous scaffolds for wound skin tissue engineering. *Colloid Surf A-Physicochem Eng Asp* [Internet]. 2012;415:454-60. Available from: <https://doi.org/10.1016/j.colsurfa.2012.09.029>
- [7] Panawes S, Ekabutr P, Niamlang P, Pavasant P, et al. Antimicrobial mangosteen extract infused alginate-coated gauze wound dressing. *J Drug Deliv Sci Technol* [Internet]. 2017;41:182-90. Available from: <https://doi.org/10.1016/j.jddst.2017.06.021>
- [8] Croisier F, Jérôme C. Chitosan-based biomaterials for tissue engineering. *Eur Polym J* [Internet]. 2013;49(4):780-92. Available from: <https://doi.org/10.1016/j.eurpolymj.2012.12.009>
- [9] Wang J, Sun B, Tian L, He X, et al. Evaluation of the potential of rhTGF-β3 encapsulated P(LLA-CL)/collagen nanofibers for tracheal cartilage regeneration using mesenchymal stem cells derived from Wharton's jelly of human umbilical cord. *Mater Sci Eng C* [Internet]. 2017;70(1):637-45. Available from: <https://doi.org/10.1016/j.msec.2016.09.044>
- [10] Devi N, Sarmah M, Khatun B, Maji TK. Encapsulation of active ingredients in polysaccharide-protein complex coacervates. *Adv Colloid Interface Sci* [Internet]. 2017;239:136-45. Available from: <https://doi.org/10.1016/j.cis.2016.05.009>
- [11] Shariatina Z. Pharmaceutical applications of chitosan. *Adv Colloid Interface Sci* [Internet]. 2019;263:131-94. Available from: <https://doi.org/10.1016/j.cis.2018.11.008>
- [12] Dhamecha D, Movsas R, Sano U, Menon JU. Applications of alginate microspheres in therapeutics delivery and cell culture: Past, present and future. *Int J Pharm* [Internet]. 2019;569:118627. Available from: <https://doi.org/10.1016/j.ijpharm.2019.118627>
- [13] Ramanathan G, Singaravelu S, Muthukumar T, Thyagarajan S, et al. Design and characterization of 3D hybrid collagen matrixes as a dermal substitute in skin tissue engineering. *Mater Sci Eng C* [Internet]. 2017;72:359-70. Available from: <https://doi.org/10.1016/j.msec.2016.11.095>
- [14] Van Nieuwenhove I, Salamon A, Peters K, Graulus G-J, et al. Gelatin- and starch-based hydrogels. Part A: Hydrogel development, characterization and coating. *Carbohydr Polym* [Internet]. 2016;152:129-39. Available from: <https://doi.org/10.1016/j.carbpol.2016.06.098>
- [15] Capanema NSV, Mansur AAP, de Jesus AC, Carvalho SM, et al. Superabsorbent crosslinked carboxymethyl cellulose-PEG hydrogels for potential wound dressing applications. *Int J Biol Macromol* [Internet]. 2018;106:1218-34. Available from: <https://doi.org/10.1016/j.ijbiomac.2017.08.124>
- [16] Yadav I, Rathnam VSS, Yagalakshmi Y, Chakraborty S, et al. Synthesis and characterization of polyvinyl alcohol- carboxymethyl tamarind gum based composite films. *Carbohydr Polym* [Internet]. 2017;165:159-68. Available from: <https://doi.org/10.1016/j.carbpol.2017.02.026>
- [17] Li Y, Tan Y, Xu K, Lu C, et al. A biodegradable starch hydrogel synthesized via thiol-ene click chemistry. *Polym Degrad Stab* [Internet]. 2017;137:75-82. Available from: <https://doi.org/10.1016/j.polymdegradstab.2016.07.015>
- [18] Nasri-Nasrabadi B, Mehrasa M, Rafienia M, Bonakdar S, Behzad T, et al. Porous starch/cellulose nanofibers composite prepared by salt leaching technique for tissue engineering. *Carbohydr Polym* [Internet]. 2014;108:232-8. Available from: <https://doi.org/10.1016/j.carbpol.2014.02.075>
- [19] Waghmare VS, Wadke PR, Dyawanapelly S, Deshpande A, et al. Starch based nanofibrous scaffolds for wound healing applications. *Bioact Mater* [Internet]. 2018;3(3):255-266. Available from: <https://doi.org/10.1016/j.bioactmat.2017.11.006>
- [20] Kalia S, Avérous L. *Biodegradable and Biobased Polymers for Environmental and Biomedical Applications*. Beverly, MA: Wiley; 2016. 501p.
- [21] Zuo Y, Liu W, Xiao J, Zhao X, et al. Preparation and characterization of dialdehyde starch by one-step acid hydrolysis and oxidation. *Int J Biol Macromol* [Internet]. 2017;103:1257-64. Available from: <https://doi.org/10.1016/j.ijbiomac.2017.05.188>
- [22] Zhang Y-R, Wang X-L, Zhao G-M, Wang Y-Z. Preparation and properties of oxidized starch with high degree of oxidation. *Carbohydr Polym* [Internet]. 2012;87:2554-62. Available from: <https://doi.org/10.1016/j.carbpol.2011.11.036>
- [23] Zhang S-D, Zhang Y-R, Wang X-L, Wang Y-Z. High Carbonyl Content Oxidized Starch Prepared by Hydrogen Peroxide and Its Thermoplastic Application. *Stärke* [Internet]. 2009;61:646-55. Available from: <https://doi.org/10.1002/star.200900130>
- [24] Wen N, Lü S, Xu X, Ning P, et al. A polysaccharide-based micelle-hydrogel synergistic therapy system for diabetes and vascular diabetes complications treatment. *Mater Sci Eng C* [Internet]. 2019;100:94-103. Available from: <https://doi.org/10.1016/j.msec.2019.02.081>
- [25] Nada AA, Soliman AAF, Aly AA, Abou-Okeil A. Stimuli-Free and Biocompatible Hydrogel via Hydrazone Chemistry: Synthesis, Characterization, and Bioassessment. *Stärke* [Internet]. 2018;71:1800243. Available from: <https://doi.org/10.1002/star.201800243>

- [26] El Sheikha AF, Ray RC. Potential impacts of bioprocessing of sweet potato: Review. *Crit Rev Food Sci Nutr* [Internet]. 2017;57(3):455-71. Available from: <https://doi.org/10.1080/10408398.2014.960909>
- [27] Smith RJ. Characterization and analysis of starches. In: Whistler RL, Paschall EF (eds.). *Starch: Chemistry and Technology*. New York: Academic Press; 1967:620-625p.
- [28] Parovuori P, Hamunen A, Forssell P, Autio K, et al. Oxidation of Potato Starch by Hydrogen Peroxide. *Stärke* [Internet]. 1995;47(1):19-23. Available from: <https://doi.org/10.1002/star.19950470106>
- [29] Ellens CJ. Design, optimization and evaluation of a free-fall biomass fast pyrolysis reactor and its products. [Master's thesis]. [Iowa]: Iowa State University, 2009: 155.
- [30] Nomani A, Nosrati H, Manjili HK, Khesalpour L, et al. Preparation and Characterization of Copolymeric Polymersomes for Protein Delivery. *Drug Res* [Internet]. 2017;67(8):458-65. Available from: <https://doi.org/10.1055/s-0043-106051>
- [31] Osundahunsi OF, Fagbemi TN, Kesselman E, Shimoni E. Comparison of the Physicochemical Properties and Pasting Characteristics of Flour and Starch from Red and White Sweet Potato Cultivars. *J Agric Food Chem* [Internet]. 2003;51(8):2232-6. Available from: <https://doi.org/10.1021/jf0260139>
- [32] Pérez S, Baldwin PM, Gallant DJ. Structural Features of Starch Granules I. In: BeMiller J, Whistler R (eds). *Food Science and Technology* [Internet]. Academic Press; 2009. 149-192p. Available from: <https://doi.org/10.1016/B978-0-12-746275-2.00005-7>
- [33] Salmi T, Tolvanen P, Wärnå J, Mäki-Arvela P, et al. Mathematical modeling of starch oxidation by hydrogen peroxide in the presence of an iron catalyst complex. *Chem Eng Sci* [Internet]. 2016;146:19-25. Available from: <https://doi.org/10.1016/j.ces.2016.02.027>
- [34] Lyu Y, Ren H, Yu M, Li X, et al. Using oxidized amylose as carrier of linalool for the development of antibacterial wound dressing. *Carbohydr Polym* [Internet]. 2017;174:1095-105. Available from: <https://doi.org/10.1016/j.carbpol.2017.07.033>
- [35] Silva R, Singh R, Sarker B, Papageorgiou DG, et al. Hydrogel matrices based on elastin and alginate for tissue engineering applications. *Int J Biol Macromol* [Internet]. 2018;114:614-25. Available from: <https://doi.org/10.1016/j.ijbiomac.2018.03.091>
- [36] Nourmohammadi J, Ghaee A, Liavali SH. Preparation and characterization of bioactive composite scaffolds from polycaprolactone nanofibers-chitosan-oxidized starch for bone regeneration. *Carbohydr Polym* [Internet]. 2016;138:172-9. Available from: <https://doi.org/10.1016/j.carbpol.2015.11.055>
- [37] Tang IM, Krishnamra N, Charoenphandhu N, Hoonsawat R, et al. Biomagnetic of Apatite-Coated Cobalt Ferrite: A Core-Shell Particle for Protein Adsorption and pH-Controlled Release. *Nanoscale Res Lett* [Internet]. 2011;6:19. Available from: <https://doi.org/10.1007/s11671-010-9761-4>
- [38] Li D, Ye Y, Li D, Li X, et al. Biological properties of dialdehyde carboxymethyl cellulose crosslinked gelatin-PEG composite hydrogel fibers for wound dressings. *Carbohydr Polym* [Internet]. 2016;137:508-14. Available from: <https://doi.org/10.1016/j.carbpol.2015.11.024>
- [39] Arockianathan PM, Sekar S, Kumaran B, Sastry TP. Preparation, characterization and evaluation of biocomposite films containing chitosan and sago starch impregnated with silver nanoparticles. *Int J Biol Macromol* [Internet]. 2012;50(4):939-46. Available from: <https://doi.org/10.1016/j.ijbiomac.2012.02.022>
- [40] Moreno O, Cárdenas J, Atarés L, Chiralt A. Influence of starch oxidation on the functionality of starch-gelatin based active films. *Carbohydr Polym* [Internet]. 2017;178:147-58. Available from: <https://doi.org/10.1016/j.carbpol.2017.08.128>
- [41] Liu Y, Ma L, Gao C. Facile fabrication of the glutaraldehyde cross-linked collagen / chitosan porous scaffold for skin tissue engineering. *Mater Sci Eng C* [Internet]. 2012;32(8):2361-6. Available from: <https://doi.org/10.1016/j.msec.2012.07.008>
- [42] Li T, Song X, Weng C, Wang X, et al. Self-crosslinking and injectable chondroitin sulfate/pullulan hydrogel for cartilage tissue engineering. *Appl Mater Today* [Internet]. 2018;10:173-83. Available from: <https://doi.org/10.1016/j.apmt.2017.12.002>
- [43] Zareidoost A, Yousefpour M, Ghaseme B, Amanzadeh A. The relationship of surface roughness and cell response of chemical surface modification of titanium. *J Mater Sci Mater Med* [Internet]. 2012;23:1479-88. Available from: <https://doi.org/10.1007/s10856-012-4611-9>
- [44] Hou Y, Xie W, Yu L, Cuellar Camacho L, et al. Surface Roughness Gradients Reveal Topography-Specific Mechanosensitive Responses in Human Mesenchymal Stem Cells. *Small* [Internet]. 2020;16(10):1905422. Available from: <https://doi.org/10.1002/sml.201905422>

[dx.doi.org/10.17488/RMIB.42.2.11](https://doi.org/10.17488/RMIB.42.2.11)

E-LOCATION ID: 1175

## Pressure Pain Threshold Values Obtained Through Algometers

### Valores de umbral de dolor por presión obtenidos mediante Algómetros

*J. H. Trueba-Perdomo<sup>1</sup>, F. Gasparini<sup>2</sup>, J. J. A. Flores Cuautle<sup>3</sup>*

<sup>1</sup>Hartwegii Capital

<sup>2</sup>Department of Informatics, Systems and Communication, University of Milano Bicocca

<sup>3</sup>CONACYT/TecNM-IT Orizaba

#### ABSTRACT

Pain intensity can provide relevant medical information; nowadays, pain measuring is still subjective; therefore, there are efforts to develop devices to measure the intensity of painful stimuli objectively. A review of the scientific literature on pressure pain obtained through algometers is carried out in this work. This literature review aims to present a database of pain pressure thresholds (PPT) related to different body parts so that future research on PPT, using an algometer, could compare their results against this research. The results of these PPT values are presented and grouped according to the body regions where previous researchers recorded their results to where they applied the pressure- trapezius muscles, back muscles, upper extremities, leg muscles, foot area, and muscles of the head. These values can be considered a reference to evaluate new algometers' accuracy and reliability. Finally, the algometers operational parameters range are defined according to all the studied algometers.

**KEYWORDS:** Pressure, Pain threshold, Manual algometer, Electromechanical algometer

## RESUMEN

La intensidad del dolor puede proporcionar información médica relevante, hasta ahora, la medición del dolor se lleva a cabo en forma subjetiva, por esta razón existen esfuerzos por desarrollar dispositivos para medir la intensidad de los estímulos dolorosos en forma objetiva. En este trabajo se realiza una revisión de la literatura científica sobre el dolor por presión obtenido mediante algómetros. El objetivo de esta revisión es presentar una base de datos de los umbrales de dolor por presión (PPT) de las diferentes partes del cuerpo, y de esta forma servir como punto de comparación para futuras investigaciones. Los resultados de estos valores de PPT son presentados y agrupados de acuerdo a las regiones del cuerpo donde los algómetros aplicaron la presión: músculos del trapecio, músculos de la espalda, extremidades superiores, músculos de las piernas, zona de los pies y músculos de la cabeza. Estos valores pueden considerarse una referencia para evaluar la precisión y la fiabilidad de los nuevos algómetros. Finalmente, se presentan los rangos de operación de las diferentes variables relacionadas con los algómetros estudiados.

**PALABRAS CLAVE:** Presión, Umbral de dolor, Algómetro manual, Algómetro electromecánico

### Corresponding author

TO: José Humberto Trueba Perdomo

INSTITUTION: Hartwegii Capital

ADDRESS: Avenida Oriente 6 #1372, Col. Centro,

C. P. 94344, Orizaba, Veracruz, México

E-MAIL: [jhtrueba1@gmail.com](mailto:jhtrueba1@gmail.com)

### Received:

24 March 2021

### Accepted:

2 July 2021

## INTRODUCTION

The International Association for the Study of Pain (IASP) [1] defines pain as "an unpleasant sensory and emotional experience associated with tissue damage or is described in terms of damage, whether the damage is real or potential." Since pain has existed throughout human evolution and is considered among the most significant public health problems of our society whether being considered a symptom or a disease [1]; especially for those people with chronic diseases, physicians have studied and compared different pain types through scientific research and experimentation in order to generate knowledge [2].

According to records, there are several pain classifications concerning intensity, frequency, or origin, even though there is scarce information regarding the threshold for a stimulus to become a pain sensation. According to its origin, the pain can be nociceptive or neuropathic; therefore, measuring its intensity can provide information about its origin. However, doctors usually use a subjective scale to assess the pain suffered by a patient; based on this scale, the type and frequency of analgesics prescribed are determined. Pain intensity determines the patient's treatment pathway and goals; pain can become a cause of disability for the patient depending on the intensity; therefore, various researchers have directed their efforts to develop devices to measure pain called algometers. Measuring a pressure pain threshold (PPT) is commonly adopted to try to quantify this sensation.

The PPT is currently defined as "the minimum necessary intensity of a nociceptive signal, derived from a pressure stimulus, to be perceived as painful [3]."

Several studies have been dedicated to finding the pain threshold in people, most of them using devices that generate a painful stimulus, like algometers [4]. An algometer is a device used for producing a controlled pain stimulus and can be either manual or electrome-

chanical. Studies have shown the feasibility of electromechanical algometers [5] [6] [7] [8]; nevertheless, these devices are not yet available in a commercial way. Thus, most of the studies reported in records have adopted manual algometers. Unfortunately, manual algometers cannot maintain a constant stimulus application speed (indentation speed) [7], and there may be data truncation because of the scales of manual algometers [9]. On the other hand, by using an electromechanical algometer, there is the possibility of normalizing the stimulus, defining the application rate of the stimulus and the penetration distance on the skin of the subject; this, in turn, increases the variables provided by the algometer, and in this way, more data can be obtained for pain analysis.

Despite articles dealing with PPT data, there is no work synthesizing assertive pain threshold values; thus, a literature review has been performed to understand better the problem of measuring a pain sensation. This work reviews the recent literature regarding the PPT values provided by manual and electromechanical algometers concerning different body regions.

This record review aims to present a database of PPTs related to different body parts so that future researchers on PPT, using an algometer, can use this work as a reference.

As a result of reading the scientific records, it was possible to define common characteristics that present electromechanical algometers have. The algometers operational parameters were defined considering all the studied algometers. These characteristics are summarized in the last section of this work and serve as a guideline to develop new electromechanical algometers.

## Literature Review methodology

A record research was performed, extracting articles from PubMed and Google Scholar databases to find articles related to PPT and the devices mentioned earlier by

using the keywords "pain, pressure pain threshold, pressure algometry, algometer, dolorimeter, electromechanical algometer, and computerized algometer."

The search made by using each word separately resulted in 185 selected articles. From these 185 articles, scientific papers published before 2013 were discarded, except for the article [5], which was included to gain more data about the electromechanical algometers.

Inclusion and exclusion criteria was adopted to select the resulting 75 articles from the original 185. The inclusion criteria considered were the studies with precise results of PPT mean values, studies that used either a manual or an electromechanical pressure algometer, and studies that involved healthy subjects and subjects who suffered some pain or illness. This latter information has also been considered to analyze the differences in PPTs between healthy and ill people. On the other hand, the exclusion criteria adopted were the use of other instruments different from pressure algometers to generate a painful stimulus, studies that do not report the mean PPTs, and studies that do not specify the area of applied stimuli. A total of 20 scientific papers met the inclusion and exclusion criteria and thus were deeply studied and classified according to the body part where the stimulus was applied—trapezius muscles, back muscles, upper limbs, leg muscles, foot area, and head muscles. Figure 1 shows the article selection process described above and the final cardinality of papers considered for the six body parts mentioned before. As a first outcome of analyzing these 20 articles, the algometers list reported in Table 1 shows the existing models of algometers used in previous works.

### Data extraction

The following data were collected and summarized in Tables 2-7. They show the subjects involved in the experiments (age, number, sex, physical conditions), algometer adopted (type, tip area, and speed rate), rest

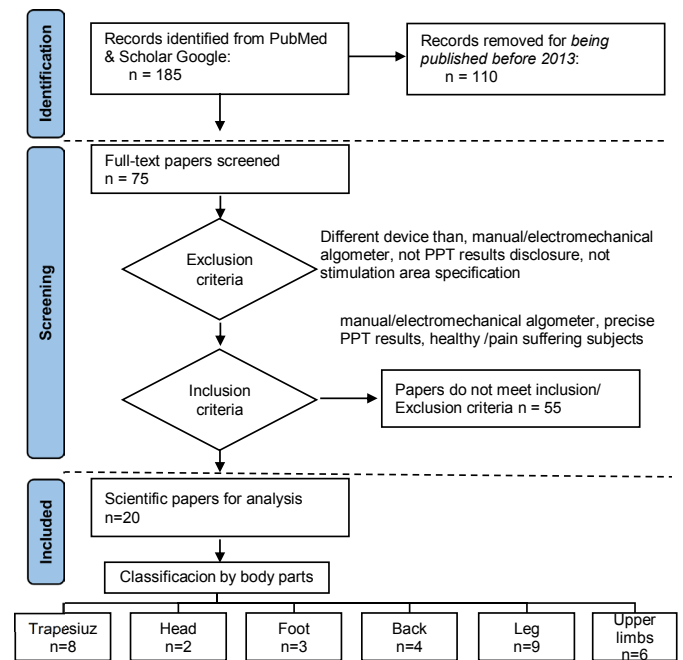


**FIGURE 1. Flow diagram of the followed methodology in paper selection.**

interval between trials, number of trials performed to obtain the mean value of PPT, the muscle on which the stimulus was applied, and in the last column the mean PPT values.

It is worth mentioning that the PPTs results were recorded when the stimulus changes from being comfortable to being uncomfortable, or a painful sensation was mentioned. Therefore, the PPT results collected from previous works have been obtained in each study as follows: a different number of trials were performed on each subject (varying from 2 to 5 applications of the stimulus), the average value of PPTs per subject was calculated over these trials, and finally, the mean values over all subjects were evaluated and corresponded to the PPT reported in Tables 2-7, for the body part where the stimulus was applied.

All the PPT values were properly converted and reported in the SI unit, kPa. For those studies where any kind of treatment was performed, only the baseline values were taken into account. For example, in

<sup>[10]</sup>, a baseline test was performed and then the subjects received a massage treatment; later on, they underwent another PPT test so, only the values of the first test were included in the tables.

A normalization of measurement units was also necessary for the stimulus application's speed rate (kPa/s) to compare all values shown in this study. As it can be seen the normalization was done for all collected data, except for the data extracted from <sup>[7]</sup> where the values used are in mm/s (see Table 6). It also shows that the range of speed rates varied from 10 to 126 kPa/s, and that in 5 studies the rate was not specified <sup>[8] [10] [11] [12] [13]</sup>. It can also be noted that the most used rate is 30 kPa/s (43.75% of the studies), followed by rates of about 124 kPa/s (18.75%), and 50 kPa/s (9.37%).

The age of the subjects involved varied from 18 to 88. In most studies, subjects were asked to stop taking any pharmaceutical drug (or medicine that alleviated pain) at least 24 hours before the test. Only in <sup>[14]</sup> were the patients allowed to continue their usual medical treatment during the experiment.

Since some studies conducted tests on different parts of the body, only the body parts that had reported values were included. Therefore, this work only presents the results of the trapezius muscles, back muscles, upper extremities and lower legs and head area. For example, in <sup>[15]</sup>, a stimulus was applied in the middle trapezius muscle, low back, hand, and quadriceps. The mean values of PPT for each body region are reported in the corresponding table (Tables 2-5).

Most of the algometers considered in the articles were manual. As seen, the Somedic algometer was the most used (10 papers), followed by the Warner algometer (6 papers), while only in one paper <sup>[12]</sup> were the tests carried out with the Baseline Dolorimeter. Finally, in 6 studies, tests were performed using an electromechanical algometer.

All articles used an algometer with a flat circular tip that varied in size from 0.5 to 2 cm<sup>2</sup> (area of stimulation). In all the studies carried out with an electromechanical algometer, the subjects had an "emergency stop button." Some studies performed with a manual algometer <sup>[2] [13] [15] [16] [17] [18] [19] [20]</sup>. The stop button provided the researcher the time to record the PPT. In other articles, the subjects gave a verbal report to the examiner to indicate the change from the sensation of pressure to pain <sup>[11] [12] [14] [21] [22] [23]</sup> in order to record the PPT value.

Finally, the range of intervals between trials varied from 10 s to 300 s, the most used is 30 s, followed by 20 s. The intervals between trials were not specified <sup>[7] [13] [21] [24]</sup>.

## RESULTS AND DISCUSSION

The analysis concerned the body part where the pressure stimulus had been applied; a summary table is populated for each of them.

### Characteristics of the electromechanical algometers used in the studies

It was possible to list the adopted algometers from the analysis of the 20 articles selected from the literature which were either manual or electromechanical. These algometers, together with the producer, the model, and the reference for further details are reported in Table 1.

The Algoforce PA3 adopted in <sup>[5]</sup> has a pressure sensor and an actuator for what concerns the electromechanical ones. This algometer is controlled by electromechanical feedback to increase the pressure when the stimulus is performed.

The electromechanical algometer presented in <sup>[6]</sup>, called multimodal automated sensory testing (MAST) system, is controlled by signals over a Bluetooth link. The subjects indicated the pain sensation using a rating scale over a touch screen on a separate computer. This algometer is portable and composed of a DC servo motor, hand-held thumbnail pressure stimulators, the

Bluetooth control system, and a load cell-type force sensor that works by resistive measurement (for measuring the pressure applied).

The so-called Automatic Tissue Tester (ATT) electro-mechanical algometer was used to apply the pressure stimulus in [7], the subjects had to stand on a platform, and then the pressure stimulus was applied from the bottom up; therefore, the body parts that were affected were at the bottom of the foot. The electromechanical algometer comprises an indentation speed control, maximum force application of 1500 kPa, a maximum indentation of 35 mm, tension-compression load cell, and a 200 step/revolution stepper motor. In [9], an electromechanical algometer similar to the one described in [7] was built.

Finally, in [8] [24], a Biaxial Algometer was used, designed with a pressure application device, a visual analog scale, a user interface, a controller, and an in-line attached load cell force sensor. The algometer can move linearly and rotationally.

**TABLE 1. Manual and electromechanical algometers used in the scientific papers included in this study.**

Algometer	Producer	Model	Reference
Manual	Somedic	Type II sales AB	somedic.com
Manual	Wagner	Force Ten FDX/Force Dial FDN 100/FDK 40/Force One FDIX 50	wagnerinstruments.com
Manual	Baseline	12-1442	fab-ent.com
Electro-mechanical	Custom-made	Algoforce PA3	www.gampt.de
Electro-mechanical	Custom-made	Computerized indentation system	[9]
Electro-mechanical	Custom-made	Multimodal Automated Sensory Testing (MAST) System	[6]
Electro-mechanical	Custom-made	Biaxial Pressure Algometer	[24]
Electro-mechanical	Custom-made	Automatic Tissue Tester (ATT)	[7]

### Analysis of PPT of the trapezius muscle area

The analysis of pain pressure applied to the trapezius muscle area in healthy participants is presented in Table 2 [15] [19] [21]. One study did not specify the condition of the subjects [17]; in 5 works, participants with some disease or pain were studied. The disease and pain conditions that affect the subjects are fibromyalgia [15], low back pain [15], neck pain [20], tension-type headache [2] [10], and pain in the upper trapezius (UT) muscle [11].

The highest mean value of PPT (512 kPa) was obtained in a test performed on healthy participants with a commercial algometer (Wagner Force Ten) in the upper trapezius muscle [15]. However, the lowest value (110 kPa) [11] has been recorded using the same manual algometer and in the same body part (upper trapezius muscle) on participants with local pain.

In two reports [2] [10], patients that suffered tension-type headache (TTH) were involved in the study. The PPT values obtained from these studies were registered using Wagner Instruments algometers [2] and Somedic AB [10]. Together with the previously cited one (110 kPa), these values were the lowest among those measured in the trapezius muscle area.

In [2], a more in-depth analysis had been performed to evaluate the PPTs on patients that suffer different types of TTH. According to the frequency of the headaches, the patients were separated into two groups: chronic tension-type headache (CTTH) and frequent episodic tension-type headache (FETTH). However, even if the tests were performed when the patients were without headaches or with a low-intensity pain (at least  $\leq 3$  points, rated on a numerical pain rate scale, 0 - 10) the PPT values registered (215 kPa for FETTH and 222 kPa for CTTH) were significantly low when compared with values obtained in other studies on healthy people (see Table 2).

**TABLE 2. Data extracted from articles assessing pressure pain threshold values in the trapezius muscle area.**

Article		Subjects					Algometer			Interval between trials (s)	Number of trials	Muscle	PPT Mean (kPa)
Reference	Year	Age (Range) Mean $\pm$ SD	Total	Males	Females	Physical health	Type	Area (cm <sup>2</sup> )	Rate (kPa/s)				
[19]	2018	(20-30) 23 SD2	35	18	17	H	Somedic	1	30	20	3	UT(ND)	418
													396
[21]	2018	(21-39) 25.8 SD3	34	21	13	H	Somedic	1	30	NS	2	UT(ND)	340
													335
[17]	2017	(18-70) SD 13.5	2199	1035	1164	NS	Somedic	1	30	20	NS	UT	446
[15]	2017	(18-64) 38 SD 13	21	9	12	H	Wagner	0.79	124	30	2	MT	512
		(18-64) 45 SD 9	26	7	19	F							395
		(18-64) 46 SD 14	16	8	8	SCLBP							396
		(18-64) 34 SD 10	15	7	8	MCLBP							425
		(18-64) 31 SD 10	23	9	14	RLBP							419
[20]	2017	40 SD 7	35	NS	NS	NP	Somedic	1	20	60	3	T (right)	424
												T (left)	434
												UN (right)	345
												UN (left)	371
		41 SD 8	34	NS	NS							T (right)	416
												T (left)	405
												UN (right)	334
												UN (left)	335
[2]	2017	NS	188	56	132	CTTH	Somedic	1	30	30	3	C5/C6joint	222
						FETTH							215
[10]	2017	(18-59)	62	NS	NS	TTH	Wagner	1	NS	30	3	UT (right)	187
												UT (left)	186
[11]	2016	(20-40)	15	NS	NS	LPUTM	Wagner	1	NS	30	3	UT	110

NS: not specified; H: healthy; F: fibromyalgia; SCLBP: severe chronic low back pain; MCLBP: mild chronic low back pain; RLBP: recurrent low back pain; NP: neck pain; CTTH: chronic tension-type headache; FETTH: frequent episodic tension-type headache; TTH: tension-type headache; LPUTM: local pain in the upper trapezius muscle; UT: upper trapezius; ND: non-dominant; MT: middle trapezius; T: trapezius; UN: upper neck.

Instead, in <sup>[10]</sup>, the pressure stimuli were applied while the patients presented a headache, obtaining even lower values (187 kPa on UT right and 186kPa on UT left) for the ones reported in <sup>[2]</sup>. From these studies,

it comes out that the intensity of pain directly affects the pain threshold, the more intense the pain, the lower the threshold. There are no articles that report the use of an electromechanical algometer on the UT.

**TABLE 3. Pressure pain threshold values in the back muscle area.**

Article		Subjects					Algometer			Interval between trials (s)	Number of trials	Muscle	PPT Mean (kPa)
Reference	Year	Age (Range) Mean ±SD	Total	Males	Females	Physical health	Type	Area (cm <sup>2</sup> )	Rate (kPa/s)				
[12]	2017	(18-30)	13	5	8	H	Baseline	1.52	NS	30	3	MR	655
												ML	659
												LR	705
												LL	676
												LDR	477
												LDL	394
[9]	2013	26 SD 4	16	8	8	H	Electromechanical (Computerized indentation system)	1	98	45	5	LB	484
							Wagner	NS					695
[13]	2016	(20-60) 36 SD 11	41	22	19	H	Wagner	1	NS	NS	NS	SJR (right)	833
												SJR (left)	814
		(18-70) 56 SD 10	31	11	20	SJP						SJR (right)	235
												SJR (left)	245
[15]	2017	(18-64) 38 SD 13	21	9	12	H	Wagner	0.79	124	30	2	LB	716
		(18-64) 45 SD 9	26	7	19	F							435
		(18-64) 46 SD 14	16	8	8	SCLBP							624
		(18-64) 34 SD 10	15	7	8	MCLBP							602
		(18-64) 1 SD 10	23	9	14	RLBP							676

NS: not specified; H: healthy; SJP: sacroiliac joint pain; F: fibromyalgia; SCLBP: severe chronic low back pain; MCLBP: mild chronic low back pain; RLBP: recurrent low back pain; MR: multifidus right; ML: multifidus left; LR: longissimus right; LL: longissimus left; LDR: latissimusdorsi right; LDL: latissimusdorsi left; LB: low back; SJR: sacroiliac joint region.

### Analysis of PPT of the back muscle area

In this section, all the studies that applied a pressure stimulus on the back muscle area are considered, and the extracted data are collected in Table 3. All these studies involved healthy participants. Two of them also performed tests on subjects who had fibromyalgia [15], back pain [15], and sacroiliac joint pain [13].

The lowest PPT value was obtained in patients with pain in the sacroiliac joint region (235 kPa), whereas healthy subjects reached the highest values (833 kPa)

[13]. Both values were obtained with a manual algometer (Wagner Force Dial TM FDK 40) that was applied to the sacroiliac joint region.

Out of the studies conducted on the back muscle area, an electromechanical algometer is used only in [9] (called computerized deformation-controlled indentation system). Therefore, tests were carried out on the lower back of healthy participants, both with a commercial Wagner FDN 100 algometer (695 kPa) and the electromechanical one (484 kPa). Since both devices

**TABLE 4. Data extracted from articles assessing pressure pain threshold values in upper limbs.**

Article		Subjects					Algometer			Interval between trials (s)	Number of trials	Muscle	PPT Mean (kPa)
Reference	Year	Age (Range) Mean $\pm$ SD	Total	Males	Females	Physical health	Type	Area (cm <sup>2</sup> )	Rate (kPa/s)				
[16]	2015	(18-65)	136	68	68	H	Somedic	1	30	20	2	BBM (D)	367
[5]	2007	(22-53) 28 SD 8	37	17	20	H	Somedic	1	50	30	4	T (right)	357
							Electromechanical (Algoforce PA3)						371
		(25-88) 58 SD 14	64	32	32	CP	Somedic						357
							Electromechanical (Algoforce PA3)						371
[6]	2013	(24-58) 41 SD 12	10		10	H	Electromechanical (MAST)	1	78	20	NS	T (D)	260
		(25-64) 45 SD 15				F							98
[18]	2017	43	40	20	20	H	Wagner	1	126	10	4	MF	897
		52	60	33	27	DC							675
[15]	2017	(18-64) 38 SD 13	21	9	12	H	Wagner	0.79	124	30	2	Hand	568
		(18-64) 45 SD 9	26	7	19	F							370
		(18-64) 46 SD 14	16	8	8	SCLBP							447
		(18-64) 34 SD 10	15	7	8	MCLBP							469
		(18-64) 31 SD 10	23	9	14	RLBP							477
[2]	2017	NS	188	56	132	CTTH	Somedic	1	30	30	3	SM	268
						FETTH							241

NS: not specified; H: healthy; CP: chronic pain; F: fibromyalgia; DC: disorder of consciousness; SCLBP: severe chronic low back pain; MCLBP: mild chronic low back pain; CTTH: chronic tension-type headache; FETTH: frequent episodic tension-type headache; MAST: Multimodal Automated Sensory Testing system; D: dominant; BBM: biceps brachii muscle; T: thumbnail; MF: middle finger; SM: second metacarpal.

applied the painful stimulus on the same area of the body and used the same sample of subjects, the values obtained should have been very similar. However, the difference between them was 211 kPa. The authors of such research explained the possibility of a mechanical problem related to the indentation speed of the system.

A value of 716 kPa obtained during the investigation in [15] on another patient using a manual Wagner algometer, further confirmed that the mechanical system

was probably wrong. This value is 232 kPa above the PPT value reported by the electromechanical algometer in [9] but shows a difference of only 21 kPa for the manual algometer result for the same research [9].

### Analysis of PPT of the upper limbs

In this section, PPT values obtained in upper limbs are collected and reported in Table 4. Among all the studies considered, only five involved healthy subjects

[5] [6] [15] [16] [18].

**TABLE 5. Pressure pain threshold values in the leg muscles.**

Article		Subjects					Algometer			Interval between trials (s)	Number of trials	Muscle	PPT Mean (kPa)	
Reference	Year	Age (Range) Mean $\pm$ SD	Total	Males	Females	Physical health	Type	Area (cm <sup>2</sup> )	Rate (kPa/s)					
[19]	2018	(20-30) 23 SD 2	35	18	17	H	Somedic	1	30	20	3	Q (D)	687	
													658	
[21]	2018	(21-39) 26 SD 3	34	21	13	H	Somedic	1	30	NS	2	Q (D)	616	
													565	
[17]	2017	(18-70) SD 13	2199	1035	1164	NS	Somedic	1	30	20	NS	TA	512	
[16]	2015	(18-65)	136	68	68	H	Somedic	1	30	20	2	Q (D)	543	
[24]	2014	24	24	12	12	H	Somedic	1	30	NS	3	TA (right)	392	
													400	
								Electromechanical (Biaxial Pressure Algometer)						427
														417
								Somedic					TA (left)	369
														363
								Electromechanical (Biaxial Pressure Algometer)						
													371	
[8]	2015	(22-36)	14	7	8	H	Electromechanical (Biaxial pressure algometer)	1	NS	50	3	TA (right)	520	
												TA (left)	391	
[15]	2017	(18-64) 38 SD 13	21	9	12	H	Wagner	0.79	124	30	2	Q	733	
		(18-64) 45 SD 9	26	7	19	F							461	
		(18-64) 46 SD 14	16	8	8	SCLBP							613	
		(18-64) 34 SD 10	15	7	8	MCLBP							607	
		(18-64) 31 SD 10	23	9	14	RLBP							633	
[2]	2017	NS	188	56	132	CTTH	Somedic	1	30	30	3	TA	435	
						FETTH							392	
[14]	2015	68 SD 9	77	34	43	OKP	Somedic	0.79	50	120	3	TA	159	
												MTJL	235	

NS: not specified; H: healthy; F: fibromyalgia; SCLBP: severe chronic low back pain; MCLBP: mild chronic low back pain; RLBP: recurrent low back pain; CTTH: chronic tension-type headache; FETTH: frequent episodic tension-type headache; OKP: osteoarthritis and knee pain; D: dominant; Q: quadriceps; TA: tibialis anterior; MTJL: medial tibiofemoral joint line.

TABLE 6. Pressure pain threshold values in the foot area.

Article		Subjects					Algometer			Interval between trials (s)	Number of trials	Muscle	PPT Mean (kPa)							
Reference	Year	Age (Range) Mean $\pm$ SD	Total	Males	Females	Physical health	Type	Area (cm <sup>2</sup> )	Rate (kPa/s)											
[7]	2010	(20-35) 26	5	5		H	Electromechanical (ATT)	1	1 mm/s	NS	2	CF	522							
																			517	
																				477
																			HP	1074
																				1039
																				1014
[18]	2017	43	40	20	20	H	Wagner	1	126 kPa/s	10	4	MF	676							
		52	60	33	27	DC													481	
[22]	2016	(37-67) 51	10	5	5	H	Somedic	0.5	50 kPa/s	300	3	I	490							
																MM	670			
																MJ	880			
													1				I	390		
																	MM	400		
																	MJ	680		
													2				I	230		
																	MM	250		
																	MJ	1230		
				(54-82) 64	11	7		4	PDN				0.5				I	730		
																	MM	700		
																	MJ	1230		
													1				I	520		
																	MM	370		
																	MJ	890		
													2				I	270		
											MM	270								
											MJ	520								

NS: not specified; H: healthy; DC: disorder of consciousness; PDN: painless diabetic neuropathy; ATT: automatic tissue tester; CF: center of the foot; HP: heel pad; MF: middle finger; I: instep; MM: medial malleolus; MJ: MTRP joints of the foot.

In [6], only female subjects are considered, while both males and females were included in the others. It should be noted that in [15], the pressure stimulus was applied between the thumb and the index finger on the dorsal part of the hand, while in the other articles, the pressure was applied on the biceps brachii muscle

[16], thumb [5] [6], the second metacarpal [2], and the middle finger [18]. In [5], tests were performed on the thumb, using a manual algometer (Algometer Type II, Somedic Production AB) and an electromechanical one, obtaining very similar PPT values, 357 kPa, and 371 kPa, respectively.

**TABLE 7. Pressure pain threshold values in the head muscle area.**

Article		Subjects					Algometer			Interval between trials (s)	Number of trials	Muscle	PPT Mean (kPa)
Reference	Year	Age (Range) Mean $\pm$ SD	Total	Males	Females	Physical health	Type	Area (cm <sup>2</sup> )	Rate (kPa/s)				
[2]	2017	NS	188	56	132	CTTH	Somedic	1	30	30	3	T	212
						FETTH							207
[10]	2017	(18-59)	62	NS	NS	TTH	Wagner	1	NS	30	3	S (right)	152
												S (left)	151

NS: not specified; TTH: tension-type headache; CTTH: chronic tension-type headache; FETTH: frequent episodic tension-type headache; S: suboccipital; T: temporalis.

The PPT values of the second metacarpal, obtained from [2], were among the lowest ones (268 kPa and 241 kPa); it is worth mentioning that the patients presented TTH. On the other hand, the highest value (897 kPa) was obtained on the middle finger in [18], using a manual algometer (Wagner Force One FDIX 50). It is observed that the PPT value of the middle finger is higher than PPTs extracted from the hand [2] [15] and even higher than those presented on the brachii muscle [16], giving the impression that a more significant muscle gives higher values. These values can be related to the fact that the nerves responsible for perceiving the fingers' painful stimulus are more distant from the brain than those present in the arm.

The study reported in [6] made use of an electromechanical algometer. The pressure on the thumb of healthy subjects and the thumb of subjects with fibromyalgia produced PPTs of 260 kPa and 98 kPa, respectively, with a difference of 162 kPa. Thus, the PPT value of the patients with fibromyalgia had the lowest value of the whole table.

**Analysis of PPT of the foot area**

In the articles presented in Table 6, related to the foot area's pain pressure, both males and females were included, except for [7], where the participants were

only five males. This article is also the only one found in the studied records that applied a pressure stimulus on the foot area with an electromechanical algometer.

In [22], an analysis of different studies was carried out, collecting the following average ranges of PPTs: from 400 to 900 kPa for the hindfoot area (medial malleolus), 200 to 500 kPa for the midfoot area (instep), and 400 to 700 kPa for the forefoot area (second or third MTP joint).

These ranges are valid only for PPT measurements in healthy people and with a stimulation tip of 1 cm<sup>2</sup>. The same study's authors performed tests for three years on healthy people and people with painless diabetic neuropathy. The Somedic algometer used had an interchangeable flat round tip of 0.5, 1, and 2 cm<sup>2</sup>. The PPT values reported with the stimulation area of 1 cm<sup>2</sup> taken in healthy people are within the previously established ranges.

The study described in [7] recorded the highest PPT values with respect not only to the foot area but concerning all the papers here considered (see Tables 2-7). In addition, they recorded three different values on healthy people- 1014 kPa, 1039 kPa, and 1074 kPa, on the heel pad with the ATT algometer aforementioned.

**TABLE 8. Design characteristics of available algometers**

Author	Probe diameter	Sensing method	Pressure rate	Sample rate	Automatic stop	Body segments	Actuator
[9]	1 cm <sup>2</sup>	Strain gauge load cell	98 KPa/s	1 KHz	15 kg/cm <sup>2</sup>	Back muscles	200 step/revolution stepper motor (KH42KM2-901)
[5]	1 cm <sup>2</sup>	Hydraulic	-	-	10 kg	Upper limbs	-
[6]	1 cm <sup>2</sup>	Load cell-type force sensor	78 KPa/s	1 KHz	-	Upper limbs	DC Servo Motor
[24]	1 cm <sup>2</sup>	Load cell-type force sensor	0.3 kg/s	1 KHz	-	Leg muscles	-
[7]	1c m2	Tension-compression load cell	1 mm/s	1 KHz	-	Foot area	200 step/revolution stepper motor (KH42KM2-901)

### Analysis of PPT of the head muscles

Table 7 reports the results obtained from 2 articles <sup>[2]</sup> <sup>[10]</sup> that considered the head muscle area. These two studies were already analyzed in section 3.2, related to the trapezius muscle area, where the involved subjects' conditions were deeply detailed.

For the part of the study performed on the head muscles, in <sup>[10]</sup>, the number of males and females that participated was not specified for both of these studies; pressure stimulations were performed in two places-suboccipital muscles and temporalis muscle, obtaining PPT values in a range from 151 to 212 kPa.

### Design characteristic for a functional electromechanical pressure algometer (EPA)

Thanks to the analysis carried out in this work, it is possible to guideline an electromechanical algometer's characteristics. It was concluded that an ideal algometer should be able to measure the PPT in different parts of the body.

An ideal algometer must be designed to be applied to the trapezius muscles, back muscles, upper and lower extremities, and the head area because those areas are the most studied. Table 8 presents an overview of the design features included in the available literature.

A functional algometer should be able to monitor the actual pressure of contact between the algometer and the patient's skin; as well as, the speed rate with which the stimulus is applied, and the penetration distance of the tip into the skin of the subject in order to obtain a more significant amount of standardized data <sup>[24]</sup>. It would then make it possible to avoid the error produced by the operator of a manual algometer.

Furthermore, error reduction in conjunction with the signals extracted from other devices (such as electroencephalograms, electrocardiograms, skin conductivity sensors, pulse oximeters) could be significantly helpful in future works related to measure physical pain <sup>[23]</sup> <sup>[25]</sup> <sup>[26]</sup>.

Based on the results obtained and the findings of the review performed in this paper, the following characteristics are proposed for the design of an electromechanical pressure algometer:

### Physical features

Physical features were proposed based on the common characteristics present in the literature; in particular, the actuator for exerting the movement was a motor because its control is relatively easy to implement; however, an encoder is needed for calculating the motor's velocity and position.

1. A motor that moves the piston, controlled by an encoder.
2. Able to measure the sinking depth of the piston tip into the skin.
3. Simultaneous control by feedback to remove vibrations and oscillations.
4. Specialized pressure sensor.
5. Able to measure the direct pressure exerted on the skin by the piston.
6. Considering possible drift either by mechanical or thermal conditions.

### Security features

1. Emergency stop button for users in case of intense pain.
2. Automatic stop after a predefined pressure threshold.

### Operating parameters

The following operating parameters are proposed to fulfill all the operating parameters present in the algometers available in the literature. The higher limit for pressure range was proposed based on [7]; while, the stimulation area was selected to make comparisons with the available algometers easier.

1. Pressure range of the piston from 10 kPa to 1500 kPa.
2. Speed rate of the pressure stimulus from 20 kPa/s to 50 kPa/s.
3. Controlled waiting time between trials from 20 s to 300 s.
4. Stimulation area 1 cm<sup>2</sup> compared with commercial manual algometers, corresponding to the range given the best pain analysis results [22] [27].

### CONCLUSIONS

In this work, an exhaustive review of PPT related articles was carried out. The review included studies related to PPT, obtained with manual and electromechanical algometers in different parts of the body

which were the trapezius muscles, back muscles, upper limbs, leg muscles, foot area, and head muscles tested on healthy, sick or with some pain patients.

The PPT values collected from several studies are referred to several parts of the body, and thus they may not be directly compared. However, with these values, we propose a database of PPTs that could serve as a benchmark for future research with pressure algometers on healthy subjects and subjects with some disease or pain. Furthermore, we also provide a list of the different types of existing algometers and the basis to design an electromechanical pressure algometer (EPA).

From the analysis of all the data collected, the PPT values obtained from people who suffer any form of pain are lower than those obtained in the same body region for healthy people. Therefore, it seems that fibromyalgia has the highest effects in lowering the pain thresholds. The lowest value found among all the considered studies is 98 kPa which was obtained from the dominant thumb [6] on fibromyalgia patients. Further confirmation comes from [15] where healthy subjects, subjects with low back pain, and patients with fibromyalgia were considered for the same test. During this investigation, it was noticed that subjects with fibromyalgia had the lowest PPT values among the three groups that were registered.

It can also be observed that a headache strongly affects the perception of pain. Several of the lowest values of PPTs were obtained while the subjects had a headache. So, the results showed 186 kPa, and 187 kPa values on the UT region [10], while it showed values of 215 kPa and 222 kPa on the C5/C6 zygapophyseal joint [2].

Another result from studies performed on patients with headaches [2] [10] is that pain intensity directly affects the pain threshold- the more intense the pain, the lower the threshold.

**TABLE 9. The highest and lowest PPT values reported in kPa, from all the 20 articles considered.**

	Trapezius muscles	Back muscles	Upper limbs	Leg muscles	Foot area	Head muscles
<b>Lowest</b>	110 (P)	235 (P)	98 (P)	159 (P)	230 (H)	151 (P)
<b>Highest</b>	512 (H)	833 (H)	897 (H)	733 (H)	1074 (H)	212 (P)

Furthermore, the analysis performed on the studies presented in Tables 2-7 permitted verification of the electromechanical algometers' validity and reliability. Only in one work <sup>[9]</sup> the mean values of PPTs, which were obtained with an electromechanical device, presented discrepancies related to the PPT values compared with the manual ones. This discrepancy is probably related to the indentation speed <sup>[9]</sup>.

It is essential to emphasize that the values obtained from healthy people <sup>[6]</sup> are notably lower than those obtained from the same body part of those in <sup>[5]</sup>. This difference may have been caused by the fact that in <sup>[6]</sup>, only female subjects were under experimentation. These lower values agree with the results and conclusions reported in several other works <sup>[13] [17] [19] [21] [27]</sup>, where PPT values evaluated on females were significantly lower than the corresponding PPTs on male subjects.

Table 9 summarizes the lowest and the highest PPT values among all these articles concerning the six different body parts. The lowest value (98 kPa) obtained in <sup>[6]</sup> was registered on patients with fibromyalgia, applying a pressure stimulus with the dominant thumb's MAST algometer. Whereas the heel pad region is the least sensitive area of the human body since all the studies presented in Tables 2-7 showed high PPT values. It was concluded that the heel pad is the body site where the highest pain thresholds are held, ranging from 1014 kPa to 1074 kPa. These PPT values were obtained using the ATT algometer on healthy subjects <sup>[7]</sup>. As it can be noticed, these extreme values have been measured with electromechanical algometers.

The measurements of several PPT values were collected and critically compared for different body areas. These values verified that healthy subjects have higher PPTs than those who present some disease or pain. Moreover, we have found evidence that the intensity of pain directly affects the pain threshold; demonstrating that as the pain level increases, the subject's pain threshold decreases regardless the type of pain.

From these values, a database of PPTs from different parts of the body is generated. This database could serve as a benchmark for future research with pressure algometers. In addition, in conjunction with other physiological and biometric signals, it could be significantly helpful in future work related to the measurement of pain.

Finally, a guideline for the characteristics that an ideal electromechanical algometer should have is provided. A portable design that measures the PPTs in different body parts and that it is also smaller, lighter, and cheaper than the existing ones is desirable.

The validity and reliability of potential new algometers- either manual or electromechanical, can be evaluated considering the PPT values collected in this paper.

### **AUTHOR CONTRIBUTIONS**

All authors contributed equally to the work.

### **ETHICAL STATEMENT**

This work does not contain any studies with human participants performed by any of the authors.

## REFERENCES

- [1] Rojas-Libano D, Gonzalo Rivera L, Egaña JI T. Actividad oscilatoria en banda gamma, un promisorio nuevo marcador electroencefalográfico de dolor con potencial utilidad en la monitorización intraoperatoria. *Rev Hosp Clin Univ Chile*. 2015;26(3):204-214. Spanish.
- [2] Palacios-Ceña M, Wang K, Castaldo M, Guerrero-Peral, et al. Assessment of deep dynamic mechanical sensitivity in individuals with tension-type headache: The dynamic pressure algometry. *Eur J Pain* [Internet]. 2017;21(8):1451-1460. Available from: <https://doi.org/10.1002/ejp.1065>
- [3] Ylinen J. Pressure algometry. *Aust J Physiother* [Internet]. 2007;53(3):207. Available from: [https://doi.org/10.1016/S0004-9514\(07\)70032-6](https://doi.org/10.1016/S0004-9514(07)70032-6)
- [4] Cabitza F. Rappresentazione del dolore: concetti e strumenti. In Donelli FM (ed). *Il Dolore in Ortopedia e Traumatologia*. Italy: Griffin; 2016. 15-34pp. Italian.
- [5] Dagtekin O, König E, Gerbershagen HJ, Marcus H, et al. Messung der druckschmerzempfindlichkeit. Vergleich eines elektromechanisch gesteuerten algometers mit etablierten methoden. *Schmerz* [Internet]. 2007;21(5):439-444. [German]. Available from: <https://doi.org/10.1007/s00482-007-0544-5>
- [6] Harte SE, Mitra M, Ichesco EA, Halvorson ME, et al. Development and validation of a pressure-type automated quantitative sensory testing system for point-of-care pain assessment. *Med Biol Eng Comput* [Internet]. 2013;51(6):633-644. Available from: <https://doi.org/10.1007/s11517-013-1033-x>
- [7] Xiong S, Goonetilleke RS, Witana CP, Rodrigo WDAS. An indentation apparatus for evaluating discomfort and pain thresholds in conjunction with mechanical properties of foot tissue in vivo. *J Rehabil Res Dev* [Internet]. 2010;47(7):629-641. Available from: <https://doi.org/10.1682/JRRD.2009.09.0152>
- [8] Adnadjevic D, Graven-Nielsen T. Temporal summation of muscle pain evoked by very fast pressure sequences and rotation. *Somatosens Mot Res* [Internet]. 2015;32(2):99-105. Available from: <https://doi.org/10.3109/08990220.2014.981650>
- [9] Koo TK, Guo JY, Brown CM. Test-Retest Reliability, Repeatability, and Sensitivity of an Automated Deformation-Controlled Indentation on Pressure Pain Threshold Measurement. *J Manipulative Physiol Ther* [Internet]. 2013;36(2):84-90. Available from: <https://doi.org/10.1016/j.jmpt.2013.01.001>
- [10] Moraska AF, Schmiede SJ, Mann JD, Butryn N, et al. Responsiveness of Myofascial Trigger Points to Single and Multiple Trigger Point Release Massages: A Randomized, Placebo Controlled Trial. *Am J Phys Med Rehabil* [Internet]. 2017;96(9):639-645. Available from: <https://doi.org/10.1097/PHM.0000000000000728>
- [11] Taleb WA, Youssef AR, Saleh A. The effectiveness of manual versus algometer pressure release techniques for treating active myofascial trigger points of the upper trapezius. *J Bodyw Mov Ther* [Internet]. 2016;20(4):863-869. Available from: <https://doi.org/10.1016/j.jbmt.2016.02.008>
- [12] Griefahn A, Oehlmann J, Zalpour C, von Piekartz H. Do exercises with the Foam Roller have a short-term impact on the thoracolumbar fascia? - A randomized controlled trial. *J Bodyw Mov Ther* [Internet]. 2017;21(1):186-193. Available from: <https://doi.org/10.1016/j.jbmt.2016.05.011>
- [13] van Leeuwen RJH, Szadek K, De Vet H, Zuurmond W, Perez R. Pain Pressure Threshold in the Region of the Sacroiliac Joint in Patients Diagnosed with Sacroiliac Joint Pain. *Pain Physician* [Internet]. 2016;19(3):147-154. Available from: <https://doi.org/10.36076/ppj/2019.19.147>
- [14] Moreton BJ, Tew V, Das Nair R, Wheeler M, et al. Pain phenotype in patients with knee osteoarthritis: Classification and measurement properties of painDETECT and self-report leads assessment of neuropathic symptoms and signs scale in a cross-sectional study. *Arthritis Care Res* [Internet]. 2015;67(4):519-528. Available from: <https://doi.org/10.1002/acr.22431>
- [15] Goubert D, Danneels L, Graven-Nielsen T, Descheemaeker F, et al. Differences in Pain Processing Between Patients with Chronic Low Back Pain, Recurrent Low Back Pain, and Fibromyalgia. *Pain Physician* [Internet]. 2017;20(4):307-318. Available from: <https://pubmed.ncbi.nlm.nih.gov/28535553/>
- [16] Graven-Nielsen T, Vaegter HB, Finocchietti S, Handberg G, Arendt-Nielsen L. Assessment of musculoskeletal pain sensitivity and temporal summation by cuff pressure algometry: A reliability study. *Pain* [Internet]. 2015;156(11):2193-2202. Available from: <https://doi.org/10.1097/j.pain.0000000000000294>
- [17] Skovbjerg S, Jørgensen T, Arendt-Nielsen L, Ebstrup JF, et al. Conditioned Pain Modulation and Pressure Pain Sensitivity in the Adult Danish General Population: The DanFunD Study. *J Pain* [Internet]. 2017;18(3):274-284. Available from: <https://doi.org/10.1016/j.jpain.2016.10.022>
- [18] Sattin D, Schnakers C, Pagani M, Arenare F, et al. Evidence of altered pressure pain thresholds in persons with disorders of consciousness as measured by the Nociception Coma Scale-Italian version. *Neuropsychol Rehabil* [Internet]. 2018;28(8):1295-1310. Available from: <https://doi.org/10.1080/09602011.2017.1290532>
- [19] Vaegter HB, Lyng KD, Yttereng FW, Christensen MH, et al. Exercise-Induced Hypoalgesia after Isometric Wall Squat Exercise: A Test-Retest Reliability Study. *Pain Med* [Internet]. 2019;20(1):129-137. Available from: <https://doi.org/10.1093/pm/pny087>
- [20] Murray M, Lange B, Nørnberg BR, Søggaard K, et al. Self-administered physical exercise training as treatment of neck and shoulder pain among military helicopter pilots and crew: A randomized controlled trial. *BMC Musculoskelet Disord* [Internet]. 2017;18(1):147. Available from: <https://doi.org/10.1186/s12891-017-1507-3>
- [21] Vaegter HB, Dørge DB, Schmidt KS, Jensen AH, et al. Test-Retest Reliability Of Exercise-Induced Hypoalgesia After Aerobic Exercise. *Pain Med* [Internet]. 2018;19(11):2212-2222. Available from: <https://doi.org/10.1093/pm/pny009>
- [22] Chantelau EA. Conventional deep pressure algometry is not suitable for clinical assessment of nociception in painless diabetic neuropathy. *Diabet Foot Ankle* [Internet]. 2016;7(1):31922. Available from: <https://doi.org/10.3402/dfa.v7.31922>
- [23] Misra G, Wang WE, Archer DB, Roy A, et al. Automated classification of pain perception using high-density electroencephalography data. *J Neurophysiol* [Internet]. 2017;117(2):786-795. Available from: <https://doi.org/10.1152/jn.00650.2016>

- [24]** Adnadjevic D, Graven-Nielsen T. Vibration And Rotation During Biaxial Pressure Algometry Is Related With Decreased And Increased Pain Sensations. *Pain Med* [Internet]. 2014;15(12):2095-2104. Available from: <https://doi.org/10.1111/pme.12550>
- [25]** Schulz E, Zherdin A, Tiemann L, Plant C, et al. Decoding an Individual's Sensitivity to Pain from the Multivariate Analysis of EEG data. *Cereb Cortex* [Internet]. 2012;22(5):1118-1123. Available from: <https://doi.org/10.1093/cercor/bhr186>
- [26]** Vatankhah M, Toliyat A. Pain Level Measurement Using Discrete Wavelet Transform. *Int J Eng Technol* [Internet]. 2016;8(5):380-384. Available from: <https://doi.org/10.7763/ijet.2016.v8.917>
- [27]** Andersen S, Petersen MW, Svendsen AS, Gazerani P. Pressure pain thresholds assessed over temporalis, masseter, and frontalis muscles in healthy individuals, patients with tension-type headache, and those with migraine-a systematic review. *Pain* [Internet]. 2015;156(8):1409-1423. Available from: <https://doi.org/10.1097/j.pain.0000000000000219>

[dx.doi.org/10.17488/RMIB.42.2.12](https://dx.doi.org/10.17488/RMIB.42.2.12)

E-LOCATION ID: 1178

## Evaluation of Parameters in PLA and PCL Scaffolds to be Used in Cartilaginous Tissues

### Evaluación de Parámetros en Andamios de PLA y PCL a ser Utilizados en Tejidos Cartilagosos

K. Cea<sup>1</sup>, M. Donoso<sup>1</sup>, G. Sérandour<sup>2,3</sup>, G. Martínez<sup>2</sup>, L. Alegría<sup>4</sup>

<sup>1</sup>Escuela de Ingeniería Civil Mecánica, Facultad de Ciencias de la Ingeniería, Universidad Austral de Chile.

<sup>2</sup>Instituto de Diseño y Métodos Industriales, Facultad de Ciencias de la Ingeniería, Universidad Austral de Chile.

<sup>3</sup>LeufüLab, Facultad de Ciencias de la Ingeniería, Universidad Austral de Chile.

<sup>4</sup>Centro de Docencia de Ciencias Básicas para Ingeniería, Facultad de Ciencias de la Ingeniería, Universidad Austral de Chile.

#### ABSTRACT

The scopes of medical treatments involving organ transplants and implants for chronic problems and trauma have changed significantly. However, these procedures are subject to multiple problems. Recently, tissue engineering has been used to address them. The present study is framed in the field of tissue engineering, particularly cartilage tissue, and proposes the evaluation of geometric and impression parameters for the manufacture of scaffolds as a basis for the growth of cells through 3D impression techniques. These scaffolds are highly porous three-dimensional supports that house donated or himself patient cells, providing a surface where the cells can adhere and proliferate. In the methodology, geometric and pore size variables are defined for scaffolding modeling by using CAD techniques and standardization of the printing process with standard 3D printers and accessible materials. The results showed that material flow, printing temperature, printing speed and ventilation are the most influential parameters in the manufacture of scaffolds. Additionally, it was found micrometric variations between the modeled design and the printing result. These scaffolds will subsequently be subjected to *in vitro* cell culture evaluating the adherence, division, and proliferation of the cells.

**KEYWORDS:** Scaffold, Cartilaginous Tissue, 3D Printing

## RESUMEN

Los alcances de los tratamientos médicos que involucran trasplantes e implantes de órganos para problemas crónicos y traumatismos han cambiado significativamente. No obstante, dichos procedimientos están sujetos a múltiples problemáticas. Recientemente, se ha recurrido a la ingeniería de tejidos, para abordarlos. El presente estudio se enmarca en el campo de la ingeniería de tejidos, particularmente de tejido cartilaginoso, y plantea la evaluación de parámetros geométricos y de impresión para la fabricación de andamios (scaffolds) como base para el crecimiento de células a través de técnicas de impresión 3D. Dichos andamios son soportes tridimensionales altamente porosos que albergan células, pudiendo ser estas del propio paciente o donadas, proporcionando una superficie donde estas se adhieran y proliferen. En la metodología se definen variables geométricas y de tamaño de poro para modelación de los andamios mediante CAD y estandarización del proceso de impresión con impresoras 3D estándar y materiales accesibles. Los resultados mostraron que el flujo de material, la temperatura de impresión, la velocidad de impresión y la ventilación son los parámetros más influyentes en la fabricación de andamios. Adicionalmente, se encontraron variaciones micrométricas entre el diseño modelado y el resultado de la impresión. Estos andamios, posteriormente, serán sometidos a cultivo celular *in vitro* evaluándose la adherencia, división y proliferación de las células.

**PALABRAS CLAVE:** Andamio, Tejido Cartilaginoso, Impresión 3D

### Corresponding author

TO: Gabriela Martínez

INSTITUTION: Universidad Austral de Chile

ADDRESS: Avenida General Lagos #2086, Valdivia,  
Los Ríos, Chile

E-MAIL: [gabriela.martinez@uach.cl](mailto:gabriela.martinez@uach.cl)

### Received:

28 April 2021

### Accepted:

19 July 2021

## INTRODUCTION

Sometimes, different diseases or physical or chemical aggressions can lead to a loss or alteration of the cells of a tissue or organ. The normal restitution of this tissue is the main purpose of regenerative medicine [1]. Tissue engineering is a new area of regenerative medicine whose objective is the construction of *in vitro* tissues for a therapeutic use, that allows to restoring, replacing, or increasing the functional activities of the organic tissues themselves [2]. Basically, tissue engineering consists of growing cells in an enriched three-dimensional matrix, where these cells can grow and later be transplanted into a recipient organ [3]. Three components can be distinguished: cells, biomaterials (the extracellular matrix or supporting scaffolds) and growth factors. This paper will focus specifically on contributing information and methodologies in the construction of scaffolds for cartilaginous tissue. Among its possible applications is the aesthetic treatment of microtia, a congenital malformation of the external ear that ranges from mild structural anomalies to the complete absence of the ear, with a prevalence rate that varies significantly between countries ranging from 0.8 to 17.4 per 10,000 births, with a higher prevalence reported in Ecuadorians, Chileans and Finns, with prevalence of 17.4; 8.8 and 4.3 respectively for every 10,000 births [4]. Current cosmetic treatment options for children include reconstruction with prosthesis, combination of prosthesis and own tissue, and autologous rib cartilage transplant.

Scaffolds, which can be manufactured by 3D printing, are highly porous three-dimensional substrates that house cells, providing a surface to which they can adhere, thrive and multiply [5]; consequently, they generate an extracellular matrix (ECM) of structural and functional proteins and saccharides that form living tissue [6]. This type of structure has been used in different organs such as bone tissues or soft tissues [7]. During the last decades, much research has been carried out regarding structural capacity [8], biocompatibility, cell growth speed [9], shape and manufacturing

process [10], among others. These investigations have generated extensive and interesting information that has made it possible to make considerable improvements in this discipline. More recently, diverse medical sub-specialties have started considering novel 3D bioprinting approaches, based on the concept of combining living cells and biomaterials, controlling cell proliferation, attachment, and migration within 3D printed scaffolds [11]. Currently, it is possible to design and manufacture cartilage in the shape of an ear, *in vitro*, which is subsequently implanted under the patient's skin. However, we must consider that these are new procedures and there is still a need to improve the methodologies and materials used. For this reason, it is important to define and evaluate manufacturing parameters to guarantee the manufacture quality of scaffolds. Different parameters such as material, geometry and pore size are evaluated, indicating how the manufacturing process can alter the expected result.

Two biocompatible and biodegradable materials, polycaprolactone (PCL) and polylactic acid (PLA), were used to manufacture the scaffolds. While there are other biocompatible materials, these two materials were used primarily because they are economic, although both present different difficulties in their manufacture. These materials will generate printing parameters that can be extrapolated to other biocompatible materials with similar characteristics.

## MATERIALS AND METHODS

The steps needed to allow the characterization of the necessary parameters for 3D scaffolding printing will be developed in the following section.

### Experiment design

Based on the information collected from studies of the geometry importance for cell growth, the size of the manufactured pores ranged between 200  $\mu\text{m}$  and 600  $\mu\text{m}$  [12] [13]. As for the shape, square, triangular and ellipsoidal geometries were defined. The repetitive-

ness of the experiment was set to 6 times for each combination. This is because the printers are manually calibrated, which interferes with the equality between one scaffold and another. Coupled with this inaccuracy, it was considered the diameter variation in the of the PLA material, it is +/- 0.05 mm which also influences the accuracy of pore size.

### Design and computational modeling of scaffolding

For the design of the PLA and PCL scaffolds, it is essential to define the following geometric parameters:  $l$  (scaffold length),  $p$  (pore size),  $h$  (scaffold height) and  $e$  (filament thickness). These parameters can be seen in Figure 1.

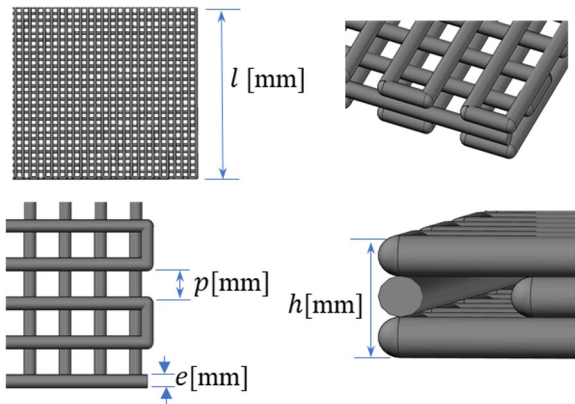


FIGURE 1. Top, three-dimensional view and dimensions (parameters) of the square scaffold. Source: self-made.

Once these parameters were defined, it was necessary to define the type of pore geometry. In this work, the geometries shown in Tables 1 and 2 were evalu-

ated. Table 1 considers the geometries manufactured with PLA and Table 2 considers the geometries manufactured with PCL.

TABLE 2. PCL scaffolding dimensions.

Square	
$p1 = 200 \mu\text{m}$ $p1 = 400 \mu\text{m}$ $p1 = 400 \mu\text{m}$	$l = 20 \text{ mm}$ $e = 400 \mu\text{m}$ $h = 1,2 \text{ mm}$

The pore size is represented by  $p$  and  $b$  parameter. For square and triangular geometries three scaffolds were defined, for ellipsoidal geometry just two scaffolds were defined. Figure 2 shows the structure of triangular and ellipsoidal scaffolding.

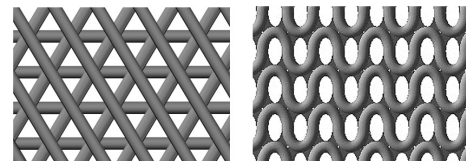


FIGURE 2. Structure of triangular and ellipsoidal scaffolding. Source: self-made.

### 3D Print

This section shows the commercial properties of the materials to be printed, the machine considered for 3D printing in both PLA and PCL, in addition to the printing protocol.

### Materials

Table 3 shows the characteristics of the materials used for the manufacture of scaffolding. The PLA filament, despite not having a biocompatibility certificate, was chosen because it is based on natural resins, without additives or colorants. It should be noted that the PLC has no additives or composts to be either persistent, bioaccumulative and toxic and its molecular weight in mass Mw is 80,000.

TABLE 1. PLA scaffolding dimensions.

Square	Triangular	Ellipsoidal
$p1 = 600 \mu\text{m}$ - $b3: 300 \mu\text{m}$ $p1 = 450 \mu\text{m}$ - $b2: 225 \mu\text{m}$ $p1 = 300 \mu\text{m}$		$l = 20 \text{ mm}$ $e = 200 \mu\text{m}$ $h = 1,2 \text{ mm}$

**TABLE 3. Characteristics of the materials.**

Features	PLA* [14]	PCL*[15]
Origin	USA	USA
Brand	3Dxtech	Sigma-Aldrich
Presentation	Filament	Granulated
Material diameter	1,75 mm +/- 0,05	3 mm
Temp. Extrusion °C	190-220	54-70
Color	Without pigment (natural)	Without pigment (natural)
Density	1,24 g/cc	1.145 g/mL at 25 °C
Tensile Strength	56 MPa	-
Tensile Modulus	2865 MPa	-
Tensile Elongation, Break	8%	-
Flexural Strength	178 MPa	-
Flexural Modulus	3185 MPa	-

\*This information is indicated by the provider.

## Machinery

Two types of printers were used, namely P1 and P2, for printing on PLA and PCL, respectively. Table 4 shows equipment information.

**TABLE 4. Commercial characteristics of the printers used.**

	P1 Printer	P2 Printer
Brand	Anet A8 Diy Prusa I3	Prototype "VitaPrint 3D"
Extruder	Brass nozzle with 0.2 diameter mm	22 gauge stainless steel needle

## Software used

The following table illustrates the software used for each application (see Table 5).

**TABLE 5. Software used.**

Activity	Software
Scaffolding design in PLA and PLC	Inventor Autodesk 2019© [16]
G code and PLA scaffolding parameters	Ultimaker Cura 4.0.0 [17]
G code and PLC scaffolding parameters	Repetier Host v2.1.6 [18]
PLA & PCL scaffolding measurement	Gwyddion 2.53 [19]

## Print care

The environmental conditions for printing were taken into account. For this, variables such as air currents, humidity, temperature, and hygiene were considered.

## Scaffold Porosity Calculation

To obtain the porosity of the PLA scaffolds, the length of the filament used in the printing of each geometry was measured and its volume is obtained by multiplying the length of the filament by its area. The area is a constant value since the filament has a diameter of 1.75 mm. Similarly, for the PCL, the advance of the syringe embolus and its diameter is 12 mm. It is then divided by the volume that the scaffold would occupy if it were solid (see Equation 1).

$$P = \left(1 - \frac{V_i}{V_s}\right) \% \quad (1)$$

Where:

P: Scaffold porosity

Vi: Volume printed

Vs: Solid volume occupied by scaffolding

## RESULTS AND DISCUSION

During the scaffolding generation, the environmental conditions for printing process was analyzed. During the printing, it is necessary to consider the following aspects:

- *Control of air currents*

The printers were encapsulated in transparent acrylic boxes to prevent the entry of air currents that may impair the printing process and, at the same time, allow checking the status of each print without opening the box. They also decrease the possibility of entry of pathogens into the printing area.

- Decreased air humidity*

A moisture absorbing filter were placed inside the box, as humidity greatly affects the properties of the materials which can, in turn, have an impact on the print quality.
- Calibration*

The printers were manually calibrated to ensure proper adhesion of the material to the base and ensure that each print is level.
- Print surface*

Glass was chosen as the printing surface to facilitate cleaning and hygiene.
- Hygiene*

For the printing process, special care was taken in the hygiene of all the implements and the surrounding area of the printing. For this, 70% (w/v) alcohol were used to disinfect the workspace and tools. This concentration is the classic and agreed recommendation of the reliable methods for decontaminating surfaces [20]. Additionally, it was contemplated the use of masks and clinical gloves.
- Room temperature*

This variable had a high impact on the scaffold's print quality. For the PLA case, the extruder temperature must be lowered to counteract the ambient temperature. If the ambient temperature exceeds 20 °C, the extruder temperature should be lowered beyond the limits recommended by the manufacturer. On the other hand, the PCL printing were more susceptible to variations on ambient temperature; when the temperature was below 10 °C, the printing was released by retraction because the material cools too quickly, and, if the temperature exceeded 20 °C, the material was kept in a viscous state for a long time, decreasing the pore size.

With consideration of those parameters, the following results are highlighted.

### Manufacturing remarks for PLA

It is evidenced that it is not possible to manufacture designs with pores of 200  $\mu\text{m}$ , because, to ensure adhesion to the glass base, the first layer of the print is wider, producing an effect that is commonly called "elephant foot". This causes the pore walls to join, which causes the pore to be "enclosed" at the bottom and not exposed on both sides of the scaffold (Figure 3).

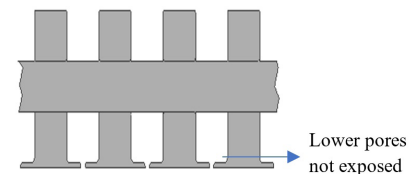


**FIGURE 3. Side view of square geometry scaffolding with "elephant foot" effect (not to scale). Source: self-made.**

It is possible to reduce this phenomenon by relying on Cura software [17]; however, this greatly hinders the adhesion of the material, which does not make its manufacture possible.

In the case of ellipsoidal scaffolding, it is evidenced that the way to print with precision, is to form each line with two thinner lines by using the option Special Modes-Surface: mode surface option [18] (Figure 4(A)) The normal option (used in the other geometries) doesn't a satisfactory result (Figure 4(B)).

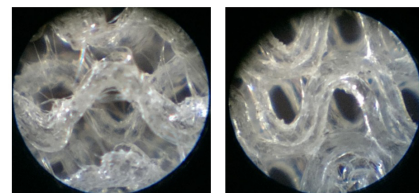


**FIGURE 4. Ellipsoidal scaffolding. The images was taken from optical microscope with x50 magnification. Printed in surface option surface mode (two lines) (A). Printed in normal option surface mode (single line) (B). Source: self-made.**

This phenomenon could be because on normal option, the extruder sometimes don't print consecutively (printing the sections in Random form (Figure 5), which does not happen with the surface option.

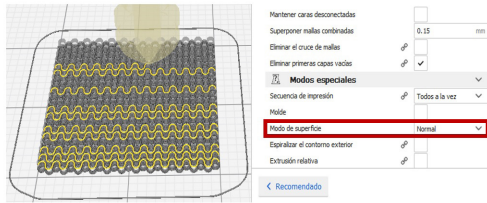


FIGURE 5. Extruder path in surface mode normal option.

The disadvantage of using two lines to form one is a thicker line results, so, the porosity of the scaffold decreases. To compensate part of this effect, the line is designed 0.01 mm smaller for this geometry.

### Print parameters for PLA

Tables 6 and 7 show the parameters obtained for optimal printing of PLA scaffolds.

TABLE 6. Printing parameters for PLA scaffolds [17].

Common print parameters for PLA geometries	
Parameter	Value
Layer height (mm)	0.1
Initial layer height (mm)	0.1
Line width <sup>1</sup> (mm)	0.18
Print plate temperature (°C)	60
Horizontal expansion of the initial layer <sup>2</sup>	-1
Z seam alignment <sup>3</sup>	User specified
Enable retraction	√
Type of print plate adhesion <sup>4</sup>	Skirt

<sup>1</sup>Line width: The width of the nozzle in the software parameters is modified to 0.18 mm to force the printer to extrude less material than it should, remembering that the actual diameter is 0.2 mm, therefore the line width used is also in 0.18 mm.

<sup>2</sup>Horizontal expansion of the initial layer: this parameter is used at 0 by default, this produces the effect previously referred to as elephant foot to facilitate the adherence to the base. Using the value -1 decreases part of this effect. A value less than -1 makes it impossible for the material to adhere to the glass plate.

<sup>3</sup>Z seam alignment: this parameter uses the random option by default which causes the start seems to be generated in any sector. This decreases the print quality, because at the beginning of each layer the extruder deposits residues of the previous layer. The option specified by the user dictates the alignment of the seams at the same point for each layer, which favors the scaffold's print quality.

<sup>4</sup>Type of print plate adhesion: The skirt option draws a line around the scaffold, the residues of each print start to be deposited there and not affect the scaffolding.

TABLE 7. Differentiated printing parameters for PLA geometries [19].

	Square	Triangle	Ellipse
Line width initial layer %	29	20	29
Printing temp. (°C)	184	184	182
Flow %	92	92	92
Initial layer flow %	83	81	78
Print speed (mm/s)	23	23	9.5
Ventilation speed %	50	50	35

## Dimensions and porosity for PLA

### Geometry

On average, all the geometries except the ellipse were approximately 50 μm smaller than the computationally modeled design. For the pore size of the ellipse to agree with that of the other geometries, an overlap had to be designed as shown Figure 6. A value of 100 μm was established to compensate for part of the material shrinkage.

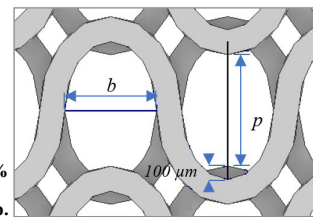


FIGURE 6. Dimensions in microns of ellipsoidal scaffolding concordant with pore. Source: self-made.

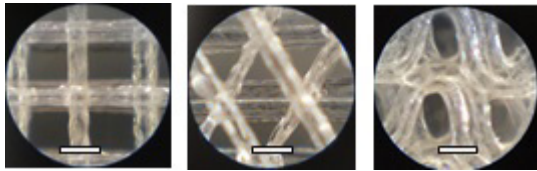
### Porosity

Table 8 shows the porosity percentage achieved for each PLA scaffold.

TABLE 8. Porosities of PLA scaffolds.

	Square	Triangle	Ellipse
p1	86%	87%	60%
p2	80%	82%	56%
p3	73%	78%	-
p1	86%	87%	60%

Finally, figure 7 shows a magnified detail of the PLA studied geometries.



**FIGURE 7. Detail of the geometries printed in PLA. Image from an optical microscope with 50x magnification. Square scaffold (A). Triangular scaffold (B). Ellipsoidal scaffold (C). Scale bars = 500  $\mu\text{m}$ . Source: self-made.**

### Manufacturing observations for PCL

For the printing of the PCL scaffolds, it was necessary to install a hot plate on the base of the printer, to avoid the adhesion problems to the base for the rapid cooling suffered by the material. This phenomenon causes a contract and forms small drops that harden and modify the height printing. When this occurs, the needle passes through the sector again, it hits the drops, and the scaffolding comes off. Together with the previous point, other conditions to ensure surface adhesion, is the use of rough tape on the hot bed.

The pore width should be maintained between 300 and 600  $\mu\text{m}$  since at the lower limit the filaments are joined and at the upper limit they are cut (Figure 8).

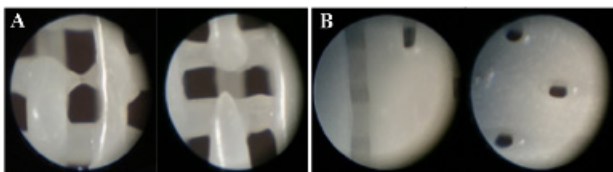


**FIGURE 8. PCL scaffolding cut filaments (A), agglomerated filaments (B). The images were taken from optical microscope with x50 magnification. Source: self-made.**

### Print parameters for PCL

Table 9 shows the parameters obtained for optimal printing of PCL scaffolds.

**TABLE 9. Printing parameters for PCL scaffolds [18].**

PCL	
Parameter	Square
Type of adhesion of the printing plate	Skirt
Layer Height (mm)	0.2
Initial layer height (mm)	0.2
Line Width (mm)	0.3
Print plate temperature <sup>1</sup> (°C)	25-35
Line width initial layer %	100
Syringe temperature (°C)	80
Needle temperature (°C)	75
Flow %	68
Initial layer Flow %	68
Print speed (mm/s)	10
Ventilation speed%	Without ventilation

<sup>1</sup>Print plate temperature °C: Change according to the ambient temperature; when ambient temperature is very low it is recommended to use 35 °C, when it is high, 25 °C.

### Dimensions and porosity for PCL

#### Geometry

Due to the characteristics and temperatures at which the PCL was printed, it was deposited in a liquid state, and as a result, the material spreads occupying a larger surface compared to the computationally modeled design. This results in the pores that were designed to 400  $\mu\text{m}$  being an average of 250  $\mu\text{m}$ .

#### Porosity

Based on the above and considering the largest diameter of the extruder, the porosity was reduced to 34% for the square geometry. Figure 9 (A) shows a magnification of the final pore size. In Figure 10 it can see a 20 mm PLC scaffold.

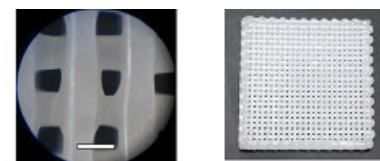


**FIGURE 9. PLC Scaffold. Detail of the geometries printed in PLC. Image from an optical microscope with 50x magnification. Scale bars = 500  $\mu\text{m}$  (A). 20 mm PLC scaffold (B). Source: self-made.**

## CONCLUSIONS

The three-dimensional elaboration of scaffolding for the regeneration of cartilaginous tissue represents a challenge for the existing manufacturing market devices. From this study, it is concluded:

For the equipment used in this work, the pore size of PLA must be greater than 200  $\mu\text{m}$  to prevent the effect called "elephant foot" enclosing the lower pores, while for manufacturing in PCL, the size of the computationally model pore should be greater than 300  $\mu\text{m}$  to prevent the filament joining together and less than 600  $\mu\text{m}$ , as the largest size, because the filaments will be cut.

It is necessary to consider the geometric design, the contraction of the geometries at least 50  $\mu\text{m}$  for the PLA.

Particularly, for the ellipsoidal scaffolds of PLA, an overlap had to be designed to compensate the material retraction.

In PCL material, this difference is intensified, therefore, it should be considered that the computationally designed pore, decreases by approximately 150  $\mu\text{m}$  in the final printed scaffold.

The extruder temperature is one of the most important variables. In PLA material, printing can be affected when the ambient temperature rises to 20  $^{\circ}\text{C}$ , the extruder temperature must be reduced below the manufacturer temperature indicates.

This is extremely important when printing is a very low speed. In PLC case, this is even more sensitive to temperatures, because it is a material that undergoes large retractions if it cools quickly, so it is necessary to implement a heat bed to the printing surface. On the other hand, the high temperature remains in a liquid state affecting the pore size.

As recommendations and future research work it is suggested:

- The cell growth in manufactured geometries could be evaluated, to observe the incidence of the geometry and/or material in cell development.
- The manufacturing options in the PLC case could be expanded, by using needles with smaller diameters, to obtain more porous scaffolds. Additionally, the possibility to combine PLC with another biocompatible material to improve its mechanical properties could be studied.
- Cell growth evaluations could be carried out in the defective manufactured scaffolds. When the computationally modeled design was not obtained, the result geometry is an interspecific and random figure. This poorly arranged patterns environment may be beneficial for cell growth.

## AUTHOR CONTRIBUTIONS

K. C. Participated in the scaffold design, definition of 3D printing parameters, 3D printing of PLA scaffolds, and writing the original draft. M. D. Participated in the scaffold design, definition of 3D printing parameters, and 3D printing of PCL scaffolds. G. M. Oversaw the project supervision, experiment planning and the analysis of results, and participated in writing, reviewing, and editing the manuscript. G. S. Supervised the project supervision, as well as the 3D printing processes, and participated in writing, reviewing, and editing the manuscript. L. A. Participated in the material selection and writing original draft.

## DECLARATION OF COMPETING INTEREST

We declare that we have no significant competing interests including financial or non-financial, professional, or personal interests interfering with the full and objective presentation of the work described in this manuscript.

### **ACKNOWLEDGEMENTS**

The authors want to show their appreciation to the School of Mechanical Civil Engineering of the Faculty of Engineering Sciences of the Universidad Austral de Chile for its support in the achievement of this work.

This work was funded by the FIC 1720 Project - "INGOMED" with resources from the FIC Competitivity Innovation Fund of the Rios Region, and Installation Project of Engineering 2020-03 n°: 13163235 of Vice Rectorate of Investigation, Development and Artistic Creation of the Austral University of Chile.

## REFERENCES

- [1] Serrato Ochoa D, Nieto Aguilar R, Aguilera Méndez A. Ingeniería de tejidos. Una nueva disciplina en medicina regenerativa. *Investigación y Ciencia* [Internet]. 2015;23(64):61-9. Available from: <https://www.redalyc.org/articulo.oa?id=67441039009>
- [2] Rosa V, Zhang Z, Grande RH, Nör JE. Dental Pulp Tissue Engineering in Full-length Human Root Canals. *J Dent Res*. 2013;92(11):970-5. Available from: <https://doi.org/10.1177/0022034513505772>
- [3] Shapira A, Kim D-H, Dvir T. Advanced micro- and nanofabrication technologies for tissue engineering. *Biofabrication*. 2014;6(2):020301. Available from: <https://doi.org/10.1088/1758-5082/6/2/020301>
- [4] Luquetti DV, Leoncini E, Mastroiaco P. Microtia-anotia: A global review of prevalence rates. *Birth Defects Res* [Internet]. 2011;91(9):813-22. Available from: <https://doi.org/10.1002/bdra.20836>
- [5] Ingber DE, Mow VC, Butler D, Niklason L, et al. Tissue Engineering and Developmental Biology: Going Biometric. *Tissue Eng* [Internet]. 2006;12(12):3265-83. Available from: <https://doi.org/10.1089/ten.2006.12.3265>
- [6] Derby B. Printing and Prototyping of Tissues and Scaffolds. *Science* [Internet]. 2012;338(6109):921-6. Available from: <https://doi.org/10.1126/science.1226340>
- [7] Azevedo Gonçalves Mota RC, Oliveira da Silva E, Fortes de Lima F, Rodrigues de Menezes L, et al. 3D Printed Scaffolds as a New Perspective for Bone Tissue Regeneration: Literature Review. *Mat Sci and Appl* [Internet]. 2016;7(8):430-52. Available from: <https://doi.org/10.4236/msa.2016.78039>
- [8] Reboledo-Grau D, Martínez-Bordes G. Metodología para el diseñocomputacional de andamios a ser utilizados en reparación ósea. *Rev UIS Ing* [Internet]. 2020;19(4):301-14. Available from: <https://doi.org/10.18273/revuin.v19n4-2020025>
- [9] Boschetti PJ, Pelliccioni O, Da Costa K, Sabino MA. Lattice Boltzmann simulation of swelling of an implant for microtia manufactured with IPN hydrogel. *Comput Methods Biomech Biomed Engin* [Internet]. 2020;23(1):491-9. Available from: <https://doi.org/10.1080/10255842.2020.1740210>
- [10] Banjanin B, Vladic G, Pal M, Balos S, et al. Consistency analysis of mechanical properties of elements produced by FDM additive manufacturing technology. *Rev Mater* [Internet]. 2018;23(4):e12250. Available from: <https://doi.org/10.1590/s1517-707620180004.0584>
- [11] Chiesa-Estomba CM, Aiastui A, González-Fernández I, Hernández-Moya R, et al. Three-Dimensional Bioprinting Scaffolding for Nasal Cartilage Defects: A Systematic Review. *Tissue Eng Regen Med* [Internet]. 2021;18(3):343-53. Available from: <https://doi.org/10.1007/s13770-021-00331-6>
- [12] Nava MM, Draghi L, Giordano C, Pietrabissa R. The Effect of Scaffold Pore Size in Cartilage Tissue Engineering. *J Appl Biomater Funct Mater* [Internet]. 2016;14(3):223-9. Available from: <https://doi.org/10.5301/jabfm.5000302>
- [13] Moroni L, de Wijn JR, van Blitterswijk CA. 3D fiber-deposited scaffolds for tissue engineering: Influence of pores geometry and architecture on dynamic mechanical properties. *Biomaterials* [Internet]. 2006;27(7):974-85. Available from: <https://doi.org/10.1016/j.biomaterials.2005.07.023>
- [14] 3DXTECH. Technical Data Sheet: ECOMAX® PLA 3D Printing Filament [Internet]; 2021. Available from: <https://www.3dxtech.com>
- [15] Meck. Polylactides (PLA) [Internet]. Sigma-Aldrich; 2021. Available from: <https://www.sigmaaldrich.com/MX/es/products/materials-science/biomedical-materials/hydrophilic-polymers->
- [16] Autodesk. Inventor [Internet]. Autodesk; 2019. Available from: <https://www.autodesk.com/education/free-software/inventor-professional>
- [17] Ultimaker. Cura 4.0.0 [Internet]. Ultimaker; 2019. Available from: <https://ultimaker.com/software/ultimaker-cura>
- [18] Hot-World GmbH & Co. KG. Repetier-Host v2.1.6 [Internet]. Repetier; 2019. Available from: <https://www.repetier.com>
- [19] Czech Metrology Institute. Gwyddion 2.53 [Internet]. Gwyddion; 2019. Available from: <http://gwyddion.net/download.php#stable>
- [20] Graziano MU, Graziano KU, Pinto FM, Bruna CQ, et al. Effectiveness of disinfection with alcohol 70% (w/v) of contaminated surfaces not previously cleaned. *Rev Latino Am. Enfermagem* [Internet]. 2013;21(2):618-23. Available from: <https://doi.org/10.1590/s0104-11692013000200020>

[dx.doi.org/10.17488/RMIB.42.2.13](https://dx.doi.org/10.17488/RMIB.42.2.13)

E-LOCATION ID: 1176

## Autonomic Face Mask Detection with Deep Learning: an IoT Application

### Detección Autonomica de Cubrebocas con Aprendizaje Profundo: una Aplicación del IoT

*V. H. Benitez-Baltazar, J. H. Pacheco-Ramírez, J. R. Moreno-Ruiz, C. Nuñez-Gurrola*

Universidad de Sonora

#### ABSTRACT

A new and deadly virus known as SARS-CoV-2, which is responsible for the coronavirus disease (COVID-19), is spreading rapidly around the world causing more than 4 million deaths. Hence, there is an urgent need to find new and innovative ways to reduce the likelihood of infection. One of the most common ways of catching the virus is by being in contact with droplets delivered by a sick person. The risk can be reduced by wearing a face mask as suggested by the World Health Organization (WHO), especially in closed environments such as classrooms, hospitals, and supermarkets. However, people hesitate to use a face mask leading to an increase in the risk of spreading the disease, moreover when the face mask is used, sometimes it is worn in the wrong way. In this work, an autonomic face mask detection system with deep learning and powered by the image tracking technique used for the augmented reality development is proposed as a mechanism to request the correct use of face masks to grant access to people to critical areas. To achieve this, a machine learning model based on Convolutional Neural Networks was built on top of an IoT framework to enforce the correct use of the face mask in required areas as it is requested by law in some regions.

**KEYWORDS:** Machine learning, COVID - 19, Cyber-Physical Systems, Internet of Things

## RESUMEN

Un virus nuevo y letal conocido como SARS-CoV-2, responsable de la enfermedad del coronavirus (COVID-19), se está propagando rápidamente por el mundo y ha provocado más de 4 millones de muertes. Por tal razón, existe una necesidad urgente de encontrar formas nuevas e innovadoras de reducir la probabilidad de infección. Una de las formas usuales de contraer el virus es al estar en contacto con las gotas de saliva de una persona enferma. Este riesgo se puede reducir usando una mascarilla tipo cubrebocas como sugiere la Organización Mundial de la Salud (OMS), especialmente en entornos cerrados como aulas, hospitales y supermercados. Sin embargo, las personas dudan en usar una mascarilla, lo que aumenta el riesgo de propagar la enfermedad, además, cuando se usa la mascarilla, a veces se usa de manera incorrecta. En este trabajo de investigación se propone un sistema autónomo de detección de mascarilla con aprendizaje profundo empoderado con la técnica de detección de imágenes que se utiliza en desarrollos de realidad aumentada como mecanismo para solicitar el correcto uso de mascarilla para permitir el acceso de personas a zonas críticas. Para lograr esto, se construyó un modelo de aprendizaje máquina basado en redes neuronales convolucionales con un enfoque de IoT para hacer cumplir el uso correcto de la máscara facial en las áreas requeridas, tal como lo exige la ley en algunas regiones.

**PALABRAS CLAVE:** Machine learning, COVID - 19, Cyber-Physical Systems, Internet of Things

### Corresponding author

TO: Victor Hugo Benitez Baltazar  
INSTITUTION: Universidad de Sonora  
ADDRESS: Blvd. Luis Encinas y Ave. Rosales S/N,  
Col. Centro, C. P. 83000, Hermosillo, Sonora, México  
E-MAIL: victor.benitez@unison.mx

### Received:

29 March 2021

### Accepted:

21 July 2021

## INTRODUCTION

Infectious diseases such as Influenza and Coronavirus Disease 19 (COVID-19) cause millions of deaths around the world <sup>[1]</sup> <sup>[2]</sup>. The pathogens of such diseases are mainly spread by droplets or aerosols as a result of cough, sneeze, etc <sup>[3]</sup>. Nowadays, due to the pandemic situation caused by the Severe Acute Respiratory Syndrome Coronavirus 2 (SARS-CoV-2) virus, there is an urgent need to limit airborne transmission of COVID-19. The target is to develop and implement effective methods or mechanisms to reduce the number of particles such as viruses from the air. Dissemination of infectious pathogens in crowded areas can be significant and, in many scenarios, the requirement is to implement mechanisms to protect people from being exposed to pathogens <sup>[4]</sup>. One of the most popular mechanisms is the use of a face mask which in some regions is required by law <sup>[5]</sup>. The World Health Organization (WHO) issued a guide to the use of face masks as a mechanism to reduce the risk of exposure to the COVID-19 <sup>[6]</sup>. In the document, the WHO states: "Place the mask carefully, ensuring it covers the mouth and nose, and tie it securely to minimize any gaps between the face and the mask". The guide aims to help people understand the benefits of using a face mask and the risks associated with not wearing or misusing. Despite the requirements and regulations, people hesitate to wear a mask, or they wear it in the wrong way.

The proliferation of SARS CoV-2 has affected all the countries over the world, and technology has an important role to play in this matter. Today's technology has enabled some areas such as schools to continue in operation, but there are some other areas or jobs that still require face-to-face contact, for instance, hospitals. To reactivate the economy, a certain level of on-site or face-to-face activity is needed <sup>[7]</sup>, but always observing healthcare regulations such as wearing a face mask. The IoT together with AI techniques could work to provide interesting solutions for the COVID-19 pandemic.

Internet of Things (IoT) techniques has been crucial against this pandemic, especially for detecting and tracking infected people. In <sup>[8]</sup> authors proposed a system using IoT for collecting vital signs from different users. With this system, important data can be collected and analyzed for a better understanding of the symptoms and from the virus. On the other hand, artificial intelligence (AI) has been very important to fight this pandemic. Examples of applications are the algorithms to detect if a person is infected or not with COVID-19. An image classification algorithm is proposed in <sup>[9]</sup> using deep learning to detect infections in X-ray images. With these algorithms, the images could be processed and improved to help the doctors to have better results in their diagnosis.

To keep track of the people wearing face masks, a surveillance camera could be used for detecting in real-time when someone is using a mask or not, this is possible thanks to the development of AI. In <sup>[10]</sup> the authors proposed a method for detecting anomalies in surveillance videos using deep learning techniques. One of the advantages of using AI is that a single person does not need to be aware of the place in every moment.

This paper shows the implementation of a face mask detection system, using augmented reality as tracking mechanism to trigger a screen projection on a mobile device which is used to request access to critical areas where the correct use of face mask is a requirement. To achieve this, a machine learning model based on Convolutional Neural Networks is built on top of an IoT framework to enforce the correct use of the face mask in required areas.

## Cyber-Physical Systems

Cyber-Physical Systems (CPS) refers to a combination or integration between the physical part and the computations of a system, mainly focused on their interaction <sup>[11]</sup>. Although this integration is not new, as embedded systems have been around for a while <sup>[12]</sup>, the term

CPS is kind of new, in 2006 Helen Gill presented this term and associated this relation with another concept called cybernetics [11].

CPS is growing very fast, and its growth is closely related to the growth of other technologies such as the internet of things and cloud computing. The applications of this kind of system are very wide, some important ones are health care, smart cities, industrial processes, and machine connectivity just to mention a few.

### Deep learning

Deep Learning is one of the main subjects of machine learning. Deep learning algorithms are composed of multiple layers to represent learning at different levels; this representation is inspired by biological neural networks [13]. Deep learning uses this Artificial Neural Networks (ANN) to feed a machine with information and generate knowledge without human interaction. Over the last few years, Deep Learning has been a trend in AI and Machine Learning systems. It's widely used in several applications such as speech recognition, object detection, natural language processing (NLP), image classification, and many more [14].

An important asset for Deep Learning is data; a lot of data is needed to give the machine enough information to make good decisions. These algorithms use the new information to change the internal parameters in the ANN for better future performance [14].

### Convolutional Neural Network

Convolutional Neural Networks (CNN) has been widely used in recent years for real-time application such as face detection [15]. This class of networks can automatically extract some features from the input data and assign relevant data, such as weight. This is called the Convolutional layer. Once the features are extracted, then the next layer processes the data in different layers to apply filters and reduce the number of parameters, this is the Pooling layers [16].

A basic example of CNN is shown in Figure 1.

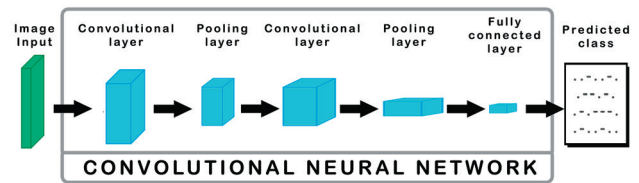


FIGURE 1. Basic CNN structure in an image classification problem.

### Image Classification

Image recognition and classification are difficult tasks for machines [17], deep learning methods are used to process the images to get better data and perform the classification, this process could be: noise reduction, slight improvement, color correction, etc. Multiple images are needed to feed the algorithms to get better results. There are techniques to improve the training data on an algorithm; these techniques are responsible for improving the quality and quantity of the data so that the algorithms work better in different types of environments; this is called data augmentation [18].

### Internet of Things

The Internet of Things (IoT) also well known as the Internet of Objects or the Internet of Everything, refers to the interconnected network of all kinds of objects, which are often equipped with data processing technology [19]. Experts estimate that by the end of the year 2025 there will be approximately 75 billion devices connected to the internet [20].

### MATERIALS AND METHODS

In this project, it is fundamental to integrate several technologies in which the communication will persist and be consistent from the diffuse to the receptor, this is, from the physical machine to the digital information visualization system. A messaging protocol for sensors and mobile devices, MQTT (Message Queue Telemetry Transport) is a well-known lightweight messaging protocol for IoT systems [21], widely used to

communicate and manage message transport from publishers to clients. This protocol must relate to other technologies to get all its potential. This section describes each one of these components that are part of all the systems to be a bridge on each layer from the overall framework.

An algorithm to explain each of the steps followed in this project is presented in Figure 2. Each step will be described in the following subsections.

Face mask detection algorithm to request access:

```

Inputs: AccessRequest, FaceMaskPrediction, User
Outputs: Access, Door
while True do
  read AccessRequest from mobile device
  if (AccessRequest = True) then
    send AccessRequest to Mosquito MQTT Server
    send User value to Dashboard
    if (FaceMaskPrediction = False) then
      Access = Denied
      Send Access value to Dashboard
    if (FaceMaskPrediction = True) then
      Access = Granted
      Door = Open
      Send Access and Door values to Dashboard
    end if
  end if
end while

```

**FIGURE 2.** Algorithm that presents the system implementation.

## Methodology

Figure 3 shows the IoT framework for this project. This framework is based on the architecture proposed and explained by the authors in [22]. In the center, it is displayed the MQTT Mosquitto Broker, which is in charge of communicating all devices and states. The clients are subscribed to the assigned topic which serves as the main communication channel. This topic contains all the user states such as the Username, ID, connection attempts, and if it is wearing the mask to grant or deny access. The message uses the JavaScript Object Notation (JSON) format, which is a lightweight data-interchange method, easy for humans to read and write and suitable for machines to process.

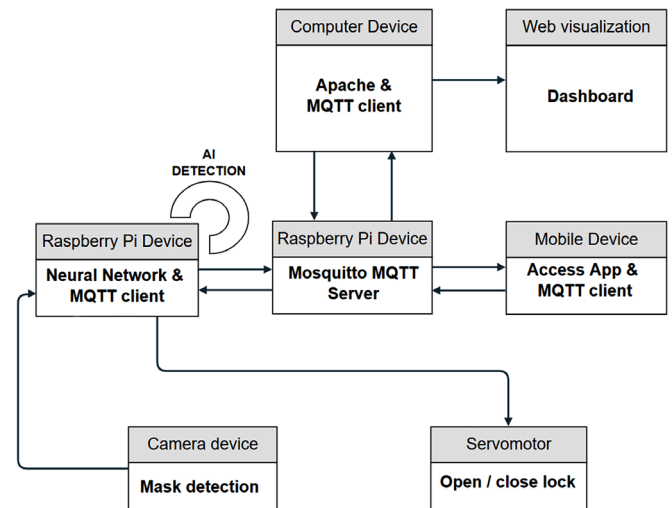


**FIGURE 3.** IoT Framework.

The three MQTT clients used for this IoT framework are one Raspberry Pi device, one computer, and the mobile device with the access request application. Raspberry Pi client controls the camera and the servomotor. Turn on the camera when access is requested and send the Open signal to the servo motor as an actuator if the access is granted. The computer client gets all the MQTT server stats to store them in the database and to update it on the dashboard. The mobile device client sends the access request within the user parameters.

The camera detects in real-time when someone requires access to the area of interest. This means that if a person puts on the mask or gets it off in a very short time, it will be detected. The Raspberry Pi receives the data from the camera and constantly communicates those values to the service layer through the internet.

The camera device and the servo motor correspond to the Physical layer. The Raspberry Pi device communicates the Physical layer status as a gateway, so it corresponds to the Communication layer. All data is transferred through the internet and stored in a database, reaching the Service layer. For this case, services are implemented on a local server configured with Apache Server.

The last layer is the Visualization one. Once the data is stored and processed it must be visualized. The parameters of the access control system are displayed on the dashboard and in the mobile device application to inform the user of its status when the access is requested. This layer also displays the ID and picture of the person requiring access.

### Face Mask Detection Algorithm

To detect in real-time whether the person in front of the camera is wearing a mask or not, a detector model was made. To train the model, the images were taken from the Kaggle Face Mask Detection Dataset [23]. This Dataset consists of 3725 images of people wearing a mask and 3728 images of people not wearing one. An example of an image used for each class can be seen in Figure 4. Masks with different colors, shapes, and textures were considered, to ensure that as many possible types of face masks were taken into consideration. For the current model, images of people wearing the mask incorrectly were not used.



FIGURE 4. Examples of the images used for the training of each class [23].

The model uses CNN and deep learning to extract and process the data to give a classification output. The CNN is designed using Keras and Tensorflow libraries from Python, and the MobileNetV2 architecture. The architecture shows an acceptable performance with low computational power [14], this makes this model suitable for embedded. Once the model was trained, it was deployed to the raspberry pi and camera to start the real-time detection, as shown in Figure 5.

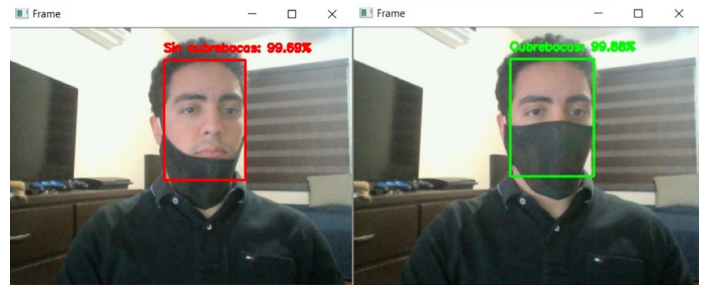


FIGURE 5. Real-time face mask detection. On the left, the interface is displayed when someone is not wearing a mask; on the right, when someone is wearing one.

### System Modelling

Cyber-physical systems, like the one presented in this paper, can be modeled using state machines to represent their behavior. For the design of the dynamics of the access control system, MATLAB’s Simulink was used. Figure 6 shows the layout where its operation is described.

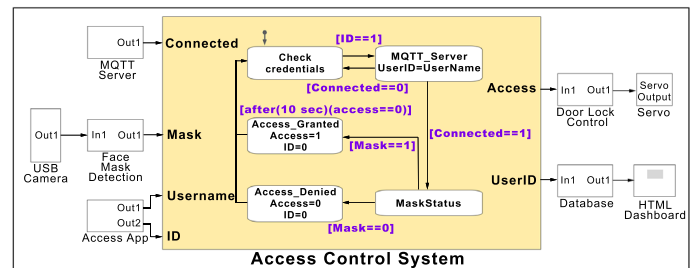


FIGURE 6. Access Control System modeled in Simulink.

The state machine represented by the Simulink Stateflow manages the behavior of the system according to the inputs it receives. These inputs are the access attempt that the person sends with their username from a mobile application, the result of the mask detection model on the image captured in real-time by the camera, and the successful or failed connection of the MQTT server. The state machine can be seen in Figure 7.

The first state is searching for an access attempt that will be made from the mobile app. Once an access attempt is detected, the system jumps to the next state which is in charge of checking the connection with the

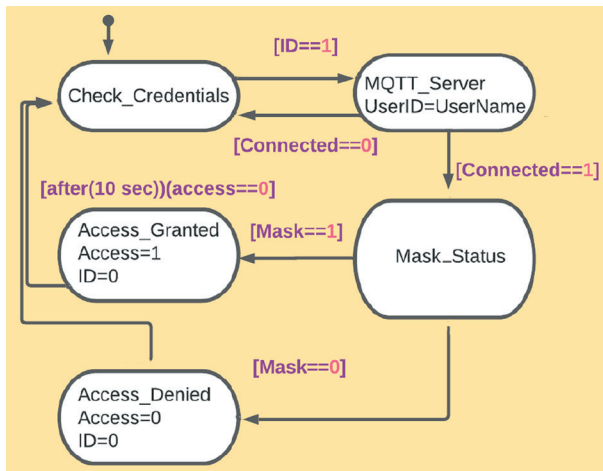


FIGURE 7. State machine for access control.

MQTT server, if the connection is successful, it goes to the other state, otherwise, it returns to the first state, and the user must retry the access until there is a successful connection; in this state, user information is sent to a database. The third state checks whether the person who wants to enter has a mask; in case of using one, the access is granted, and the door lock state is sent to be opened, in case of not having the mask, entry will be denied.

The database subsystem is receiving the user's information, store and transmit it to a dashboard designed in HTML where all the access attempts can be visualized. The door lock subsystem is responsible for controlling the servo motor or any other lock mechanism that may be selected.

### Mobile Application

The Android-based mobile application runs the Image Tracking Detection developed with the Graphical Motor Unity 3D and the Vuforia SDK Engine.

Unity is a very popular video game engine to create the most sophisticated video games and a wide range of interactive apps for several kinds of users and industries.

Vuforia Engine is a straightforward integration software development kit (SDK), that uses the newer techniques in Computer Vision for tracking or recog-

nizing images and objects for Augmented Reality applications [24]. It consists of controlling a camera sensor that captures the frames and passes them to the computer vision algorithms that analyze the datasets that detect and track real-world objects and compare them with the Vuforia web-based developer registered targets [25].

The Vuforia Engine SDK and Unity Engine's advantages to track and display content on the handheld device are applied to this work.

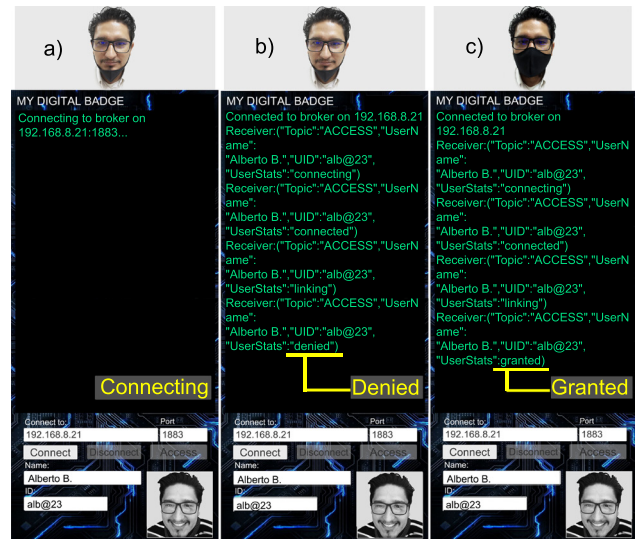


FIGURE 8. Control Access Application: a) User is connecting. b) Accessed denied. c) Access granted.

In this project, the Vuforia Engine SDK and the Unity Engine were used to develop a tracking app to trigger a mobile User Interface where the user insert its credentials to access (Figure 8).

The app is installed on a hand-held device which displays in a full-screen mode the user interface in which the control access connection will be done. The mobile application uses the M2Mqtt library, an MQTT client available for all .Net platforms for IoT and M2M communication. The Android-based mobile application runs the Image Tracking Detection developed with Unity and Vuforia SDK Engines.

## RESULTS AND DISCUSSION

### Detection Model Performance

The metrics used to evaluate the performance of the detection model are Precision, Recall, F1-score, and Accuracy. The explanation of these metrics is described below.

$$Precision = \frac{TruePos}{TruePos + FalsePos} \tag{1}$$

$$Recall = \frac{TruePos}{TruePos + FalseNeg} \tag{2}$$

$$F1\ Score = 2 \cdot \frac{Precision \cdot Recall}{Precision + Recall} \tag{3}$$

$$Accuracy = \frac{TruePos + TrueNeg}{TruePos + TrueNeg + FalsePos + FalseNeg} \tag{4}$$

In the equations (1) to (4), True Positives (TruePos) are the images that were classified correctly as positives, in this case, people wearing masks.

Similarly, True Negatives (TrueNeg) are the images correctly classified as negatives, people not wearing masks. False Positives (FalsePos) are those cases when the image is classified as positive, but it is labeled as negative. False Negatives (FalseNeg), on the other hand, are those cases when the image is classified as a negative but is labeled as a positive.

The obtained metrics for the face mask detector model after the training are presented in Figure 9.

	precision	recall	f1-score	support
with_mask	0.99	0.92	0.96	745
without_mask	0.93	0.99	0.96	766
accuracy			0.96	1511
macro avg	0.96	0.96	0.96	1511
weighted avg	0.96	0.96	0.96	1511

FIGURE 9. Classification Report.

The model presents an average accuracy of 96% when classifying if a person is wearing a mask or not.

The behavior of the model after 20 epochs of training can be seen in Figure 10. As it can be seen, the training loss decreases as the model is being trained, while the accuracy of the model increases. The total training time was close to 40 minutes.

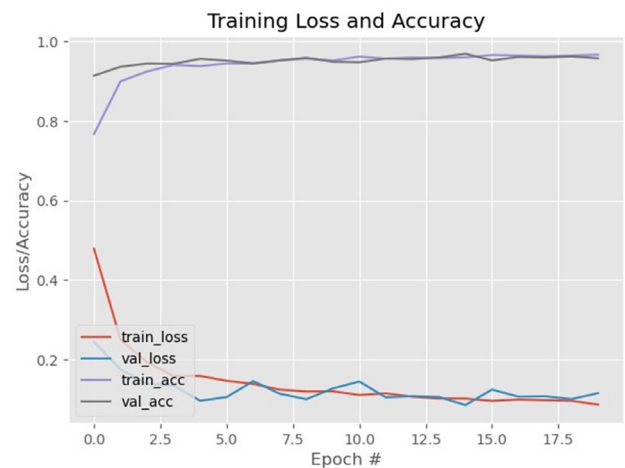


FIGURE 10. Training Loss and Accuracy of the model.

The Confusion Matrix presented in Figure 11 can lead to a better understanding of the model’s results and shows where it gets confused.

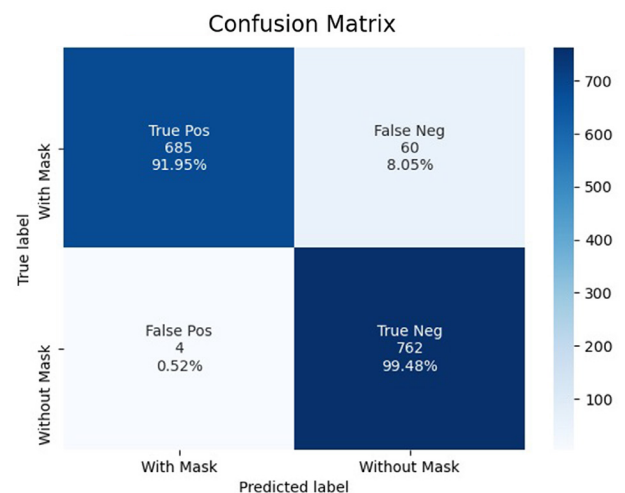


FIGURE 11. Confusion Matrix.

This model successfully identified 685 images of people wearing masks (91.95 % of True Positives) and 762 images of people not wearing masks (99.48% of True Negatives). Nevertheless, the model incorrectly

classified 60 images of people not wearing masks, when in fact they were (8.05% False Negatives). And finally, it also incorrectly classified 4 images of people wearing a mask when they weren't wearing them (0.52% False Positives), which is good for our proposal, as it will have a minimal error if a person wants to enter without a mask.

The ROC Curve displayed in Figure 12, shows the performance of the model when it is trying to differentiate one class from the other with the default threshold of 0.5. An ideal model will have an Area Under the Curve (AUC) of 1. This model presents an AUC of 0.96, which represents a good performance to distinguish between the 2 classes.

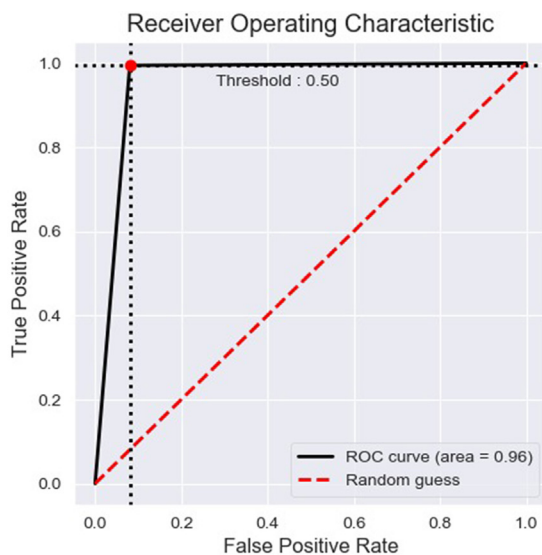


FIGURE 12. ROC Curve.

### Limitations and Future work

One limitation of the current model presented in this paper is that it was only trained with people wearing or not wearing a mask. Cases, where the person may be using the mask incorrectly, were not taken into consideration, although these cases usually classify them as not wearing masks (see Figure 5). A third class could be added with cases when the person is wearing the mask incorrectly, this would help the detector to perform better.

Another limitation of this project is the hardware of the embedded system. For this proposal, a raspberry pi 4 is used, which has certain constraints when working with real-time object detection.

Currently, the time elapsed from when the user requests access until it is recognized if the person is wearing a mask and access is granted, are 2 to 2.5 seconds. This would improve with a device with a higher GPU capacity.

The device number could be reduced by running the MQTT Mosquitto server and the Apache server in the same Raspberry Pi.

Considering that this work employs the Target Tracking technique using the Unity and Vuforia Engine's, Augmented Reality technology can be exploited to the next level by adding useful and attractive information in the field of view of the user's mobile device, having unlimited representations for user interfaces, videos, 3D objects, visual animations, or other developed features, like security and health information.

This system is flexible and adaptable to any area, section, room, department, or other places according to the needs of the company or institution. The door lock mechanism may be different from each control access, and it could be as simple or complex as it is required. For example, using a servomotor or using electromagnetic door locks.

Another implementation possibility is to add control parameters to the system, such as the ID of the Access Point or other health measures from the person.

Push-up notifications or alert messages can be applied to notify supervisors. The database could save the surveillance frame when a person is not using the mask and store the evidence for future references.

## CONCLUSIONS

In this paper, an autonomic face mask detection system applying deep learning was proposed for controlling access to critical areas. The face mask detector showed an average accuracy of 96% when detecting if the user requesting access is wearing a mask, which can be considered good performance considering that the model was created using a CNN with the MobileNetV2 architecture for low computational devices. Through the confusion matrix, it can be seen that the model classified correctly 91.95% of the True Positives (people wearing masks), 99.48% of the True Negatives (people not wearing a mask) and got confused by 8.05% with False Negatives, but only 0.52% with False Positives, which can be interpreted as good, since the system will make fewer mistakes when given access to people not wearing a mask.

The integration and connection between all the devices are made possible thanks to the application of IoT. User access is requested with their mobile device through image tracking (with the Vuforia app), this access reaches a Mosquitto server with MQTT which is also responsible for sending this request to the embedded device (raspberry pi 4) in charge of granting the access using the camera and the face detection model. This occurs in a time between 2 to 2.5 seconds, which can be reduced if a higher graphics processing device is used.

The use of face masks is essential in times of pandemic, and measures must be taken to ensure that people who leave their homes always use one when entering public places or where there is a lot of contact with other people, conditions of high risk for the infec-

tion of COVID-19. This project shows how technologies such as the IoT, artificial intelligence, and augmented reality can be integrated to help with this problem. With this system, a healthy culture can also be educated where the use of the mask is mandatory and essential to the “new normal” life.

The access system has the potential to be installed in different areas and adapted according to the needs of the establishment. The results shown in this work revealed an efficient system to control and collect information remotely, without the need for face-to-face monitoring.

A face mask detection system using artificial intelligence and powered by IoT technologies, like the one shown in this paper, has a wide application potential. Everything seems to indicate that the use of face masks will be a measure that should be adopted in different work centers and crowded places. The experience with COVID-19 should be used for the next health contingencies that could potentially occur in the following years.

## AUTHOR CONTRIBUTIONS

V. H. B. oversaw and administrated the project and obtained funding. J. P. oversaw and administrated the project. R. M. R. and C. N. realized the data curation, validation, the study of the state of the art, and prepared the original draft. R. M. R. was responsible for software implementation and data visualization. All authors methodology implementation and design, participated equally in the conception and design of the project, carried out the analysis, writing and reviewing draft.

## REFERENCES

- [1] Stilianakis NI, Drossinos Y. Dynamics of infectious disease transmission by inhalable respiratory droplets. *J R Soc Interface* [Internet]. 2010;7(50):1355-1366. Available from: <https://doi.org/10.1098/rsif.2010.0026>
- [2] Çelik I, Saatçi E, Eyüboğlu FO. Emerging and reemerging respiratory viral infections up to Covid-19. *Turk J Med Sci* [Internet]. 2020;50(SI-1):557-562. Available from: <https://doi.org/10.3906/sag-2004-126>
- [3] Lipsitch M, Cohen T, Cooper B, Robins JM, et al. Transmission Dynamics and Control of Severe Acute Respiratory Syndrome. *Science* [Internet]. 2003;300 (5627):1966-70. Available from: <https://doi.org/10.1126/science.1086616>
- [4] Blackburn RM, Frampton D, Smith CM, Fragaszy EB, et al. Nosocomial transmission of influenza: A retrospective cross-sectional study using next generation sequencing at a hospital in England (2012-2014). *Influenza Other Respir Viruses* [Internet]. 2019;13(6): 556-563. Available from: <https://doi.org/10.1111/irv.12679>
- [5] Mendelson L. Facing Your Face Mask Duties - A List of Statewide Orders. *Insight* [Internet]; 2021. Available from: <https://www.littler.com/publication-press/publication/facing-your-face-mask-duties-list-statewide-orders>
- [6] World Health Organization. Advice on the use of masks in the context of COVID-19: interim guidance-2. *World Health Organization* [Internet]; 2020. Available from: <https://apps.who.int/iris/handle/10665/332293>
- [7] Fadinger H, Schymik J. The Costs and Benefits of Home Office during the Covid-19 Pandemic - Evidence from Infections and an Input-Output Model for Germany. *COVID Economics* [Internet]. 2020;9(1):107-134. Available from: <https://doi.org/10.3886/E124902V2>
- [8] Ootom M, Otoum N, Alzubaidi MA, Etoom Y, et al. An IoT-based framework for early identification and monitoring of COVID-19 cases. *Biomed Signal Process Control* [Internet]. 2020;62:102149. Available from: <https://doi.org/10.1016/j.bspc.2020.102149>
- [9] Sahlol AT, Yousri D, Ewees AA, Al-Qaness MAA, et al. COVID-19 image classification using deep features and fractional-order marine predators algorithm. *Sci Rep* [Internet]. 2020;10(1):15364. Available from: <https://doi.org/10.1038/s41598-020-71294-2>
- [10] Khaleghi A, Moin MS. Improved anomaly detection in surveillance videos based on a deep learning method. 2018 8th Conference of AI & Robotics and 10th RoboCup Iranopen International Symposium (IRANOPEEN) [Internet]. Qazvin: IEEE; 2018:73-81. Available from: <http://doi.org/10.1109/RIOS.2018.8406634>
- [11] Lee EA, Seshia SA. *Introduction to Embedded Systems, A Cyber-Physical Systems Approach* [Internet]. Version 1.8. Berkeley: MIT Press; 2011. Available from: [https://ptolemy.berkeley.edu/books/leeseshia/releases/LeeSeshia\\_DigitalV1\\_08.pdf](https://ptolemy.berkeley.edu/books/leeseshia/releases/LeeSeshia_DigitalV1_08.pdf)
- [12] Lee EA. *Cyber Physical Systems: Design Challenges*. 2008 11th IEEE International Symposium on Object and Component-Oriented Real-Time Distributed Computing (ISORC) [Internet]. Orlando: IEEE; 2008:363-369. Available from: <http://doi.org/10.1109/ISORC.2008.25>
- [13] LeCun Y, Bengio Y, Hinton G. Deep learning. *Nature* [Internet]. 2015;521(7553):436-444. Available from: <https://doi.org/10.1038/nature14539>
- [14] Jin KH, McCann MT, Froustey E, Unser M. Deep Convolutional Neural Network for Inverse Problems in Imaging. *IEEE Trans Image Process* [Internet]. 2017;26(9):4509-4522. Available from: <http://doi.org/10.1109/TIP.2017.2713099>
- [15] Li H, Lin Z, Shen X, Brandt J, et al. A convolutional neural network cascade for face detection. 2015 IEEE Conference on Computer Vision and Pattern Recognition (CVPR) [Internet]. Boston: IEEE; 2015:5325-5334. Available from: <http://doi.org/10.1109/CVPR.2015.7299170>
- [16] Zhu W, Ma Y, Zhou Y, Benton M, et al. Deep Learning Based Soft Sensor and Its Application on a Pyrolysis Reactor for Compositions Predictions of Gas Phase Components. *Comput Aided Chem Eng* [Internet]. 2018;44(1):2245-2250. Available from: <http://doi.org/10.1016/b978-0-444-64241-7.50369-4>
- [17] Chan T, Jia K, Gao S, Lu J, et al. PCANet: A Simple Deep Learning Baseline for Image Classification? *IEEE Trans Image Process* [Internet]. 2015;24(12):5017-5032. Available from: <http://doi.org/10.1109/TIP.2015.2475625>
- [18] Shorten C, Khoshgoftaar T. A survey on Image Data Augmentation for Deep Learning. *J Big Data* [Internet]. 2019;6:60. Available from: <https://doi.org/10.1186/s40537-019-0197-0>
- [19] Escamilla-Ambrosio PJ, Rodríguez-Mota A, Aguirre-Anaya E, Acosta-Bermejo R, et al. Distributing Computing in the Internet of Things: Cloud, Fog and Edge Computing Overview. In Maldonado Y, Trujillo L, Schütze O, Riccardi A, et al (eds). *Studies in Computational Intelligence* [Internet]. Vol 731. Cham: Springer; 2018. Available from: [http://doi.org/10.1007%2F978-3-319-64063-1\\_4](http://doi.org/10.1007%2F978-3-319-64063-1_4)
- [20] Al-Bahri M, Yankovsky A, Borodin A, Kirichek R. Testbed for Identify IoT-Devices Based on Digital Object Architecture. In: Galinina O, Andreev S, Balandin S, Koucheryav Y (eds). *Internet of Things, Smart Spaces, and Next Generation Networks and Systems. NEW2AN 2018, ruSMART 2018* [Internet]. Vol. 11118. Cham: Springer. 2018. Available from: [https://doi.org/10.1007/978-3-030-01168-0\\_12](https://doi.org/10.1007/978-3-030-01168-0_12)
- [21] Yassein MB, Shatnawi MQ, Aljwarneh S, Al-Hatmi R. Internet of Things: Survey and open issues of MQTT protocol. 2017 International Conference on Engineering & MIS (ICEMIS) [Internet]. Monastir: IEEE; 2017:1-6. Available from: <https://doi.org/10.1109/ICEMIS.2017.8273112>
- [22] Pacheco J, Tunc C, Satam P, Hariri S. Secure and Resilient Cloud Services for Enhanced Living Environments. *IEEE Cloud Comput* [Internet]. 2016;3(6):44-52. Available from: <https://doi.org/10.1109/MCC.2016.129>
- [23] Gurav O. Face Mask Detection Dataset. *Kaggle* [Internet]; 2021. Available from: <https://www.kaggle.com/omkargurav/face-mask-dataset>
- [24] Getting Started with Vuforia Engine in Unity | VuforiaLibrary. PTC Inc [Internet]. [cited 2021 May 24]. Available from: <https://library.vuforia.com/articles/Training/getting-started-with-vuforia-in-unity.html>
- [25] Amin D, Govilkar S. Comparative Study of Augmented Reality SDK's. *Int J Comput Sci Appl* [Internet]. 2015;5(1):11-26. Available from: <https://doi.org/10.5121/ijcsa.2015.5102>